Scientific Research

JBiSE

ISSN: 1937-6871

Volume 3 Number 2 February 2010

Journal of Biomedical Science and Engineering

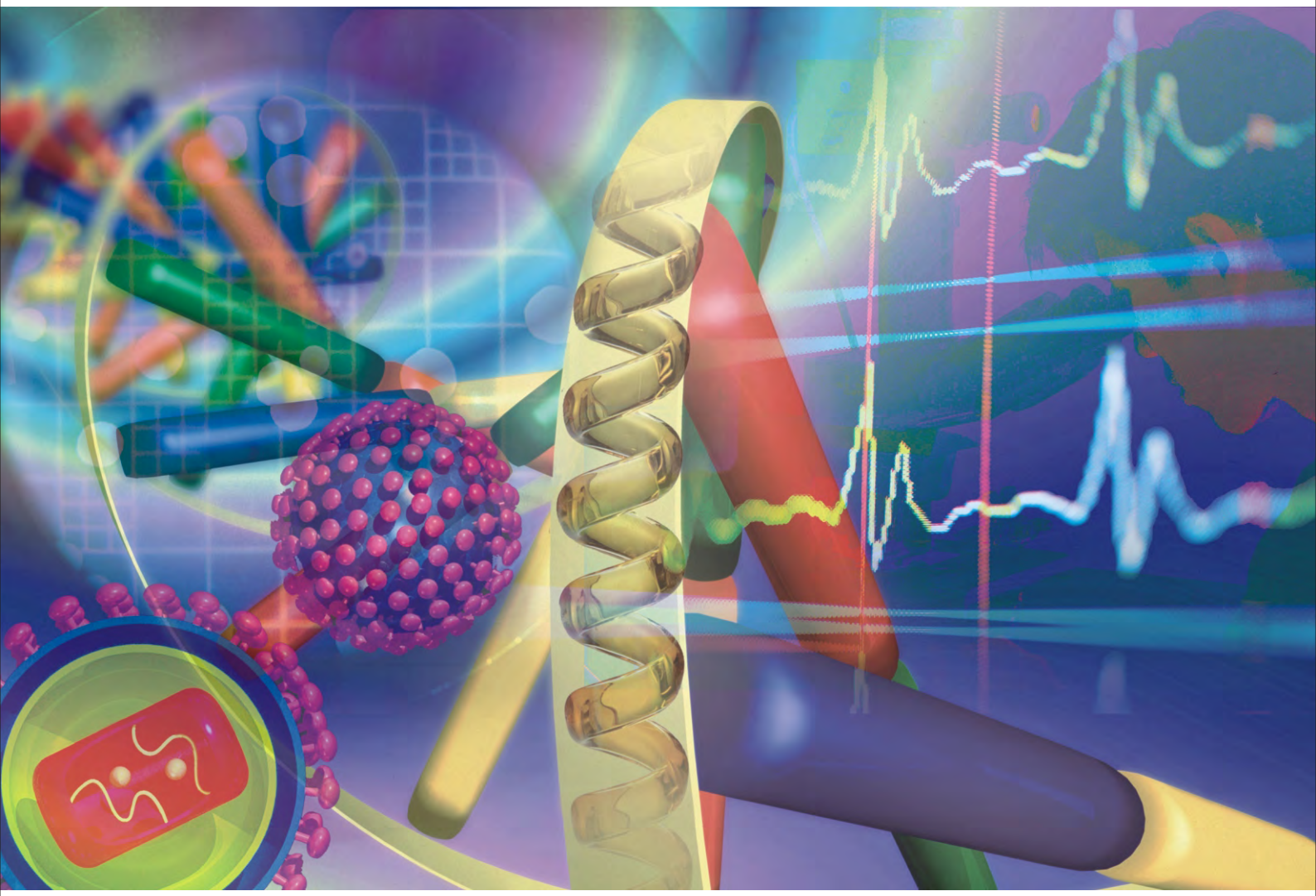

www.scirp.org/journal/jbise

Editor-in-Chief
Kuo-Chen Chou

Journal Editorial Board

ISSN 1937-6871 (Print) ISSN 1937-688X (Online)

http://www.scirp.org/journal/jbise

Editor-in-Chief

Prof. Kuo-Chen Chou Gordon Life Science Institute, San Diego, California, USA

Editorial Board (According to Alphabet)

Prof. Christopher J. Branford-White London Metropolitan University, UK
Prof. Thomas Casavant University of Iowa, USA
Dr. Arezou Ghahghaei University of Sistan ad Baluchistan, Iran
Prof. Reba Goodman Columbia University, USA
Prof. Fu-Chu He Chinese Academy of Science, China
Prof. Robert L. Heinrikson Proteos, Inc., USA
Prof. Zeng-Jian Hu Howard University, USA
Prof. Sami Khuri San Jose State University, USA
Prof. Takeshi Kikuchi Ritsumeikan University, Japan
Prof. Rob Krams Imperial College, UK
Prof. Lukasz Kurgan University of Alberta, Canada
Dr. Girdhar K. Pandey University of Delhi South Campus, India
Prof. Zhi-Pei Liang University of Illinois, USA
Prof. Juan Liu Wuhan University, China
Dr. Patrick Ma The Hong Kong Polytechnic University, Hong Kong (China)
Dr. Bouzid Menaa Nanotechnology Senior Advisor (SA), Fluorotronics, Inc. (San Diego, CA, USA), USA
Prof. Eddie Ng Technological University, Singapore
Prof. Harold A. Scheraga Cornell University, USA
Prof. Hong-Bin Shen Shanghai Jiaotong University, China
Prof. Mingui Sun University of Pittsburgh, USA
Prof. Yanmei Tie Harvard Medical School, USA
Dr. Elif Derya Ubeyli TOBB University of Economics and Technology, Turkey
Prof. Ching-Sung Wang Oriental Institute Technology, Taiwan (China)
Prof. Dong-Qing Wei Shanghai Jiaotong University, China
Prof. Zhizhou Zhang Harbin Institute of Technology, China
Prof. Jun Zhang University of Kentucky, USA

Editorial Assistants

Feng Liu Scientific Research Publishing, USA. Email: fengliu@scirp.org
Shirley Song Scientific Research Publishing, USA. Email: jbise@scirp.org

Guest Reviewers(According to Alphabet)

Odilio B. G. Assis
Jacques M.T. de Bakker
Adrian Baranchuk
P. K. Chan
Long Cheng
Chua Kuang Chua
Giuseppe Ferri
Yong Hu
Darius Jegelevicius
Kyu-young Kim
Shuzo Kobayashi
Michael Komaitis
A. Maratea
Nahel N. Saied MB
Jagadish Nayak
Adriaan van oosterom
Rangaraj M. Rangayyan
Ajit Sadana
Nina F. Schor
Pier Andrea Serra
Jong-pil Son
Qingping Sun

Journal of Biomedical Science and Engineering (JBiSE)
Published Online February 2010 in SciRes (http://www.scirp.org/journal/jbise).

TABLE OF CONTENTS

Volume 3, Number 2, February 2010

Novel method for discerning the action of selection during evolution
M. Yang, A. Solidar, G. J. Wyckoff.....109

Identification of highly conserved domains in hemagglutinin associated with the receptor binding specificity of influenza viruses: 2009 H1N1, avian H5N1, and swine H1N2
W. Hu.....114

Effect of deformation rate on the mechanical properties of arterie
J. O. V. Delgadillo, S. Delorme, V. Mora, R. DiRaddo, S. G. Hatzikiriakos.....124

A method to fabricate small features on scaffolds for tissue engineering via selective laser sintering
S. Lohfeld, M. A. Tyndyk, S. Cahill, N. Flaherty, V. Barron, P. E. McHugh.....138

Senescence of human vocal fold fibroblasts in primary culture
G. M. Adams, C. C. Xu, R. W. Chan.....148

Study on synchrony of two uncoupled neurons under the neuron's membrane potential stimulation
Y. P. Peng, J. Wang, Q. X. Miao, H. Y. Lu.....160

Design and development of a new dedicated RF sensor for the MRI of rat brain
A. Asfour.....167

Imaging characteristics of metallic interbody spacers: in vitro score evaluation of susceptibility artifacts considering different MRI sequences
T. Ernstberger, G. Heidrich, G. Buchhorn.....181

Iterative spectral subtraction method for millimeter-wave conducted speech enhancement
S. Li, J. Q. Wang, M. Niu, X. J. Jing, T. Liu.....187

Classification of non stationary signals using multiscale decomposition
M. Chendeb, M. Khalil, D. Hewson, J. Duchêne.....193

Performance comparison of three artificial neural network methods for classification of electroencephalograph signals of five mental tasks
V. Khare, J. Santhosh, S. Anand, M. Bhatia.....200

Pressure shift mediated anoikis of endothelial cells in the flow field in vitro
J. Hu, E. Y. Zhang, J. Wu, W. L. Xu, H. Q. Chen, Y. K. Shi, Y. Q. Guo.....206

Mg/Al complex oxides-A new type of solid basic catalyst for epoxidation
H. Miao, S. C. Xu, H. N. Wang, W. X. Qin, L. L. Zhang, J. M. Zhang, J. Yang, Z. Dai, G. Zheng, E. Q. Tang.....213

Biclustering of time-lagged gene expression data using real number
F. Liu, L. B. Wang.....217

Restriction fragment length polymorphism in the exon 2 of the BoLA-DRB3 gene in Chinese Holstein of the south China
X. X. Wu, Z. P. Yang, X. L. Wang, Y. J. Mao, S. C. Li, X. K. Shi, Y. Chen.....221

Copyright © 2010 SciRes.

Journal of Biomedical Science and Engineering (JBiSE)

SUBSCRIPTIONS

The ***Journal of Biomedical Science and Engineering*** (Online at Scientific Research Publishing, www.scirp.org) is published monthly by Scientific Research Publishing, Inc., USA.
E-mail: service@scirp.org

Subscription Rates: Volume 3 2010

Printed: $50 per copy.

Electronic: freely available at www.scirp.org.

To subscribe, please contact Journals Subscriptions Department at service@scirp.org.

Sample Copies: If you are interested in obtaining a free sample copy, please contact Scientific Research Publishing, Inc at service@scirp.org.

SERVICES

Advertisements

Contact the Advertisement Sales Department at service@scirp.org.

Reprints (a minimum of 100 copies per order)

Contact the Reprints Co-ordinator, Scientific Research Publishing, Inc., USA.
E-mail: service@scirp.org

COPYRIGHT

Copyright © 2010 Scientific Research Publishing, Inc.

All Rights Reserved. No part of this publication may be reproduced, stored in a retrieval system, or transmitted, in any form or by any means, electronic, mechanical, photocopying, recording, scanning or otherwise, except as described below, without the permission in writing of the Publisher.

Copying of articles is not permitted except for personal and internal use, to the extent permitted by national copyright law, or under the terms of a license issued by the national Reproduction Rights Organization.

Requests for permission for other kinds of copying, such as copying for general distribution, advertising or promotional purposes, for creating new collective works or for resale, and other enquiries should be addressed to the Publisher.

Statements and opinions expressed in the articles and communications are those of the individual contributors and not the statements and opinion of Scientific Research Publishing, Inc. We assumes no responsibility or liability for any damage or injury to persons or property arising out of the use of any materials, instructions, methods or ideas contained herein. We expressly disclaim any implied warranties of merchantability or fitness for a particular purpose. If expert assistance is required, the services of a competent professional person should be sought.

PRODUCTION INFORMATION

For manuscripts that have been accepted for publication, please contact:
E-mail: jbise@scirp.org

J. Biomedical Science and Engineering, 2010, 3, 109-113 **JBiSE**
doi:10.4236/jbise.2010.32016 Published Online February 2010 (http://www.SciRP.org/journal/jbise/).

Novel method for discerning the action of selection during evolution

Ming Yang[1], Ada Solidar[2], Gerald J. Wyckoff[1]

[1]Division Molecular Biology and Biochemistry, University of Missouri-Kansas City, Kansas City, Missouri, USA
[2]VaSSA Informatics, LLC Kansas City, Missouri, USA
Email: wyckoffg@umkc.edu, ada@vassainformatics.com

Received 10 October 2009; revised 10 December 2009; accepted 15 December 2009.

ABSTRACT

A common problem in molecular comparative genomics is the identification of genes that are under positive, adaptive selection [1]. Such genes are likely to be crucial for speciation, species differentiation, and functional specialization. However, discerning the difference between positive selection and relaxation of functional constraint can be difficult using current methods. Both processes generally increase the rate of amino acid change relative to synonymous changes within coding regions, and unless the amino acid rate is overwhelmingly high across an entire gene, the signature of positive selection can be obscured [2]. Some methodologies do not explicitly determine the difference between a relaxation of functional constraint and positive selection, leaving researchers to determine via other means whether the trajectory of a gene has been specialization or creation of a new function, or removal from the genome via a process of degeneration.

Keywords: Utilizing Information Theory; Action of Selection during Evolution

1. INTRODUCTION

Most current methods evaluate the possibility of positive selection based on the exchangeabilities of amino acids. The rationale is that if an observed amino acid substitution has a low probability in terms of their amino acids' physio-chemical properties, then it is more probable that the substitution may be driven by selection events. There are several kinds of matrices that can be used to evaluate the probability of substitutions. Function, charge, and amino acid structural properties (via Karlin and Ghandour [3]) and genetic and structural similarity (from Feng *et al*., [4]) are common methods. However, Dayhoff's PAM-250 matrix is easily the most common. Based on evolutionary distance measures from a 1,572 amino acid change data set in 71 closely related proteins, PAM stands for "percent-accepted matrix" [5]. It set the path for most matrices to come.

Henikoff and Henikoff proposed the BLOSUM (BLOcks of Amino Acid Substitution Matrix) matrices based on a large number of proteins to get a better measure of differences between two proteins specifically for more distantly related proteins [6]. To create the matrices, the BLOCKS database was searched for ungapped, highly conserved protein domains within protein families and amino acid frequency substitutions were determined, scaled by relative amino acid frequency. [7] They then calculated a log- odds score for each of the 210 possible substitutions of the 20 standard amino acids. BLOSUM was designed for search algorithms when relatively close protein relationships are being examined, such as FASTA and BLAST. However, this work set the stage for other research looking at more fine-grained matrices for evolutionary comparison and ultimately led to the work described in this paper.

Contrasting both PAM and BLOSUM matrices that are based on amino acids, Tang and co-workers proposed a universal evolutionary index (EI) for amino acid changes based on the genetic code [8]. The EIs are defined as the observed/expected amino acid changes based on the transition and transversion rate between related codons. The high correlations between EIs derived from genes with various functions in divergent species suggest that the amino acid properties are strong determinants of their substitution patterns. The EIs can be used to classify proteins based on their exchangeability and detect the positive selection in each of the groups.

There is another category of methodologies that are based on the sequence information content at specific sites. In an alignment of DNA or amino acid sequences, the information content for each position is calculated based on the distribution of the variations at that site, and they are measured in bits [9]. The information contents are smaller for divergent sites and larger for conserved sites. It can therefore be thought of as giving a measure of the tolerance for substitutions at the position: higher information content indicates that the site can

tolerate less replacements and so is more conserved, and a lower information content in a site means it can tolerate more substitutions and has been subjected to more mutations. Sequence LOGOS are graphical representations of sequence alignments [10]. Each LOGO consists of "stacks" of nucleotide or amino acid symbols, with the overall height of the stack representative of the "total" information content at that position. The height of each symbol corresponds to the relative contribution to information content of each symbol at that position within the alignment.

Although the above methods are useful, only one evolutionary variable is examined. Further sequence logos, though useful, are essentially graphic methods of illustrating the sequence conservation for the sites in an alignment, but not for the each individual sequence. Given the above problems, we are aiming at utilizing two independent parameters to access the nature of the amino acid substitutions more reliably. As Tang's EI is included, another parameter should be evolution-independent; protein structure for example, however the structure data are expensive to collect and there is no proven methods to justify the differences. Linear sequence complexity is a promising parameter as the technique is inexpensive and can be quantified for comparison across a wide range of data types.

We argue that information theory allows us to determine the gain or loss of entropy within a sequence married to evolutionary methodologies that look at the likelihood of amino acid change and rate changes allow us to determine whether a gene is evolving in an essentially neutral fashion, whether it is specializing it's function, likely gaining a new function, or heading towards non-functionalization. While information theory has been applied to non-coding regions to examine transcription factor binding sites and regulatory elements and to coding regions to examine intron/exon boundaries and alternative protein splicing [11-13], its application to comparative genomics in combination with other proven methodologies yields an interesting analysis tool for further study.

2. METHODS

2.1. Universal Evolutionary Index

For each pair-wise protein alignment, we adopted the universal evolutionary index to quantify the likelihood of the amino acid substitution [8]. This index is a universal ranking of the likelihood of amino acid change and was proposed based upon the high correlation of EIs from different sets of genes of different taxa. Comparing with other indexes, the universal evolutionary index is scaled such that its weighted average is 1, and it is easy for comparison and can be adjusted to specific species by multiplying the average Ka/Ks ratios of the given dataset.

2.2. Information Content Analysis

We adopted the program VaSSA program from VaSSA Informatics, LLC to examine linear information content. The change of information content in aligned sequences is checked and their functional meaning is accessed. The sequence subsections with fixed size are scanned across, and their linear information content is measured. The contribution of each single position in the sequence to the total information content of the sequence is evaluated.

Information content, in this specific example, is essentially a measure of the entropy rate of a particular sequence (vis a vis Shannon [14]); that is the measure of the ability to compress the sequence via some encoding. In our usage, this measure is then normalized by the channel carrier capacity of the sequence; that is, given the lexicon and it's representation, how complex could the sequence be if the symbols were arranged such that they were minimally subject to compression. Formally, the channel carrier capacity is the limiting rate for information transmittal in the medium. While over an entire genome, this rate can be calculated and would be relatively fixed, it varies within the genome based on codon usage, representation of the lexicon, and other factors (such as rate of duplication). In this case, then, we're examining what the local channel (gene or locus) could have carried across evolution vs. what the observed entropy rate within that channel is at a given point in time. This is rather different than standard definitions of bit-wise information content used in LOGOS and BLOCKS (and other usage), as in those cases information is said to be transmitted across species and the measure of the data transmittal rate is measured as a function of the frequency of inter-species change for a particular point within a sequence.

By combining the information content and universal evolutionary index, we can examine each amino acid change between sequences and plots them on a two-axis chart **(Figure 1)**; the chart is broken into quadrants, and where the majority of amino acid changes sit within the chart determines the likely evolutionary pressures acting upon a gene. This quadrants division is based on an empirical study that shows the sequences without functions (e.g. introns, intergenic sequences) are less complicated than the functional ones. Thus an unlikely amino acid change (low EI) that increases the complexity of the sequence (positive information content change) is more probable to be driven under positive selection; similarly an unlikely amino acid change (low EI) that decreases the complexity of the sequence (negative information content change) is more probable to be driven under non-functionalization of the protein. A likely (high EI) amino acid change is within the constraint. Positive information change may indicate it is within functional con-

Copyright © 2010 SciRes.

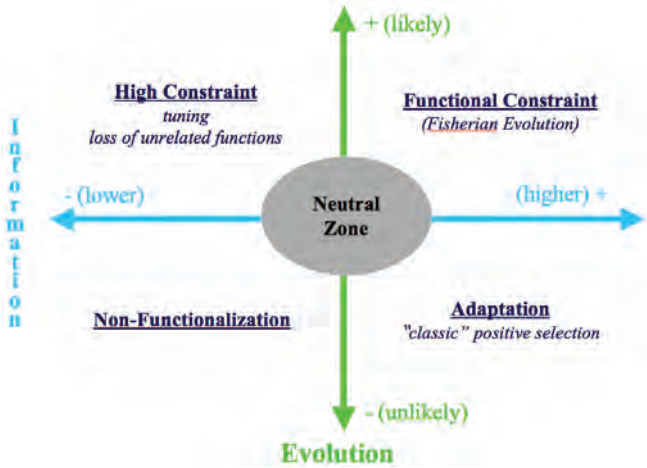

Figure 1. Functional sorting of the amino acid substitution using the information content and evolutionary index.

Omega Sub Zero sorted by ref

Ref#	Sequence	Length	Omega
1	>AEBP2_53 AEBP 2_53	123	577
2	>AEBP2_87 AEBP2_87	123	566
3	>AEBP2_120 AEBP2_120	123	582
4	>AF316573_235 AF316573_235	123	670
5	>AF316573_268 AF316573_268	123	643
6	>AF316573_301 AF316573_301	123	621
7	>AF316573_331 AF316573_331	123	672
8	>AF316573_362 AF316573_362	123	639
9	>BTEB2_135 BTEB2_135	123	496
10	>BTEB2_165 BTEB2_165	123	638
11	>BTEB2_195 BTEB2_195	123	685
12	>PACC_68 PACC_68	123	621
13	>PACC_104 PACC_104	123	571
14	>PACC_134 PACC_134	123	544
15	>WT1_323 WT1_323	123	600
16	>WT1_353 WT1_353	123	561
17	>WT1_383 WT1_383	123	493
18	>WT1_414 WT1_414	123	586
19	>ZAP1SCprot_579 ZAP1SCprot_579	123	522
20	>ZAP1SCprot_614 ZAP1SCprot_614	123	550
21	>ZAP1SCprot_705 ZAP1SCprot_705	123	554
22	>ZAP1SCprot_738 ZAP1SCprot_738	123	503
23	>ZAP1SCprot_768 ZAP1SCprot_768	123	488
24	>ZAP1SCprot_796 ZAP1SCprot_796	123	466
25	>ZAP1SCprot_824 ZAP1SCprot_824	123	513
26	>ZIC4_60 ZIC4_60	123	978
27	>ZIC4_101 ZIC4_101	123	597
28	>ZIC4_134 ZIC4_134	123	432

Figure 2. The information content of the 28 zinc finger proteins.

straint, while a negative one may hint the protein is losing some of the unrelated functions.

3. RESULTS

Zinc finger proteins are a group of protein families classified based upon their conserved sequence motif, and they are capable of binding DNA, RNA, protein and/or lipid substrates following their coordination with one or more zinc atoms [15-17]. The primary amino acid sequences, the folding, the number of fingers and their spatial arrangement jointly determine the protein's binding properties. Among the many zinc finger families with various binding modes and unique functions, the Cys2/His2(C2H2) zinc fingers were the first group to be characterized [18,19]. This subset of zinc finger proteins plays pivotal roles in DNA transcription and development in organisms. About 400 C2H2 zinc finger proteins known exist in humans, which makes them one of the largest protein families in animals. The C2H2 zinc fingers are identified by their conserved sequence motif (CX2–4FX8HX3–5H). A zinc atom can be coordinated with the two cysteines and two histidines within the motif to form a compact structure that can bind sequence specifically to DNA in its major groove. More recently, Laity and co-workers [20] found a sub-set of C2H2 zinc fingers that contains two interacting fingers, and they are evolutionarily distinct. We performed an evolutionary analysis of these data using our information theory based methods.

The data set contains 28 interacting two-finger C2H2 zinc fingers, and there is a conserved tryptophan between the first two Cysteine residues of the proteins. The information content of each sequence is calculated using VaSSA (**Figure 2**). To illustrate the site-specific change of information content, we align the DNA sequence 26 and 27 based on their peptide alignment (**Figure 3**), and calculate their information content (**Figure 4**).

The site-specific comparison of the proteins is plotted

Copyright © 2010 SciRes.

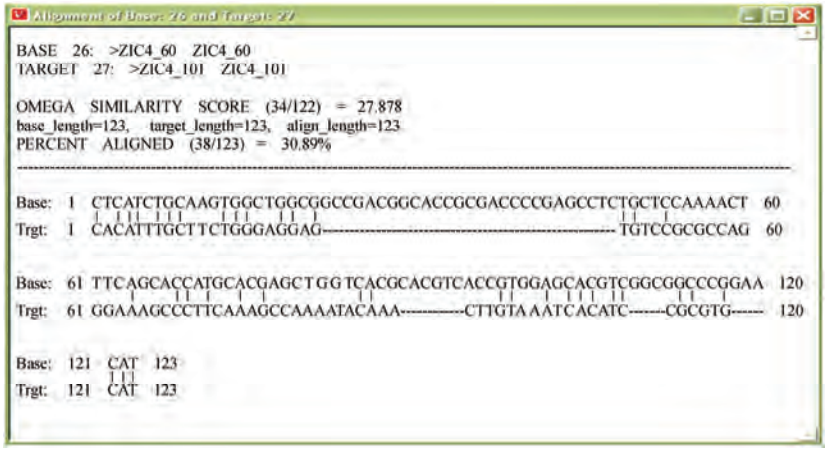

Figure 3. The DNA alignment of the zinc finger sequence 26 and 27 from **Figure 2**.

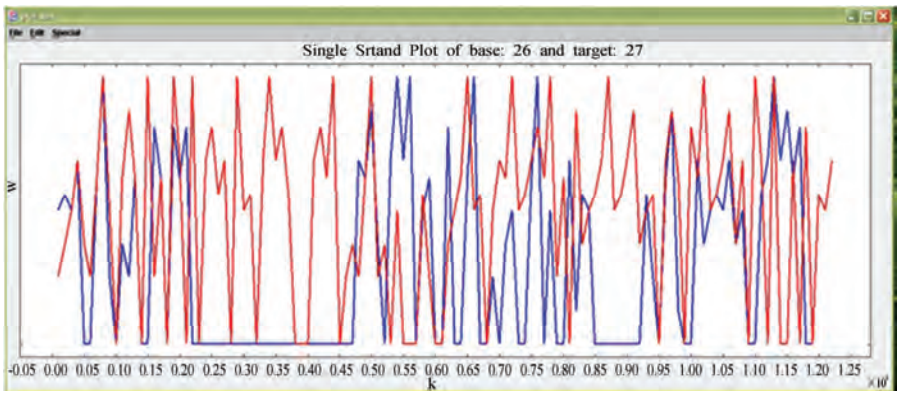

Figure 4. Change in information content along and between two sequences, the gaps show as "no information".

in **Figure 4**. The comparison is directional with sequence 26 as the basis for comparison. The sequence 26 has been posited to have a regulatory function through the interaction between fingers mediated by zinc concentration. For sequence 26, the pattern of changes is versatile: there are some regions of likely changes tied to a gain in information content, several regions of unlikely changes with an information content gain, and a few areas of unlikely changes with loss of information. These various combinations of the substitution likelihood and the change of information content may indicate the different regions of the proteins are under different kinds of evolutionary effects.

Using information content change between sequences as an evolution-independent variable will allow us to determine what factors drove sequence diversification. The method is highly reliable but data intensive, which is not currently an obstacle as the program can run in distributed mode across a cluster computer. While this paper only explores nucleotide data, we have adapted this method to protein data as well through the addition of protein semantics. In addition, we have developed this methodology further for organic molecules in general using an alternative lexicon. Our overall goal is to allow evolutionary methods to work in conjunction with information content measures within proteomics without the need of making evolutionary conclusions based on nucleotide sequences.

4. DISCUSSION

We here propose a novel method for fine mapping different evolutionary effects within proteins by simultaneously checking two independent parameters. This is promising to solve the classical problem in evolutionary studies: the difficulty of distinguishing the relaxation of functional constraints and positive selection. This method is currently in testing and development with over 50,000 protein domains for stability. The broad applicability of this method for coding region and non-coding region genomic analysis is being tested, and proteomic analysis and integration with polymorphism scoring pipelines is being developed.

Copyright © 2010 SciRes.

REFERENCES

[1] Graur, D. and Li, W.H. (2000) Fundamentals of molecular evolution. *Sinauer Associates.*

[2] Fay, J.C., Wyckoff, G.J. and Wu, C.I. (2001) Positive and negative selection on the human genome. *Genetics*, **158**, 1227-34.

[3] Karlin, S. and Ghandour, G. (1985) Multiple-alphabet amino acid sequence comparisons of the immunoglobulin kappa-chain constant domain. *Proc Natl Acad Sci U S A*, **82**, 8597-601.

[4] Feng, D.F., Johnson, M.S. and Doolittle, R.F. (1985) Aligning amino acid sequences: Comparison of commonly used methods. *J. Mol. Evol.*, **21**, 112-125.

[5] Dayhoff, M.O., Schwartz, R.M. and Orcutt, B.C. (1978) A model of evolutionary change in proteins, in Dayhoff, M.O. Edition, Atlas of Protein Sequence and Structure. *Natl. Biomed. Res. Found.*, Washington DC, **5(3)**, 345-352.

[6] Henikoff, S. and Henikoff, J.G. (1992) Amino acid substitution matrices from protein blocks. *Proc Natl Acad Sci U S A*, **89**, 10915-9.

[7] Henikoff, J.G. and Henikoff, S. (1996) Blocks database and its applications. *Methods Enzymol*, **266**, 88-105.

[8] Tang, H., Wyckoff, G.J., Lu, J. and Wu, C.I. (2004) A universal evolutionary index for amino acid changes. *Mol Biol Evol*, **21**, 1548-56.

[9] Minsky, A. (2004) Information content and complexity in the high-order organization of DNA. *Annu Rev Biophys Biomol Struct*, **33**, 317-42.

[10] Schneider, T.D. and Stephens, R.M. (1990) Sequence logos: A new way to display consensus sequences. *Nucleic Acids Res*, **18**, 6097-100.

[11] Smith, A.D., Sumazin, P. and Zhang, M.Q. (2005) Identifying tissue-selective transcription factor binding sites in vertebrate promoters. *Proc Natl Acad Sci U S A*, **102**, 1560-5.

[12] Nalla, V.K. and Rogan, P.K. (2008) Automated splicing mutation analysis by information theory. *Hum Mutat*, **29**, 1168.

[13] Nalla, V.K. and Rogan, P.K. (2005) Automated splicing mutation analysis by information theory. *Hum Mutat*, **25**, 334-42.

[14] Shannon, C.E. (1948) A mathematical theory of communication. *Bell System Technical Journal*, **27**, 379-423, 623-656.

[15] Hall, T.M. (2005) Multiple modes of RNA recognition by zinc finger proteins. *Curr Opin Struct Biol*, **15**, 367-73.

[16] Brown, R.S. (2005) Zinc finger proteins: Getting a grip on RNA. *Curr Opin Struct Biol*, **15**, 94-8.

[17] Klug, A. (1999) Zinc finger peptides for the regulation of gene expression. *J Mol Biol*, **293**, 215–8.

[18] Schuh, R. *et al*. (1986) A conserved family of nuclear proteins containing structural elements of the finger protein encoded by Kruppel—a drosophila segmentation gene. *Cell*, **47**, 1025-32.

[19] Miller, J., McLachlan, A.D. and Klug, A. (1985) Repetitive zinc-binding domains in the protein transcription factor IIIA from Xenopus oocytes. *Embo J*, **4**, 1609-14.

[20] Wang, Z. *et al.* (2006) Solution structure of a Zap1 zinc-responsive domain provides insights into metalloregulatory transcriptional repression in Saccharomyces cerevisiae. *J Mol Biol*, **357**, 1167-83.

Copyright © 2010 SciRes.

J. Biomedical Science and Engineering, 2010, 3, 114-123 **JBiSE**
doi:10.4236/jbise.2010.32017 Published Online February 2010 (http://www.SciRP.org/journal/jbise/).

Identification of highly conserved domains in hemagglutinin associated with the receptor binding specificity of influenza viruses: 2009 H1N1, avian H5N1, and swine H1N2

Wei Hu

Department of Computer Science, Houghton College, Houghton, New York, USA.
Email: wei.hu@houghton.edu

Received 11 December 2009; revised 14 December 2009; accepted 15 December 2009.

ABSTRACT

The hemagglutinin (HA) of influenza viruses facilitates receptor binding and membrane fusion, which is the initial step of virus infection. Human influenza viruses preferentially bind to receptors with α2-6 linkages to galactose (SAα2,6Gal), whereas avian influenza viruses prefer receptors with α2-3 linkages to galactose (SAα2,3Gal). The current 2009 H1N1 pandemic is caused by a novel influenza A virus that has its genetic materials from birds, humans, and pigs. Its pandemic nature is characterized clearly by its dual binding to the α2-3 as well as α2-6 receptors, because the seasonal human H1N1 virus only binds to the α2-6 receptor. In a previous study, the informational spectrum method (ISM), a bioinformatics technique, was applied to uncover one highly conserved region in the HA protein associated with receptor binding preference in each of various influenza subtypes. In the present study, we extended the previous work by discovering multiple such domains in HA of 2009 H1N1 and avian H5N1 to expand our repertoire of known key regions in HA responsible for receptor binding affinity. Three such domains in HA of 2009 H1N1 were found at residue positions 106 to 130, 150 to 174, and 191 to 221, and another three domains in HA of avian H5N1 were located at residue positions 46 to 65, 136 to 153, and 269 to 286. These identified domains could be utilized as therapeutic and diagnostic targets for the prevention and treatment of influenza infection.

Keywords: Binding Specificity; Discrete Fourier Transform; Electron-Ion Interaction Potential; Entropy; Hemagglutinin; Influenza; Informational Spectrum Method

1. INTRODUCTION

Influenza A viruses have two surface proteins, hemagglutinin (HA) and neuraminidase (NA). HA is a homotrimer, in which each monomer comprises two subdomains, HA1 and HA2. HA1 initializes the contact with the cell membrane and HA2 mediates membrane fusion. The first step in the infection of influenza viruses is binding of their surface protein HA to sialylated glycan receptors on the host cells. In general, human influenza and avian viruses preferentially bind to the α2-3 sialylated and α2-6 sialylated glycan receptors, respectively. Pigs have receptors for both human and avian influenza viruses on their tracheal epithelial cells, thus they can serve as a mixing vessel to re-assort genes from different species to make new influenza viruses.

The interaction between HA and its receptors has been studied biologically, genetically, and structurally. The different binding phenotypes of human and avian influenza viruses suggest that the avian viruses could not readily infect humans. However, the human infection by H5N1 chicken viruses in Hong Kong in 1997 implied for the first time that it is possible for avian viruses to infect humans directly, which was explained in part by the finding that human airway epithelium harbors α2–3-linked sialic acids on ciliated cells [1]. It is believed that HA binding affinity for receptors is a critical factor of host switch. In addition to the current 2009 pandemic H1N1, the past three flu pandemics, the Spanish flu in 1918, the Asian flu in 1957, and the Hong Kong flu in 1968, all had arisen through reassortment among avian, human, and swine strains. Hence, the importance of expanding our knowledge on the receptor-binding affinity of the influenza viruses is apparent.

Various approaches such as structural analysis, protein evolution, and mathematical modeling have been used to study the interactions between HA and its receptors. To quantitatively elucidate the binding specificity of HA to avian and human receptors, the interaction energy between HA and its receptors were analyzed with the ab initio fragment molecular orbital (FMO) method [2], which clarified the role of the mutated residues Glu190 and Gln226 in the binding patterns of H5 HA. The report

in [3] discovered that the mutations at positions 182 and 192 in HA1 independently switch H5N1 virus binding preferences from avian to human type, which could serve as molecular markers for measuring the pandemic potential of H5N1 isolates.

Using sequence analysis and homology modeling [4], the HA protein of 2009 H1N1 was found to have the signature amino acid Asp190 and Asp225 known to confer binding affinity to α2-6 sialylated glycan receptors. The mutation Glu190Asp between avian and human H1 HA normally would lead to the loss of a critical contact with α2-3 glycans, which, however, was compensated by the presence of Lys145 in HA of 2009 H1N1. There were four loops in 2009 H1N1 HA, 130 loop, 140 loop, 150 loop, and 220 loop, each containing one Lys, to form a positively charged 'lysine fence' at the base of the binding site to support optimal contacts with the α2-6 and α2-3 receptors. Based on this structural analysis, it was predicted that the HA protein of 2009 H1N1 virus can bind to the α2-6 as well as α2-3 sialylated glycan receptors, which was verified later by the carbohydrate microarray analysis in [5].

There were several other efforts in expanding the knowledge on 2009 H1N1. One study [6] investigated the three aspects of NA: the mutations and co-mutations, the stalk motifs, and the phylogenetic analysis. The potential mutations and strongly co-mutated positions of NA were found. A special NA stalk motif of high virulence, which was dominant in the past H5N1 strains, was discovered in H1N1 in 2009 for the first time. Another study [7] focused on HA and the interaction between HA and NA. The mutations of HA in 2009 H1N1 were found and mapped to the 3D homology model of H1, and the mutations on the five epitope regions on H1 were identified. The distinct response patterns of HA to the changes of NA stalk motifs were discovered, illustrating the functional dependence between HA and NA. With help from the results of the first study in [6], two co-mutation networks were uncovered, one in HA and one in NA, where each mutation in one network co-mutates with the mutations in the other network across the two proteins HA and NA. These two networks residing in HA and NA separately may provide a functional linkage between the mutations that can change the drug binding sites in NA and those that can affect the host immune response or vaccine efficacy in HA.

The informational spectrum method (ISM) [8] is a bioinformatics technique to study the biological functions of proteins with their physicochemical properties, which first translates a protein sequence into a numerical sequence based on each amino acid's electron-ion interaction potential (EIIP) and then the discrete Fourier transformation (DFT) is applied to it to create an informational spectrum. It is believed that the protein functions including the protein-protein interaction are encoded in the peaks of the informational spectrum.

Highly conserved regions in a protein sequence usually have functional or structural values. The active site of enzymes and the binding sites of protein receptors are typical examples of these highly conserved regions.

In references [9-11], the ISM was applied successfully to characterize the conserved information pertinent to the interaction between HIV-1 and their CD4, CCR5, and CXCR4 receptors. In [12,13] the same research group applied the ISM to investigate the interaction between HA and its receptors. Their findings showed that HA1 of different flu subtypes encodes one highly conserved domain that might be determinants of HA binding affinity. Our goal in this study is to extend the results in [12,13] by identifying multiple domains in HA1 associated with each receptor interaction pattern. These conserved domains in HA1 might be used to develop targets for new drugs and infection control.

In [12,13] it was found that the consensus informational spectrum (CIS) of HA1 of influenza strains have the following characteristic dominant peaks at different IS frequencies as presented in **Table 1**. In this study, F(0.295) will be referred to as pandemic human H1N1 receptor interaction frequency, F(0.055) as swine receptor interaction frequency, F(0.076) as avian receptor interaction frequency, and F(0.236) as seasonal human H1N1 receptor interaction frequency.

Table 1. Characteristic IS frequencies of HA proteins in 2009 H1N1, swine H1N1/H1N2, avian H5N1, and seasonal human H1N1.

Subtype	2009 H1N1	Swine H1N2/H1N1	Avian H5N1	Seasonal human H1N1
Frequency	F(0.295)	F(0.055)	F(0.076)	F(0.236)

Table 2. The receptor recognition domains of HA proteins in H1N1, H3N2, H5N1, and H7N7 influenza viruses.

Strain	Frequency	Residues
A/California/04/2009 (H1N1)	F(0.295)	284 – 326
A/Hong Kong/213/03 (H5N1)	F(0.076)	42 – 75
A/New Caledonia/20/99 (H1N1)	F(0.236)	262 – 295
A/New York/383/2004 (H3N2)	F(0.363)	57 – 90
A/equine/Prague/56 (H7N7)	F(0.285)	28 – 61
A/Egypt/0636-NAMRU3/2007(H5N1)	F(0.236)	99 – 132
A/South Carolina/1/18 (H1N1))	F(0.258)	87 – 120

Copyright © 2010 SciRes.

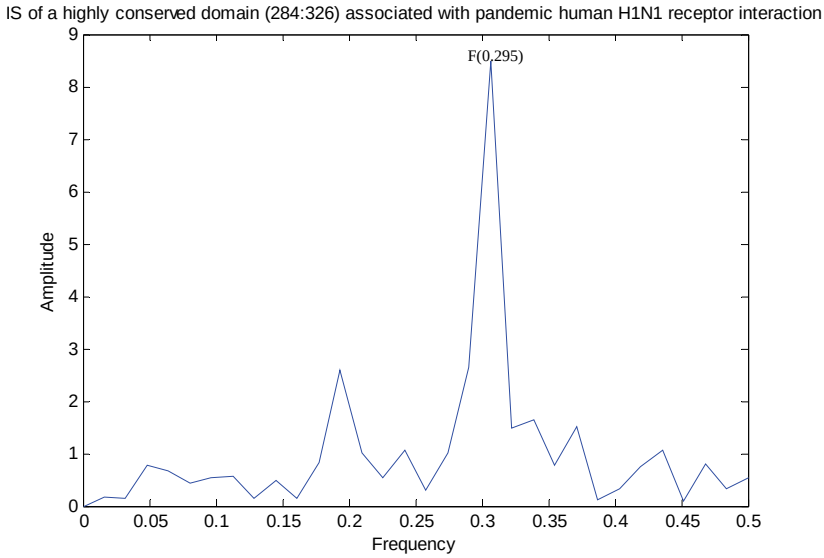

Figure 1. The informational spectrum of a highly conserved domain in 2009 H1N1 found in [12], which is also a part of **Figure 5** in [12].

Their analysis also found the following receptor recognition domains in HA proteins from H1N1, H3N2, H5N1, and H7N7 (**Table 2**). The IS of one such domain in A/California/04/2009 was displayed in **Figure 1**, which was a reproduced figure in [12].

2. MATERIALS AND METHODS

2.1. Sequence Data

All HA sequences were retrieved from the Influenza Virus Resource (http://www.ncbi/nlm.nih.giv/genomes/FLU/FLU.html) of the National Center for Biotechnology Information (NCBI) on Nov. 20, 2009. Only the full length and unique sequences were selected. There were 450 HA sequences of human 2009 H1N1, 1228 HA sequences of avian H5N1 from 1959 to 2009, and 83 HA sequences of swine H1N2 from 1980 to 2009. All the sequences used in the study were aligned with MAFFT [14].

2.2. Entropy

In information theory [15], entropy is a measure of disorder or randomness associated with a random variable. Let x be a discrete random variable that has a set of possible values $\{a_1, a_2, a_3, \ldots a_n\}$ with probabilities $\{p_1, p_2, p_3, \ldots p_n\}$ where $P(x = a_i) = p_i$. The entropy H of x is

$$H(x) = -\sum_i p_i \log p_i$$

In the current study, each of the n columns in a multiple sequence alignment of a set of HA sequences of N residues is considered as a discrete random variable x_i (1 ≤i ≤N) that takes on one of the 20 (n=20) amino acid types with some probability. $H(x_i)$ has its minimum value 0 if all the residues at position i are the same, and achieves its maximum if all the 20 amino acid types appear with equal probability at position i, which can be verified by the Lagrange multiplier technique. A position of high entropy means that the amino acids are often varied at this position. $H(x_i)$ measures the genetic diversity at position i in our current study. A brief overview of the extensive applications of entropy in sequence analysis, in particular the flu virus sequences, can be found in [6].

2.3. Important Sites in HA

Although there is a great variation due to high selection pressure in the HA1 sequences of various flu subtypes, the active site of HA1 is well conserved, which is located in a cleft composed of the residues 91, 150, 152, 180, 187, 191, and 192 [16]. The three amino acids at positions 187, 191 and 192 are a part of the 190 helix. The active site cleft of HA is formed by its right edge (131_GVTAA) and left edge (221_RGQAGR) (H1 numbering), which are also commonly referred to as the 130 loop and 220 loop, respectively [17].

The human immune system responds primarily to the five epitope regions, A, B, C, D, and E, of the HA protein in H1N1. **Table 3** presents the 160 amino acids on the five epitope regions of HA in H1 subtype as discovered in [18].

2.4. Informational Spectrum Method

The informational spectrum method is a bioinformatics

Copyright © 2010 SciRes.

technique that can be utilized to analyze protein sequences. Prior to this analysis, the protein sequences have to be translated into numerical sequences. One such approach is to assign each amino acid to its electron-ion interaction potential (EIIP), which represents the average energy of the valence electrons in the amino acid (**Table 4**). The application of EIIP to protein function analysis assumes that the strength of the electromagnetic field surrounding the protein is indicative of its biological function. This method was successful in revealing various protein properties [8].

The numerical sequence $x(m)$ of a protein sequence is transformed into the frequency domain using DFT. The DFT coefficients $x(n)$ are defined as

$$X(n) = \sum x(m) e^{-j\left(\frac{2\pi}{N}\right)nm} \qquad n = 1, 2, \ldots N/2$$

where N is the length of sequence $x(m)$.

The energy density spectrum is defined as

$$S(n) = X(n)X^*(n) = |X(n)|^2, \qquad n = 1, 2, \ldots N/2$$

The informational spectrum (IS) of a sequence $x(m)$ comprises the frequencies and the amplitudes of its DFT.

Peak frequencies of IS of a protein sequence reflect its biological or biochemical functions. To determine the same biological or biochemical functions of a group of protein sequences, a consensus informational spectrum (CIS) can be used, which is defined as the product of energy density spectrum $S(n)$ of each sequence in the group. A measure of similarity for each peak is a signal-to-noise ratio (S/N), which is defined as a ratio of signal density to the mean value of the whole spectrum [12]. The theory of CIS [8] states that:

1) One peak only exits for a group of protein sequences sharing the same biological function.

2) No signal peak exists for biologically unrelated protein sequences.

3) Peak frequencies are different for different biological functions.

Table 3. Amino acids on epitopes A, B, C, D, and E of H1 subtype (A/California/04/2009 numbering) from [18].

Epitope	Amino acids	Number of amino acids
A	118,120,121,122,126,127,128,129,132,133,134,135,137,139,140,141,142,143,146,147,149,165,252,253	24
B	124,125,152,153,154,155,156,157,160,162,183,184,185,186,187,189,190,191,193,194,195,196	22
C	34,35,36,37,38,40,41,43,44,45,269,270,271,272,273,274,276,277,278,283,288,292,295,297,298,302,303,305,306,307,308,309,310	32
D	170,171,172,173,174,176,179,198,200,202,204,205,206,207,208,209,210,211,212,213,214,215,216,222,223,224,225,226,227,235,237,239,241,243,244,245	48
E	47,48,50,51,53,54,56,57,58,66,68,69,70,71,72,73,74,75,78,79,80,82,83,84,85,86,102,257,258,259,260,261,263,267	34

Table 4. The electron-ion interaction potential (EIIP) of amino acids used to encode amino acids.

Amino acid	EIIP	Amino acid	EIIP
L	0.0000	Y	0.0516
I	0.0000	W	0.0548
N	0.0036	Q	0.0761
G	0.0050	M	0.0823
E	0.0057	S	0.0829
V	0.0058	C	0.0829
P	0.0198	T	0.0941
H	0.0242	F	0.0946
K	0.0371	R	0.0959
A	0.0373	D	0.1263

Copyright © 2010 SciRes.

2.5. Three Consensus HA1 Sequences of 2009 Human H1N1, Avian H5N1, and Swine N1N2

We employed MAFFT to align the three consensus HA1 sequences of 2009 H1N1, avian H5N1, and swine H1N2 (**Figure 2**). Each consensus sequence was then used in the ISM analysis to find the highly conserved domains in HA1 of different influenza subtypes.

3. RESULTS

As demonstrated in [12,13], the HA1 sequences in various influenza subtypes had a distinct propensity to interact with a specific receptor, and there was a region in HA1 encoding highly conserved information that might be associated with the binding preference. The main task of the present study is to explore the other parts of the HA1 sequences to find domains of the same biological function. Entropy of HA1 in each subtype of 2009 H1N1, swine H1N2, and avian H5N1 was calculated, which illustrated the most conserved positions in the HA1 sequences of each subtype (**Figures 5**, **7**, and **10**). The ISM bioinformatics technique was applied to the three consensus HA1 sequences as presented in **Figure 2** to uncover the conserved domains in HA1, which might modulate receptor specificity in each subtype. In contrast, the ISM analysis in [12,13] was applied to a particular selected strain in a subtype such as A/California/04/2009 in 2009 H1N1 to find a conserved region. On the whole, the conserved domains discovered by our approach using a consensus sequence had more coverage to different sequences in a subtype than the single strain approach in [12,13].

3.1. Conserved Domains in HA1 of 2009 H1N1

We discovered three domains in HA1 of 2009 H1N1, which were located at residue positions 106 to 130, 150 to 174, and 191 to 221. The consensus sequences of theses domains were SSVSSFERFEIFPKTSSWPNHDSNK,

```
                                 1                                                          60
1 2009  H1N1                     DTLCIGYHANNSTDTVDTVLEKNVTVTHSVNLLEDKHNGKLCKLRGVAPLHLGKCNIAGW
2 Swine H1N1                     DTLCIGYHANNSTDTVDTVLEKNVTVTHSVNLLEDRHNGKLCKLRGVAPLHLGKCNIAGW
3 Avian H5N1                     DQICIGYHANNSTEQVDTIMEKNVTVTHAQDILEKTHNGKLCDLDGVKPLILRDCSVAGW
                                 * :**********: ***::********: ::**. ******.* ** ** * .*.:***

                                 61                                                        120
1 2009  H1N1                     ILGNPECESLSTASSWSYIVETSSSDNGTCYPGDFIDYEELREQLSSVSSFERFEIFPKT
2 Swine H1N2                     LLGNPECESLFTASSWSYIVETSNSDNGTCYPGDFINYEELREQLSSVSSFERFEIFPKE
3 Avian H5N1                     LLGNPMCDEFINVPEWSYIVEKANPANDLCYPGNFNDYEELKHLLSRINHFEKIQIIPK-
                                :**** *:.: ....******.:.. *. ****:* :****:. ** :. **:::*:**

                                 121          right edge                                   180
1 2009  H1N1                     SSWPNHDSNKGVTAACPHAGAKSFYKNLIWLVKKGNSYPKLSKSYINDKGKEVLVLWGIH
2 Swine H1N2                     SSWPNHDTNRGVTAACPHAGANSFYRNLIWLVKKGNSYPKLSKSYINNKEKEVLVLWGIH
3 Avian H5N1                     SSWSDHEASSGVSSACPYQGRSSFFRNVVWLIKKNNAYPTIKRSYNNTNQEDLLVLWGIH
                                 ***.:*::. **::***: * .**::*::**:**.*:**.:.:** * : :::*******

                                 181                                         left edge      240
1 2009  H1N1                     HPSTSADQQSLYQNADAYVFVGSSRYSKKFKPEIAIRPKVRDQEGRMNYYWTLVEPGDKI
2 Swine H1N2                     HPSTSADQQSLYQNADAYVFVGSSHYSKKFTPEIAKRPKVRDQAGRMNYYWTLVEPGDTI
3 Avian H5N1                     HPNDAAEQTRLYQNPTTYISVGTSTLNQRLVPKIATRSKVNGQSGRMEFFWTILKPNDAI
                                 **. :*:*  ****. :*: **:*  .::: *:** *.**..* ***:::**:::*.* *

                                 241                                                        300
1 2009  H1N1                     TFEATGNLVVPRYAFAMERNAGSGIIISDTPVHDCNTTCQTPKGAINTSLPFQNIHPITI
2 Swine H1N2                     TFEATGNLVVPRYAFALKRGSGSGIIISDTSVHDCNTTCQTPKGAINTSLPFQNIHPVTI
3 Avian H5N1                     NFESNGNFIAPEYAYKIVKKGDSTIMKSELEYGNCNTKCQTPMGAINSSMPFHNIHPLTI
                                 .**:.**::.*.**: : : ..* *: *:    :***.**** ****:*:**:****:**

                                301                          328
1 2009  H1N1                     GKCPKYVKSTKLRLATGLRNVPSIQSR-
2 Swine H1N2                     GECPKYVKSTKLRMATGLRNIPSIQSR-
3 Avian H5N1                     GECPKYVKSNRLVLATGLRNSPQRERRR
                                 *:*******.:* :****** *. : *
```

Figure 2. Multiple sequence alignment of three consensus HA1 sequences in 2009 H1N1, swine H1N2, and avian H5N1. The binding sites in HA are colored in red, and the left and right edges of the binding cleft are printed in boldface type.

Copyright © 2010 SciRes.

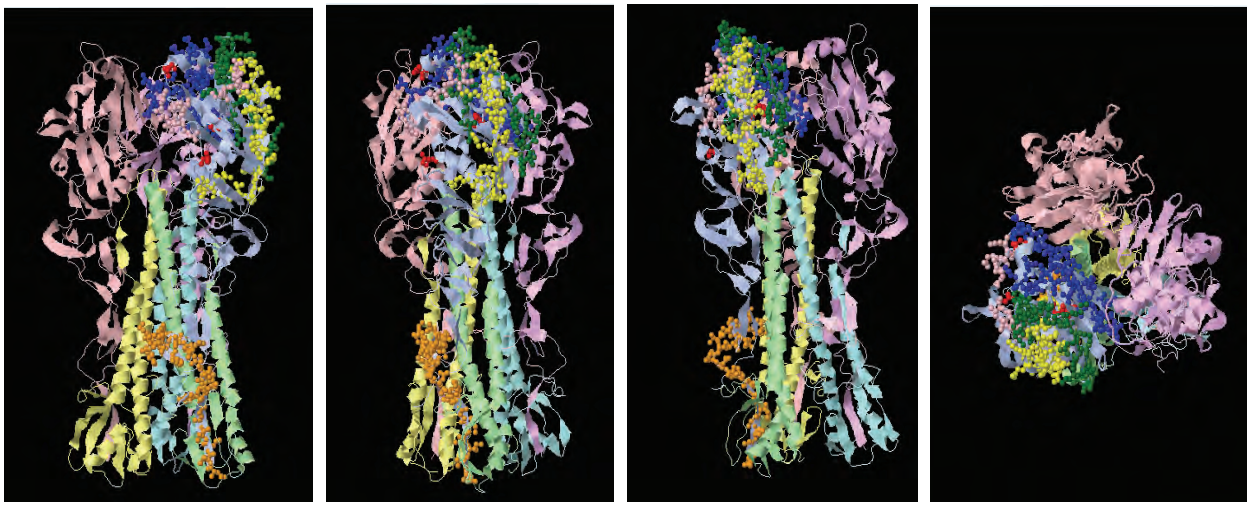

Figure 3. The four plots show in 3D structure the four highly conserved domains found in this study, three domains in 2009 H1N1 and one domain in swine H1N2. Binding sites are colored in red, two edges of the binding cleft in pink, domain 106:130 in 2009 H1N1 in yellow, domain 150:174 in 2009 H1N1 in green, domain 191:221 in 2009 H1N1 in blue, and domain 1:29 in swine H1N2 in orange (PDB code: 1RU7).

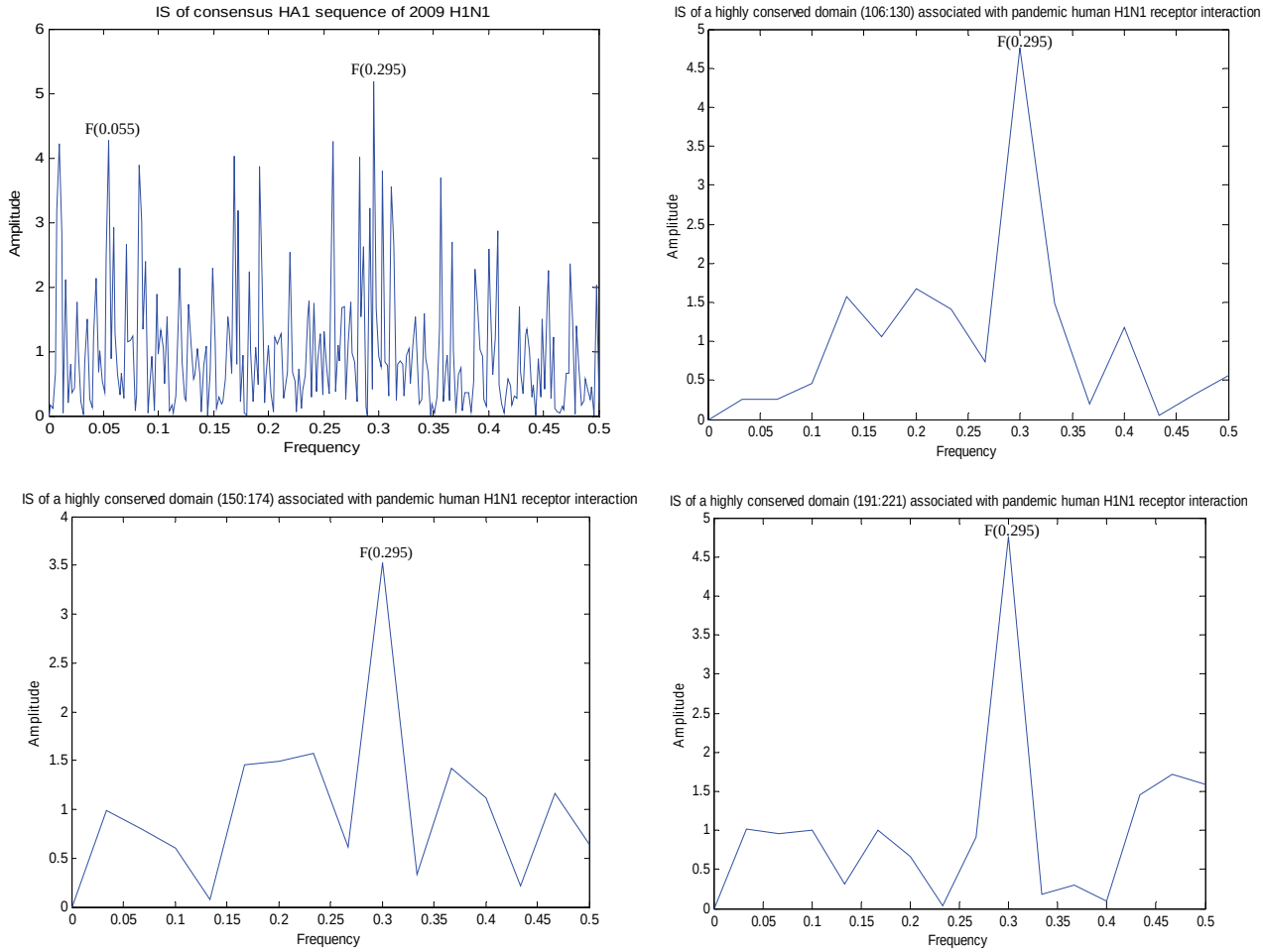

Figure 4. The top left plot shows the informational spectrum of consensus HA1 sequence in 2009 H1N1. The other three plots show the informational spectrum of the three conserved domains in 2009 H1N1 found in this study, 106:130, 150:174, and 191:221, respectively.

Copyright © 2010 SciRes.

WLVKKGNSYPKLSKSYINDKGKEVLV, and LYQNDAYVFVGSSRYSKKFKPEIAIRPKVR, respectively, and the ISs of these three domains and the consensus HA1 sequence in 2009 H1N1 were plotted in **Figure 4**. The IS of the consensus HA1 sequence in 2009 H1N1displayed a dominant peak at frequency F(0.295) and a less prominent peak at frequency F(0.055). The domain 106:130 was next to the right edge of the active site cleft of HA1 and overlapping with epitopes A and B **(Table 1)**, the domain 150:174 contained two binding sites 150 and 152 and overlapping with epitopes B and D, and the domain 191:221 contained the 190 helix and was overlapping with epitopes B and D. The important locations of these three domains found in HA1 exhibited their significant roles in the binding affinity for 2009 H1N1. As seen from the entropy distribution in **Figure 5**, these three domains were highly conserved. They were displayed with four different views in the H1 3D model in **Figure 3**. In [12], a similar domain was found in the C-terminus of the HA protein consisting of residues 284 – 326.

3.2. Conserved Domains in HA1 of Swine H1N2

In [12], the sequences of swine H1N1 and H1N2 were combined into a single dataset for analysis. Here the swine H1N2 was discussed as a single dataset. We found one domain in HA1 of swine H1N2, which was located in the N-terminus of the protein at residues 1 to 29, and its consensus sequence was DTLCIGYHANNSTDTVDTVLEKNVTVTHS. The domain 1:29 found here was presented with four different views in the H1 3D model in **Figure 3**, along with the three domains discovered in HA1 in 2009 H1N1. The ISs of the domain 1:29 and the consensus HA1 sequence in swine H1N2 were displayed in **Figure 6**. The IS of the consensus HA1 sequence in swine H1N2 revealed two dominant peaks at frequencies of F(0.055) and F(0.295). The entropy in **Figure 5** suggested that the domain 1:29 was well conserved.

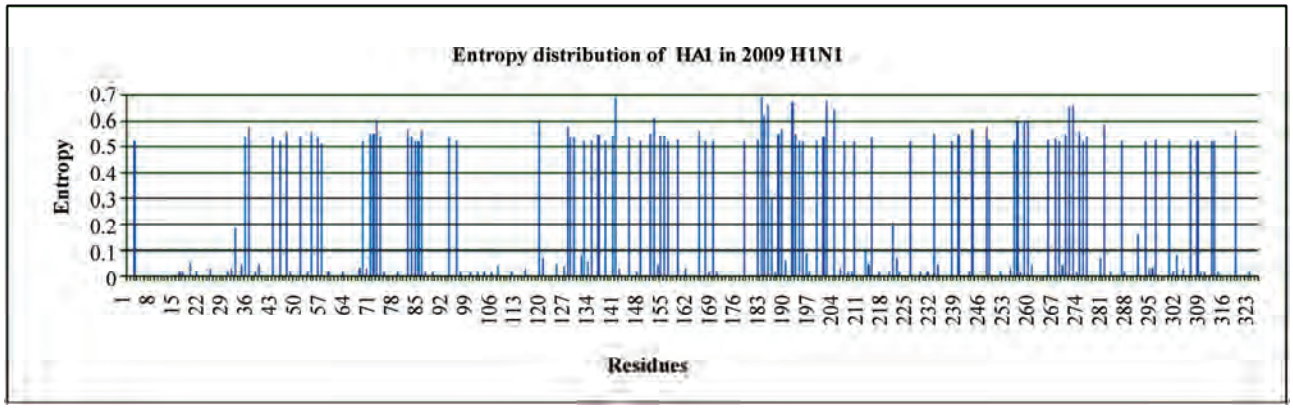

Figure 5. Entropy distribution of HA1 in 2009 H1N1.

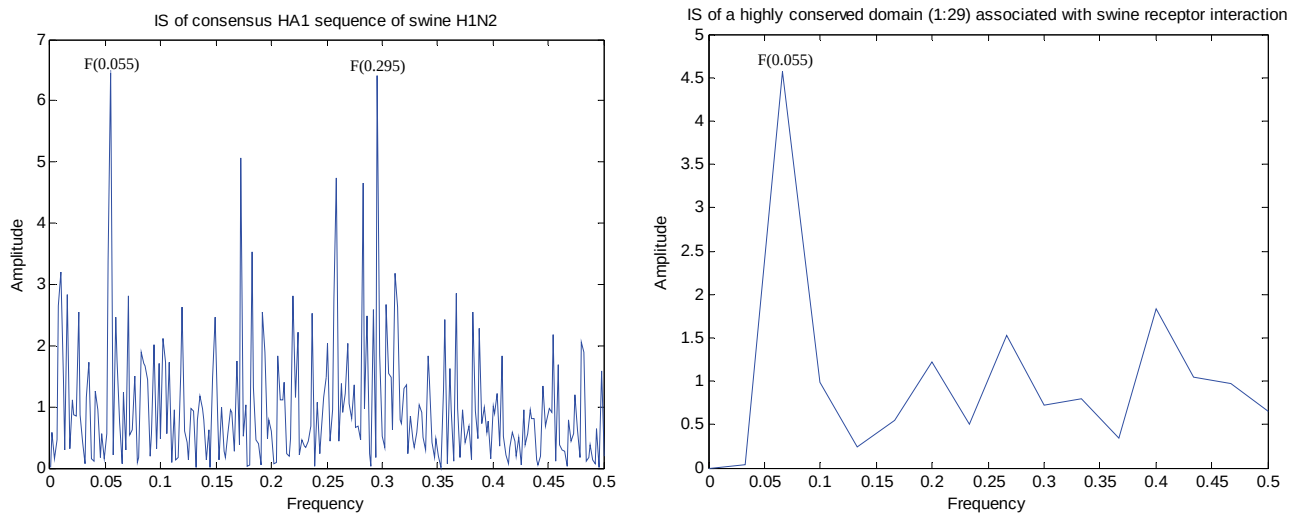

Figure 6. The left plot shows the informational spectrum of consensus HA1 sequence of swine H1N2, and the right plot shows the informational spectrum of one conserved domain 1:29 in swine H1N2 found in this study.

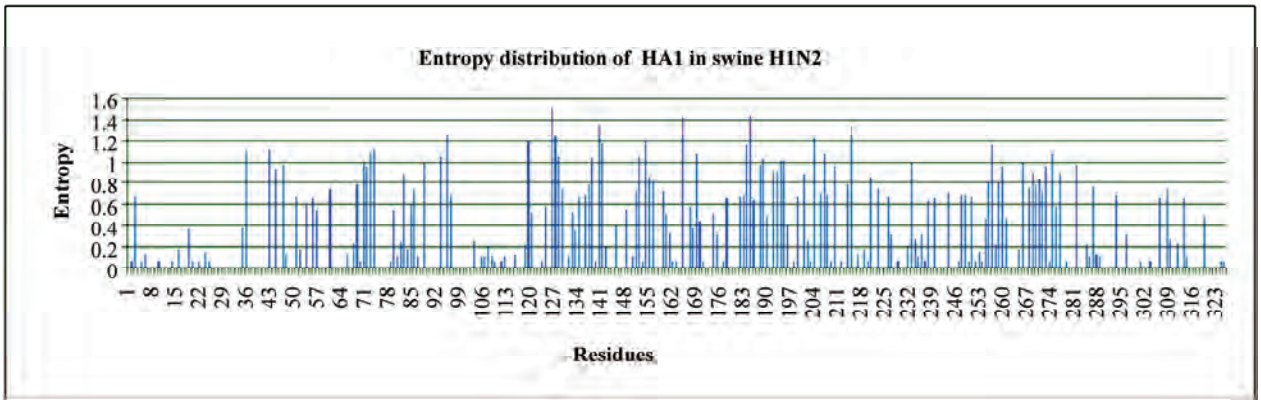

Figure 7. Entropy distribution of HA1 in swine H1N2.

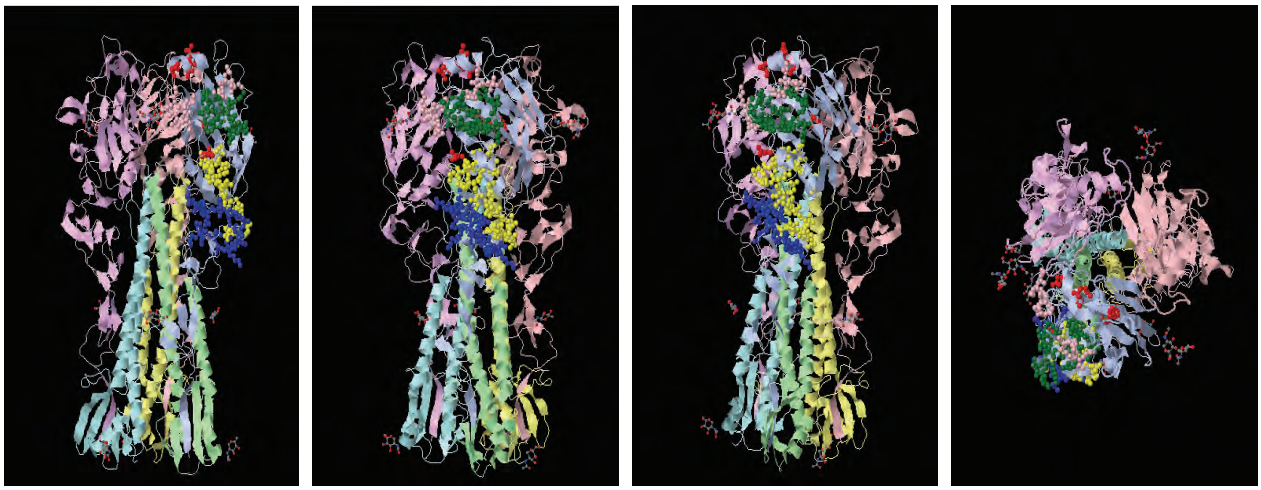

Figure 8. The four plots show in 3D structure the three highly conserved domains found in this study in avian H5N1. Binding sites are colored in red, two edges of the binding cleft in pink, domain 45:65 in yellow, domain 136:153 in green, and domain 269:286 in blue (PDB code: 2IBX).

3.3. Conserved Domains in HA1 of Avian H5N1

We uncovered three domains in HA1 of avian H5N1, which were located at residue positions 46 to 65, 136 to 153, and 269 to 286. Their consensus sequences were GVKPLILRDCSVAGWLLGNP, PYQGRSSFFRNVVW-LIKK, and LEYGNCNTKCQTPMGAIN, respectively, and the ISs of these three domains and the consensus H-A1 sequence in avian H5N1 were illustrated in **Figure 9**. The IS of the consensus HA1 sequence in avian H5N1 demonstrated two dominant peaks at frequencies F (0.076) and F(0.236). The three highly conserved domains identified here were exhibited with four different views in the H5 3D model in **Figure 8**. The entropy distribution in **Figure 10** implied that the three domains were well conserved, and the HA1 sequences of avian H5N1 were quite stable, in contrast to that of 2009 H1N1 and swine H1N2. In [12], a similar domain was found in the N-terminus of the HA protein comprising residues 42 – 75, which encompassed the domain 46:65 found in this study. The epitope mapping analysis in [19,20,21] reported that several anti-HA monoclonal antibodies (MAbs) could recognize the amino acids of HA at positions 1 – 86, 20 – 312, 136 – 141, 151 – 162, and 273 – 342, illustrating that our domains might be recognized by these MAbs.

4. DISCUSSION

The main findings of this study were presented in **Table 5**, which showed the locations, the characteristic frequencies, and the consensus sequences of the highly conserved domains in HA1 discovered in each subtype. The domains in **Table 5** are shorter than those discovered in [12,13], implying that they were more easily conserved by the HA sequences than their longer counterparts. Furthermore, the identified multiple domains in HA1 could provide more options than those found in the previous studies to design new therapeutic targets for drug development. Finally, because a consensus sequence of each subtype was employed to find these multiple

Copyright © 2010 SciRes.

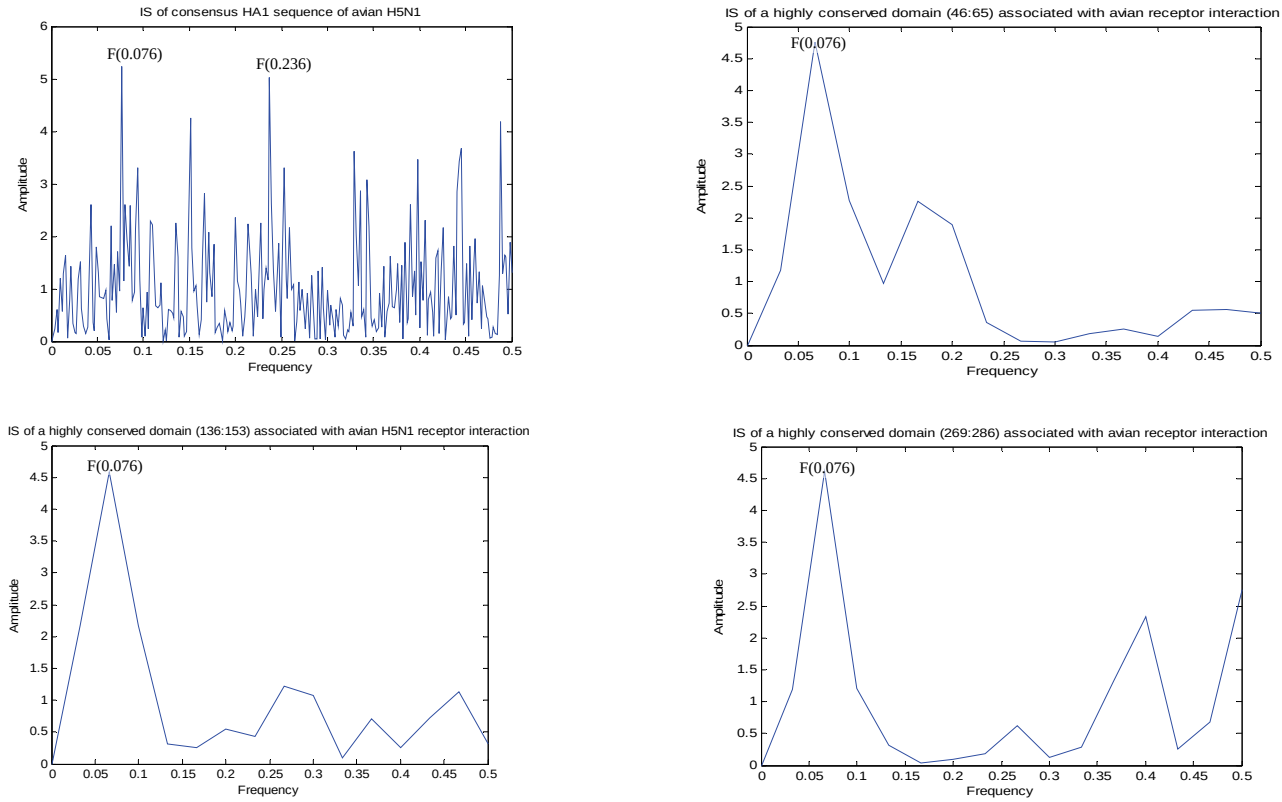

Figure 9. The top left plot shows the informational spectrum of consensus HA1 sequence in avian H5N1. The other three plots show the informational spectrum of the three conserved domains in avian H5N1 found in this study, 46:65, 136:153, and 269:286, respectively.

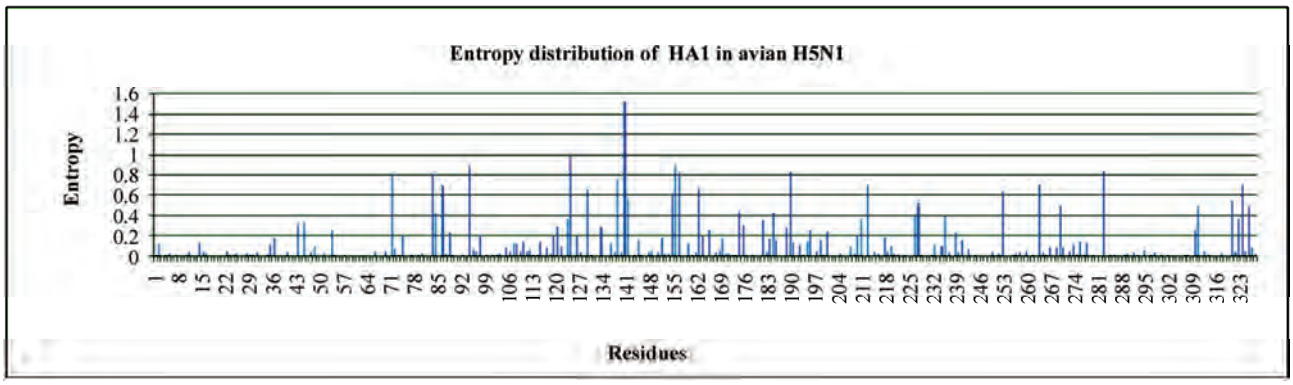

Figure 10. Entropy distribution of HA1 in avian H5N1.

Table 5. The receptor recognition domains of HA proteins in 2009 H1N1, swine H1N2, and avian H5N1 influenza viruses.

Subtype	Frequency	Residues	Consensus Sequence
2009 H1N1	F(0.295)	106 – 130	SSVSSFERFEIFPKTSSWPNHDSNK
2009 H1N1	F(0.295)	150 – 174	WLVKKGNSYPKLSKSYINDKGKEVLV
2009 H1N1	F(0.295)	191 – 221	LYQNADAYVFVGSSRYSKKFKPEIAIRPKVR
Swine H1N2	F(0.055)	1 – 29	DTLCIGYHANNSTDTVDTVLEKNVTVTHS
Avian H5N1	F(0.076)	46 – 65	GVKPLILRDCSVAGWLLGNP
Avian H5N1	F(0.076)	136 – 153	PYQGRSSFFRNVVWLIKK
Avian H5N1	F(0.076)	269 – 286	LEYGNCNTKCQTPMGAIN

Copyright © 2010 SciRes.

domains in HA1, they are more representative of the strains in each subtype than those obtained in the previous studies.

5. CONCLUSIONS

Identifying the conserved characteristics of influenza viruses relevant to receptor binding preference is an important topic in flu research. The informational and structural properties of HA1 associated with receptor-virus interaction in different subtypes were investigated in [12,13]. To extend the previous results, we aimed to uncover multiple domains in HA1 of 2009 H1N1 and avian H5N1 that might modulate the receptor binding patterns, thus to expand our repertoire of these key regions in HA1. Due to the important locations of these domains, they might serve as potential targets for new drugs and treatment of influenza infection.

The observations in [12,13] suggested that the 2009 H1N1 strains will continue to mutate in their HA gene, which could further favor the human interaction pattern by increasing the amplitude at frequency F(0.295) and at the same time decreasing that at frequency F(0.055). Given this trend, we must remain vigilant for additional mutations that can render a switch of the binding preference of 2009 H1N1.

6. ACKNOWLEDGEMENTS

We thank Houghton College for its financial support.

REFERENCES

[1] Alexandra, G., Alexander, T., Galina, P., Nicolai, B., Amanda, B. and Alexander, K. (2006) Evolution of the receptor binding phenotype of influenza A (H5) viruses. *Virology*, **344**, 432-438.

[2] Tatsunori, I., Kaori, F., Katsuhisa, N., Sachiko, A.H., Yuji, M., Hirofumi, W. and Shigenori, T. (2008) Theoretical analysis of binding specificity of influenza viral hemagglutinin to avian and human receptors based on the fragment molecular orbital method. *Computational Biology and Chemistry*, **32**, 198-211.

[3] Shinya, Y., Yasuo, S., Takashi, S., Mai, Q.L., Chairul, A. N.S., Yuko, T., Yukiko, M. *et al.* (2006) Haemagglutinin mutations responsible for the binding of H5N1 influenza A viruses to human-type receptors. *Nature*, **444(7117)**, 378-82.

[4] Venkataramanan, S., Kannan, T., Rahul, R., Raguram, S., Zachary, S., Sasisekharan, V. and Ram, S. (2009) Extrapolating from sequence—the 2009 H1N1 "swine" influenza virus. *Nature Biotechnology*, **27**, 510-513.

[5] Robert, A.C., Angelina, S.P., Steve, W., Tatyana, M., Liu, Y., Chai, W., Maria, A.C.R., Zhang, Y., Markus, E., Makoto, K., Alan, H., Mikhail, M. and Ten, F. (2009) Receptor-binding specificity of pandemic influenza A (H1N1) 2009 virus determined by carbohydrate microarray. *Nature Biotechnology*, **27**, 797-799.

[6] Hu, W. (2009) Analysis of correlated mutations, stalk motifs, and phylogenetic relationship of the 2009 influenza a virus neuraminidase sequences. *Journal of Biomedical Science and Engineering*, **2(7)**, 550-558.

[7] Hu, W. (2010) The interaction between the 2009 H1N1 influenza a hemagglutinin and neuraminidase: Mutations, co-mutations, and the NA stalk motifs. *Journal of Biomedical Science and Engineering*, **3**, 1–12.

[8] Cosic, I. (1997) The resonant recognition model of macromolecular bioreactivity—theory and application. *Birkhauser Verlag*, Berlin.

[9] Veljkovic, V. and Metlas, R. (1988) Identification of nanopeptide from HTLV3, LAV and ARV-2 envelope gp120 determining binding to T4 cell surface protein. *Cancer Biochem Biophys*, **10**, 91-106.

[10] Veljkovic, V., Veljkovic, N., Este, J.A., Huther, A. and ietrich, D.U. (2007) Application of the EIIP/ISM bioinformatics concept in development of new drugs. *Curr Med Chem*, **14**, 441-453.

[11] Veljkovic, V., Veljkovic, N. and Metlas, R. (2004) Molecular makeup of HIV-1 envelope protein. *Int Rev Immunol*, **23**, 383-411.

[12] Veljkovic, V., Niman, H.L., Glisic, S., Veljkovic, N., Perovic, V. and Muller, C.P. (2009) Identification of hemagglutinin structural domain and polymorphisms which may modulate swine H1N1 interactions with human receptor. *BMC Structural Biology*, **9**, 62.

[13] Veljkovic, V., Veljkovic, N., Muller, C.P., Müller, S., Glisic, S., Perovic, V. and Köhler, H. (2009) Characterization of conserved properties of hemagglutinin of H5N1 and human influenza viruses: Possible consequences for therapy and infection control. *BMC Struct Biol*, **7**, 9-21.

[14] Katoh, K., Kuma, K., Toh, H. and Miyata, T. (2005) MAFFT version 5: Improvement in accuracy of multiple sequence alignment. *Nucleic Acids Res*, **33**, 511-518.

[15] MacKay, D. (2003) Information theory, inference, and learning algorithms. *Cambridge University Press*.

[16] KováccaronOVá, A., Ruttkay-Nedecký, G., HaverlíK, I. K. and Janecccaronek, S. (2002) Sequence similarities and evolutionary relationships of influenza virus a hemagglutinins. *Virus Genes*, **24**, 57-63.

[17] Gamblin, S.J., Haire, L.F., Russell, R.J., Stevens, D.J., Xiao, B., Ha, Y. *et al.* (2004) The structure and receptor binding properties of the 1918 influenza hemagglutinin. *Science*, **303**, 1838-1842.

[18] Michael, W.D. and Pan, K. (2009) The epitope regions of H1-subtype influenza A, with application to vaccine efficacy. *Protein Engineering, Design & Selection*, **22**, 543-546.

[19] Du, A., Daidoji, T., Koma, T., Ibrahim, M.S., Nakamura, S., de Silva, U.C., Ueda, M., Yang, C.S., Yasunaga, T., Ikutu, K. and Nakaya, T. (2009) Detection of circulating Asian H5N1 viruses by a newly established monoclonal antibody. *Biochem Biophys Res Commun*, **378**, 197-202.

[20] Kaverin, N.V., Rudneva, I.A., Govorkova, E.A., Timofeeva, T.A., Shilov, A.A., Kochergin-Nikitsky, K.S., Krylov, P.S. and Webster, R.G. (2007) Epitope mapping of the hemagglutinin molecule of a highly pathogenic H5N1 influenza virus by using monoclonal antibodies. *J. Virol.*, **81**, 12911-12917.

[21] Yang, M., Clavijo, A., Graham, J., Salo, T., Hole, K., Berhane, Y. (2009) Production and diagnostic application of monoclonal antibodies against influenza virus H5, *J Virol Methods*, **162**, 194-202.

Copyright © 2010 SciRes.

J. Biomedical Science and Engineering, 2010, 3, 124-137 **JBiSE**
doi:10.4236/jbise.2010.32018 Published Online February 2010 (http://www.SciRP.org/journal/jbise/).

Effect of deformation rate on the mechanical properties of arteries

Jorge O. Virues Delgadillo[1], Sebastien Delorme[2], Vincent Mora[2], Robert DiRaddo[2], Savvas G. Hatzikiriakos[1]

[1]Department of Chemical & Biological Engineering, UBC, Vancouver, BC, Canada
[2]Industrial Materials Institute, National Research Council of Canada, Boucherville, QC, Canada
Email: hatzikir@interchange.ubc.ca; Sebastien.Delorme@imi.cnrc-nrc.gc.ca

Received 27 June 2008; revised 18 December 2009; accepted 20 December 2009.

ABSTRACT

Pig aorta samples were tested uniaxially and equibiaxially at deformation rates from 10 to 200 %/s. Under uniaxial and biaxial testing, loading forces were reduced up to 20% when the deformation rate was increased from 10 to 200 %/s, which is the opposite to the behaviour seen in other biological tissues. A rate-dependent isotropic hyperelastic constitutive equation, derived from the Mooney-Rivlin model, was fitted to the experimental results (e.g. aorta specimens) using an inverse finite element technique. In the proposed model, one of the material parameters is a linear function of the deformation rate. The inverse relationship between stiffness and deformation rate raises doubts on the hypothesized relationship between intramural stress, arterial injury, and restenosis.

Keywords: Mechanical Properties; Artery; Uniaxial & Biaxial Testing; Deformation Rate; Viscoelasticity; Constitutive Model

1. INTRODUCTION

The knowledge of the viscoelastic properties is important to predict the biomechanical behaviour of soft tissues. To model their viscoelastic behaviour, first one performs appropriate mechanical tests to characterize deformation-rate effects, and then one selects a constitutive equation capable of representing those effects. Material parameter estimation is fundamental for posterior simulation of soft tissue at boundary conditions not selected in the experimental protocol.

The effect of deformation rate on the mechanical properties of soft biological tissues has been investigated, in particular for ligaments [1-7], tendons [4,7-9], spines [10-13], bones [14-17], liver [18], heart valves [19,20] and myocardium [21,22]. Most biological tissues stiffen with increasing deformation rate [4,7,9,11-13, 17]. This time-dependent behavior has been described by viscoelastic constitutive models [6,22-26]. However, it was recently demonstrated that some biological tissues, such as liver, myocardium and skin, soften with increasing deformation rate [18,22]. Deformation rate effects of arteries, in particular thoracic aorta, were not included in previous studies.

Overstretch injury to the arterial wall during an angioplasty or stenting procedure has been shown to be correlated to the incidence of restenosis, i.e. in-growing tissue re-blocking the artery lumen [26,27]. Based on the hypothesis that lower deformation rate results in lower intramural stresses, slow balloon inflation has been proposed as a means to minimize vascular injury and reduce restenosis incidence [28]. Early studies did not conclude there was any difference in restenosis rates between conventional and slow balloon inflation [28-30], while some observed better immediate results [31,32]. In more recent studies, significantly lower restenosis rates were clinically observed with slow balloon inflation [33,34]. Slow stent deployment has also been proposed as a means to minimize arterial injury [35].

Finite element simulation of angioplasty and stenting can be used to optimize angioplasty procedure parameters, such as inflation pressure [36-40]. Optimization of inflation pressure rate requires accurate constitutive modeling of artery behavior including the effect of deformation rate. Numerous experimental studies have been performed to characterize the mechanical behaviour of arteries *in vitro* [41-44]. However, only a single deformation rate was used.

The objective of this study is thus to measure and model the effect of deformation rate on the tensile behavior of the arteries (e.g. pig aortas). In other words, the intention of this paper is to investigate experimentally the dependence of uniaxial and biaxial extensional stretching of arterial wall on the deformation-rate, and consequently to modeling the experimental data by means of an appropriate constitutive equation.

2. MATERIALS AND METHODS

2.1. Experimental Setup

Five thoracic aortas were harvested within the day of death of pigs from a local slaughterhouse and cleaned of remaining connective tissue. Then each artery was cut open along its length, and cut out in rectangular and cruciform-shaped specimens. The thickness of all specimens was measured with a vernier caliper (mean 2.4 mm, standard deviation 0.2 mm). Twelve samples were obtained from the five aortas: 8 rectangular samples (4 were cut in circumferential direction and 4 in axial direction) and 4 cruciform samples. Samples were stored in isotonic saline solution at 4℃ for no longer than 8 hours prior to testing.

Rectangular and cruciform samples were used for uniaxial and biaxial testing, respectively. Rectangular samples were 40 mm long and 4 mm wide, but only 20 mm of the sample were free to deform. The distance between grips in cruciform samples was 40 mm. A nominal stretch ratio of 1.5 was applied to avoid permanent deformation on the tissue.

Uniaxial and biaxial testing was carried on a planar biaxial test bench (Bose Corporation, Minnetonka, MN) capable of applying a peak force of 200 N over a displacement range of 12 mm per actuator. A saline bath maintained at body temperature (37℃) was used. Samples were mounted in horizontal configuration with the help of grip clamps to the arms extending from the actuators over the top of the bath.

Each sample was subjected to triangular wave form displacements of 1.5 stretch ratio of amplitude, and deformation rates of 10, 50, 100, 120, 140, 160, 180 and 200 %/s, which correspond to frequencies of 0.1, 0.5, 1.0, 1.2, 1.4, 1.6, 1.8 and 2.0 Hz. Half of the samples were subjected to deformation rates in the following order: 160, 120, 50, 200, 140, 100, 10 and 180 %/s (randomly tested), and the other half were tested from 10 to 200 %/s in ascending order in order to be confident that the deformation rate effect observed do not depend on the testing procedure order. In vivo, the artery is constantly submitted to stresses while the tissue is inflated-deflated due to blood pressure. In order to mimic in vivo loading conditions during in vitro tests, pre-conditioning cycles are required. Each test lasted for ten cycles. The first five cycles were used to pre-condition the tissue in order to reach a steady-state behavior. The force-stretch data was averaged over the last five cycles.

2.2. Statistical Analysis

The experimental data obtained in uniaxial and biaxial testing are represented in mostly all figures in this chapter as the mean value ± the standard errors (i.e. **Figure 3**). The medians rather than the means are plotted only in **Figure 6**. As shown in **Table 1**, twenty loading-unloading cycles were used to obtain the circumferential and axial force-stretch mean curves per deformation rate and testing condition. Circumferential and axial forces at 1.5 stretch ratio from both uniaxial and biaxial tests were used to calculate the medians, ranges (percentile between 75% – 25%) and p values with the help of the statistical tests selected. A multiple comparison between forces belonging to all groups (i.e. experimental forces obtained at each deformation rate belong to one group) was performed to study the significance of the effect of deformation rate using the ANOVA Friedman statistic test for dependent variables. The Wilcoxon test was also used to compare all deformation rate forces by pairs (i.e. forces at the highest deformation rate, 200%/s, with forces at the lowest deformation rate, 10%/s). In order to identify if the effect of deformation rate is more significant than the effect of anisotropy, circumferential and axial forces at each deformation rate were also compared using the Wilcoxon test. A 0.05 level of significance ($p = 0.05$) were selected for the Friedman and Wilcoxon tests.

2.3. Inverse Modeling

An inverse modeling technique was used to adjust the parameters of the proposed constitutive model (described below in the results section). The reaction forces at the boundaries (grips) were predicted by finite element simulation of the experiment consisting of applying displacement conditions on a mesh of the same size and shape as the sample. In an optimization loop, the material properties were iteratively adjusted until the following objective function was minimized, which occurs when a set of force-displacement experimental data matches the values calculated by the model:

$$S(c) = S(c)_{Biaxial} + S(c)_{Uniaxial} \quad (1)$$

The objective function to be minimized is the sum of uniaxial and biaxial cruciform objective functions.

Table 1. Number of force-stretch experimental data averaged per deformation rate.

Testing condition	Specimen direction	Number of specimens	Number of cycles per specimen	Total number of cycles
Uniaxial	Circumferential	4	5	20
	Axial	4	5	20
Biaxial	-	4	5	20

Copyright © 2010 SciRes.

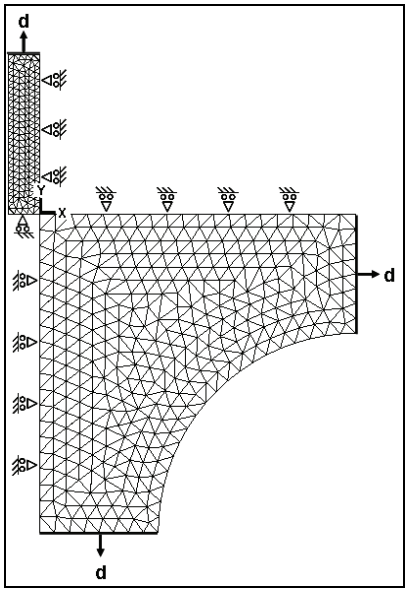

Figure 1. Mesh and boundary conditions used in simultaneous simulation of uniaxial and biaxial testing.

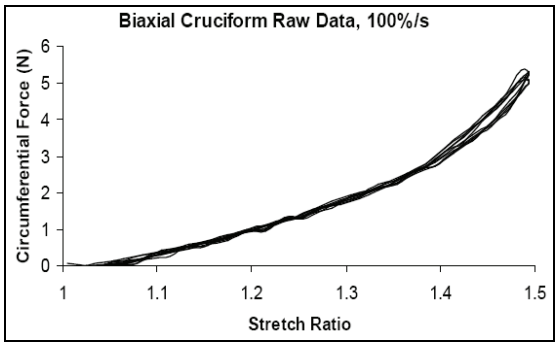

Figure 2. Loading-unloading circumferential forcestretch cycles of a typical biaxial cruciform sample: Five steady-state cycles at a deformation rate of 100%/s.

$$S(c)_{Biaxial} = \sum_{i=1}^{N} \left[\begin{array}{l} \left(F_x(d_x,d_y) - f_x(d_x,d_y,c)\right)^2 + \\ \left(F_y(d_x,d_y) - f_y(d_x,d_y,c)\right)^2 \end{array} \right]_i \quad (2)$$

where c is the vector of unknown material properties; d_x and d_y are the applied displacements; $F_x(d_x,d_y)$ and $F_y(d_x,d_y)$ are the experimentally measured reaction forces at the grips; and $f_x(d_x,d_y,c)$ and $f_y(d_x,d_y,c)$ are the reaction forces predicted by the finite element model in biaxial cruciform extension; N is the total number of data points gathered in the experiments.

$$S(c)_{Uniaxial} = \sum_{i=1}^{N} \left[\left(F(d) - f(d,c)\right)^2 \right]_i \quad (3)$$

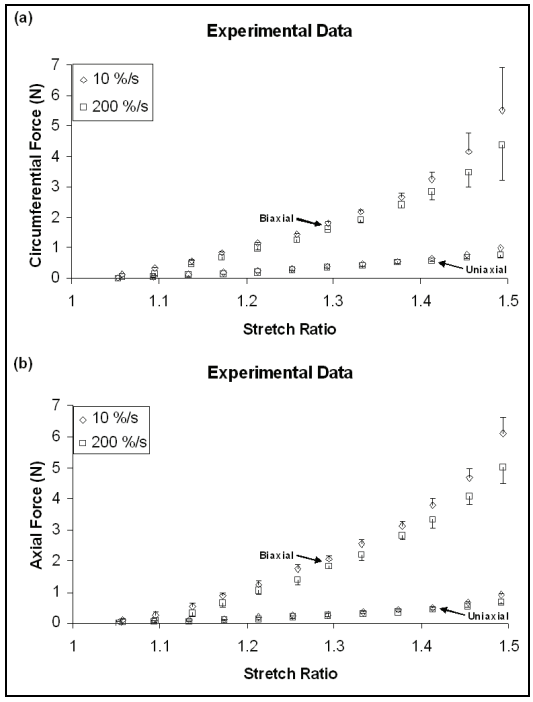

Figure 3. Sample to sample variability of thoracic aorta. Open diamonds and squares represent the mean force-stretch behavior at 10 and 200 %/s, respectively (n = 4): (a) circumferential, and (b) axial directions. Standard error bars are also shown.

Uniaxial extension predicted forces ($f(d,c)$) were fitted to the average of circumferential and axial reaction forces ($F(d)$); d is the applied displacement in uniaxial extension.

A combined uniaxial-biaxial mesh was used to simultaneously simulate uniaxial and biaxial testing conditions (**Figure 1**). Only one quarter of the rectangular and the cruciform sample area free to deform between the grips was meshed due to symmetry. The uniaxial and biaxial cruciform mesh-sections are linked together at the origin. Boundary conditions are shown in **Figure 1**. In some cases, a small stretch shift was applied to the experimental results to obtain better agreement between uniaxial and biaxial fits.

3. RESULTS

3.1. Experimental Results

Figure 2 shows cycle-to-cycle variability between cycles 6 and 10, for a typical sample tested biaxially at a deformation rate of 100%/s. Cycle-to-cycle variability was observed to be small for all cases.

Figure 3 shows the standard error bars (sample-to-sample variability) of circumferential and axial forces at the lowest (10 %/s) and highest (200 %/s) deformation

Copyright © 2010 SciRes.

rates. Similar standard errors were obtained with the other deformation rates.

Figure 4 shows the effect of deformation rate on the circumferential behavior of thoracic aorta from uniaxial and biaxial testing. Lower forces were observed at higher than at lower deformation rates. In particular, a 20% lower force was observed at 1.5 stretch ratio with the lowest deformation rate (10%/s) compared to the highest deformation rate (200%/s). The same phenomenon was observed in the axial direction **(Figure 5)**.

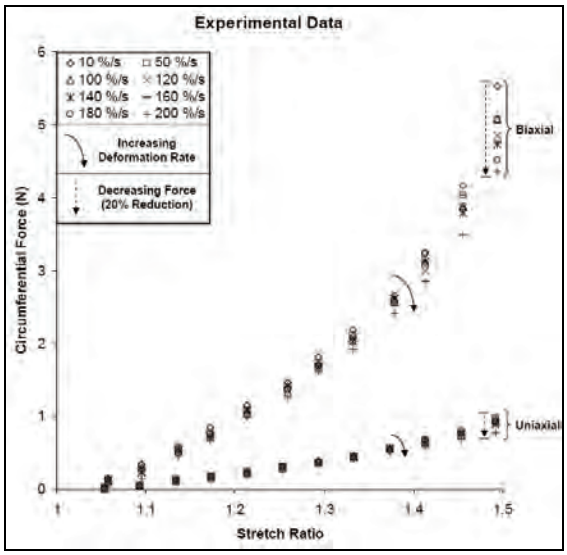

Figure 4. Effect of deformation rate on the force vs. stretch ratio curve of arteries: Circumferential force vs. stretch ratio curves in uniaxial and biaxial testing.

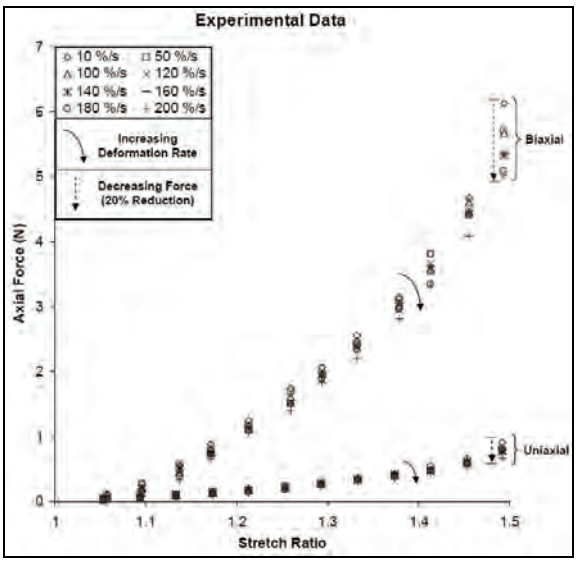

Figure 5. Effect of deformation rate on the force vs. stretch ratio curve of arteries: Axial force vs. stretch ratio curves in uniaxial and biaxial testing.

Figure 6 shows the median, percentiles (75% – 25%) and the ANOVA Friedman test p value obtained using the forces at 1.5 stretch ratio for each deformation rate. Significant differences ($p < 0.05$) were observed, with the highest significant differences under biaxial testing ($p \le 0.002$).

Table 2 shows Wilcoxon test p values of uniaxial and biaxial data of some of the deformation rate pairs analyzed (i.e. comparison of the force at the maximum deformation rate with the forces at other deformation rates). Marginally significant differences were observed in the forces of mostly all deformation rates. Similar p values were obtained in the other comparisons (i.e. 50%/s vs. all deformation rates).

In **Figure 7**, circumferential and axial forces at 1.5 stretch ratio of a typical sample are plotted against deformation rate. In this figure, one can observe that the effect of deformation rate (20 % difference in force between smallest and highest deformation rate) is approximately twice as large as the effect of anisotropy (difference in force between circumferential and axial directions). This supports the hypothesis of modelling deformation-rate effects with an isotropic model.

Table 3 shows p values calculated using the Wilcoxon test comparing the circumferential force to the axial force at 1.5 stretch ratio per each deformation rate.

3.2. Constitutive Modeling

Based on the experimental results, it was assumed that the arterial wall behaves as a pseudoelastic material [45], where the stress is independent of the loading path. Thus, we propose a new rate-dependant isotropic hyperelastic model, based on the Mooney-Rivlin model [46] given by the following strain energy density function:

$$W(I_1, I_2) = \sum_{i,j=0}^{\infty} a_{ij} (I_1 - 3)^i (I_2 - 3)^j \tag{4}$$

The Mooney-Rivlin model is a function of the 1st and 2nd invariants (I_1, I_2) of the Green-Cauchy tensor:

$$I_1 = \lambda_1^2 + \lambda_2^2 + \lambda_3^2 \tag{5}$$

$$I_2 = \lambda_1^2\lambda_2^2 + \lambda_2^2\lambda_3^2 + \lambda_3^2\lambda_1^2 \tag{6}$$

where λ_1, λ_2 and λ_3 are the principal stretch ratios.

In its most common expression, only five parameters are selected ($a_{10}, a_{01}, a_{11}, a_{20}, a_{30}$) and the strain energy function reduces to:

$$\begin{aligned} W = {} & a_{10}(I_1 - 3) + a_{01}(I_2 - 3) + a_{11}(I_1 - 3)(I_2 - 3) \\ & + a_{20}(I_1 - 3)^2 + a_{30}(I_1 - 3)^3 \end{aligned} \tag{7}$$

The underlying hypothesis for using the Mooney-Rivlin model is that one or some of the five parameters vary with deformation rate. This can be modeled by

Copyright © 2010 SciRes.

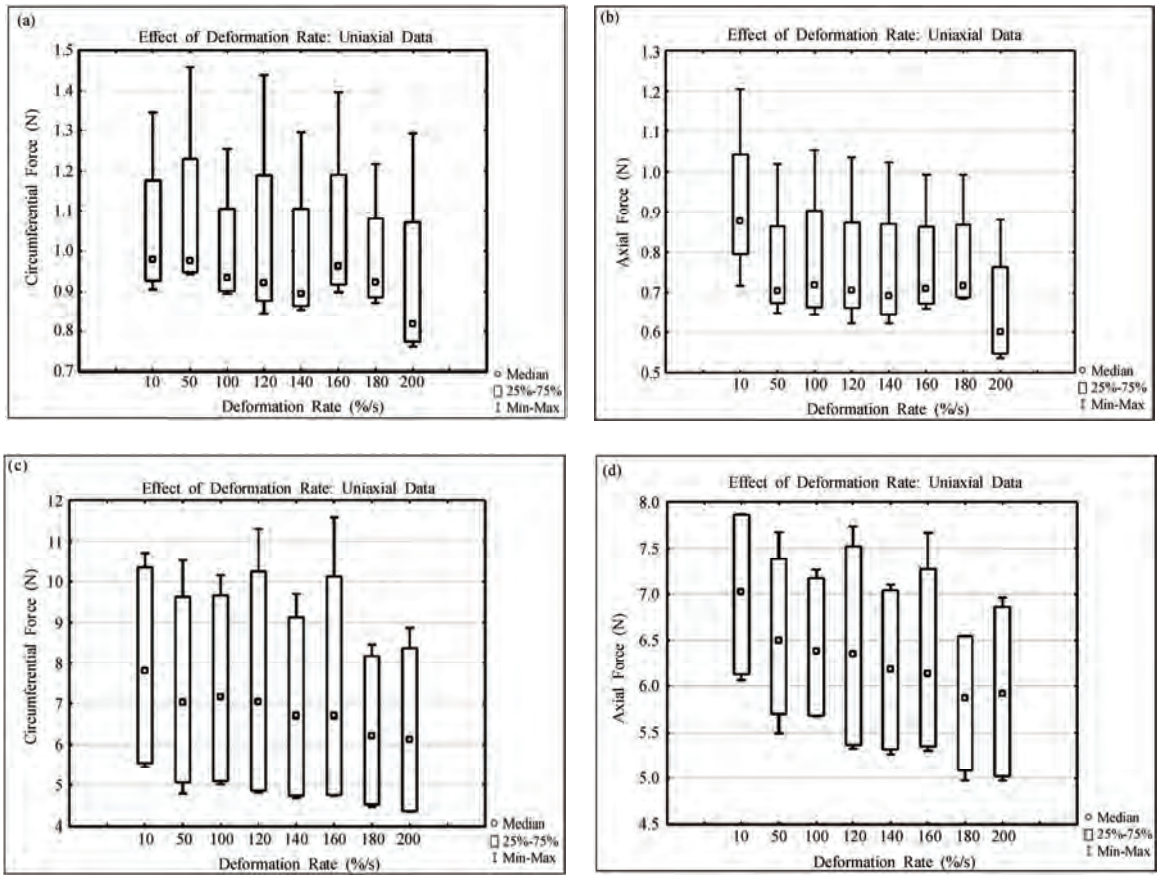

Figure 6. Deformation rate effect on (a, b) uniaxial and (c, d) biaxial forces at maximum stretch ratio ($\lambda = 1.5$): (a, c) circumferential and (b, d) axial direction.

Table 2. Effect of deformation rate:Wilcoxon test *p* values.

Type of test	Uniaxial		Biaxial	
Force	Circumferential	Axial	Circumferential	Axial
Deformation rate (%/s)		200		
10	0.07	0.07	0.07	0.07
50	0.07	0.07	0.07	0.07
100	0.14	0.07	0.07	0.07
120	0.07	0.07	0.07	0.07
140	0.07	0.07	0.07	0.07
160	0.07	0.07	0.07	0.07
180	0.37	0.07	0.72	0.42

Table 3. Effect of anisotropy (Circumferential vs. axial forces, $n = 4$): Wilcoxon test *p* values.

Deformation rate (%/s)	Uniaxial	Biaxial
10	0.47	0.47
50	0.14	0.47
100	0.27	0.47
120	0.14	0.47
140	0.27	0.47
160	0.14	0.47
180	0.14	0.47
200	0.14	0.47

Copyright © 2010 SciRes.

Table 4. First simulation results (material parameters) of uniaxial and biaxial cruciform tests.

M-R Fitted Parameter Values (kPa)						
Deformation Rate (%/s)	a_{10}	a_{01}	a_{11}	a_{20}	a_{30}	SUM/n x 10^{-03} (n = 24)
10	9.25	7.57	5.77	6.94	4.43	2.69
50	9.21	7.45	5.45	6.58	3.64	2.09
100	8.90	7.23	5.51	6.66	3.86	1.76
120	9.46	7.66	5.38	6.52	3.03	1.66
140	9.96	8.07	5.30	6.45	2.36	3.45
160	9.22	7.47	5.29	6.40	3.24	2.72
180	9.07	7.32	5.34	6.49	2.95	2.80
200	8.86	7.17	5.24	6.36	2.80	1.90
Linear Regression Coefficients & R^2				$\left(a_{ij} = A + B\dot{\lambda}\right)$		
A	9.32	7.60	5.69	6.85	4.27	
B x 10^{-03}	-0.70	-0.90	-2.40	-2.50	-8.20	
R^2	0.01	0.04	0.80	0.78	0.65	

Table 5. Second simulation results (material parameters) of uniaxial and biaxial cruciform tests.

M-R Fitted Parameter Values (kPa)						
Deformation Rate (%/s)	a_{10}	a_{01}	a_{11}	a_{20}	a_{30}	SUM/n x 10^{-03} (n = 24)
10					4.99	2.64
50					3.66	2.18
100					3.74	1.88
120	9.24	7.79	5.41	6.55	3.16	1.68
140					2.75	3.56
160					3.06	2.83
180					2.72	2.98
200					2.26	1.98
Linear Regression Coefficients & R^2				$\left(a_{ij} = A + B\dot{\lambda}\right)$		
A	-	-	-	-	4.76	
B x 10^{-03}	-	-	-	-	-12.20	
R^2	-	-	-	-	0.88	

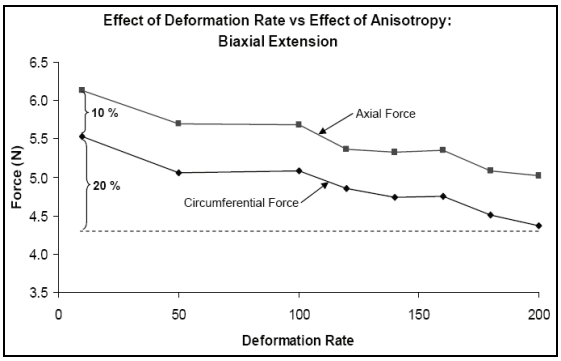

Figure 7. Comparison of the effect of deformation rate versus the effect of anisotropy. Typical sample forces at maximum stretch ratio (1.5).

making these parameters functions of the deformation rate. Those relationships are explored in this work.

3.3. Inverse Modeling Results

Initially, all five Mooney-Rivlin parameters were allowed to vary while being limited to a 10^{-4} kPa to 10^{4} kPa value range. **Table 4** summarizes the fitted parameters obtained for the uniaxial and biaxial cruciform force vs. stretch ratio curve averaged for each deformation rate.

In a second simulation only parameter a_{30} was allowed to vary because this was the parameter with the highest slope (absolute value of B) in the linear regressions reported in **Table 4**. The remaining parameters were maintained constant by using the average of the fitted values obtained for all deformation rates. The fitted parameters obtained are summarized in **Table 5**. The sum of least squares (last column in **Tables 4** and **5**) were almost unchanged when the first four parameters were kept constant, supporting the hypothesis that only a_{30} varies with deformation rate.

Other fits were performed assuming that $a_{11} = a_{20} = 0$ to see if the model could be reduced to a simpler form (**Table 6**). First, parameters a_{10}, a_{01} and a_{30} were allowed to vary. The highest regression coefficient (absolute value of B) and the highest correlationcoefficient (R^2) were obtained for a_{30}. Thus parameters a_{10}

Copyright © 2010 SciRes.

and a_{01} were assumed to be constant (i.e. $a_{10} = 12.59\ kPa$, $a_{01} = 9.54\ kPa$) which were calculated as the average value of the fitted results obtained for all deformation rates. Parameter a_{30} was fitted again (**Table 7**). The sum of least squares remained small although higher than in the **Table 4**. Repeated optimization with different initial parameter values consistently converged towards the same solution.

Uniaxial and biaxial simulations fitted values of parameter a_{30} (**Table 7**) are plotted against deformation rate in **Figure 8**. This parameter decreased from 11 to 8 kPa when the deformation rate increased from 10 to 200 %/s, respectively. A quadratic polynomial was also used to model the variation of a_{30} with deformation rate but its correlation coefficient was similar to that obtained with a linear relationship, i.e. 0.89 and 0.88 respectively. Therefore, the linear fit was preferred over the polynomial fit due to its simplicity.

Table 6. Third simulation results (material parameters) of uniaxial and biaxial cruciform tests.

M-R fitted parameter values (kPa)						
Deformation rate (%/s)	a_{10}	a_{01}	a_{11}	a_{20}	a_{30}	SUM/n x 10^{-03} (n = 24)
10	12.90	9.72	0.00	0.00	10.76	2.61
50	12.35	9.31			9.82	2.68
100	12.39	9.35			9.86	2.61
120	12.73	9.65			8.91	3.04
140	13.38	10.14			7.92	5.17
160	12.37	9.36			9.12	3.40
180	12.27	9.35			8.74	4.96
200	12.35	9.41			8.17	4.09
Linear regression coefficients & R^2			$(a_{ij} = A + B\dot{\lambda})$			
A	12.76	9.61	-	-	10.66	
B x 10^{-03}	-1.50	-0.60	-	-	-12.50	
R^2	0.07	0.02	-	-	0.73	

Table 7. Final simulation results (material parameters) of uniaxial and biaxial cruciform tests.

M-R fitted parameter values (kPa)						
Deformation rate (%/s)	a_{10}	a_{01}	a_{11}	a_{20}	a_{30}	SUM/n x 10^{-03} (n = 24)
10	12.59	9.54	0.00	0.00	10.91	2.62
50					9.45	2.78
100					9.53	2.70
120					8.87	3.07
140					8.41	5.33
160					8.76	3.50
180					8.38	5.13
200					7.85	4.21
Linear regression coefficients & R^2			$(a_{ij} = A + B\dot{\lambda})$			
A	-	-	-	-	10.66	
B x 10^{-03}	-	-	-	-	-13.70	
R^2	-	-	-	-	0.88	

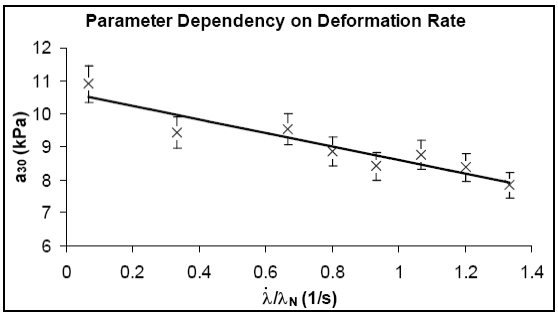

Figure 8. Parameter a_{30} dependency on deformation rate for both, uniaxial and biaxial extensions.

Table 8. Linear regression adjusted parameters.

Parameter	Units	Uniaxial & biaxial cruciform
A	kPa	10.66
$\hat{B}$	kPa*s	-2.06

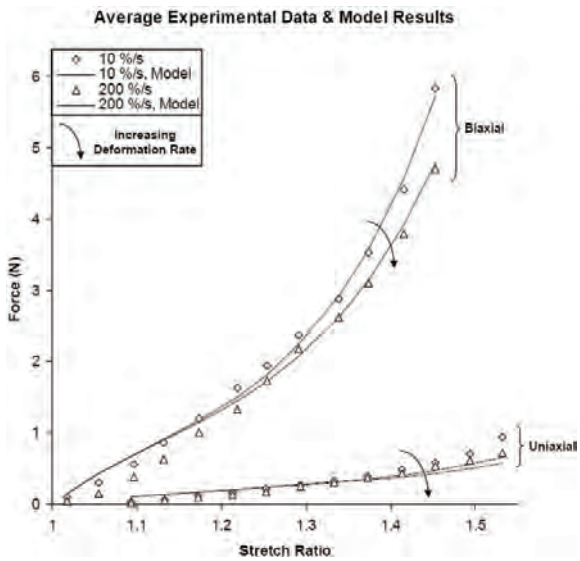

Figure 9. Mooney-Rivlin computed reaction forces versus stretch ratios in uniaxial and biaxial testing at 10 and 200 %/s. An increase in the deformation rate decreases the reaction forces at a particular stretch ratio.

The following linear equation is proposed for parameter a_{30}:

$$a_{30} = f\left(\dot{\lambda}\right) = A + \hat{B}\left(\frac{\dot{\lambda}}{\lambda_N}\right) \tag{8}$$

where $\dot{\lambda}$ is the deformation rate in s^{-1}, λ_N is the nominal stretch ratio (λ_N = 1.5), A and $\hat{B}$ are the linear regression coefficients. The strain rate was normalized by the nominal stretch ratio, in order to account for the biological variability in peak stretch of aorta samples. **Table 8** summarizes the adjusted parameters of Equation 8.

Figure 9 shows the computed forces at the lowest (10 %/s) and highest (200 %/s) deformation rates. Circumferential and axial forces were averaged in order to clearly exemplify the model prediction of the arterial behavior when the deformation rate is increased.

Although an excellent fit is observed between the biaxial data and biaxial simulation, the Modified Mooney-Rivlin model does not predict well the uniaxial behavior, especially in the nonlinear part of the curve at high stretch ratios (> 1.45).

Minimization of the objective function and parameter a_{30} estimation, using the data gathered at 100%/s deformation rate, is shown in **Figure 10**. **Figure 10a** shows the value of the objective function plotted against the iteration number in the optimization loop, for three different initial guesses. The objective function was evaluated 50 times in iterations 0 (initial guess) to 9. **Figure 10b** illustrates optimization of material parameter a_{30}.

Figure 11 shows the stress and stretch ratio distributions (at 1.5 stretch ratio) during uniaxial and biaxial testing. Scalar bars of the results at 10, 100 and 200 %/s deformation rates are shown for their comparison: One can observe the overall reduction of the stresses when the deformation rate was increased. The highest non uniform stress distribution was obtained in biaxial testing.

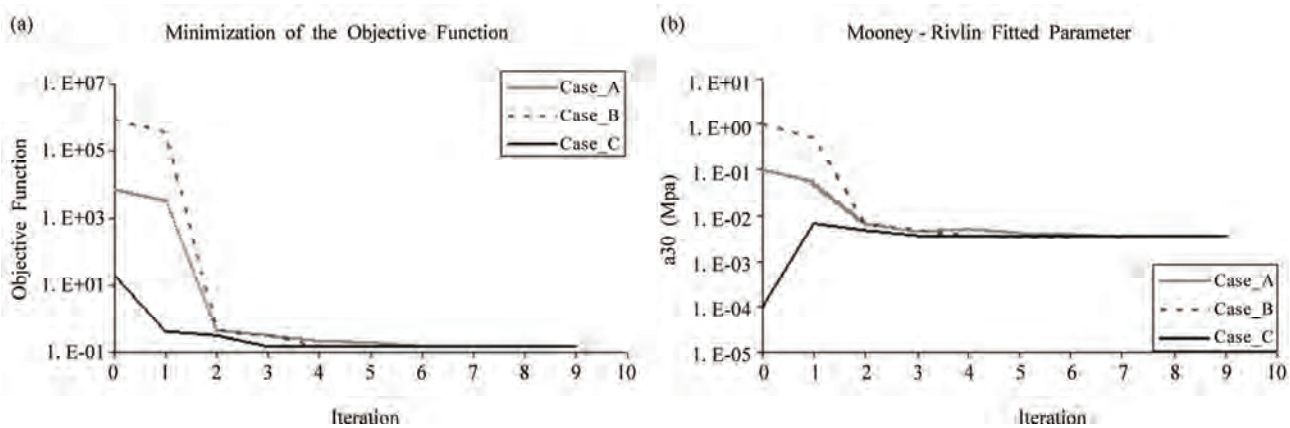

Figure 10. Optimization of the Mooney-Rivlin parameters for both uniaxial and biaxial tests at a deformation rate of 100%. (a) objective function, and (b) parameter a_{30} values as a function of iteration number, for three different initial guesses for material parameter a_{30}: Case_A (a_{30}, = 0.1 MPa), Case_B (a_{30}, = 1.0 MPa), and Case_C (a_{30}, = 0.0001 MPa).

Copyright © 2010 SciRes.

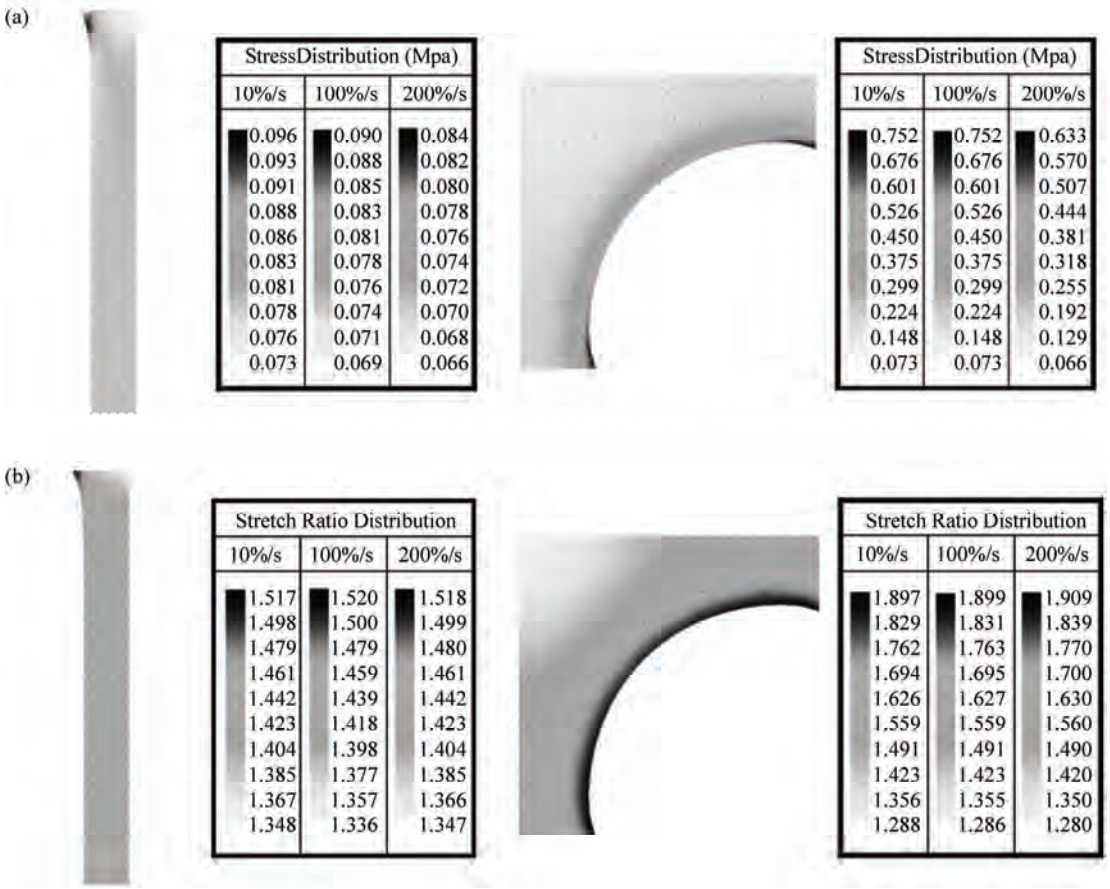

Figure 11. Deformed configurations at 1.50 nominal stretch ratio for uniaxial and cruciform mesh: Distribution of (a) σ_{xx} stress and (b) stretch ratio in the principal direction. The stress and stretch distributions at 10, 100, and 200 %/s are shown inside the tables.

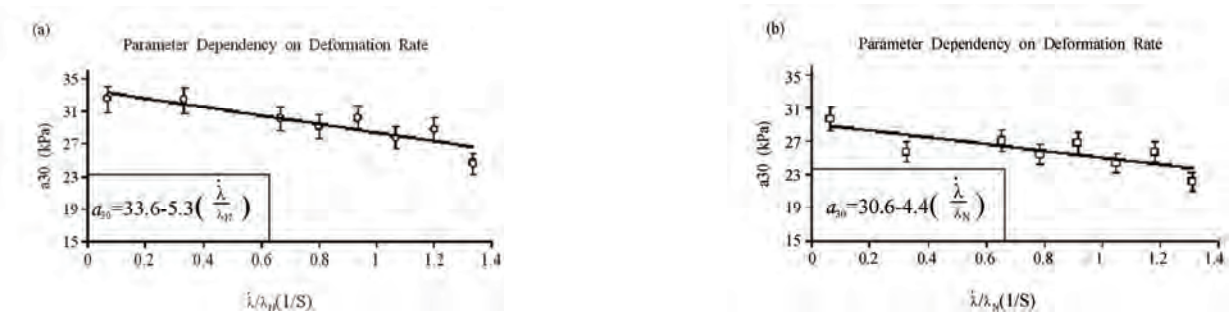

Figure 12. Parameter a_{30} dependency on deformation rate for uniaxial extension: (a) circumferential and (b) axial directions.

3.3.2. Uniaxial Fit

In order to improve uniaxial simulations, two objective functions were defined, one for each direction:

$$S(c) = \sum_{i=1}^{N} \left[\left(F_x(d_x) - f_x(d_x, c) \right)^2 \right]_i \quad (9)$$

$$S(c) = \sum_{i=1}^{N} \left[\left(F_y(d_y) - f_y(d_y, c) \right)^2 \right]_i \quad (10)$$

These objective functions were used to better predict the uniaxial extension experimental data. Different material properties were obtained for the circumferential and for the axial directions.

Uniaxial simulations fitted values of parameter a_{30} per deformation rates are shown in **Figure 12**. This parameter was reduced roughly from 33 to 23 kPa when the deformation rate was increased, following the same

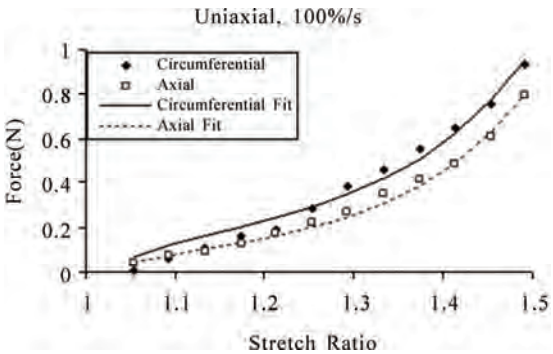

Figure 13. Mooney-Rivlin computed reaction forces versus stretch ratios in uniaxial testing at a deformation rate of 100 %/s.

Table 9. Mooney-Rivlin fitted parameters in uniaxial extension.

Mooney-Rivlin	Parameters (kPa)	
	Circumferential	Axial
a_{10}	9.56	9.56
a_{01}	18.01	7.87
a_{11}	0.00	0.00
a_{20}	0.00	0.00
A	33.64	30.62
$\hat{B}$	-5.32	-4.40

trend in circumferential and axial directions. It was also observed that material parameter a_{30} changed linearly as a function of the deformation rate.

Table 9 summarizes Mooney-Rivlin fitted parameters obtained just for uniaxial tests. The values of a_{30} obtained per deformation rate were almost 4 times greater than a_{30} values calculated with the combined uniaxial-biaxial simulation. Parameters a_{10} and a_{01} remained almost unchanged in both the uniaxial and combined uniaxial-biaxial simulations, with exception of parameter a_{01} in circumferential direction (i.e. 18 kPa).

The computed circumferential and axial forces obtained using the Mooney-Rivlin fitted parameters from **Table 9** in uniaxial tests, at a deformation rate of 100%/s, are shown in **Figure 13**. Uniaxial behaviour in both directions was well predicted.

Figure 14 shows the stress and stretch ratio distribution of rectangular samples. The reduction of the stresses as the deformation rate increases is observed when the stress distribution at each deformation rate is compared (scalar bars at 10, 100 and 200 %/s).

4. DISCUSSION

Contrary to the conventional understanding of biological

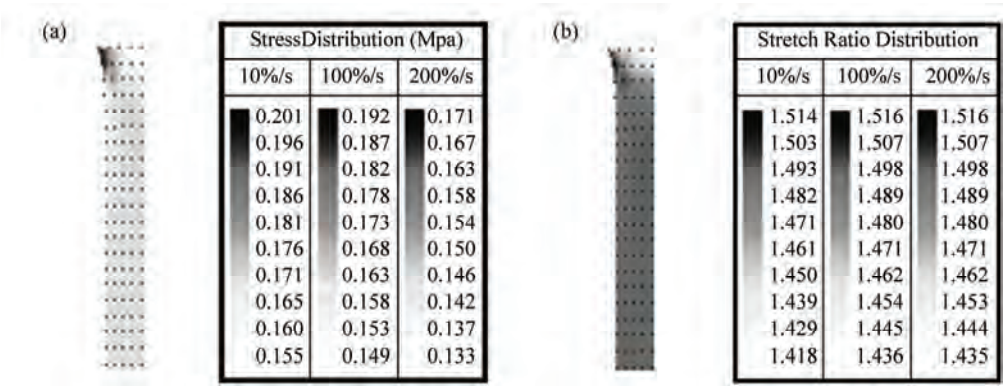

Figure 14. Deformed configurations at 1.50 nominal stretch ratio for uniaxial mesh using the material parameters of **Table 6.3** (Circumferential direction): distribution of (a) σ_{xx} stress and (b) stretch ratio in the principal direction. The stress and stretch distributions at 10, 100, and 200 %/s are shown inside the tables.

tissue behaviour, it was discovered in this study that the stiffness of thoracic aorta decreases with deformation rate, which was confirmed by the use of two statistical methods. Overall significant differences ($p \le 0.02$) in the mechanical forces of uniaxial and biaxial experiments were found using the ANOVA Friedman statistic test. In addition, the Wilcoxon test help us to observe which particular pair of deformation rates likely had a tendency to be significantly different (i.e. almost all deformation rates were different than 200%/s, $p = 0.07$). An increase in the sample size for further studies will certainly reduce the Wilcoxon test p values obtained.

Giles *et al.* [22] observed a similar behaviour in load controlled planar biaxial laboratory tests of myocardium and skin samples. Hu and Desai [18] studied the variation of the elastic modulus of pig liver tissue at different deformation rates under compression tests, and found that at higher strain rates the liver has an apparently lower resistance (i.e. softer) to deformation than at lower deformation rates. However, under uniaxial displace-

Copyright © 2010 SciRes.

ment controlled tests, Pioletti *et al.* [7] found that an increase in the deformation rate results in a stiffer material response. In their work, they submitted ligament samples to deformation rates within 0.1 – 40%/s in ascending order. In the present study, thoracic aortas were tested over a 10 – 200%/s range of deformation rates. In both, uniaxial and biaxial tests, the peak force on the arterial samples was around 20% smaller at a deformation rate of 200%/s than at 10%/s **(Figures 3** and **4)**. These results were observed on the average of the five steady-state loading cycles, after five-preconditioning cycles for each deformation rate. However, similar results were also observed on the first loading cycle at each deformation rate, eliminating the possibility of this behavior being due to pre-conditioning. The experimental procedure was validated by repeating the same experiments on latex and nitrile samples. As expected, the effect of deformation rate was opposite in these rubbers to what was observed in the arterial samples. An experiment without any sample was performed to measure the combined effects of inertia, friction, and water drag force, which were found to be negligible, i.e. less than 10 % of the effect of deformation rate.

Sample variability between circumferential and axial force vs. stretch ratio curves was found to be lower than the effect of deformation rate, supporting the use of an isotropic constitutive equation to predict the behavior of the arterial wall. Isotropic models have also been used to model the artery in other studies [43,47-50]. Forces instead of stresses were reported here due to the non-homogeneous stress and strain distributions found in speci- mens subjected to biaxial tests, where the highest and lowest stresses are found near the curved boundaries and near the center of the sample, respectively [51]. Moreover, researchers who are focused (like us) on experimental rather than theoretical work will appreciate to report the data as raw as possible.

The main constituents of arterial tissues are collagen and elastin. The elastic response of arteries is largely due to elastin because elastin is about 1000 times more extensible than collagen. The proportion of elastin to the other arterial constituents is the highest in the aorta. Elastin chains are crosslinked together to form rubberlike, elastic fibers [52]. Each elastin molecule uncoils into a more extended conformation when the fiber is stretched and recoils spontaneously as soon as the stretching force is relaxed. Its elasticity is based on changes in the entropy of the molecular chains, while the material is deformed. An imposed strain increases the order in the molecular network and thus decreases its entropy. According to the thermodynamic laws, the network would try to recover its former shape, increasing their entropy.

One possible explanation for the observed phenomenon is that when elastin is stretched at high rates it would attain a highly oriented conformation and as a result the cross-links would not be able to bear the load due to slippage. However, as the stretch occurs at lower rates, the elastin molecules would have more time ava- ilable to adjust in order to prevent slippage of the cross-links and as a result would be able to bear a higher load. This effect can be viewed as an energy dissipation effect where at high rates of stretching the energy is dissipated rather by the associative flow and the slippage between cross-links. At lower rates the energy dissipation is less. This effect is similar to the stretching behaviour of branched polymers when compared to that of their linear counterparts [53,54]. Here elastin at high extensional rates would behave more like a linear polymer where the linear polymers can slip one past the other to exhibit a reduced load mainly due to high oriented conformation imposed by the high stretching rate. On the other hand, elastin at low extensional rates would behave like a branched polymer where the presence of branches prevent cross-linking slippage and as a result bear higher loads.

Moreover, Trepat *et al.* [55] subjected human airway smooth muscle cells to a transient stretch-unstretch maneuver with zero residual macroscale strain, observing that the cell promptly fluidizes and then slowly resolidifies. Therefore, is it possible that changes in the alignment and configuration of adjacent fibers within the extracellular matrix occurs as soon as one fiber begins to shear over the other (i.e. fluid-like behavior), making softer the overall response in the tissue when stretching the arterial sample at the highest deformation rate (minimum relaxation in the tissue due to short testing time). At lower deformation rates, the fibers have more time to move back to their original configuration, thus restraining their ability to flow (stiffer response).

The constitutive equation selected here is capable of representing the nonlinear elastic behavior of the artery, including the effect of deformation rate, with only four parameters. It produces a unique curve fitting solution to experimental results for each deformation rate. More importantly, it was observed that Mooney Rivlin parameters a_{10} and a_{01} were not a function of the deformation rate. This could imply that they are related to the elastic behavior of the artery. A linear relationship was obtained between parameter a_{30} and the deformation rate, where the partially elastic contribution is given by coefficient A and the deformation rate response is given by coefficient $\hat{B}$.

As shown in **Figure 9**, the model better fits the biaxial data than the uniaxial data. Using higher weights for the uniaxial least square differences, it was possible to obtain a better fit for uniaxial data, at the expense of a deterioration of the fit for biaxial data. The use of material parameters a_{11} and a_{20} did not improve the fits significantly enough to justify increasing the complexity of

Copyright © 2010 SciRes.

the model with these two extra parameters. The use of anisotropic constitutive equations in future studies might reduce this discrepancy between predicted and experimental forces in uniaxial direction.

Clinical results have shown that slow balloon inflation might reduce restenosis. It was hypothesized that the slower deformation rate gives as a result lower intramural stresses and lower arterial injury. This hypothesis is contradictory to our results, which would indicate that a lower inflation rate would result in higher intramural stresses. Other mechanisms might play a role in leading to lower restenosis rates, such as endothelium denudation or artery injury being dependent on stretch ratio rather than on intramural stress.

5. CONCLUSIONS

In the present study, the effect of deformation rate on the mechanical behavior of arteries in vitro under uniaxial and biaxial extensions was investigated. It was found that the loading force at a stretch ratio of 1.5 is reduced by 20 % when the deformation rate is increased from 10 to 200 %/s, implying that the stiffness of arteries decreases with deformation rate. This behavior might be a consequence of the faster fluidization and small resolidification that occurs in the cell at higher deformation rates. This effect of deformation rate was observed to be higher than the effect of anisotropy. The development of an isotropic hyperelastic rate-dependent constitutive model, derived from the Mooney-Rivlin hyperelastic model, is capable of representing this behavior. In its proposed form, the model has only 4 parameters, only one of which varies with deformation rate. The small number of material parameters and simple formulation increase the applicability of this model to numerical simulations. The inverse relationship between stiffness and deformation rate raises doubts on the hypothesized relationship between intramural stress, arterial injury, and restenosis.

Future work might be helpful in order to account the entire loading history of the arterial wall by performing additional characterizations such as relaxation time experiments, and with the aim of a viscoelastic model. The ratio between maximum stretch with balloon and inflation time might be computed as well to observe if the same phenomenon appears.

6. ACKNOWLEDGEMENTS

This research was possible thanks to the PhD scholarship given by the Mexican Council of Science and Technology (Consejo Nacional de Ciencia y Tecnología), CONACYT. The authors would also like to thank Marc-Andre Rainville for his guidance and assistance in sample preparation and mechanical testing.

REFERENCES

[1] Thornton, G.M., Schwab, T.D. and Oxland, T.R. (2007a) Fatigue is more damaging than creep in ligament revealed by modulus reduction and residual strength. *Annals of Biomedical Engineering*, **35,** 1713-1721.

[2] Thornton, G.M., Schwab, T.D. and Oxland, T.R. (2007b) Cyclic loading causes master rupture and strain rate than static loading in medial collateral ligament at high stress. *Clinical Biomechanics*, **22,** 932-940.

[3] Provenzano, P., Lakes, R., Keenan, T. and Vanderby Jr., R. (2001) Nonlinear ligament viscoelasticity. *Annals of Biomedical Engineering*, **29,** 908-914.

[4] Pioletti, D. And Rakotomanana, L.R. (2000) Non-linear viscoelastic laws for soft biological tissues. *Eur. J. Mech. A/Solids*, **19,** 749-759.

[5] Pioletti, D., Rakotomanana, L.R., Benvenuti, J.F. and Leyvraz, P.F. (1998) Viscoelastic constitutive law in large deformations: Application to human knee ligaments and tendons. *Journal of Biomechanics*, **31,** 753-757.

[6] Kwan, M.K., Lin, T.H.C. and Woo, S.L.Y. (1993) On the viscoelastic properties of the anteromedial bundle of the anterior cruciate ligament. *J. Biomechanics*, **26**, 447-452.

[7] Pioletti, D., Rakotomanana, L.R. and Leyvraz, P.F. (1999) Strain rate effect on the mechanical behavior of the anterior cruciate ligament-bone complex. *Medical Engineering & Physics*, **21,** 95-100.

[8] Haut, R.C. (1983) Age-dependent influence of strain rate on the tensile failure of rat-tail tandon. *Journal of Biomechanical engineering*, **105,** 296-299.

[9] Haut, R.C. and Little, R.W. (1972) A constitutive equation for collagen fibers. *Journal of Biomechanics*, **5,** 423-430.

[10] Gay, R.E., Ilharreborde, B., Zhao, K., Boumediene, E. and An, K.N. (2008) The effect of loading rate and degeneration on neutral region motion in human cadaveric lumbar motion segments. *Clinical Biomechanics*, **23**, 1-7.

[11] Wang, J.L., Parnianpour, M., Shirazi-Adl, A. and Engin, A.E. (1999) Rate effect on sharing of passive lumbar motion segment under load-controlled sagittal flexion: Viscoelastic finite element analysis. *Theoretical and Applied Fracture Mechanics*, **32,** 119-128.

[12] Yingling, V.R., Callaghan, J.P. and McGill, S.M. (1997) Dynamic loading affects the mechanical properties and failure site of porcine spines. *Clinical Biomechanics*, **12**, 301-305.

[13] Tran, N.T., Watson, N.A., Tencer, A.F., Ching, R.P. and Anderson, P.A. (1995) Mechanism of the burst fracture in the thoracolumbar spine: The effect of loading rate. *Spine*, **20**, 1984-1988.

[14] De Smet, E., Jaecques, S.V.N., Jansen, J.J., Walboomers, F., Van Der Sloten, J. and Naert, I.E. (2007) Effect of constant strain rate, composed of varying amplitude and frequency, of early loading on peri-implant bone (re)modeling. *Journal of Clinical Periodontology*, **34,** 618-624.

[15] Ebacher, V., Tang, C., McKay, H., Oxland, T.R., Guy, P. and Wang, R. (2007) Strain redistribution and cracking behavior of human bone during bending. *Bone*, **40**, 1265-1275.

[16] Hsieh, Y.F., Wang, T. and Turner, C.H. (1999) Viscoelastic response of the rat loading model: Implications for studies of strain-adaptive bone formation. *Bone*, **25**, 379-382.

[17] Schaffler, M.B., Radin, E.L. and Burr, D.B. (1989) Me-

chanical and morphological effects of strian rate on fatigue of compact bone. *Bone*, **10,** 207-214.

[18] Hu, T. and Desai, J.P. (2004) Soft-tissue material properties under large deformation: Strain rate effect. *Proceedings of the 26th Annual International Conference of the IEEE EMBS*, San Francisco, CA, USA (September 1-5, 2004), 2758-2761.

[19] Doehring, T.C., Carew, E.O. and Vesely, I. (2004) The effect of strain rate on the viscoelastic response of aortic valve tissue: A direct-fit approach. *Annals of Biomedical Engineering*, **32**, 223-232.

[20] Wells, S. and Sacks, M.S. (2002) Effects of fixation pressure on the biaxial mechanical behavior of porcine bioprosthetic heart valves with long-term cyclic loading. *Biomaterials*, **23,** 2389-2399.

[21] Demer, L.L. and Yin, F.C.P. (1983) Passive biaxial mechanical properties of isolated canine myocardium. *Journal of Physiology*, **339**, 615-630.

[22] Giles, J.M., Black, A.E. and Bischoff, J.E. (2007) Anomalous rate dependence of the preconditioned response of soft tissue during load controlled deformation. *Journal of Biomechanics*, **40,** 777-785.

[23] Nekouzadeh, A., Pryse, K.M., Elson, E.L. and Genin, G. M. (2007) A simplified approach to quasi-linear viscoelastic modeling. *Journal of Biomechanics*, **40,** 3070-3078.

[24] Sarver, J.J., Robinson, P.S. and Elliott, D.M. (2003) Methods for quasi-linear viscoelastic modeling of soft tissue: Application to incremental stress-relaxation experiments. *Journal of Biomechanical Engineering*, **125,** 754-785.

[25] Vena, P., Gastaldi, D. and Contro, R. (2006) A constituent-based model for the nonlinear viscoelastic behavior of ligaments. *Journal of Biomechanical Engineering*, **128,** 449-457.

[26] Zhang, W., Chen, H.Y. and Kassab, G.S. (2007) A rate-insensitive linear viscoelastic model for soft tissues. *Biomaterials*, **28,** 3579-3586.

[27] Schwartz, R.S., Holmes Jr., D.R. and Topol, E.J. (1992) The restenosis paradigm revisited: An alternative proposal for cellular mechanism. *Journal of the American College of Cardiology*, **20,** 1284-1293.

[28] Tenaglia, A.N., Quigley, P.J., Kereiakes, D.J., Abbottsmith, C.W., Phillips, H.R., Tcheng, J.E., Rendall, D. and Ohman, E.M. (1992) Coronary angioplasty performed with gradual and prolonged inflation using a perfusion balloon catheter: Procedural success and restenosis rate. *Am. Heart J.*, **124**, 585-589.

[29] Miketic, S., Carlsson, J. and Tebbe, U. (1998) Influence of gradually increased slow balloon inflation on restenosis after coronary angioplasty. *American Heart Journal*, **135**, 709-713.

[30] Timmis, S.B.H., Hermiller, J.B., Burns, W.H., Meyers, S. N. and Davidson, C.J. (1999) Comparison of immediate and in-hospital results of conventional balloon and perfusion balloon angioplasty using intracoronary ultrasound. *American Journal of Cardiology*, **83,** 311-316.

[31] Eltchaninoff, H., Cribier, A., Koning, R., Chan, C., Jolly, N., Tan, A. and Letac, B. (1996) Effects of prolonged sequential balloon inflations on results of coronary angioplasty. *Am. J. Cardiol*, **77**, 1062-1066.

[32] Ohman, E.M., Marquis, J.F., Ricci, D.R., Brown, R.I., Knudtson, M.L., Kereaikes, D.J., Samaha, J.K., Margolis, J.R., Niederman, A.L. and Dean, L.S. (1994) A randomized comparison of the effects of gradual prolonged versus standard primary balloon inflation on early and late outcome: Results of a multicenter clinical trial. Perfusion balloon catheter study group, *Circulation*, **89**, 1118-1125.

[33] Umeda, H., Iwase, M., Kanda, H., Izawa, H., Nagata, K., Ishiki, R., Sawada, K., Murohara, T. and Yokota, M. (2004) Promising efficacy of primary gradual and prolonged balloon angioplasty in small coronary arteries: A randomized comparison with cutting balloon angioplasty and conventional balloon angioplasty. *American Heart Journal*, **147,** 1-8.

[34] Weiss, T., Leibovitz, D., Katz, I., Danenberg, C., Varshitsky, B. and Lotan, C. (2007) The value of computerized angioplasty in patients undergoing coronary stenting: A prospective, randomized trial. *Am. J. Cardiol.*, **100,** 118L.

[35] Thériault, P., Terriault, P., Brailovski, V. and Gallo, R. (2006) Finite element modeling of a progressively expanding shape memory stent. *Journal of Biomechanics*, **39,** 2837-2844.

[36] Gasser, T.C. and Holzapfel, G.A. (2007) Modeling plaque fissuring and dissection during balloon angioplasty intervention. *Annals of Biomedical Engineering*, **35,** 711-723.

[37] Holzapfel, G.A., Stadler, M. and Schulze-Bauer, C.A. (2002) A layer-specific three-dimensional model for the simulation of balloon angioplasty using magnetic resonance imaging and mechanical testing. *Ann. Biomed. Eng*, **30**, 753-767.

[38] Lally, C., Dolan, F. and Prendergast, P.J. (2005) Cardiovascular stent design and vessel stresses: A finite element analysis. *Journal of Biomechanics*, **38,** 1574-1581.

[39] Oh, S., Kleinberger, M. and McElhaney, J.H. (1994) Finite-element analysis of balloon angioplasty. *Med. & Biol. Eng. & Comput.*, **32,** S108-S114.

[40] Wu, W., Qi, M., Liu, X.P., Yang, D.Z. and Wang, W.Q. (2007) Delivery and release of nitinol stent in carotid artery and their interactions: A finite element analysis. *Journal of Biomechanics*, **40,** 3034-3040.

[41] Lally, C., Reid, A.J. and Prendergast, P.J. (2004) Elastic behavior of porcine coronary artery tissue under uniaxial and equibiaxial tension. *Ann. Biomed. Eng.*, **32,** 1355-1364.

[42] Okamoto, R.J., Wagenseil, J.E., Delong, W.R., Peterson S.J., Kouchoukos, N.T. and Sundit III, T.M. (2002) Mechanical properties of dilated human ascending aorta. *Ann. Biomed. Eng.*, **30,** 624-635.

[43] Prendergast, P.J., Lally, C., Daly, S., Reid, A.J., Lee T. C., Quinn, D. and Dolan, F. (2003) Analysis of prolapse in cardiovascular stents: A constitutive equation for vascular tissue and finite-element modelling. *Journal of Biomechanical Engineering*, **125,** 692-699.

[44] Waldman, S.D. and Lee, J.M. (2002) Boundary conditions during biaxial testing of planar connective tissues: Part 1: Dynamic behavior. *Journal of Materials Science, Materials in Medicine*, **13**, 933-938.

[45] Fung, Y.C. (1993) Biomechanics: Mechanical properties of living tissues, 2nd edition, Springer-Verlag, New York, 261-262.

[46] Mooney, M.A. (1940) Theory of large elastic deformation. *J. Appl. Phys.*, **11,** 582-592.

[47] Raghavan, M.L. and Vorp, D.A. (2000) Toward a bio-

mechanical tool to evaluate rupture potential of abdominal aortic aneurysm: Identification of a finite strain constitutive model and evaluation of its applicability. *Journal of Biomechanics*, **33,** 475-482.

[48] Scotti, C.M. and Finol, E.A. (2007) Compliant biomechanics of abdominal aortic aneurysms: A fluid-structure interaction study. *Computers & Structures*, **85,** 1097-1113.

[49] Tezduyar, T.E., Sathe, S., Cragin, T., Nanna, B., Conklin B.S., Pausewang, J. and Schwaab, M. (2007) Modelling of fluid-structure interactions with the space-time finite elements: Arterial fluid mechanics. *Int. J. Num. Meth. Fluids*, **54,** 901-922.

[50] Wang, D.H.J., Makaroun, M., Webster, M.W. and Vorp, D.A. (2001) Mechanical properties and microstructure of intraluminal thrombus from abdominal aortic aneurysm. *Journal of Biomechanical Engineering*, **123,** 536-539.

[51] Virues-Delgadillo, J.O., Delorme, S., Diraddo, R. and Hatzikiriakos, S.G. (2007) Effect of deformation rate on the mechanical properties of rectangular and cruciform arterial samples: Uniaxial and biaxial testing. *Proceedings ASME 2007 Summer Bioengineering Conference Keystone*, Colorado, USA.

[52] Shadwick, R.E. (1999) Mechanical design in arteries. *J. Exp. Biol*., **202**, 3305-3313.

[53] McLeish, T.C.B. and Larson, R.G. (1998) Molecular constitutive equations for a class of branched polymers: The pom-pom model. *J. Rheol*, **42,** 81-110.

[54] Sentmanat, M., Muliawan, E.B. and Hatzikiriakos, S.G. (2005) Fingerprinting the processing of polyethylenes from transient extensional flow and peel experiments in the melt state. Rheologica Acta, **44,** 1-15.

[55] Trepat, X., Deng, L., An, S.S., Navajas, D., Tschumperlin, D.J., Gerthoffer, W.T., Butler, J.P. and Fredberg, J.J. (2007) Universal physical responses to stretch in the living cell. *Nature*, **447**, 592-596.

Copyright © 2010 SciRes.

J. Biomedical Science and Engineering, 2010, 3, 138-147 **JBiSE**
doi:10.4236/jbise.2010.32019 Published Online February 2010 (http://www.SciRP.org/journal/jbise/).

A method to fabricate small features on scaffolds for tissue engineering via selective laser sintering

S. Lohfeld[1], M. A. Tyndyk[1], S. Cahill[1,2], N. Flaherty[1], V. Barron[1], P. E. McHugh[1,2]

[1]National Centre for Biomedical Engineering Science, National University of Ireland, Galway, Ireland
[2]Department of Mechanical and Biomedical Engineering, College of Engineering and Informatics, National University of Ireland, Galway, Ireland
Email: Stefan.Lohfeld@nuigalway.ie

Received 24 November 2009; revised 18 December 2009; accepted 21 December 2009.

ABSTRACT

Purpose: Selective laser sintering (SLS) is a rapid prototyping technique applied to produce tissue-engineering scaffolds from powder materials. The standard scanning technique, however, often produces struts of extensive thickness, which means fabrication of highly porous scaffolds with small overall dimensions is quite difficult. Nevertheless, this study aims to overcome this shortfall. Design/methodology/approach: To this end, three scanning methods were evaluated in terms of minimum feature size and freedom of design, using a test polyamide (PA) material. Polycaprolactone (PCL) was then employed to create highly porous 3D scaffolds using the preferred scanning method to produce thin struts. Findings: While in normal scanning mode some features were well above the laser spot diameter, strut thicknesses below the laser spot diameter were achieved when using the "outline scan" function for PA material. Those achieved for PCL were slightly higher and in the 500-800 µm range, with an average pore size of 400 µm. Investigations on the properties of the scaffolds revealed an effective compression modulus of the PCL scaffold of 6.5 MPa. Furthermore, there was no change in physical or chemical properties when the scaffolds were stored in a physiological environment for 7 weeks. Originality/value: Though SLS is considered as a fabrication technique for tissue engineering scaffolds, actually produced scaffolds did not comply with porosity requirements and limitations of the SLS process in producing features at the size of the laser beam spot have not been discussed. The present paper shows the capabilities of the SLS process based on two materials and presents a method to minimize feature size in scaffolds.

Keywords: Selective Laser Sintering; Rapid Prototyping; Scaffolds; Polycaprolactone; Tissue Engineering

1. INTRODUCTION

Over the last ten years, there has been significant interest in tissue engineering since it offers an alternative approach with great potential for reconstruction or replacement of damaged bone tissues [1-5]. Three main elements are required to engineer tissue, namely (i) a scaffold, (ii) cells and (iii) a dynamic environment in which the cell-scaffold construct are conditioned [6-8]. Current bone tissue engineering techniques employ the use of porous, 3D, biodegradable, biocompatible, and bioresorbable scaffolds, which act as temporary platforms for initial cell attachment and subsequent tissue formation. However, to date there is no optimum scaffold structure available, which matches the material properties of native bone tissue, and at the same time allows for sequential growth of the neotissue as the scaffold degrades with time.

Recently, several novel materials and processing techniques have been developed to address this shortfall [9-12]. With recent advances in design and manufacturing capabilities, there has been significant interest in developing biomimetic scaffolds with similar microarchitectures, mechanical and biological properties that are similar to those of native tissue. In recent years, the advanced manufacturing technique of rapid prototyping (RP) has played an increasingly important role in scaffold fabrication, with the potential to overcome the limitations of conventional manual-based fabrications techniques [12-15]. One such technique is selective laser sintering (SLS), which has the advantage that complex 3D shapes with various pore sizes, shapes and interconnectivities can be produced from CAD files. Additionally, this technique is a fully automated system that employs a CO_2 laser to melt polymeric powders and form scaffold geometries without the use of any toxic chemicals, blowing agents or support structures [16].

Porosity has always been cited as an important requirement for cell growth on tissue engineering scaffolds. Using SLS fabrication methods, porosity can be manipulated by varying scaffold parameters such as pore size and strut thickness. Yang *et al.* [17] reported that the minimum feature size of the SLS process is limited to

400 µm, which basically is due to the laser spot diameter. In this situation a requirement for high porosity, combined with a small pore size, necessitates the generation of a low scaffold strut thickness. However, specific details about scaffold strut thickness in the literature are difficult to obtain. When strut thickness values are quoted, as for example by Das *et al.* [18] and Partee *et al.* [19], they are deemed to be multiples of the proposed laser spot diameter; at least 700 µm. Some studies concentrate on the size of the pores without giving details on the achieved strut thickness [20,21], while Smith *et al.* [22] gave no dimensions of the actual scaffold features at all. Other studies discussed selective laser sintering of scaffolds, however, for the experiments simple flat disks were manufactured to investigate sintering of the material used. In these cases the pore size and shape were not the specific focus, but the porosity was generated by adjusting the process parameters [16,23]. A comparison between intended design (CAD) and actual achieved structure is often missing. Williams *et al.* [21] designed pores of 1.75 to 2.5 mm and calculated porosities of 63.1% to 79%, while the porosity of the fabricated scaffolds actually achieved was consistently 27 percentage points lower than the values aimed for. This was due to particle size and growth of the struts by heat conduction into adjacent powder particles.

Strut thickness is an important consideration in SLS fabricated scaffolds to achieve high porosities with small pores. Due to the importance of being able to generate thin struts, the study presented here was focussed on an examination of the different SLS scan options with a view to generating a minimum strut thickness. With process parameters for sintering of polycaprolactone ("PCL"), determined as part of the study, scaffolds were fabricated and characterised in terms of strut morphology and mechanical properties.

2. MATERIALS AND METHODS

2.1. SLS Processing Methods

In this study, a Sinterstation 2500^{plus} (DTM, USA) was employed to fabricate the scaffolds. Initially, Duraform PA powder (polyamide, "PA") (3D Systems, UK) was employed to optimise the build parameters. Thereafter, PCL (CAPA6501, Solvay, UK) was used to fabricate the scaffolds. The software "Sinter v3.3" (3D Systems) was used to prepare the builds. The Sinterstation 2500^{plus} is actually optimised to build large models and the optics focus the CO_2 laser spot to a diameter of about 400 to 500 µm. To achieve feature sizes in the appropriate range for tissue engineering scaffolds, as a first step, the laser processing parameters have to be optimised.

The main sintering path of the laser is along the x-axis of the machine, which is parallel to the front wall of the build chamber. In general, the cross sections of the 3D models are sintered with parallel line scans in the x-direction, incrementally shifted in the y-direction (fill scan). In the y-direction, thin walls or struts are fabricated by single dot-like shots, building up to form a line parallel to the y-axis, as pictured in **Figure 1**. Ideally, a strut built this way has a thickness similar to the laser spot diameter.

Surfaces that have not been parallel to the y-axis during fabrication may appear stepped due to the scanning technique. To reduce this, a so-called "outline scan" can be added to improve the surface quality. After performing the fill scan, the laser scans along the edge of the part in each cross section similar to a plotter. As laser power and offset values of both the fill scan and the outline scan can be controlled separately, the latter can be used to fabricate thin, smooth walls in any direction in the x-y-plane by turning off the "fill scan" completely.

To compensate for the diameter of the laser spot when scanning, the laser usually is offset from the edges of the cross section. Depending on the offset value and the dimensions of the strut in the 3D design, one or two main struts in the fabricated scaffold can be created. This will be explained further below.

In order to find the most suitable method to fabricate thin struts in scaffolds, the present paper investigated three approaches:

a) using the fill scan and a laser offset of about half of the strut thickness

b) using the outline scan, but no laser offset (laser path along the edge of the strut)

c) using the outline scan and a laser offset of about half of the strut thickness

Method a) is the common sintering technique used for all models fabricated using the Sinterstation. Therefore,

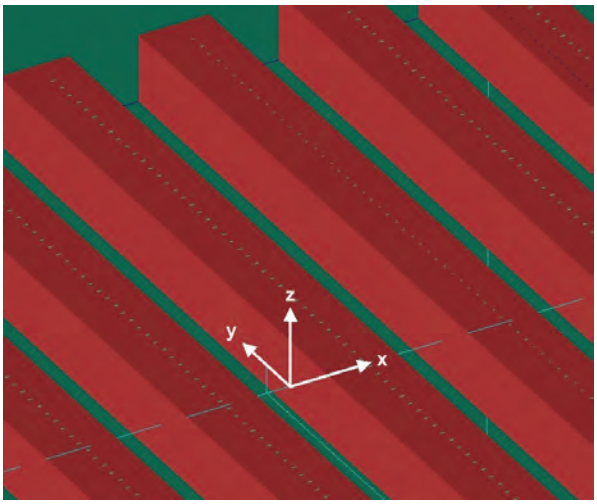

Figure 1. Build preview showing the laser scan paths. Thin lines parallel to the y direction of the build chamber consist of single laser shots aligned along the y axis.

Copyright © 2010 SciRes.

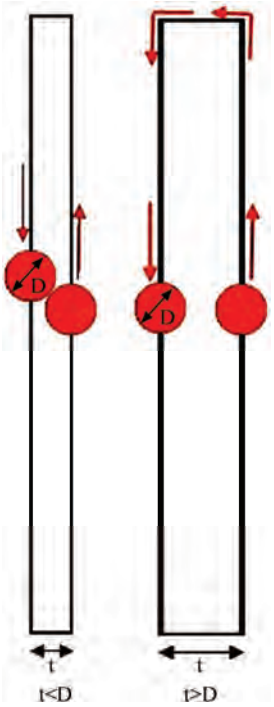

Figure 2. Laser spot overlap when the strut thickness t is smaller than the laser spot diameter D.

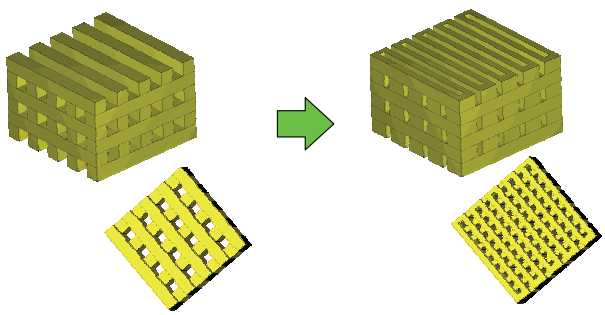

Figure 3. Designed 3D model (left) and actually built model (right).

it was investigated to examine the accuracy of the scaffolds generated using the standard sintering technique.

Method b) fabricated a frame around the designed strut with two short and two long edges. During the design stage it was taken into account that the long edges were likely to be fused together if their distance (= strut width) was less than the laser spot diameter of 410 µm. This is due to an overlap of the laser spot in the centre of the strut when scanning around the edge of the strut (**Figure 2**). Therefore, the strut width was set to 800 µm, and the distance between the struts was set to be the same to ensure even distances between the sintered paths. Each single strut in the 3D design actually resulted in

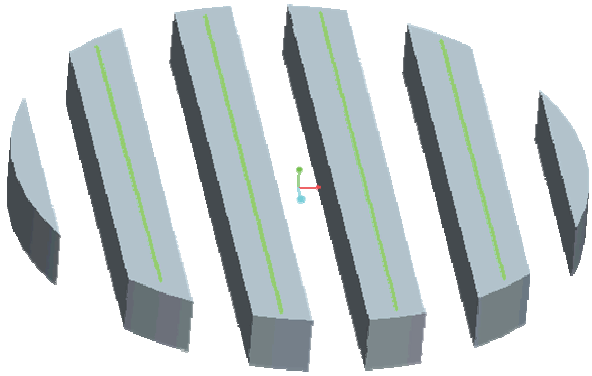

Figure 4. Laser scans along the centreline of each strut.

two struts connected at the ends in the fabricated scaffold (**Figure 3**). As only one pass of the laser per strut was used here, these struts were expected to have the smallest achievable dimensions. For Method c) the offset value was set to approximately half the thickness of a designed strut to make the laser scan along the centre line of each strut (**Figure 4**). As the outline has to be a closed line, the laser scanned along the centre line twice. It was assumed that this adds to the thickness of the final fabricated strut. On the other hand, unlike Method b), the fabricated scaffold resembled the 3D design as the actual strut thickness achieved by this method has been anticipated in the design.

2.2. Scaffold Design Dependence of SLS Parameter settings

All scaffolds were designed using Pro/Engineer Wildfire (PTC, USA) and exported into the. STL file format. Scaffolds designed for Method a) consisted of four struts per layer, each strut 500 µm wide and with 2 mm distance between the centrelines of the struts. For Method b) four struts per layer were necessary in the 3D design to result in eight struts in the fabricated model. In this case, the struts were designed with a width of 1 mm, a height of 500 µm and a centreline separation distance of 2 mm. Scaffolds designed for Method c) consisted of eight struts per layer, each 500 µm wide, with a distance of 1 mm between the strut centrelines. In all cases the layers were oriented alternating parallel to the x or to the y-axis. Three layers with a height of 500 µm each and, to distinguish between top and bottom of the scaffold, a top layer of 1000 µm height, were included. CAD images of the models are illustrated in **Figure 5**.

The important sintering parameters can be seen in **Table 1**. The laser power was reduced for Methods b) and c) because the laser scan speed is slower in the "outline scan" mode. When not reducing the laser power, the energy density

$$ED = \frac{LP}{SS \times LS} \quad (1)$$

(with *ED* = energy density in J/mm², *LP* = laser power in Watt, *SS* = scan spacing in mm, and *LS* = laser scan speed in mm/s), as described in Caulfield *et al.* [24], would have been excessive over Method a), resulting in thicker struts.

Using the laser scan method that was found to be most suitable to fabricate thin struts, a parameter study was performed to find process parameters most suitable for sintering PCL scaffolds. The variable parameters were laser power (3.5 up to 11.5 W with 0.5 W increments), number of scans (one or two) and preheat temperature for the powder (38℃ up to 50℃). Subsequently, cylindrical scaffolds with diameters of 5 and 8 mm **(Figure 6)** were fabricated from PCL. Resulting from the parameter study, the powder bed preheat temperature was set to 38 ℃ and sintering was performed with a single scan at a laser power of 4 W. The scaffolds were sliced into 45 horizontal layers with a layer thickness of 0.11 mm each. Each set of struts consisted of 5 layers.

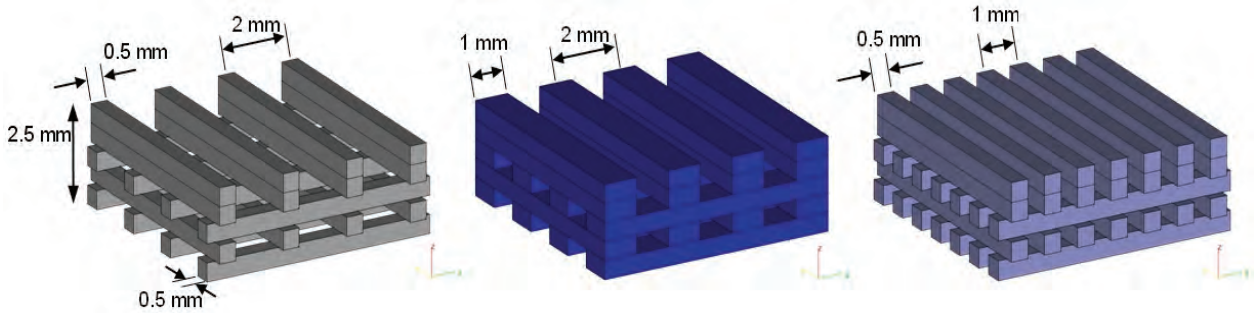

Figure 5. CAD models for scan method experiments.

Table 1. Sintering parameters for the polyamide scaffolds.

Fabrication method	Laser offset		Laser power W	Scan spacing mm
	x-direction µm	y-direction µm		
a)	240	200	9	0.10
b)	0	0	5	n/a
c)	243	243	5	n/a

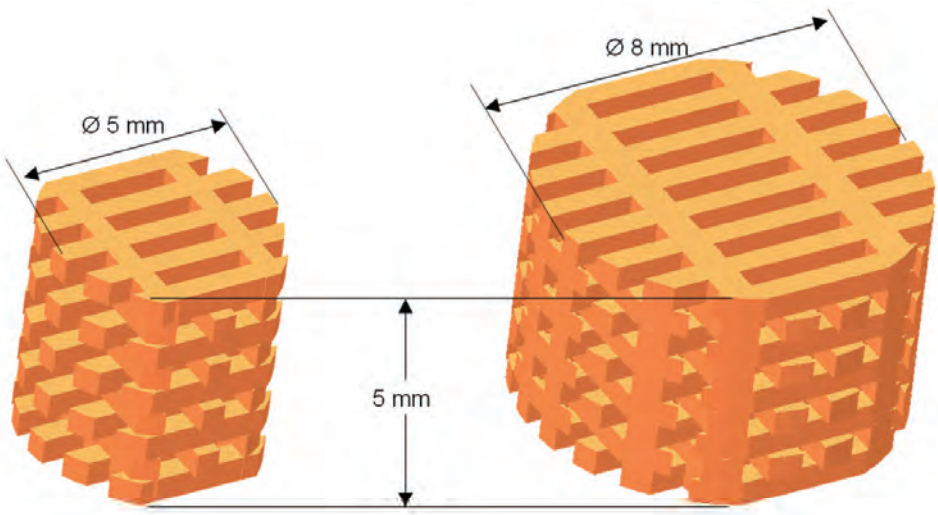

Figure 6. CAD models for PCL scaffolds.

Copyright © 2010 SciRes.

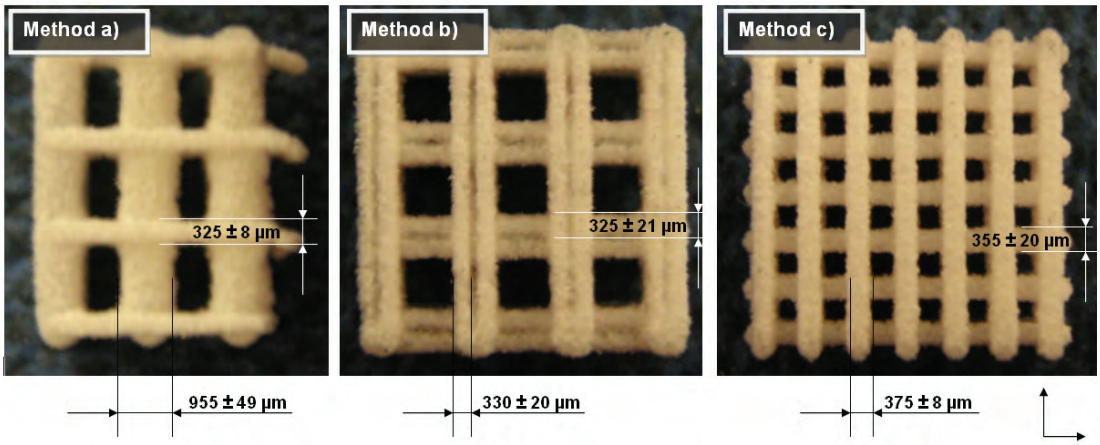

Figure 7. Polyamide models fabricated via the three scan methods.

Table 2. Strut width in x and y directions for each SLS fabrication method.

Strut Width	Method a)	Method b)	Method c)
x - direction [µm]	325 +/- 8	325 +/- 21	355 +/- 20
y - direction [µm]	955 +/- 49	330 +/- 20	375 +/- 8

2.3. Characterisation of Scaffold Properties

2.3.1. Strut Morphology

The scaffold structures were examined by scanning electron microscopy (SEM) (Hitachi, UK). All surfaces were coated with gold using an Emitech K550 gold coater (Emitech, UK) to avoid charging under the electron beam. The pore size, pore area, and strut thickness values as well as the surface topography were obtained using ImageJ analysis software (NIH, Public Domain).

2.3.2. Compression Tests

To determine the effective modulus of the scaffolds, the PCL scaffolds (diameter 5 mm) were tested in compression (n=6). The influence of cells and physiological conditions on the effective modulus were investigated using two additional scaffolds, one of which was seeded with SaOs-2 cells in a well ($3x10^4$ cells/well) and left in the physiological solution described below for seven weeks, while the other was stored as is in the solution for seven weeks. All compression tests were carried out on a Zwick Z2.5 (Zwick Testing Machines Ltd., UK) using a 1 kN load cell and at a compression rate of 1 mm/min. The modulus values were determined from subsequent stress-strain graphs.

2.3.3. Stability of the SLS Fabricated Scaffold in a Physiological Environment

To examine the physical integrity of the SLS fabricated constructs in a physiological environment, scaffolds were stored in the cell media solutions. Subsequently, the scaffolds were covered with 1 ml of media containing 500 ml RPMI-1640, 5 ml penicillin-strep- tomycin, 5 ml L-glutamine, 50 ml and 10 % foetal bovine serum and incubated at 37℃, 100 % humidity and 5 % CO_2 for 7 weeks (n=6). Thereafter, the scaffolds were visually examined using scanning electron microscopy; the porosity and surface topography were also examined. Because of the non-conductive nature of the polymer, samples were gold-coated prior to imaging. Samples were viewed and images captured over a range of magnifications. Furthermore, to determine if there were any adverse affects on the chemical composition of the scaffolds after storage in the cell culture media over a 7-week period, Fourier transform infra red spectroscopy (FTIR-ATR Shimadzu, UK) was employed (n=6). Spectra were recorded in the wavelength range of 4000 and 400 cm^{-1} by 2 cm^{-1} resolution in 16 scans.

3. RESULTS

3.1. Optimisation of Scaffold Structure

While for the struts in the x-direction the thickness was satisfying when using the standard scanning method, perpendicular struts had an excessive thickness, see **Figure 7**. As shown in **Table 2**, the struts in y-direction fabricated using Method a) were found to be more than twice the laser diameter, possibly caused by too much energy applied to a small area in the fast shot of the laser, or due to an inaccurate control of the laser beam movement. Though the laser spot diameter is only 410 µm, the struts were 955 ± 49 µm wide. There were no gaps found between them. This was in contrast to the struts parallel

Copyright © 2010 SciRes.

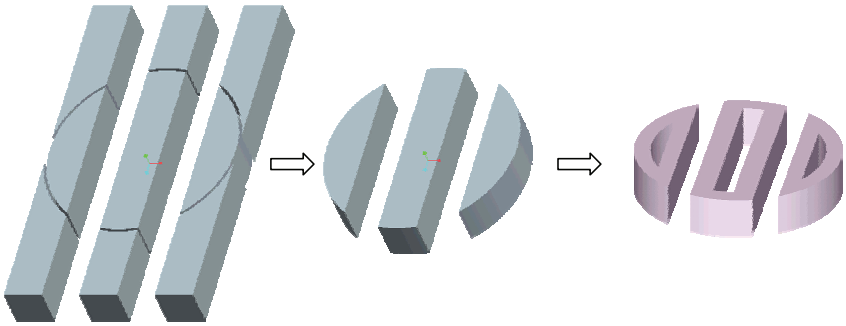

Figure 8. Curved struts following cutting a cylindrical section from the original design → approach not suited for cylindrical scaffolds.

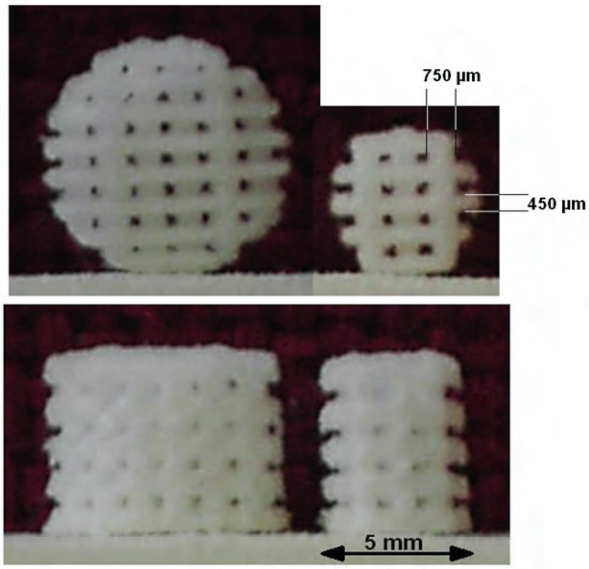

Figure 9. Photograph of the 8 mm and 5 mm PCL scaffolds.

to the main sintering direction of the laser along the x-axis of the build chamber, which tended to match the size of the laser spot diameter. Hence, this method was deemed unsuitable for scaffold fabrication. Methods b) and c), on the other hand, resulted in scaffold struts that were in both x- and y-direction even less thick than the laser beam spot diameter. For Method b), struts in the x-direction and y-direction were about the same widths of 325 +/- 20 µm. This matched the width of the struts in the x-direction achieved with Method a), because for this direction the scanning technique is the same for these two methods. With Method c) slightly higher widths as Method b) were achieved in both directions. This was attributed to the fact that with Method c) each strut was scanned twice along its centre.

Method b) gave the best results in achieving minimal strut thickness. However, it has a few general drawbacks. Using this method it is quite difficult to foresee the structure of the fabricated scaffold based on the designed one, as each strut in the 3D design results in two struts in the built model. In addition, this method is only suitable when the edges of the design are parallel. Using a cylindrical design, some of the fabricated struts would be curved **(Figure 8)**. Therefore, Method b) is not suited for scaffolds with curved surfaces, such as cylindrical scaffolds. Finally, the flow through the structure from the sides is obstructed, because some of the struts are connected at their ends, unless this part is cut away. Due to the good results obtained using Method c), it was chosen for further scaffold fabrication. The thickness achieved was only slightly higher than for Method b), it allows for more complex designs, and, when anticipating the fabricated strut thickness in the 3D design, final outcome and design do not differ. Non-parallel shapes can be built as intended, and there is virtually no limitation in the macroscopic shape of the scaffold, i.e. cylindrical scaffolds can be fabricated.

It was observed that when processing PCL with method c), the achievable minimal strut thickness was higher then when processing PA. In the x-direction it was 450 µm, while it was approximately 700 to 800 µm in y-direction. The increased thickness compared to the PA samples is due to the different process parameters used and different thermal properties of the material. The difference between struts in x- and y-direction, however, is surprising, as sintering conditions for both directions were the same. In an additional test of all three methods applied to PCL material, however, Method c still gave the best results. In order to achieve pores of 300 to 400 µm diameter, the number of struts in the y-direction was reduced to three compared to five struts parallel to the x-axis in a 5 mm diameter cylindrical scaffold. In an 8 mm diameter scaffold there were six struts parallel to the y-axis and eight parallel to the x-axis. At the bottom and at the top of the scaffolds, two perpendicular struts were added to increase the mechanical stability and prevent inclining when loaded with compression forces. Based on the CAD design, the scaffolds had a porosity of 50 %. The fabricated scaffolds are shown in **Figure 9**.

Copyright © 2010 SciRes.

3.2. Materials Properties of the Scaffolds

3.3.1. Strut Morphology

Visual inspection of the PCL constructs using SEM revealed strut thickness values of approximately 500 µm and 800 µm, respectively, depending on their orientation. The average pore size was around 400 µm **(Figure 10a)**. On the microscale each strut within the scaffold consisted of a large number of randomly oriented grains **(Figure 10 a, b, c)**. The grains had different shapes and their surface area ranged from 500 to 5000 mm². The surface of the single particles appeared smooth and each grain had rounded, regular edges **(Figure 10d)**. The grains were usually connected by molten material through sintering, however, many grains were connected to each other by a system of thin struts, leaving an internal microporosity within each strut.

3.3.2. Compression Tests

The effective modulus for the untreated scaffolds was determined to be 6.5 ± 0.7 MPa. The effective moduli for both scaffolds stored in the physiological solution for seven weeks, whether or not seeded with cells, are within one standard deviation of this value.

3.3.3. Stability of the SLS Fabricated Scaffold in a Physiological Environment

The surface topography of the scaffolds stored in the physiological solution **(Figure 11)** appeared to be slightly different to the as-fabricated PCL scaffolds. The number of grains in the struts appeared to be reduced; there were more areas where no separate grains were attached. The grains appeared to have irregular shapes with uneven, jagged surfaces **(Figure 11 d)**.

As-fabricated scaffolds

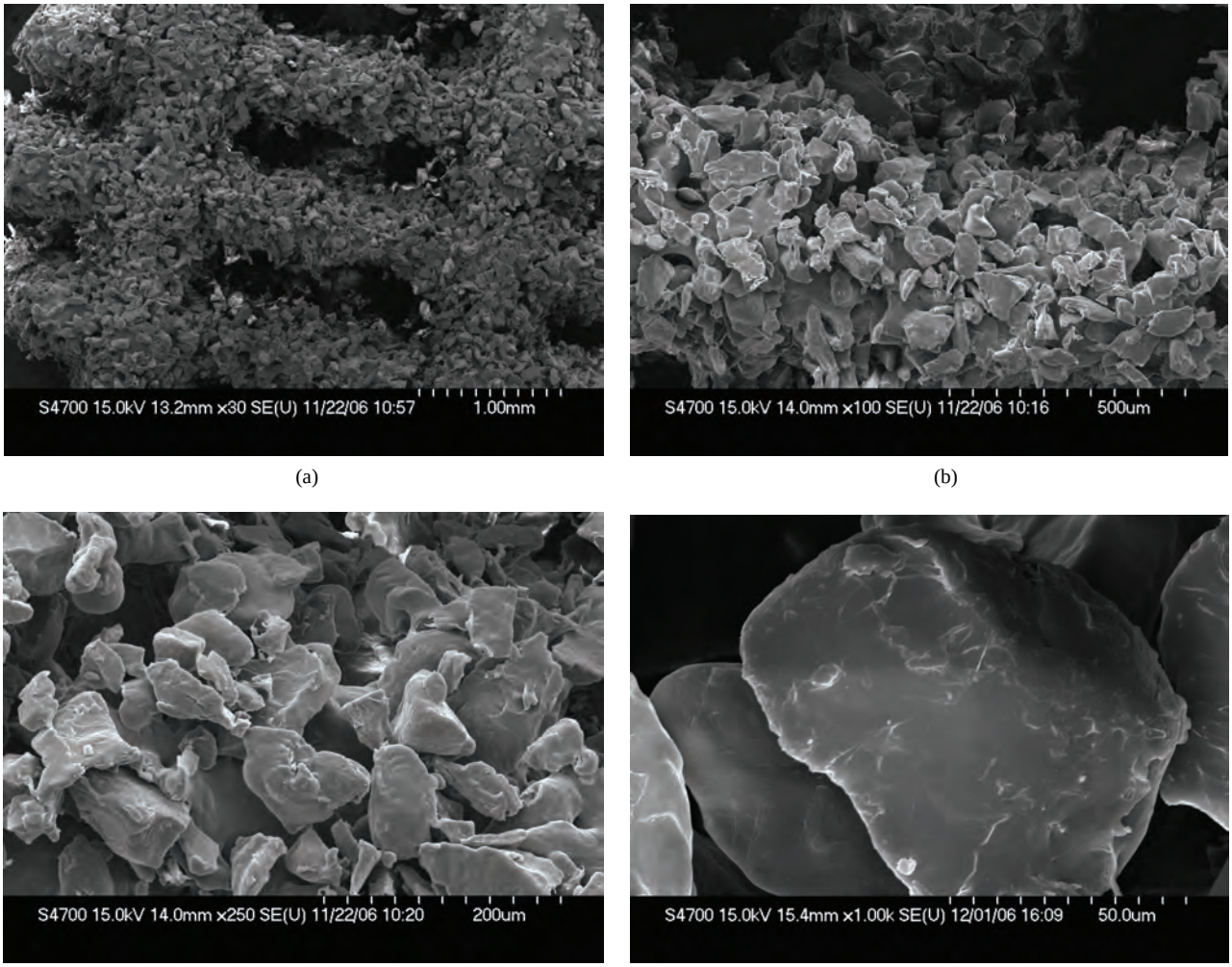

(a) (b)

(c) (d))

Figure 10. SEM analysis of strut morphology. Untreated scaffold at various magnifications, (a) X30, (c) X100, (e) X 250, (g) X 1000.

Copyright © 2010 SciRes.

Scaffold after immersion in physiological solution

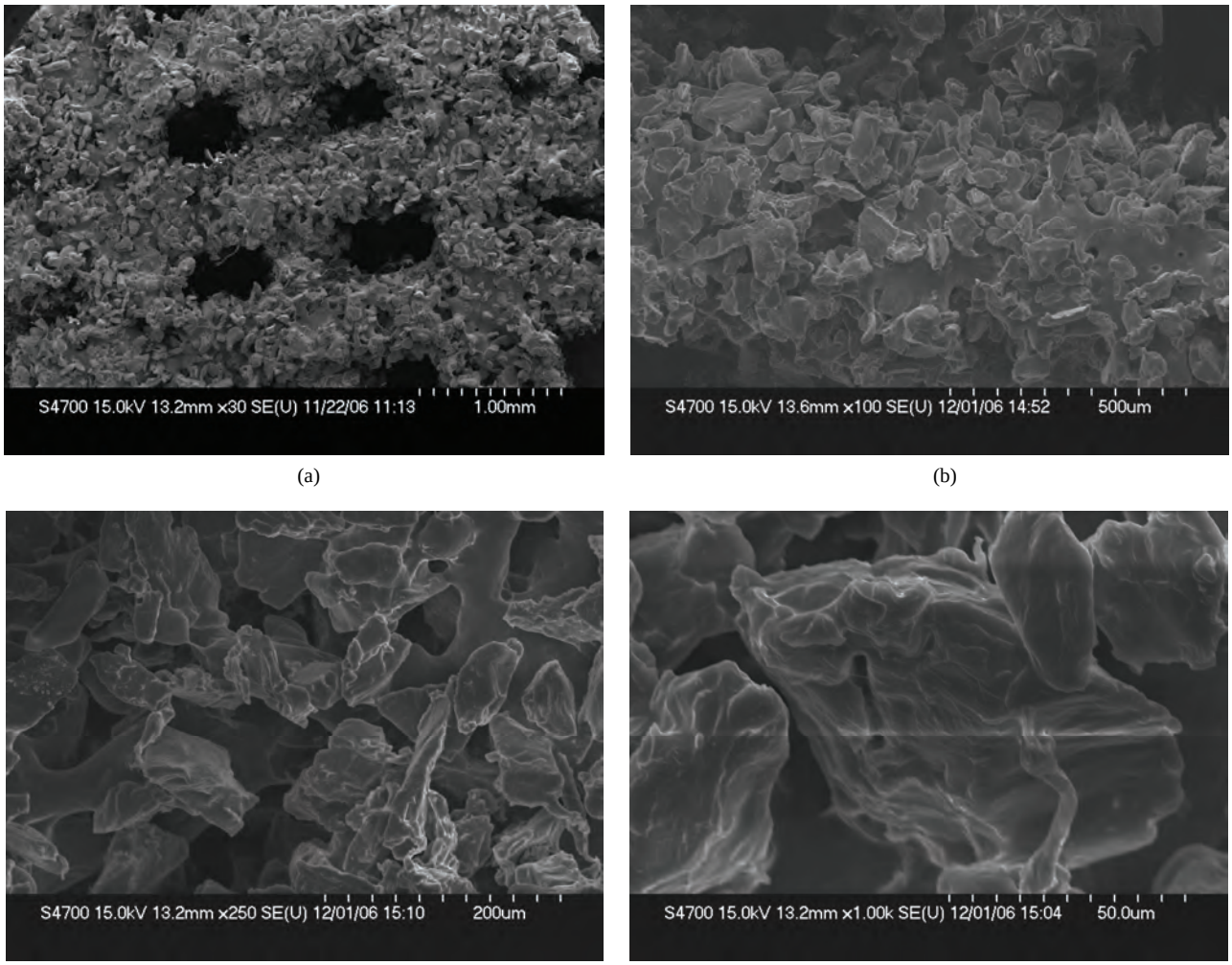

(a) (b)

(c) (d))

Figure 11. SEM images of scaffold after seven weeks in media at various magnifications, (b) X 30, (d) X100, (f) X 250, (h) X1000.

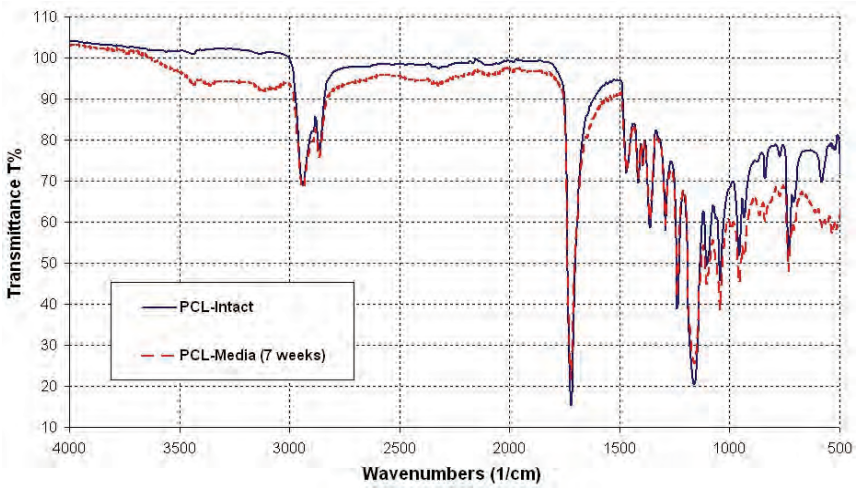

Figure 12. FTIR spectra showing chemical composition of SLS scaffolds. There is no change in the functional groups after 7 weeks in media, suggesting the SLS fabricated scaffold maintains its chemical integrity.

Copyright © 2010 SciRes.

Based on the FTIR analysis, it was seen that the chemical composition of the scaffolds stored in the media did not change over a 7-week period **(Figure 12)**. The characteristic C–H stretching of CH_2 and CH_3 groups of saturated structures was observed in the range 2980–2850 cm^{-1}. Typical absorption frequencies associated with ester moieties present in PCL were readily evidenced mainly at 1740 cm^{-1} (C=O stretching). The absorption band at 1220 cm^{-1} was attributable to the C(O)–O and C–N stretching and N–H bending (amide III) vibrations. Thereby, no alteration in the chemical composition of the scaffolds was observed.

4. DISCUSSION

The selected approach to fabricate scaffolds using the outline scan function of the Sinterstation proved to be successful with respect to producing minimal strut thicknesses, which to date had not been seen for selective laser sintered PCL scaffolds. The phenomenon of different strut thicknesses in x- and y-directions is more obvious for the PCL scaffolds than for PA. This is probably due to the different heat conduction properties of this material and will be further investigated. However, as it occurs for both tested materials, an influence of the prototyper's non-accessible scan parameters is undeniable. Nonetheless, porous PCL scaffolds were fabricated by selective laser sintering, using a Sinterstation, with a pore size range of 300–400 m in diameter and a minimum wall thickness of 450 m in the x-direction and 700 m in the y-direction.

In addition, there was no dramatic change in the physical properties or chemical composition of the SLS fabricated scaffolds stored in a cell culture environment for 7 weeks. This was echoed in the mechanical properties. Though signs of degradation of the material were obvious, the mechanical performance of the scaffolds remained unchanged after 7 weeks under the influence of the physiological solution and cells. Degradation appeared to be limited to surface particles that did not contribute to the mechanical properties as they did not have a strong mechanical bond to the main structure. Moreover, the mechanical property values were at the lower end of the compressive modulus values quoted for cancellous bone [25].

Taken together, these results highlight the potential of the described selective laser sintering method as an alternative fabrication technique for highly porous tissue engineering scaffolds with minimal strut thickness. Optimisation of process parameters to further reduce the strut thickness, in particular for PCL, is currently in progress.

5. ACKNOWLEDGEMENTS

The authors acknowledge research funding from the European Union through the STEPS FP6 project (contract number FP6-500465) and also the partners in the STEPS project for their input. M.A. Tyndyk acknowledges funding from the Irish Research Council for Science, Engineering and Technology (IRCSET) through a Postdoctoral Fellowship. The authors acknowledge support from the Programme for Research in Third Level Institutions (PRTLI) administered by the Higher Education Authority.

REFERENCES

[1] Cancedda, R., Dozin, B., Giannoni, P. and Quarto, R. (2003) Tissue engineering and cell therapy of cartilage and bone. *Matrix Biology*, **22**, 81-91.

[2] Hollister, S.J., Maddox, R.D. and Taboas, J.M. (2002) Optimal design and fabrication of scaffolds to mimic tissue properties and satisfy biological constraints. *Biomaterials*, **23**, 4095-4103.

[3] Holy, C.E., Shoichet, M.S. and Davies, J.E. (2000) Engineering three-dimensional bone tissue in vitro using biodegradable scaffolds: Investigating initial cell-seeding density and culture period. *Journal of Biomedical Materials Research*, Part A, **51**, 376-382.

[4] Hutmacher, D.W. (2000) Scaffolds in tissue engineering bone and cartilage. *Biomaterials*, **21**, 2529-2543.

[5] Schimandle, J.H. and Boden, S.D. (1997) Bone substitutes for lumbar fusion: Present and future. *Operative Techniques in Orthopaedics*, **7**, 60-67.

[6] Bancroft, G.N., Sikavitsas, V.I. and Mikos, A.G. (2003) Technical note: Design of a flow perfusion bioreactor system for bone tissue-engineering applications. *Tissue Engineering*, **9**, 549-554.

[7] Bilodeau, K. and Mantovani, D. (2006) Bioreactors for tissue engineering: Focus on mechanical constraints, a comparative review. *Tissue Engineering*, **12(8)**, 2367-2383.

[8] Yu, X., Botchwey, E.A., Levine, E.M., Pollack, S.R. and Laurencin, C.T. (2004) Bioreactor-based bone tissue engineering: The influence of dynamic flow on osteoblast phenotypic expression and matrix mineralization. *Proceedings of the National Academy of Sciences of the United States of America*, **101**, 11203-11208.

[9] Adachi, T., Osako, Y., Tanaka, M., Hojo, M. and Hollister, S.J. (2006) Framework for optimal design of porous scaffold microstructure by computational simulation of bone regeneration. *Biomaterials*, **27**, 3964-3972.

[10] Green, D., Walsh, D., Mann, S. and Oreffo, R.O.C. (2002) The potential of biomimesis in bone tissue engineering: Lessons from the design and synthesis of invertebrate skeletons. *Bone*, **30**, 810-815.

[11] Lohfeld, S., Barron, V. and Mchugh, P.E., (2005) Biomodels of bone: A review. *Annals of Biomedical Engineering*, **33**, 1295-1311.

[12] Hutmacher, D.W., Sittinger, M. and Risbud, M.V. (2004) Scaffold-based tissue engineering: Rationale for computer-aided design and solid free-form fabrication systems. *Trends in Biotechnology*, **22**, 354-362.

[13] Leong, K.F., Cheah, C.M. and Chua, C.K. (2003) Solid freeform fabrication of three-dimensional scaffolds for engineering replacement tissues and organs. *Biomaterials*, **24**, 2363-2378.

[14] Moroni, L., De Wijn, J.R. and Van Blitterswijk, C.A. (2006) 3D fiber-deposited scaffolds for tissue engineering: Influence of pores geometry and architecture on dynamic mechanical properties. *Biomaterials*, **27**, 974-985.

Copyright © 2010 SciRes.

[15] Woesz, A., Rumpler, M., Stampfl, J., Varga, F., Fratzl-Zelman, N., Roschger, P., Klaushofer, K. and Fratzl, P. (2005) Towards bone replacement materials from calcium phosphates via rapid prototyping and ceramic gel-casting. *Materials Science and Engineering C*, **25**, 181-186.

[16] Tan, K.H., Chua, C.K., Leong, K.F., Cheah, C.M., Cheang, P., Abu Bakar, M.S. and Cha, S.W. (2003) Scaffold development using selective laser sintering of polyetheretherketone-hydroxyapatite biocomposite blends. *Biomaterials*, **24**, 3115-3123.

[17] Yang, S., Leong, K.F., Du, Z. and Chua, C.K. (2002) The design of scaffolds for use in tissue engineering. Part II. Rapid prototyping techniques. *Tissue Engineering*, **8**, 1-11.

[18] Das, S., Hollister, S.J., Flanagan, C., Adewunmi, A., Bark, K., Chen, C., Ramaswamy, K., Rose, D. and Widjaja, E. (2003) Freeform fabrication of nylon-6 tissue engineering scaffolds. *Rapid Prototyping Journal*, **9**, 43-49.

[19] Partee, B., Hollister, S.J. and Das, S. (2006) Selective laser sintering process optimization for layered manufacturing of CAPA 6501 polycaprolactone bone tissue engineering scaffolds. *Journal of Manufacturing Science and Engineering*, **128**, 531-540.

[20] L. Liulan, H. Qingxi, H. Xianxu, and X. Gaochun, (2007) Design and fabrication of bone tissue engineering scaffolds via rapid prototyping and CAD. *Journal of Rare Earths*, **25(2)**, 379-383.

[21] Williams, J.M., Adewunmi, A., Schek, R.M., Flanagan, C. L., Krebsbach, P.H., Feinberg, S.E., Hollister, S. J. and Das, S. (2005) Bone tissue engineering using polycaprolactone scaffolds fabricated via selective laser sintering. *Biomaterials*, **26**, 4817-4827.

[22] Smith, M.H., Flanagan, C.L., Kemppainen, J.M., Sack, J. A., Chung, H., Das, S., Hollister, S.J. and Feinberg, S.E. (2007) Computed tomography-based tissue-engineered scaffolds in craniomaxillofacial surgery. *The International Journal of Medical Robotics and Computer Assisted Surgery*, **3**, 207-216.

[23] Wiria, F.E., Leong, K.F., Chua, C.K. and Liu, Y. (2007) Poly-[epsilon]-caprolactone/hydroxyapatite for tissue engineering scaffold fabrication via selective laser sintering. *Acta Biomaterialia*, **3**, 1-12.

[24] Caulfield, B., Mchugh, P.E. and Lohfeld, S. (2007) Dependence of mechanical properties of polyamide components on build parameters in the SLS process. *Journal of Materials Processing Technology*, **182**, 477-488.

[25] An, Y.H. (1999) Mechanical properties of bone, in An, Y. H. & Draughn, R.A. Editions. Mechanical testing of bone and the bone-implant interface. CRC Press, Boca Raton, Florida, USA, 41–64.

Copyright © 2010 SciRes.

J. Biomedical Science and Engineering, 2010, 3, 148-159 **JBiSE**
doi:10.4236/jbise.2010.32020 Published Online February 2010 (http://www.SciRP.org/journal/jbise/).

Senescence of human vocal fold fibroblasts in primary culture

George M. Adams[1], Chet C. Xu[1], Roger W. Chan[1,2]

[1]Otolaryngology, Head and Neck Surgery, University of Texas Southwestern Medical Center, Dallas, USA;
[2]Biomedical Engineering, University of Texas Southwestern Medical Center, Dallas, USA.
Email: roger.chan@utsouthwestern.edu

Received 1 October 2009; revised 18 December 2009; accepted 21 December 2009.

ABSTRACT

This study examined the replicative senescence of primary-culture human vocal fold fibroblasts, in terms of changes in gross chromosomal structure with sub-culturing, and population doubling time (PDT). The mRNA expressions of 14 target genes were also examined. The objectives were to identify the onset of senescence for establishing the acceptable limit of sub-culturing, and to better understand the effect of cellular aging on matrix protein regulation in the vocal fold. Gross chromosomal changes in vocal fold fibroblasts from a 58-year-old woman were karyotyped with Giemsa stain. Proliferation of the fibroblasts was determined with cell recovery and PDT calculation. Transcript levels of the target genes were found by RT-PCR. Onset of significant chromosomal anomalies was seen with passage 5. For mRNA expressions, significant increases with passaging were observed in collagenase, macrophage elastase, lysyl oxidase and fibromodulin, whereas significant down-regulation was detected in decorin, procollagen I, hyaluronic acid-synthase 2 and collagen III. This modulation pattern suggested that fibroblasts underwent *in vitro* aging, consistent with the significant increase in PDT. The inception of senescence did not occur until passage 5. These findings may facilitate the development of representative *in vitro* models for testing tissue engineering approaches involving primary-culture fibroblasts.

Keywords: Larynx; Extracellular Matrix; Cell Proliferation; Replicative Senescence; Tissue Engineering

1. INTRODUCTION

A better understanding of the biology of vocal fold fibroblasts is fundamental for establishing representative and consistent *in vitro* models of the vocal fold lamina propria extracellular matrix (ECM), where fibroblasts are the predominant cell type [1,2]. Such *in vitro* models are critical for the development of tissue engineering approaches for the treatment of a variety of vocal pathologies. Tissue engineering, or regenerative medicine approaches involve the fabrication of tissue substitutes that can be used to surgically augment, replace, and functionally repair tissue defects in the lamina propria, e.g., vocal fold scarring, atrophy, sulculs vocalis, and tissue deficiencies left with the surgical removal of tumors [3]. Vocal fold fibroblasts are responsible for the homeostatic expressions of key ECM components of the lamina propria, including fibrous proteins (e.g., collagen, elastin), proteoglycans (e.g., decorin, fibromodulin, versican, biglycan), glycosaminoglycans (e.g., hyaluronic acid), and structural glycoproteins (e.g., fibronectin) [1,2]. Expressions of these ECM proteins contribute to the optimal tissue viscoelastic properties crucial for functional voice production, since the lamina propria is the primary tissue layer responsible for flow-induced self-oscillation of the vocal fold [4]. The structural and functional integrity of the ECM depends on the proliferation, metabolic activities, and turnover rate of vocal fold fibroblasts. ECM changes have often been studied with cultured vocal fold fibroblasts, yet it is well established that fibroblasts *in vitro* are influenced by a phenomenon known as replicative senescence, an *in vitro* form of aging somewhat parallel to the senescent processes *in vivo* [5]. Cells undergo replicative senescence after repeated subculturing for a number of passages. Replicative senescence is characterized by decreased cellular proliferation, resistance to mitosis, and avoidance of programmed cell death or apoptosis [5,6].

Thibeault *et al.* examined the karyotypes of normal vocal fold fibroblasts and tracheal scar fibroblasts from primary culture, across different passages (passages 3, 4, 5, 6 and 10) [7]. Normal vocal fold fibroblasts displayed multiple chromosomal abnormalities including loss of the Y chromosome, translocations, multiple rearrangements, and tetraploidy of all chromosomes excluding the Y chromosome. With tracheal scar fibroblasts, no aberrations were detected in the early passages while 15 of 20 cells analyzed in the late passage showed tetraploidy in all but the sex chromosome. While these data provided an initial understanding of chromosomal abnormalities in primary vocal fold fibroblasts, the onset of

these abnormalities with passaging was not known, particularly in early passages (before passage 3). This study attempted to determine the inception of these anomalies using detailed cytogenetic analyses of early and late passages (passages 1-5, and passage 10) of normal primary-culture human vocal fold fibroblasts. The expressions of key matrix proteins in the lamina propria ECM and their protein precursors, as well as those of the matrix-synthesizing and matrix-degrading enzymes at the mRNA level were examined by reverse transcriptase-polymerase chain reaction (RT-PCR). The rate of proliferation of the fibroblasts was also investigated by measurement of the population doubling time (PDT). Our goals were: 1) to identify the onset of senescent mechanisms for establishing an acceptable limit of sub-culturing; and 2) to better understand the effect of cellular aging on the homeostatic regulation of matrix proteins in the vocal fold lamina propria, so that one could establish representative, consistent *in vitro* models of the ECM based on the acceptable limit of sub-culturing. Such models can serve as a platform for evaluating the impact of tissue engineering approaches on functional tissue remodeling and reconstruction, e.g., approaches based on the use of acellular bioscaffolds, polymeric substrates, or growth factors [8,9,10].

2. MATERIALS AND METHODS

2.1. Vocal Fold Tissue Culture

Primary-culture vocal fold fibroblasts were obtained from the vocal ligament (intermediate and deep layers of the lamina propria) of a larynx excised from a 58-year-old Hispanic female who underwent total laryngectomy due to papillary columnar thyroid carcinoma. The laryngeal specimens were examined by an otolaryngologist as well as by a pathologist, and were certified to be free of cancerous tissue, i.e., without any epithelial to mesenchymal transition [11]. The protocols for the procurement of the laryngeal specimens and the subsequent experimental procedures were approved by the Institutional Review Board of UT Southwestern Medical Center. Using primary explant techniques as described in Xu *et al*. the specimens were disinfected with 70% ethanol, washed twice with phosphate-buffered saline (PBS), dissected using phonomicrosurgical instruments and cut into 1- to 2-mm^3 sections [8]. The tissue sections were then placed in a 24-well plate (one section per well) and supplemented with DMEM fortified with 20% fetal bovine serum (FBS) and 2% penicillin/streptomycin. Primary fibroblasts reproduced and migrated from the tissue sections over a two-week period prior to being subcultured, or passaged. The primary cells were authenticated as conventional vocal fold fibroblasts according to their morphological characteristics under light microscopy [12]. For sub-culturing, cells were grown to 60% confluence and treated with trypsin-EDTA for 3-4 min at 37°C with 5% CO_2. An equal volume of complete media was then added to the trypsinized suspension prior to centrifuging for 3 min at 1500 rpm. After removal of the supernatant, the pellet was resuspended in 8 ml of complete media with 1 ml added to a 75-cm^2 tissue culture flask (T-75), at 1:8 dilution. DMEM was then added (20-25 ml) to the resuspension and cells were incubated at 37°C with 5% CO_2.

2.2. Karyotype Analysis

Karyotype analysis of primary-culture vocal fold fibroblasts of passages one through five (P1-P5) and ten (P10) and grown to 60% confluence was conducted at the Veripath Laboratories of UT Southwestern Medical Center (Dallas, TX). To induce cell cycle arrest and obtain sufficient numbers of cells in metaphase, colcemid (Roche Laboratories, Nutley, NJ) was added (50 ng/ml final concentration) overnight for 12-16 hours prior to harvest. After trypsinization and centrifugation (1500 rpm for 5 min) along with subsequent aspiration of the supernatant, cells were treated with a hypotonic solution (75 mM KCl) for 25-30 min at 37°C to promote swelling and to allow for proper spreading and clear microscopic examination of the chromosomes.

Cells were fixed using a 3:1 mixture of methanol to glacial acetic acid (one ml volume) and mixed thoroughly prior to centrifugation (1500 rpm for 5 min). After a second fixation step using a larger volume of fixative (7 ml), cells were dropped onto microscope slides in an incubation chamber (Thermotron, Holland, MI) with constant humidity for proper spreading of the chromosomes. To allow for adsorption of chromosomes onto the glass surface, slides were incubated at 90°C for 30 min prior to G-banding by trypsin using Giemsa (GTG) stain.

For the G-banding procedure, heat-treated slides were immersed in trypsin (1:50 dilution with Isoton II buffer (Curtis Matheson Scientific, Houston, TX) for 1-2 min to remove extra chromosomal debris, then in Isoton II twice to remove trypsin. Two successive washes with 75% and 95% ethanol removed remnants of Isoton II and a subsequent wash in Gurr buffer eliminated any ethanol residue. Slides were stained (for 1-2 min) using Wright's solution (eosin methylene blue), rinsed with deionized water and dried with compressed air.

Images of G-banded chromosomes (or karyotypes) were acquired using the Case Data Manager Version 5.5.2.2 software (Applied Spectral Imaging, Vista, CA), which arranged chromosomes in a pairwise fashion. Karyotypes were generated for passages 1-5 and 10 using 20 metaphase cells. By using the standard number of 20 cells counted, mosaicism of greater than 14% frequency may be excluded at the 95% confidence level (i.e., $p<0.05$) [13]. To ensure the reliability and validity of the analysis, images were analyzed by four individuals certified in cytogenetic analysis and the karyotypes were documented.

Copyright © 2010 SciRes.

Table 1. Primer sequences and polymerase chain reaction parameters.

Target	Primer Sequence	RNA (ng)	AT (°C)	bp
GAPDH (control)	F: GGTGTGAACCATGAGAAG R: CTGTTGAAGTCAGAGGAGAC	100	50	464
HA Receptor (CD44)	F: GAAAGGAGCAGCACTTCAGG R: CACTTGGCTTTCTGTCCTC	100	50	397
Decorin	F: GATGCAGCTAGCCTGAAAGG R: TCACACCCGAATAAGAAGCC	100	50	274
MMP-1 (Collagenase)	F: CAACTTACATCGTGTTGCGG R: ACCGGACTTCATCTCTGTCG	100	50	395
GAPDH (control)	F: ACCCAGAAGACTGTGGATGG R: TGAGCTTGACAAAGTGGTCG	100	56	382
Procollagen I	F: GTTGGTGCTAAGGGTGAAGC R: ACCGGACTTCATCTCTGTCG	100	56	294
Fibronectin	F: TACCAACCTACGGATGACTCG R: CATCATCGTAACACGTTGCC	100	56	300
GAPDH (control)	F: AAGGTCGGAGTCAACGGATTTGGT R: AGTGATGGCATGGACTGTGGTCAT	100	60	534
HA-synthase 2	F: TACCAACCTACGGATGACTCG R: CATCATCGTAACACGTTGCC	100	60	403
Collagen I (α2)	F: TACCCTGGCAATATTGGTCCCGTT R: GGCAGACCTTGCAATCCATTGTGT	100	60	248
Collagen III (α1)	F: CTTGATGTGCAGCTGGCATTCCTT R: AGTCATTGCTCTGCAGATGGGCTA	100	60	686
Hyaluronidase I	F: ACTGCAGCAATCACAAAGGCTGAC R: TATTTGCTGGACTGGTGCCTCTCA	100	60	294
Hyaluronidase II	F: AACGTGTGGAGCACTACATTCGGA R: GAACTGCTGTGCTGCGAACTCAAA	100	60	215
Hyaluronidase III	F: TTACAGTCAACCCTCCCAAGCACA R: TTAGCACTTTACCGACCTTCGCCA	100	60	280
Lysyl Oxidase	F: ATGATCACAGGGTGCTGCTCAGAT R: GTGTGCAGTACATGCAAATCGCCT	100	60	260
GAPDH (control)	F: TGGCAAATTCCATGGCACCGTCAA R: TTGACAAAGTGGTCGTTGAGGGCA	100	62	768
Fibromodulin	F: CACTTTCCTCCACAGATGCC R: GCTGCTTTCTCAATCCAGCC	100	62	387
MMP-12 (macrophage elastase)	F: CTGCTGATGACATACGTGGC R: GTTTGGGATAACCAGGGTCC	100	62	498

AT=annealing temperature; bp=product base pairs; F=forward; R=reverse;
GAPDH=glyceraldehyde 3-phosphate dehydrogenase; MMP=matrix metalloproteinase

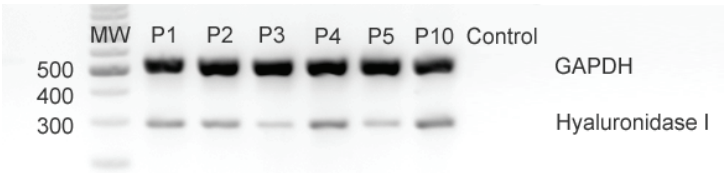

Figure 1. An example of PCR agarose gel, showing PCR products generated from RNA extracted from primary-culture human vocal fold fibroblasts of passages 1-5 (P1-P5) and passage 10 (P10) for the hyaluronidase I target primer as shown in **Table 1** (MW=100 base pair DNA molecular weight marker, Amresco, Solon, OH).

Copyright © 2010 SciRes.

2.3. Measurement of Population Doubling Time

In order to examine the rate of proliferation of the primary vocal fold fibroblasts, the cumulative doubling of the cells was measured by the population doubling time (PDT). PDT is the time interval required for dividing cells to double in number [14]. To calculate PDT, a fixed number (1×10^4 cells) of vocal fold fibroblasts of a certain passage (passages 2 to 10) were seeded in each well of a 6-well plate. After 72 hours, the cells from each well were collected and counted with a hemocytometer, with the number of cells designated as N_T. Assuming that the number of cells increases exponentially, at the end of *n* generations; each single cell would yield 2^n cells. Thus, after 72 hours, 1×10^4 seeded cells would produce $N_T = (10^4\times2^n)$ cells at harvest. The number of generations (*n*) equals to 3.32 ($\log N_T - \log 10^4$). By definition, PDT is the total time elapsed divided by the number of generations. PDT of the corresponding passage can be obtained by the following equation [14]:

$$PDT=72/3.32\ (\log N_T - \log 10^4)$$

2.4. Reverse Transcriptase-Polymerase Chain Reaction (RT-PCR)

Total RNA was extracted with TRIzol reagent (2 ml) (Invitrogen, Carlsbad, CA) using a modification of the method of Chomczynski and Sacchi [15] from fibroblasts grown to 80% confluence (~$2\text{x}10^6$ cells) in two 175 cm^2 flasks, for each of passages 1-5 and 10.

All primers for PCR analysis were obtained through Invitrogen (Carlsbad, CA). Primers for specific targets and the standard control, glyceraldehyde 3-phosphate dehydrogenase (GAPDH), are listed in **Table 1** along with annealing temperature (AT), product size in base pairs (bp), and the source of the primer sequences. Primer sequences for those targets designed in the present study were based on sequences published by the NIH GenBank database, using the SciTools software of Integrated DNA Technologies (Coralville, IA). Targets were chosen based on their contributions to and demonstrated roles in the maintenance of the vocal fold extracellular matrix [1,16,17]. Furthermore, analyses of collagenase (MMP-1), macrophage elastase (MMP-12) and the three isoforms of hyaluronidases (I, II, and III) were analyzed for conversion of fibroblasts from a matrix-synthesizing to a matrix-degrading phenotype. This transition serves as a hallmark indicator of the process of replicative senescence [5].

A master stock (1mM) of each primer was used to generate a working stock (10 μM) for each PCR reaction. All reactions were carried out using the OneStep RT-PCR kit (Qiagen, Valencia, CA) coupling the cDNA synthesis and PCR steps. For each reaction (12.5 μl total volume), the following components were added, with the final concentrations or amounts noted in brackets: target forward and reverse primers [400-600 nM], GAPDH forward and reverse primers [600nM-1500 nM], 1× RT-PCR buffer (including $MgCl_2$ [12.5 mM]), nucleotides [400 μM of each], template RNA (100 ng), RNasin® RNAse inhibitor [7 U] (Promega, Houston, TX) and the OneStep RT-PCR Enzyme Mix [1:25] (Qiagen, Valencia, CA). Four pairs of primers for the GAPDH control were used to match four different target annealing temperatures (**Table 1**).

Reactions were incubated using a Mastercycler personal thermal cycler (Eppendorf, Westbury, NY) using a protocol with an initial denaturation (94°C for 3 min) and 29-37 cycles of the following steps: denaturation (94°C for 30 sec), annealing (50°C , 56°C, 60°C or 62°C for 30 sec) and elongation (72°C for 1 min). As a final step, PCR products were extended for 7 min at 72°C. PCR products were electrophoresed in 0.5×TAE buffer on 2% agarose gels and visualized for densitometric analysis using a FluorChem HD2 gel documentation system (Alpha Innotech, San Leandro, CA). An example of an agarose gel containing PCR products for the hyaluronidase I target primer is shown in **Figure 1**. To verify that the optical density of the PCR products was in the linear range, three reactions, each with RNA purified from a different passage, were loaded using two different volumes (3 and 5 μl). PCR products for each target and for GAPDH were compared using densitometric analysis with the gel documentation system. To indicate the relative mRNA expression for each target gene, the densitometric ratio of the target relative to GAPDH was plotted as a function of the passage number.

2.5. Statistical Analysis

For the population doubling time data, one-way analysis of variance (ANOVA) was conducted to determine if the proliferation rates of the vocal fold fibroblasts in different passages were significantly different from one another. The level of significance (alpha) was set at 0.01.

For the densitometric results of mRNA expressions obtained from RT-PCR, one-way ANOVA was also performed across all passages for each given target. If the ANOVA results reached statistical significance ($p<0.01$), post-hoc analysis was done using the Tukey honestly significant difference (HSD) test for all possible pairwise comparisons of passages (e.g., P1-P2, P3-P4, P5-P10, etc.). Those pairwise comparisons that contribute to an overall trend of increase or decrease in the mRNA expressions of a particular target were deemed particularly important for the purpose of examining the effect of passaging or replicative senescence. Also, the results of the P5-P10 comparisons are shown separate to the other pairwise comparisons, in order to highlight the effect of replicative senescence in late passages.

Copyright © 2010 SciRes.

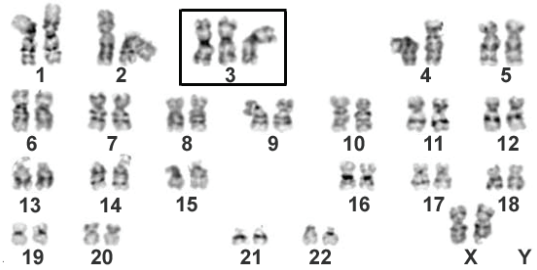

Figure 2. Passage 1 (P1) karyotype: Systematic array (karyotype) of G-banded chromosomes from P1 visualized by Giemsa stain showing an allotment of 23 pairs of chromosomes including the sex chromosomes, with three copies of chromosome 3 observed in 3 of 20 cells examined (boxed area) (only arrays with chromosomal aberrations are shown).

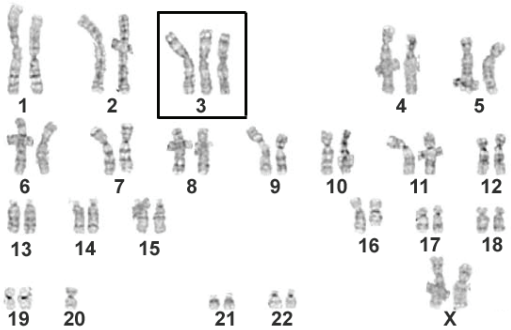

Figure 3. Passage 2 (P2) karyotype: An array showing three copies of chromosome 3 (boxed area). Karyotypically normal according to Mitelman [18].

3. RESULTS

3.1. Characterization of Vocal Fold Fibroblast Karyotype

Chromosomal analysis indicated the presence of an additional cell line (noted in 3 of 20 metaphase cells analyzed) in passage 1 (P1) with three copies of chromosome 3 (47, XX, +3[3]/46, XX [17]) (**Figure 2**, boxed area). The same anomaly was also found in both passage 2 (P2) and passage 3 (P3), revealing a degree of pseudo-mosaicism in 5% of the cells karyotyped (**Figures 3** and **4**, boxed areas). The term "pseudo-mosaicism" can be used because the number of cells (one) displaying the +3 karyotype fell below the minimum number of cells (two) to be considered a separate clone [18]. The finding of trisomy 3 can then be considered as statistically insignificant, i.e., a "random gain". Hence, P2 and P3 are considered to be karyotypically normal based on this criterion. For passage 4 (P4), trisomy of chromosome 3 similar to that of P1 was observed in 3 of 20 cells, while the other cells displayed a normal female karyotype (**Figure 5**, boxed area).

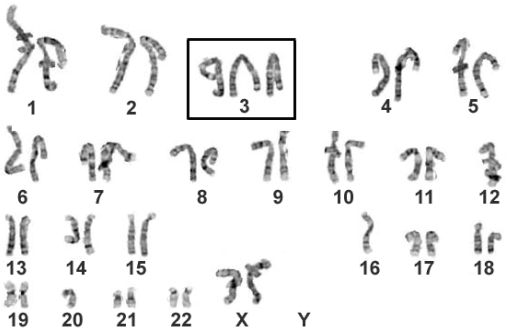

Figure 4. Passage 3 (P3) karyotype: As in P2, three copies of chromosome 3 were found (boxed area). Karyotypically normal according to Mitelman [18].

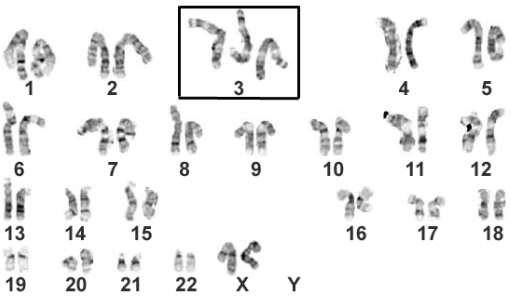

Figure 5. Passage 4 (P4) karyotype: Hyperploidy in P4 as indicated by three copies of chromosome 3 (boxed area).

For passage 5 (P5), three distinct cell lines were apparent. In 3 of 20 cells, three copies of chromosome 3 were observed (**Figure 6A**, boxed area), along with two cells showing trisomy of both chromosomes 3 and 8 (**Figure 6B**, boxed and circled areas, respectively). Hence, the karyotype for P5 was 47, XX, +3[3]/48, XX, +3+8[2]/46, XX [15]. For passage 10 (P10), 4 of 20 cells exhibited the following chromosomal aberrations: translocation occurring as a two-break rearrangement; breakage and reunion at bands 13 and 13.1 of the short arms (p) of chromosomes 1 and 19, respectively (**Figure 7A**, boxed area). The regions distal to these bands have been swapped. In addition, one of the sex chromosomes has been deleted, yielding the following karyotype: 45, X, -X, t(1, 19)(p13, p13.1) [cp4]/46, XX [16]. Trisomy 8 (**Figure 7B**, circled area) was not listed in the karyotype, as it was considered a "random gain" [18]. Results for the cytogenetic analysis are summarized in **Table 2**.

3.2. Population Doubling Time

Figure 8 shows the mean cumulative population doubling time (PDT) of the vocal fold fibroblasts as a function of sub-culturing. The cumulative PDT was seen to increase across different passages, from approximately 30 hours in P2 to over 600 hours for P10. An especially sharp rise in PDT was associated with the transition

Copyright © 2010 SciRes.

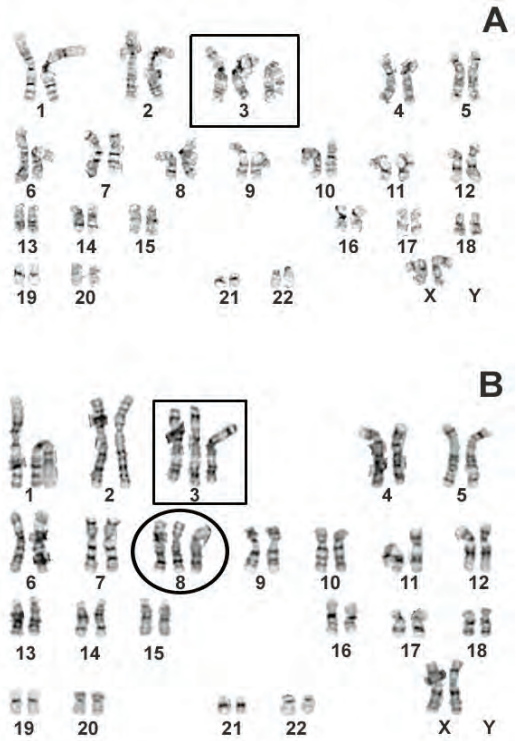

Figure 6. Passage 5 (P5) karyotype: (A) Triploidy of chromosome 3 as seen in P1-P4 (boxed area); (B) An additional clone was detected displaying +8 abnormality (circled area).

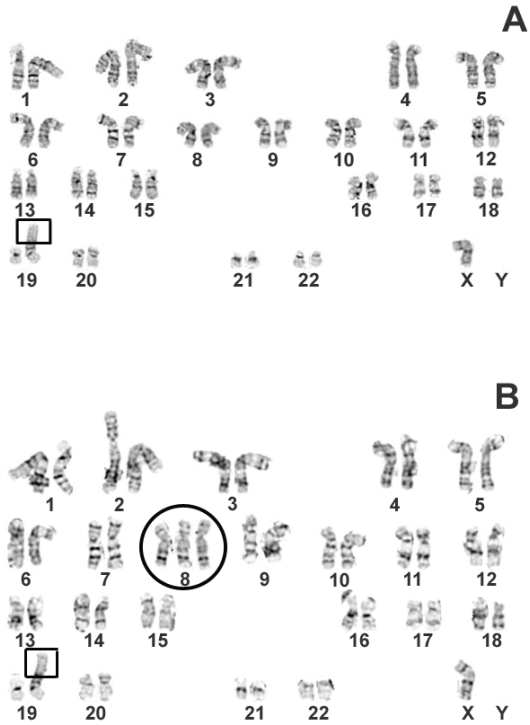

Figure 7. Passage 10 (P10) karyotype: (A) A translocation has occurred as a two break rearrangement. The region distal to band 13 on the short arm of chromosome 1 has attached to band 13.1 of chromosome 19 (translocation portion indicated in the boxed area). There was also the loss of one sex chromosome; (B) One cell out of four also displayed three copies of chromosome 8 (circled area) and was considered a "random gain".

Table 2. Results of cytogenetic analysis.

Passage number	Cells with normal diploid karyotype / Total no. of cells	Karyotype[a]
1	17 / 20	47, XX, +3[3] / 46, XX[17]
2	19 / 20	47, XX, +3[1] / 46, XX[19]
3	19 / 20	47, XX, +3[1] / 46, XX[19]
4	17 / 20	47, XX, +3[3] / 46, XX[17]
5	15 / 20	47, XX, +3[3] / 48, XX, +3+8[2] / 46, XX[15][b]
10	16 / 20	45, X, -X, t(1;19)(p13;p13.1) [cp4] / 46, XX[16][c]

[a]The normal diploid clone was listed at the end of the karyotype, along with square brackets [ ], indicating the absolute number of cells in each clone [18]. [b]Abnormal clones were listed according to their size with the greatest absolute number first [18]. [c]The designation "cp" for composite karyotype was used because 1 out of 4 cells displayed an additional copy of chromosome 8 (+8) as seen in **Figure 7B**. As a result, the four cells represented a composite of three aberrations. Trisomy 8 was not listed in the karyotype as it was considered a "random gain".

from P7 to P8, suggesting a significant slowing down of cellular proliferation. Results of single-factor ANOVA indicated that the differences in PDT across the passages were statistically significant (F (8, 18)=4.8450, p<0.005). These findings suggested that the vocal fold fibroblasts have undergone the process of replicative senescence, since it has been shown that replicative senescence is partially signified by an increase in PDT [19].

3.3. RT-PCR

The changes in mRNA expressions of the select target genes across different passages are shown as densitometric ratios of the targets versus the standard control, glyceraldehyde 3-phosphate dehydrogenase (GAPDH) in **Figure 9**. **Table 3** summarizes the results of statistical analysis on the dependence of these mRNA expressions

Copyright © 2010 SciRes.

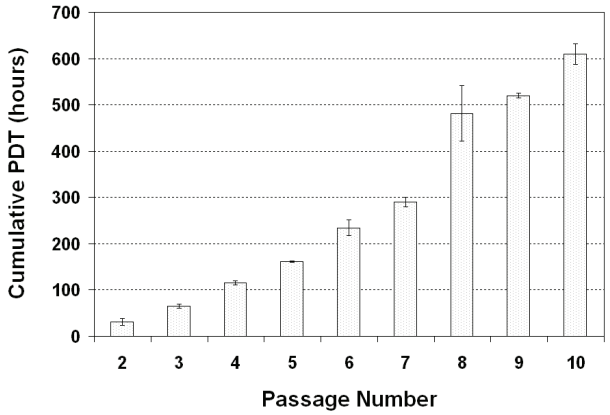

Figure 8. Cumulative population doubling time (PDT) of primary vocal fold fibroblasts as a function of passaging (means ± standard error of the mean; n=3).

on passaging. Pairwise comparisons of passages were analyzed to detect any possible trends over the passages. P5-P10 differences are listed separately for targets that are consistent with induction of senescence. First, for matrix-degrading enzymes, the transcript levels of MMP-1 (collagenase) showed significant increases from the early passages to passage 10, e.g., a three-fold increase from P5 to P10 (**Figure 9A**) ($p<0.01$). For MMP-12 (macrophage elastase), there was a gradual and significant increase in its mRNA expressions from P2 to P5 ($p<0.01$), and then a dramatic, significant decrease to P10 ($p<0.01$) (**Figure 9B**). Both MMP-1 and MMP-12 are implicated in the remodeling process of the vocal fold ECM, and the upregulation of MMP-12 has been closely associated with aging [20]. Hyaluronidase I showed a considerable upregulation from the early passages to P10, particularly from P5 to P10 ($p<0.01$) (**Figure 9C**). The levels of hyaluronidase II showed a significant increase from the early passages to P5, and then a significant decrease to P10 (both at the $p<0.01$ level) (**Figure 9D**). For the cross-linking enzyme lysyl oxidase, significant increases in mRNA levels were observed with passaging from P3 to P5, and from P4 to P10 ($p<0.01$). The increases were approximately two-fold (**Figure 9E**).

For procollagen I, the precursor to the a1 peptide of collagen I, there was a pronounced decrease in mRNA levels across the passages ($p<0.01$) (**Figure 9F**). For collagen III, the transcript levels of collagen III α1 decreased significantly across the passages ($p<0.01$) (**Figure 9G**). For fibromodulin (a proteoglycan important for the structural organization of collagen), there was an overall reduction in its mRNA levels across the passages, particularly from P1 to P3 and then from P5 to P10, where the decrease was 17-fold ($p<0.01$) (**Figure 9H**). For decorin, also important for collagen organization,

Table 3. Results of ANOVA and post-hoc pairwise comparisons of mRNA expressions of target genes across different passages.

ANOVA			Post-hoc Tukey HSD Test	
Target	F (5, 12)	p	Significant differences for the following comparisons	Significant differences for P5-P10 ?
MMP-1 (Collagenase)	218.1	2.4×10^{-11}	P5-P10	Yes
MMP-12 (macrophage elastase)	10.3	5.14×10^{-4}	P2-P5, P4-P10, P5-P10	Yes
Hyaluronidase Type I	9.5	7.4×10^{-4}	P5-P10	Yes
Hyaluronidase Type II	196.5	4.5×10^{-11}	P1-P5, P2-P5, P3-P5, P3-P10, P4-P5, P5-P10	Yes
Lysyl Oxidase	101.6	2.15×10^{-9}	P1-P2, P1-P3, P1-P4, P2-P3, P2-P4, P2-P5, P2-P10, P3-P10, P4-P5, P4-P10	No
Procollagen I	126.1	6.1×10^{-10}	P1-P3, P1-P4, P1-P5, P1-P10, P2-P3, P2-P4, P2-P5, P2-P10, P3-P5, P3-P10, P4-P5, P4-P10	No
Collagen III (α1)	848.9	7.3×10^{-15}	P2-P3, P2-P4, P2-P5, P2-P10, P3-P4, P3-P5, P3-P10, P4-P5, P4-P10, P5-P10	Yes
Fibromodulin	126.2	6.1×10^{-10}	P1-P2, P1-P3, P1-P4, P1-P5, P1-P10, P2-P3, P2-P10, P3-P5, P3-P10, P5-P10	Yes
Decorin	30.2	2.12×10^{-6}	P1-P5, P1-P10, P2-P4, P2-P5, P2-P10, P3-P10, P4-P10	No
HA-synthase 2	15.16	7.92×10^{-5}	P1-P3, P1-P5, P1-P10	No
Collagen I (α2)	1.7	0.21	not applicable	not applicable
HA Receptor (CD44)	2.1	0.137		
Fibronectin	2	0.149		
Hyaluronidase Type III	1.5	0.264		

Copyright © 2010 SciRes.

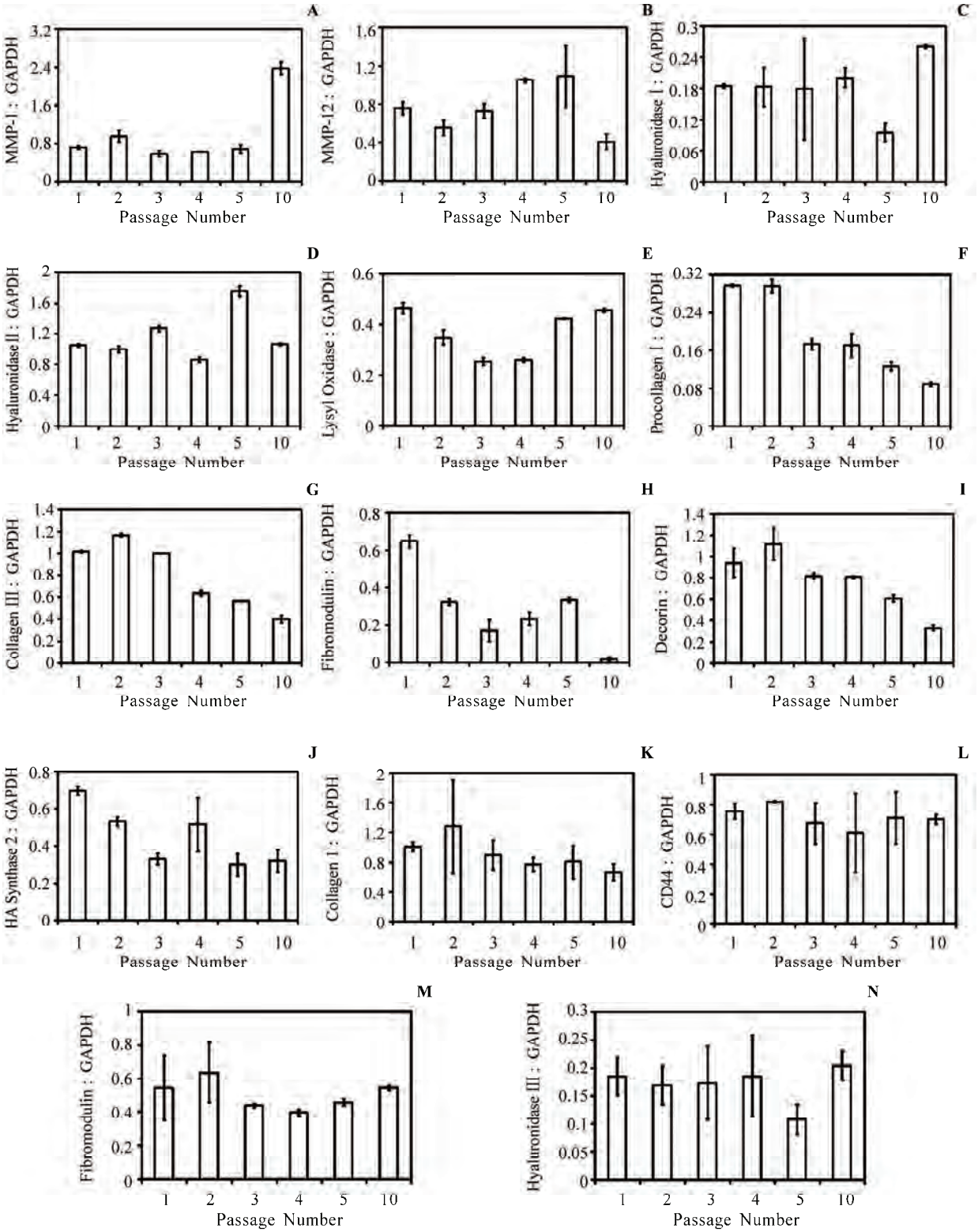

Figure 9. Densitometric ratios for select extracellular matrix target genes (means ± standard deviations; n=3), showing the integrated density volumes (IDV) or cumulative grey scale values of PCR agarose gel bands for each target relative to those of the standard control (GAPDH): (A) MMP-1* (collagenase), (B) MMP-12* (macrophage elastase), (C) hyaluronidase I*, (D) hyaluronidase II*, (E) lysyl oxidase*, (F) procollagen I*, (G) collagen III*, (H) fibromodulin*, (I) decorin*, (J) HA-synthase 2*, (K) collagen I, (L) CD44, (M) fibronectin, and (N) hyaluronidase III (*p<0.01).

Copyright © 2010 SciRes.

there was a significant decrease in its mRNA levels across the passages. For instance, the overall reduction from P1 to P10 was approximately three-fold ($p<0.01$) (**Figure 9I**). For the matrix-synthesizing enzyme HA-synthase 2, there was a significant overall trend of decrease from P1 to P10 ($p<0.01$), despite an increase from P3 to P4. In particular, significant differences were found from the early passages to P10 (**Figure 9J**).

For the following target genes, no statistically significant changes in mRNA expressions were detected as a function of passaging ($p>0.01$): collagen Iα2 (**Figure 9K**), the HA receptor CD44 (**Figure 9L**), fibronectin (**Figure 9M**) and hyaluronidase III (**Figure 9N**).

4. DISCUSSIONS

One objective of this study was to establish the onset and extent of gross chromosomal aberrations in human vocal fold fibroblasts associated with *in vitro* aging, or replicative senescence. Chromosomal aberrations were documented by karyotyping as a function of sub-culturing, or passaging. Next, alterations in the mRNA expressions for some key matrix proteins at the transcript level were observed for the vocal fold fibroblasts across passages, in order to characterize the consequence of the chromosomal aberrations due to aging *in vitro*.

From the cytogenetic analysis, the +3 karyotype observed in the first four passages (P1-P4) should not be considered as a significant chromosomal aberration, particularly for P2 and P3, where the fibroblasts were classified as karyotypically normal according to ISCN standards [18]. Beyond passage 4, however, it was apparent that an additional cell line has appeared with the karyotype (+3, +8) which conceivably could be the result of a nondisjunction with mother cell with a +3 karyotype. Aberrations observed in passage 5 in this study were comparable to those of passage 4 in Thibeault *et al.* [7]. Yet the severity of the aberrations in this study was relatively modest, e.g., trisomy 8 in 3 cells of 20 in P4 in this study versus the numerous anomalies in P4 of Thibeault *et al.* [7], including the loss of sex chromosome in 6 of 21 cells, translocation in 3 of 21 cells; and rearrangement involving chromosomes 2, 5, 10, 14, 15. This disparity in the number and severity of chromosomal abnormalities was likely due to the difference in age of the donors of the studies (58 years old in this study versus 78 years old in Thibeault *et al.* [7]). The susceptibility of vocal fold fibroblasts to these aberrations apparently increased with age and should be targeted in future studies.

Based on the RT-PCR analysis for those target genes demonstrating statistically significant differences across different passages, our data on the changes in mRNA expressions of the targets can be divided roughly into two categories: 1) target genes involving matrix-synthesizing enzymes and matrix-degrading enzymes, including MMP-1, MMP-12, hyaluronidases, and HA-synthase 2; and 2) targets contributing to the regulation of the ECM organization, including procollagen I, collagen III, decorin, fibromodulin, and lysyl oxidase.

For target genes involving matrix-synthesizing and matrix-degrading enzymes, it has been considered that the shift of fibroblasts from a matrix-synthesizing to a matrix-degrading phenotype is one of the hallmark indicators for replicative senescence [5]. This notion was supported by numerous studies that showed upregulation of matrix metalloproteinases (MMPs) in senescent fibroblasts [21,22,23]. Such a shift towards a matrix-degrading phenotype was demonstrated in the present study by the modulations observed in the following targets.

The upregulation of both MMP-1 (collagenase) and MMP-12 (macrophage elastase) with passaging of human vocal fold fibroblasts is consistent with *in vitro* aging seen in other kinds of fibroblasts, such as dermal fibroblasts [24,25,26]. Hyaluronidases are responsible for the cleavage of hyaluronic acid (HA). Type I and type II hyaluronidases are the most common isoforms expressed in human somatic tissues [27]. HA, a highly polarized long-chain glycosaminoglycans molecule, is abundantly found in the vocal fold lamina propria [28]. It is critical to the regulation of tissue hydration and is important for the maintenance of an optimal viscoelasticity of the lamina propria for vocal fold vibration [2,4,28]. From the PCR analysis, the upregulation of hyaluronidase II from P1 to P5 and the upregulation of hyaluronidase I from P5 to P10 were consistent with a proposed model for their concerted action in the degradation of HA [28]. Specifically, hyaluronidase II cleaves HA first into 20 kDa fragments, followed by hyaluronidase I digesting them into smaller fragments [29]. Accumulation of the 20 kDa fragments leads to an increase in transcripts of hyaluronidase I by mass action, as seen in P10. The actions of these enzymes in concert were consistent with a shift towards a matrix-degrading phenotype.

Mammalian HA synthesis is accomplished in part by HA-synthase 2 [16]. The levels of HA-synthase 2 showed a steady decrease from P1 to P3, and remained at low levels for P5 and P10, indicating that the synthesis of HA has been reduced in these fibroblasts. This finding further supported our argument that across the passages, vocal fold fibroblasts have shifted from a matrix-synthesizing to a matrix-degrading phenotype, consistent with replicative senescence.

The changes in mRNA expressions of the remaining targets strongly implicated that the *in vitro* aging of these fibroblasts would lead to a disorganized and structurally compromised lamina propria ECM. First, for collagen III α1, which is a major structural fibrous protein of the vocal fold lamina propria and macula flava [30,31], there was a steady and significant decrease in the transcript level with passaging. Type III collagen fibers were found

Copyright © 2010 SciRes.

to be thicker than type I fibers, with their interactions likely contributing to the viscoelasticity of the lamina propria and the tensile strength of the macula flava necessary for bearing the mechanical stresses of vocal fold vibration [32]. For procollagen I, a significant decrease in its mRNA levels was also seen with passaging. This downregulation did not correspond to a significant decrease in collagen I mRNA levels, because different peptides were coded for the two targets (α1 for procollagen I and α2 for collagen I). Our findings of collagen III, collagen I and procollagen I expressions suggested a lower turnover rate for collagen, leading to an ECM increasingly cross-linked and difficult to degrade, as observed in aged human vocal folds [33].

Decorin contributes to regulate the organization and overall size of collagen fibrils via its glycosaminoglycans moiety [34], presumably reducing collagen fiber size and density [35]. Lower levels of decorin have been associated with disorganized collagenous supramolecular assemblies in scar tissue [36]. The observed decrease in the transcript levels of decorin along with the decrease in collagen III suggested that the capability of fibroblasts for facilitating structural ECM organization has been impaired due to aging *in vitro*.

Fibromodulin is a small proteoglycan that facilitates the construction of other proteins such as collagens I and II into fibrillar structures [17]. It has been shown that fibromodulin-knockout mice have disorganized collagen fibrils in their Achilles tendons, with reduced overall cross-sectional area when compared to normal control [37]. Our results showed a dramatic, significant 17-fold decrease in the level of fibromodulin from P5 to P10. Combined with the decorin data, lower fibromodulin levels supported the notion that the capability of the fibroblasts for ECM protein organization is compromised with passaging.

The cross-linking enzyme lysyl oxidase catalyzes the removal of amino groups from certain hydroxylysine and lysine residues in collagen, cross-linking one collagen molecule to another [38]. Lysyl oxidase is apparently the only known enzyme responsible for cross-linking elastin monomers [39]. Such cross-linking would likely increase the elastic modulus for both collagen and elastin fibers. Increases in tissue stiffness of the vocal fold lamina propria and the macula flava have been seen with aging [17,37], which could be related to the increased cross-linking of collagen and elastin fibers. Our data showed a clear upregulation in lysyl oxidase from P3 to P10, consistent with this modulation in vocal fold tissue stiffness with aging.

These results, along with the dramatic decrease in macrophage elastase (MMP-12) from P5 to P10, suggested that the gene expressions of senescent vocal fold fibroblasts *in vitro* are consistent with a proposed model for *in vivo* aging of the vocal fold. This model suggests that as vocal folds age, elastin fibers accumulate with a prolonged half-life due to lower elastase levels and undergo extensive cross-linking via lysyl oxidase, contributing to increased tensile strength and tissue stiffness. The increase in lysyl oxidase levels with passaging in our study contradicted the results for aged rats in Ding and Gray [39], but may nonetheless reflect inherent differences between the species, and between *in vitro* and *in vivo* models.

Overall, based on our data on cytogenetic analysis, PDT and mRNA expressions of target genes, we have established the sub-culturing limit beyond which replicative senescence was observed in primary-culture human vocal fold fibroblasts. This limit of 5 passages was critical for establishing representative *in vitro* models for tissue engineering approaches involving the use of primary-culture fibroblasts. For example, primary vocal fold fibroblasts seeded in decellularized ECM scaffolds have been shown to be promising for vocal fold regeneration [8]. The therapeutic potential of injection of autologous fibroblasts as well as the incorporation of growth factors or biomaterial implants with fibroblasts for treating vocal fold scarring has also been targeted [9,10,40]. In those studies, autologous fibroblasts were harvested by biopsy and sub-cultured for up to the sixth passage, for up to 30 days. The current findings suggested that some of the fibroblasts in those studies may have become senescent, compromising their findings and conclusions.

Nonetheless, it should be noted that the results of this study should be considered preliminary, based on the harvest of vocal fold fibroblasts from only a single individual. Also, the vocal fold fibroblasts were only cultured statically, unlike in physiological situations when they are subjected to a variety of mechanical stresses, particularly vibratory stresses. Titze *et al.* showed that axial and vibratory strains applied to human vocal fold fibroblasts cultured on a polymeric substrate resulted in significant changes in mRNA expressions of a number of matrix proteins [9]. Further studies involving bioreactors capable of simulating the micromechanical environment *in vivo* are required to address this important issue. In addition, the measurement of gene expressions at the transcript level does not always directly reflect expressions of the corresponding proteins. Changes in mRNA expression of a certain protein would depend on the half-life of that protein, and on its regulation pathways. Future studies should therefore involve the measurement of protein levels with methods such as enzyme-linked immunosorbent assays.

5. CONCLUSIONS

In summary, the patterns of chromosomal abnormalities and mRNA expressions of matrix proteins across different passages of primary-culture vocal fold fibroblasts indicated that the fibroblasts underwent replicative se-

Copyright © 2010 SciRes.

nescence, with the onset of senescence not occurring before the fifth passage. These preliminary data suggested that an acceptable limit of sub-culturing may be established to facilitate the development of representative *in vitro* models of the vocal fold ECM, allowing for the evaluation of a variety of tissue engineering approaches for vocal fold reconstruction.

6. ACKNOWLEDGEMENTS

This study was supported by the National Institutes of Health, NIDCD Grant No. R01 DC006101. The authors would like to thank Dr. J.T. Hsieh for the use of his gel documentation system, and Glendon Plumton for his assistance in the RT-PCR work.

REFERENCES

[1] Gray, S.D. (2000) Cellular physiology of the vocal folds. *Otolaryngologic Clinics of North America*, **33,** 679-698.

[2] Gray, S. D., Titze, I. R., Chan, R. and Hammond, T.H. (1999) Vocal fold proteoglycans and their influence on biomechanics. *Laryngoscope*, **109,** 845-854.

[3] Hirano, S. (2005) Current treatment of vocal fold scarring. *Current Opinion in Otolaryngology & Head and Neck Surgery*, **13,** 143-147.

[4] Chan, R.W., Gray, S.D. and Titze, I.R. (2001) The importance of hyaluronic acid in vocal fold biomechanics. *Otolaryngology Head and Neck Surgery*, **124,** 607-614.

[5] Cristofalo, V.J., Lorenzini, A., Allen, R.G., Torres, C. and Tresini, M. (2004) Replicative senescence: A critical review. *Mechanisms of Ageing & Development*, **125,** 827-848.

[6] Campisi, J. (1998) The role of cellular senescence in skin aging. *Journal of Investigative Dermatology Symposium Proceedings*, **3,** 1-5.

[7] Thibeault, S.L., Li, W., Gray, S.D. and Chen, Z. (2002) Instability of extracellular matrix gene expression in primary cell culture of fibroblasts from human vocal fold lamina propria and tracheal scar. *Annals of Otology, Rhinology, Laryngology*, **111,** 8-14.

[8] Xu, C.C., Chan, R.W. and Tirunagari, N. (2007) A biodegradable, acellular xenogeneic scaffold for regeneration of the vocal fold lamina propria. *Tissue Engineering*, **13,** 551-566.

[9] Titze, I.R., Hitchcock, R.W., Broadhead, K. *et al.* (2004) Design and validation of a bioreactor for engineering vocal fold tissues under combined tensile and vibrational stresses. *Journal of Biomechanics*, **37,** 1521-1529.

[10] Hirano, S., Bless, D.M., Nagai, H., Rousseau, B., Welham, N.V., Montequin, D.W. and Ford, C.N. (2004) Growth factor therapy for vocal fold scarring in a canine model. *Annals of Otology, Rhinology, Laryngology*, **113,** 777-785.

[11] Alberts, B., Johnson, A., Lewis, J., Raff, M., Roberts, K. and Walter, P. (2002) *Molecular Biology of the Cell, 4th Edition*. Garland Science, New York, 1313-1362.

[12] Sato, K., Miyajima, Y., Izumaru, S. and Nakashima, T. (2008) Cultured stellate cells in human vocal fold mucosa. *Journal of Laryngology & Otology*, **122,** 1339-1342.

[13] Richardson, A. (1997) Chromosome analysis. In Barch, M., Knutsen, T. and Spurbeck, J. (eds.), *The AGT Cytogenetics Laboratory Manual*. Lippincott-Raven, Philadelphia, 495-496.

[14] McAteer, J. and Davis, J. (2002) Basic cell technique and the maintenance of cell lines. In Davis, J. (ed.), *Basic Cell Culture: A Practical Approach*. Oxford University Press, New York, 135-189.

[15] Chomczynski, P. and Sacchi, N. (1987) Single-step method of RNA isolation by acid guanidinium thiocyanate-phenol-chloroform extraction. *Analytical Biochemistry*, **162,** 156-159.

[16] Girish, K.S. and Kemparaju, K. (2007) The magic glue hyaluronan and its eraser hyaluronidase: A biological overview. *Life Sciences*, **80,** 1921-1943.

[17] Hedbom, E. and Heinegard, D. (1993) Binding of fibromodulin and decorin to separate sites on fibrillar collagens. *Journal of Biological Chemistry*, **268,** 27307-27312.

[18] Mitelman, F. (1995) *ISCN 1995: An International System for Human Cytogenetic Nomenclature: Recommendations of the International Standing Committee on Human Cytogenetic Nomenclature*. S. Karger Publishers, Basel, Switzerland.

[19] Campisi, J. (1997) The biology of replicative senescence. *European Journal of Cancer*, **33,** 703-709.

[20] Tsai, K.K., Chuang, E.Y., Little, J.B. and Yuan, Z.M. (2005) Cellular mechanisms for low-dose ionizing radiation-induced perturbation of the breast tissue microenvironment. *Cancer Research*, **65,** 6734-6744.

[21] Frechet, M., Warrick, E., Vioux, C. *et al*. (2008) Overexpression of matrix metalloproteinase 1 in dermal fibroblasts from DNA repair-deficient/cancer-prone xeroderma pigmentosum group C patients. *Oncogene*, **27,** 5223-5232.

[22] Liu, D. and Hornsby, P.J. (2007) Senescent human fibroblasts increase the early growth of xenograft tumors via matrix metalloproteinase secretion. *Cancer Research*, **67,** 3117-3126.

[23] Rijken, F., Kiekens, R.C., van den Worm, E., Lee, P.L., van Weelden, H. and Bruijnzeel, P.L. (2006) Pathophysiology of photoaging of human skin: Focus on neutrophils. *Photochemical & Photobiological Sciences*, **5,** 184-189.

[24] Millis, A.J., Hoyle, M., McCue, H.M. and Martini, H. (1992) Differential expression of metalloproteinase and tissue inhibitor of metalloproteinase genes in aged human fibroblasts. *Experimental Cell Research*, **201,** 373-379.

[25] Millis, A.J., McCue, H.M., Kumar, S. and Baglioni, C. (1992) Metalloproteinase and TIMP-1 gene expression during replicative senescence. *Experimental Gerontology*, **27,** 425-428.

[26] West, M.D., Pereira-Smith, O.M. and Smith, J.R. (1989) Replicative senescence of human skin fibroblasts correlates with a loss of regulation and overexpression of collagenase activity. *Experimental Cell Research*, **184,** 138-147.

[27] Csoka, A.B., Scherer, S.W. and Stern, R. (1999) Expression analysis of six paralogous human hyaluronidase genes clustered on chromosomes 3p21 and 7q31. *Genomics*, **60,** 356-361.

[28] Butler, J.E., Hammond, T.H. and Gray, S.D. (2001) Gender-related differences of hyaluronic acid distribution in the human vocal fold. *Laryngoscope*, **111,** 907-911.

[29] Csoka, A.B., Frost, G.I. and Stern, R. (2001) The six hyaluronidase-like genes in the human and mouse ge-

Copyright © 2010 SciRes.

nomes. *Matrix Biology*, **20,** 499-508.

[30] Madruga de Melo, E.C., Lemos, M., Aragao Ximenes Filho, J., Sennes, L.U., Nascimento Saldiva, P.H. and Tsuji, D.H. (2003) Distribution of collagen in the lamina propria of the human vocal fold. *Laryngoscope*, **113,** 2187-2191.

[31] Paulsen, F., Kimpel, M., Lockemann, U. and Tillmann, B. (2000) Effects of ageing on the insertion zones of the human vocal fold. *Journal of Anatomy*, **196,** 41-54.

[32] Tateya, T., Tateya, I. and Bless, D.M. (2006) Collagen subtypes in human vocal folds. *Annals of Otology, Rhinology, Laryngology*, **115,** 469-476.

[33] Sato, K., Hirano, M. and Nakashima, T. (2002) Age-related changes of collagenous fibers in the human vocal fold mucosa. *Annals of Otology, Rhinology, Laryngology*, **111,** 15-20.

[34] Ruhland, C., Schonherr, E., Robenek, H. *et al.* (2007) The glycosaminoglycan chain of decorin plays an important role in collagen fibril formation at the early stages of fibrillogenesis. *FEBS Journal*, **274,** 4246-4255.

[35] Hahn, M.S., Kobler, J.B., Zeitels, S.M. and Langer, R. (2005) Midmembranous vocal fold lamina propria proteoglycans across selected species. *Annals of Otology, Rhinology, Laryngology*, **114,** 451-462.

[36] Thibeault, S.L., Bless, D.M. and Gray, S.D. (2003) Interstitial protein alterations in rabbit vocal fold with scar. *Journal of Voice*, **17,** 377-383.

[37] Svensson, L., Aszodi, A., Reinholt, F.P., Fassler, R., Heinegard, D. and Oldberg, A. (1999) Fibromodulin-null mice have abnormal collagen fibrils, tissue organization, and altered lumican deposition in tendon. *Journal of Biological Chemistry*, **274,** 9636-9647.

[38] Lucero, H.A. and Kagan, H.M. (2006) Lysyl oxidase: An oxidative enzyme and effector of cell function. *Cellular and Molecular Life Sciences*, **63,** 2304-2316.

[39] Ding, H. and Gray, S.D. (2001) Senescent expression of genes coding tropoelastin, elastase, lysyl oxidase, and tissue inhibitors of metalloproteinases in rat vocal folds: Comparison with skin and lungs. *Journal of Speech, Language, Hearing Research*, **44,** 317-326.

[40] Chhetri, D.K., Head, C., Revazova, E., Hart, S., Bhuta, S. and Berke, G.S. (2004) Lamina propria replacement therapy with cultured autologous fibroblasts for vocal fold scars. *Otolaryngology Head and Neck Surgery*, **131,** 864-870.

Copyright © 2010 SciRes.

J. Biomedical Science and Engineering, 2010, 3, 160-166 **JBiSE**
doi:10.4236/jbise.2010.32021 Published Online February 2010 (http://www.SciRP.org/journal/jbise/).

Study on synchrony of two uncoupled neurons under the neuron's membrane potential stimulation

Yue-Ping Peng[1,2], Jue Wang[1], Quan-Xing Miao[2], Hong-Yan Lu[2]

[1]Key Laboratory of Biomedical Information Engineering of Education Ministry, Xi'an Jiaotong University, Xi'an, China;
[2]Communication Department, Engineering College of Armed Police Force, Xi'an, China.
Email: percy001@163.com

Received 27 June 2009; revised 5 December 2009; accepted 7 December 2009.

ABSTRACT

The input current of two uncoupled Hindmarsh-Rose neurons under different initial conditions is modulated by the membrane potential of the Hindmarsh-Rose neuron; and the synchronization characteristics of the two uncoupled neurons are discussed by analyzing their membrane potentials and their inter spike interval (ISI) distribution. Under the stimulation of the neuron's membrane potential whose discharge pattern is period or the chaos, the two uncoupled neurons under different initial conditions, whose parameter *r* (the parameter *r* is related to the membrane penetration of calcium ion, and reflects the changing speed of the slow adaptation current) is different or the same, can realize the full synchronization (state synchronization) or discharge synchronization (phase synchronization), and can only be synchronized to the discharge pattern of the stimulation neuron. The synchronization characteristics are mainly related to the discharge pattern and the strength of the stimulation neuron's membrane potential, and are little related to the parameter r and the initial state of the two uncoupled neurons. This investigation shows the characteristics of the neuron's membrane potential affecting the synchronization process of neurons, and the neurons' discharge patterns and synchronization process can be adjusted and controlled by the discharge pattern and the strength of the stimulation neuron's membrane potential. This result is helpful to study synchronization and encode of many neurons or neural network.

Keywords: The Membrane Potential; The HR Neuron; Synchronization; ISI

1. INTRODUCTION

Since system synchronization was presented by Pecora, *et al.* [1,2] in 1991, synchronization research has been causing researchers' wide focus in neuroscience field. Nervous activities' synchronization is found not only among coupled neuron groups in the same brain region, but also among uncoupled neuron groups in the same brain region or among different cortical areas; Moreover, it can cross over two semispheres of the brain [3]. So in the nervous system, synchronization activities are presented not only among the coupled neurons, but also among the uncoupled neurons. Studies on neuron synchronization are mainly focused on two cases: the coupled neurons and the uncoupled neurons; and the synchronization of coupled neurons are studied more.

The Hindmarsh-Rose neuron (HR neuron) has several characteristics of the excitable cell's physical model and many time scale discharge action [4,5,6,13]. There are some literatures of studies on synchronization of HR neurons [3,7,9,10,12,14,15,16,17]. Huerta, R. and Rabinovich, M.I. studied the period rhythm's change of two HR neurons coupled by the circuit and the synapse [7]. Two uncoupled HR neurons can be realized synchronization by applying input signals to modulate the neuron model's parameter or by applying the noise and the HR neuron's membrane potential to stimulate these neurons [8,9,10]. The phase synchronization of two coupled HR neurons was discussed by Shuai, JianWei and Durand, D.M., and they concluded that the phase synchronization is the discharge synchronization, the frequency synchronization is the cluster synchronization, and the full synchronization is the state synchronization [11]. Synchrony of two uncoupled neurons under half wave sine current stimulation was discussed, and it was concluded that the two uncoupled HR neurons under different initial conditions, whose parameter *r* is different or the same, can realize discharge synchronization (phase synchronization) or the full synchronization (state synchronization) [12].

In this study, we take two uncoupled HR neurons as the object, and make the HR neurons different initial discharge patterns by setting the value of the parameter *r*, and apply the membrane potential of the Hindmarsh-

This work is supported by the National Natural Science Foundation of China (No. 30670660).

Rose neuron to modulate the two uncoupled HR neurons' input current, and discuss the HR neurons' synchronization characteristics by calculating and analyzing the two neurons' membrane potentials and their inter spike intervals (ISIs).

2. THE DISCHARGE PATTERNS OF THE HR NEURON MODEL

The HR neuron has many time scale dynamics action, and its equation is set of three dimension ordinary differential equations [4,5,6]:

$$x = y - ax^3 + bx^2 - z + I$$

$$y = c - dx^2 - y$$

$$z = r[s(x - X) - z] \quad (1)$$

The HR neuron has three time variables: the membrane potential variable x which has the quick depolarization ability, the quick recovery variable y and slow adaptation current variable z. I is the input stimulation current; a, b, c, d, s, r and X are parameters. The parameter r is related to the membrane penetration of calcium ion, and reflects the changing speed of the slow adaptation current variable z. Other parameters have no specific physical meaning. The equations are nondimensional, and at numerical calculation, value of parameters is as follows: $a=1.0$, $b=3.0$, $c=1.0$, $d=5.0$, $s=4.0$, $I=3.0$, $X=-1.56$, and you can set the neuron at different discharge patterns by changing the parameter r.

The discharge threshold value is −0.25, and if the membrane potential is more than −0.25, the neuron will produce one discharge process. **Figure 1** is the ISI bifurcation figure of the neuron, where parameters except r are set to the above values, and the initial state of the neuron is (1.0, 0.2, 0.2). From **Figure 1**, the discharge pattern of the neuron begins from the chaos state(r is about 0.008~0.009), and evolves period 6 discharge pattern(r is near 0.01), and via the adverse period doubling bifurcation passes period 3(r is about 0.0105~0.012) and enters the chaos state(r is about 0.0125~0.015) again, and at last via the adverse period doubling bifurcation passes period 4(r is about 0.016~0.018) and comes into period 2(r is about 0.0185 ~0.022).

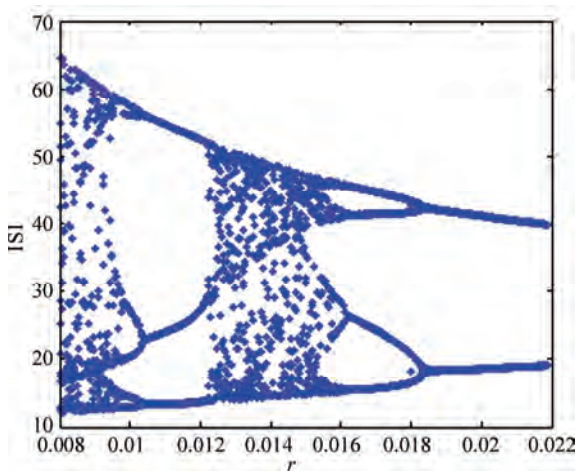

Figure 1. Bifurcation figure of the HR neuron under the parameter r changing from 0.008 to 0.022.

Table 1. The values of the two neurons' parameter r.

Case	The values of r_1 and r_2
The same	r_1=r_2=0.009, r_1=r_2=0.011, r_1=r_2=0.013, r_1=r_2=0.0171, r_1=r_2=0.02
A little different	r_1=0.0085 and r_2=0.009, r_1=0.011 and r_2=0.0115, r_1=0.014 and r_2=0.0141, r_1=0.017 and r_2=0.0171, r_1=0.021 and r_2=0.0215
Much different	r_1=0.0082 and r_2=0.0115, r_1=0.014 and r_2=0.0085, r_1=0.0085 and r_2=0.017, r_1=0.009 and r_2=0.021, r_1=0.011 and r_2=0.0145, r_1=0.0112 and r_2=0.017, r_1=0.0115 and r_2=0.021, r_1=0.014 and r_2=0.017, r_1=0.022 and r_2=0.013, r_1=0.017 and r_2=0.021

3. THE SYNCHRONIZATION OF TWO UNCOUPLED HR NEURONS UNDER THE STIMULATION OF THE NEURON'S MEMBRANE POTENTIAL

The equation set of two uncoupled HR neurons' model is:

$$\dot{x}_i = y_i - a_i x_i^3 + b_i x_i^2 - z_i + (I_i + I_S(t))$$

$$\dot{y}_i = c_i - d_i x_i^2 - y_i$$

$$\dot{z}_i = r_i[s_i(x_i - X_i) - z_i] \quad (i = 1, 2) \quad (2)$$

Time variables of these two neurons are respectively (x_1, y_1, z_1) and (x_2, y_2, z_2), and the parameters of these two neurons are respectively (a_1, b_1, c_1, d_1, r_1, s_1, I_1, X_1) and (a_2, b_2, c_2, d_2, r_2, s_2, I_2, X_2).

The equations are also nondimensional. At numerical calculation, the values of these two neurons' parameters (except r) are as follows: a_1=a_2=1.0, b_1=b_2 =3.0, c_1=c_2=1.0, d_1=d_2=5.0, s_1=s_2=4.0, X_1=X_2=−1.56, I_1=I_2=3.0; and the values of the initial states of these two neurons are respectively (1.0, 0.2, 0.2) and (−1.0, 0.8, 0.3); and you can set these two neurons at different discharge patterns by controlling values of the parameter r_i (i=1, 2).

According to the difference of these two neurons' parameter r, there are three cases: the parameter r is the same, a little different ($|r_1 - r_2| \le 0.0005$), and much

different ($|r_1 - r_2| \geq 0.003$). **Table 1** shows the values of the two neurons' parameter *r*, and the discharge patterns of these two neurons are correspondingly showed in the **Figure 1**.

The value of the initial state of the stimulation neuron is (0.2, 1, −0.2). The values of the parameters except *r* of the stimulation neuron are as follows: a=1.0, b=3.0, c=1.0, d=5.0, s=4.0, I=3.0, X=−1.56. The stimulation neuron can be made different discharge patterns by changing the parameter *r* according to **Figure 1**.

Total stimulation current includes two parts: the bias current (I_1 and I_2) and the input stimulation current I_S(t): $I_S(t) = kx(t)$. x(t) is the membrane potential of the stimulation neuron, and k is the stimulation strength of the membrane potential. The stimulation neuron begins to stimulate the system model after the bias current (I_1 and I_2) has been working for 500. The simulation time of the system model is often 0~4000.

3.1. Synchronization under the Stimulation of the Period Discharge Pattern

The values of the parameters of these two uncoupled neurons are above given values. The parameter *r* of the stimulation neuron is respectively 0.011, 0.017, and 0.02, and its discharge pattern is respectively period 3, period 4, and period 2. Under each discharge pattern, the stimulation strength *k* is respectively 0.5, 1, 2, 3, 6, 9, and 12.

The parameter *r* of the stimulation neuron is 0.011 (the discharge pattern is period 3). As it begins to stimulate the two neurons, in above all cases, the two uncouple neurons' discharge patterns totally change into dynamic period discharge pattern from the initial discharge patterns with the stimulation strength *k* increasing, and the changing trend of their membrane potentials' ISI is the same, namely gradually evolves into period 3 discharge pattern which is the same as the stimulation neuron's. When the stimulation strength is 0.5 and 1, these two neurons don't realize synchronization, and when the stimulation strength is 3, 6, 9 and 12, these two neurons realize discharge synchronization (phase synchronization) or the full synchronization (state synchronization) [11]. When the stimulation strength is 2, only several groups of these two neurons realize discharge synchronization or the full synchronization. When the parameter *r* is the same, these two neurons realize the full synchronization. When the parameter *r* is a little different, these two neurons realize the full synchronization or discharge synchronization. When the parameter *r* is much different, these two neurons realize discharge synchronization or the approximate full synchronization. The synchronization discharge pattern is the same as the stimulation neuron's discharge pattern (period 3).

The parameter *r* of the stimulation neuron is 0.017 (the discharge pattern is period 4). As it begins to stimulate the two neurons, in above all cases, the two uncouple neurons' discharge patterns totally change into dynamic period discharge pattern from the initial discharge patterns with the stimulation strength *k* increasing, and the changing trend of their membrane potentials' ISI is the same, namely gradually evolves into period 4 discharge pattern which is the same as the stimulation neuron's. When the stimulation strength is 0.5 and 1, these two neurons don't realize synchronization, and when the stimulation strength is 3, 6, 9 and 12, these two neurons realize discharge synchronization or the full synchronization. When the stimulation strength is 2, only several groups of these two neurons realize discharge synchronization or the full synchronization. When the parameter *r* is the same, these two neurons realize the full synchronization. When the parameter *r* is a little different, these two neurons realize the full synchronization or discharge synchronization. When the parameter *r* is much different, these two neurons realize discharge synchronization or the approximate full synchronization. The synchronization discharge pattern is the same as the stimulation neuron's discharge pattern (period 4).

The parameter *r* of the stimulation neuron is 0.02 (the discharge pattern is period 2). As it begins to stimulate the two neurons, in above all cases, the two uncouple neurons' discharge patterns totally change into dynamic period discharge pattern from the initial discharge patterns with the stimulation strength *k* increasing, and the changing trend of their membrane potentials' ISI is the same, namely gradually evolves into period 2 discharge pattern which is the same as the stimulation neuron's. When the stimulation strength is 0.5 and 1, these two neurons don't realize synchronization, and when the stimulation strength is 6, 9 and 12, these two neurons realize discharge synchronization or the full synchronization. When the stimulation strength is 2 or 3, only several groups of these two neurons realize discharge synchronization or the full synchronization. When the parameter *r* is the same, these two neurons realize the full synchronization. When the parameter *r* is a little different, these two neurons realize the full synchronization or discharge synchronization. When the parameter *r* is much different, these two neurons realize discharge synchronization or the approximate full synchronization. The synchronization discharge pattern is the same as the stimulation neuron's discharge pattern (period 2).

Limited to the length, **Figure 2** only shows the synchronization process of the two neurons, where the parameter *r* of the stimulation neuron is 0.02, and the stimulation strength *k* is 9. In **Figure 2**, from (a) and (d), (b) and (e), (c) and (f), these two neurons respectively realize the full synchronization, the full synchronization, and the discharge synchronization; and the synchronization discharge pattern is all period 2, which is the same as the stimulation neuron's discharge pattern.

Copyright © 2010 SciRes.

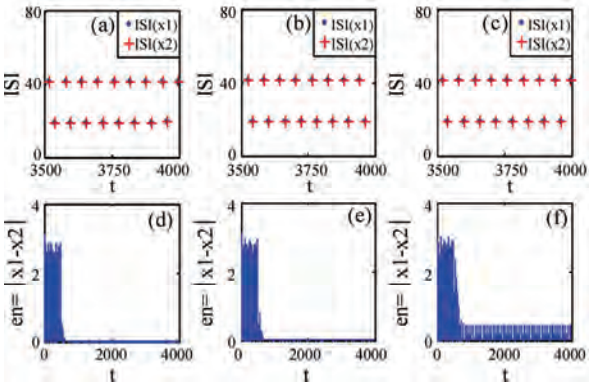

Figure 2. The synchronization process of the two neurons, where the parameter r of the stimulation neuron is 0.02 and the stimulation strength is 9. (a) The membrane potential's ISI changing chart of the two neurons with time, where r_1 is 0.013 and r_2 is 0.013. (b) The membrane potential's ISI changing chart of the two neurons with time, where r_1 is 0.014 and r_2 is 0.0141. (c) The membrane potential's ISI changing chart of the two neurons with time, where r_1 is 0.022 and r_2 is 0.013. (d) The two neurons' membrane potential's synchronization error ($err = |x_1 - x_2|$) changing chart with time, where r_1 is 0.013 and r_2 is 0.013. (e) The two neurons' membrane potential's synchronization error changing chart with time, where r_1 is 0.014 and r_2 is 0.0141. (f) The two neurons' membrane potential's synchronization error changing chart with time, where r_1 is 0.022 and r_2 is 0.013.

Synchronization state of two neurons can also be classified by the phase function [11]. The phase function of these two neurons is here defined as: $\varphi_i(t) = \arctan[\dot{x}_i(t-0.5)/(\dot{x}_i(t)+0.1)]$ (i=1, 2), where x(t) is the membrane potential. Limited to the length, **Figure 3** only shows the trajectory projection in the $\dot{x}_i(t-0.5)-(\dot{x}_i(t)+0.1)$ plane and the phase of the neuron changing with time. From **Figures 3(a)**, **3(b)** and **3(c)**, it can be seen that the attractor has a single rotation center in the $\dot{x}_i(t-0.5)-(\dot{x}_i(t)+0.1)$ plane. The phases of the neuron are given in **Figure 3(g)**, 3**(h)** and 3**(i)** with time from 3500 to 4000. The corresponding membrane potentials of the neuron are given in **Figure 3(d)**, **3(e)** and **3(f)**.

The absolute phase difference of two neurons ($|\Delta\phi(t)|$) is defined as: $|\Delta\phi(t)| = |\phi_1(t) - \phi_2(t)|$. When the maximum absolute phase difference of these two neurons ($|\Delta\phi(t)|_{\max}$) is no more than 2π, these two neurons realize discharge synchronization; When $|\Delta\phi(t)|_{\max}$ approximates to zero, these two neurons realize the full synchronization; when $|\Delta\phi(t)|_{\max}$ can be as large as 4π for some small time intervals, these two neurons can be viewed as an intermittent discharge synchronization.

Limited to the length, **Figure 4** only partly shows the

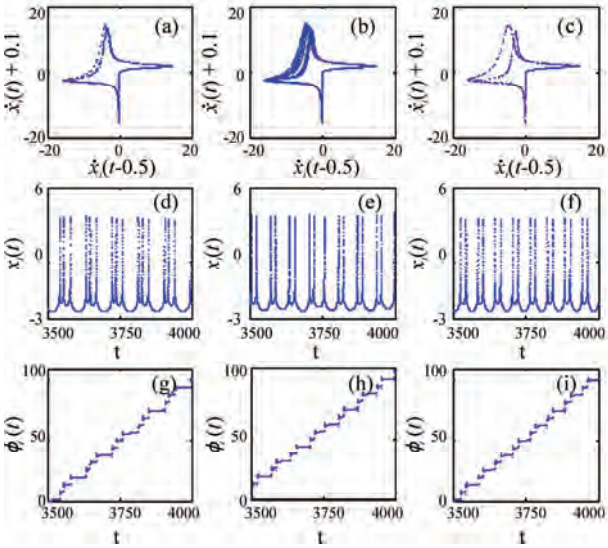

Figure 3. The trajectory projection in the $\dot{x}_i(t-0.5)-(\dot{x}_i(t)+0.1)$ plane and the phase of neuron changing with time, where the strength k of the stimulation neuron is 9. (a) The trajectory projection in the plane of the neuron, whose parameter r is 0.021, where the parameter r of the stimulation neuron is 0.011. (b) The trajectory projection in the plane of the neuron, whose parameter r is 0.009, where the parameter r of the stimulation neuron is 0.013. (c) The trajectory projection in the plane of the neuron, whose parameter r is 0.011, where the parameter r of the stimulation neuron is 0.02. (d) The membrane potential changing chart with time of the neuron, whose parameter r is 0.021, where the parameter r of the stimulation neuron is 0.011. (e) The membrane potential changing chart with time of the neuron, whose parameter r is 0.009, where the parameter r of the stimulation neuron is 0.013. (f) The membrane potential changing chart with time of the neuron, whose parameter r is 0.011, where the parameter r of the stimulation neuron is 0.02. (g) The phase function changing chart with time of the neuron, whose parameter r is 0.021, where the parameter r of the stimulation neuron is 0.011. (h) The phase function changing chart with time of the neuron, whose parameter r is 0.009, where the parameter r of the stimulation neuron is 0.013. (i) The phase function changing chart with time of the neuron, whose parameter r is 0.011, where the parameter r of the stimulation neuron is 0.02.

changing diagram of $|\Delta\phi(t)|_{\max}$ with the stimulation strength k changing, where the parameter r of the stimulation neuron is 0.02. From **Figure 4**, when the stimulation strength k changes from 0 to 8 according to the step 0.02, these two neurons' discharge patterns begin with asynchronization, and gradually realize discharge synchronization or the full synchronization via the quick intermittent discharge synchronization process. When the stimulation strength k is near 2.6, and these two neurons in **Figure 4(a)** go into the intermittent discharge synchronization state, so the critical value of these two neurons realizing synchronization is about 2.6. When the stimulation strength k is near 2.1, and these two neurons

Copyright © 2010 SciRes.

in **Figure 4(b)** go into the intermittent discharge synchronization state, so the critical value of these two neurons realizing synchronization is about 2.1. When the stimulation strength k is near 2.5, and these two neurons in **Figure 4(c)** go into the intermittent discharge synchronization state, so the critical value of these two neurons realizing synchronization is about 2.5. When the stimulation strength k is near 2, and these two neurons in **Figure 4(d)** go into the intermittent discharge synchronization state, so the critical value of these two neurons realizing synchronization is about 2. When the stimulation strength k is near 2.9, and these two neurons in **Figure 4(e)** go into the intermittent discharge synchronization state, so the critical value of these two neurons realizing synchronization is about 2.9. So, under the same stimulation signal, the stimulation strength's critical value of the two neurons whose parameter r is at 0.008~0.009, is bigger than that of the two neurons whose parameter r is at 0.0125~0.015. Under the same stimulation signal, the less the difference between the two neurons is the smaller stimulation strength k of the two neurons' realizing synchronization and the easier the two neurons realize synchronization. In addition, the bigger the stimulation strength k is easier the neurons realize synchronization.

3.2. Synchronization under the Stimulation of the Chaos Discharge Pattern

The values of the parameters of these two uncoupled neurons are above given values. The parameter r of the stimulation neuron is respectively 0.0085 and 0.013, and its discharge pattern is the chaos. Under each parameter r, the stimulation strength k is respectively 0.5, 1, 2, 3, 6, 9, and 12.

The parameter r of the stimulation neuron is 0.0085 (the discharge pattern is the chaos). As it begins to stimulate the two neurons, in above all cases, the two uncouple neurons' discharge patterns totally change into dynamic period discharge pattern from the initial discharge patterns with the stimulation strength k increasing, and the changing trend of their membrane potentials' ISI is the same, namely gradually evolves into the chaos discharge pattern which is the same as the stimulation neuron's. When the stimulation strength is 0.5 and 1, these two neurons don't realize synchronization, and when the stimulation strength is 3, 6, 9 and 12, these two neurons realize discharge synchronization or the full synchronization. When the stimulation strength is 2, these two neurons except r_1=0.009 and r_2=0.021, r_1=0.022 and r_2=0.013, realize discharge synchronization or the full synchronization. When the parameter r is the same, these two neurons realize the full synchronization. When the parameter r is a little different, these two neurons realize the full synchronization or discharge synchronization. When the parameter r is much different, these two neurons realize discharge synchronization or the approximate full synchronization. The synchronization discharge pattern is the same as the stimulation neuron's discharge pattern (the chaos).

The parameter r of the stimulation neuron is 0.013 (the discharge pattern is the chaos). As it begins to stimulate the two neurons, in above all cases, the two uncouple neurons' discharge patterns totally change into dynamic period discharge pattern from the initial discharge patterns with the stimulation strength k increasing, and the changing trend of their membrane potentials' ISI is the same, namely gradually evolves into the chaos discharge pattern which is the same as the stimulation neuron's. When the stimulation strength is 0.5 and 1, these two neurons don't realize synchronization, and when the stimulation strength is 3, 6, 9 and 12, these two neurons realize discharge synchronization or the full synchronization. When the stimulation strength is 2, only several groups of these two neurons realize discharge synchronization or the full synchronization. When the parameter r is the same, these two neurons realize the full synchronization. When the parameter r is a little different, these two neurons realize the full synchronization or discharge synchronization. When the parameter r is much different, these two neurons realize discharge synchronization or the approximate full synchronization. The synchronization discharge pattern is

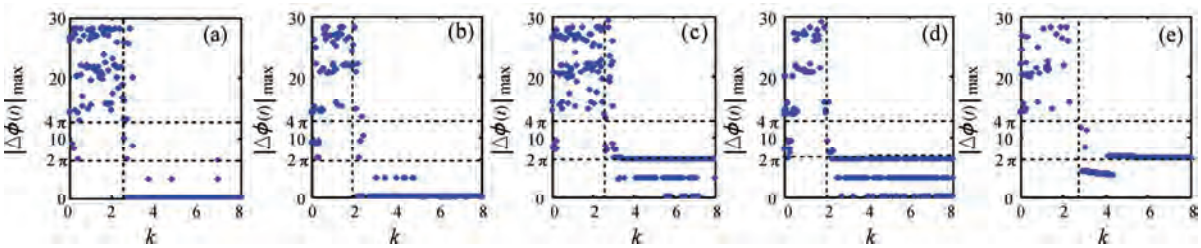

Figure 4. The changing diagram of $|\Delta\phi(t)|_{max}$ is changing with the stimulation strength k changing, where the parameter r of the stimulation neuron is 0.02, and the changing step of the stimulation strength k is 0.02. (a) The parameter r of these two neurons is the same: r_1=r_2=0.009. (b) The parameter r of these two neurons is the same: r_1=r_2=0.013. (c) The parameter r of these two neurons is a little different: r_1=0.0085 and r_2=0.009. (d) The parameter r of these two neurons is a little different: r_1=0.014 and r_2=0.0141. (e) The parameter r of these two neurons is much different: r_1=0.014 and r_2=0.0085.

Copyright © 2010 SciRes.

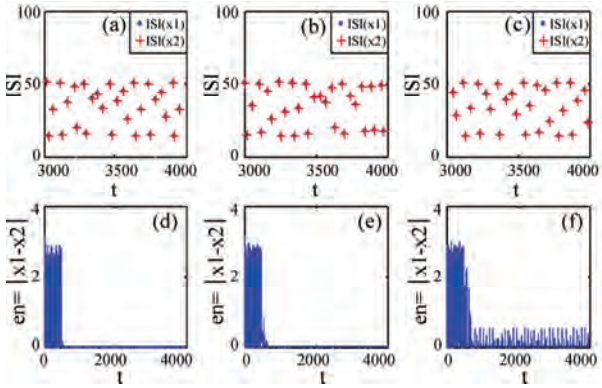

Figure 5. The synchronization process of the two neurons, where the parameter r of the stimulation neuron is 0.013 and the stimulation strength k is 9. (a) The membrane potential's ISI changing chart of the two neurons with time, where r_1 is 0.013 and r_2 is 0.013. (b) The membrane potential's ISI changing chart of the two neurons with time, where r_1 is 0.014 and r_2 is 0.0141. (c) The membrane potential's ISI changing chart of the two neurons with time, where r_1 is 0.022 and r_2 is 0.013. (d) The two neurons' membrane potential's synchronization error ($err = |x_1 - x_2|$) changing chart with time, where r_1 is 0.013 and r_2 is 0.013. (e) The two neurons' membrane potential's synchronization error changing chart with time, where r_1 is 0.014 and r_2 is 0.0141. (f) The two neurons' membrane potential's synchronization error changing chart with time, where r_1 is 0.022 and r_2 is 0.013.

the same as the stimulation neuron's discharge pattern (the chaos).

Limited to the length, **Figure 5** only shows the synchronization process of the two neurons. In **Figure 5**, from (a) and (d), (b) and (e), (c) and (f), these two neurons respectively realize the full synchronization, the full synchronization, and the discharge synchronization; and the synchronization discharge pattern is all the chaos, which is the same as the stimulation neuron's discharge pattern.

Limited to the length, **Figure 6** only shows the changing diagram of $|\Delta\phi(t)|_{\max}$ with the stimulation strength k changing. From **Figure 6**, when the stimulation strength k changes from 0 to 8 according to the step 0.02, these two neurons' discharge patterns begin with asynchronization, and gradually realize discharge synchronization or the full synchronization via the quick intermittent discharge synchronization process.

When the stimulation strength k is near 1.7, and these two neurons in **Figure 6(a)** go into the intermittent discharge synchronization state, so the critical value of these two neurons realizing synchronization is about 1.7. When the stimulation strength k is near 1.3, and these two neurons in **Figure 6(b)** go into the intermittent discharge synchronization state, so the critical value of these two neurons realizing synchronization is about 1.3. When the stimulation strength k is near 1.6, and these two neurons in **Figure 6(c)** go into the intermittent discharge synchronization state, so the critical value of these two neurons realizing synchronization is about 1.6. When the stimulation strength k is near 1.4, and these two neurons in **Figure 6(d)** go into the intermittent discharge synchronization state, so the critical value of these two neurons realizing synchronization is about 1.4. When the stimulation strength k is near 1.8, and these two neurons in **Figure 6(e)** go into the intermittent discharge synchronization state, so the critical value of these two neurons realizing synchronization is about 1.8. So, under the same stimulation signal, the stimulation strength's critical value of the two neurons whose parameter r is at 0.008~0.009, is bigger than that of the two neurons whose parameter r is at 0.0125~0.015. Under the same stimulation signal, the less the difference between the two neurons is, the smaller the stimulation strength k of the two neurons' realizing synchronization is, and the easier the two neurons realize synchronization. From **Figures 4** and **6**, for the two neurons, the critical value of the chaos signal's stimulation strength is less than that of the period signal's stimulation strength, so the chaos signal's stimulation is easier to realize the synchronization of two neurons than the period signal's stimulation. In addition, the bigger the stimulation strength k is, the easier the neurons realize synchronization.

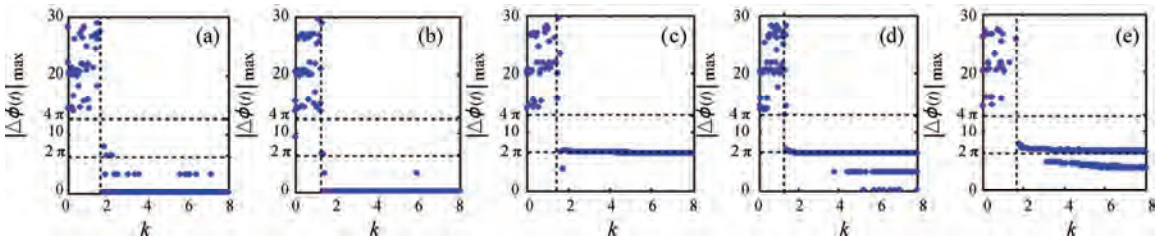

Figure 6. The changing diagram of $|\Delta\phi(t)|_{\max}$ is changing with the stimulation strength k, where the parameter r of the stimulation neuron is 0.0085, and the changing step of the stimulation strength k is 0.02. (a) The parameter r of these two neurons is the same: r_1=r_2=0.009. (b) The parameter r of these two neurons is the same: r_1=r_2=0.013. (c) The parameter r of these two neurons is a little different: r_1=0.0085 and r_2=0.009. (d) The parameter r of these two neurons is a little different: r_1=0.014 and r_2=0.0141. (e) The parameter r of these two neurons is much different: r_1=0.014 and r_2=0.0085.

Copyright © 2010 SciRes.

4. CONCLUSIONS

Under the stimulation of the neuron's membrane potential whose discharge pattern is period or the chaos, the two uncoupled neurons under different initial conditions, whose parameter *r* is different or the same, can realize the full synchronization or discharge synchronization, and can only be synchronized to the response being in synchronization with stimulation signal. The synchronization discharge patterns are the same as the stimulation neuron, and the synchronization characteristics are mainly related to the discharge pattern and the strength of the stimulation neuron's membrane potential, and are little related to the parameter *r* and the initial state of the two uncoupled neurons. And the bigger the strength of the stimulation signal is, the easier the two neurons realize synchronization. The critical strength value of these two neurons realizing synchronization is related to, not only the two neurons' parameter *r* and the initial state, but also the stimulation signal. For the two neurons, the critical value of the chaos signal's stimulation strength is less than that of the period signal's stimulation strength. The chaos signal's stimulation is easier to realize synchronization of two neurons than the period signal's stimulation.

This investigation shows characteristics of the neuron's membrane potential affecting the synchronization process of two uncoupled neurons, and the two neurons' discharge patterns and synchronization process can be adjusted and controlled by the discharge pattern and the strength of the stimulation neuron's membrane potential. This result is helpful to study synchronization and encode of many neurons or neural network.

5. ACKNOWLEDGEMENTS

The authors would like to thank "The Journal of Biomedical Science and Engineering" for providing the chance and really appreciate the anonymous reviewers for the valuable comments on the paper.

REFERENCES

[1] Pecora, L.M. and Carroll, T.L. (1990) Synchronization in chaotic systems. *Physical Review Letter*, **64,** 821-824.

[2] Pecora, L.M. and Carroll, T.L. (1991) Driving systems with chaotic signals. *Physical Review: A*, **44,** 2374-2383.

[3] Gray, C.M. *et al.* (1989) Oscillatory response in cat visual cortex exhibit inter-columnar synchronization which reflects global stimulus properties. *Nature*, **338,** 334-337.

[4] Hindmarsh, J.L. and Rose, R.M. (1982) A model of the nerve impulse using two first-order differential equation. *Nature*, **296,** 162-165.

[5] Hindmarsh, J.L. and Rose, R.M. (1984) A Model of neuronal bursting using three coupled first order differential equations. *Series B, Biological Sciences*, **221,** 87-102.

[6] Peng, Y.P., Jian, Z. and Wang, J. (2006) Study on discharge patterns of Hindmarsh-Rose neurons under slow wave current stimulation. *Lecture Notes in Computer Science*, **4221,** 127-134.

[7] Huerta, R. and Rabinovich, M.I. (1997) Spike-train bifurcation in two coupled chaotic neurons. *Physical Review: E*, **55,** R2108-R2110.

[8] Wu, Y. *et al.* (2005) Study on nonlinear characteristic of two synchronizing uncoupled Hindmarsh-Rose neurons. *Physics Letters: A*, **54,** 3457-3464.

[9] He, D.H., Shi, P.L. and Stone, L. (2003) Noise-induced synchronization in realistic models. *Physical Review: E*, **67,** 0272011-0272013.

[10] Wu, Y. *et al.* (2005) Complete synchronization and phase synchronization of two uncoupled neurons through parametrical drive. *Journal of Xi'an Jiaotong University*, **39,** 544-547.

[11] Shuai, J.W. and Durand, D.M. (1999) Phase synchronization in two coupled chaotic neurons. *Physics Letters: A*, **264,** 289-296.

[12] Peng, Y.P., Wang, J. and Jian, Z. (2009) Synchrony of two uncoupled neurons under half wave sine current stimulation. *Communications in Nonlinear Science and Numerical Simulation*, **14,** 1570-1575.

[13] Peng, Y.P. and Wang, J. (2007) Discharge patterns' change of Hindmarsh-Rose neurons under slow ramp current stimulation. *BIC-TA IEEE*, 52-55.

[14] Shi, X. and Lu, Q.S. (2005) Coherence resonance and synchronization of Hindmarsh-Rose neurons with noise. *Chinese Physics*, **14(6),** 1088-1094.

[15] Wu, Y., Xu, J.X., He, D.H. and David, J.D. Earn (2005) Generalized synchronization induced by noise and parameter mismatching in Hindmarsh-Rose neurons. *Chaos, Solitons and Fractals*, **23,** 1605-1611.

[16] Katsutoshi, Y., Keijin, S. and Atsushi, S. (2006) Noise-induced synchronization of uncoupled nonlinear systems. *Journal of Sound and Vibration*, **290,** 34-47.

[17] Wu, Y., Xu, J.X., Jin, W.Y. and Hong, L. (2007) Detection of mechanism of noise-induced synchronization between two identical uncoupled neurons. *Chin. Phys. Lett*, **24(11),** 3066-3069.

Copyright © 2010 SciRes.

J. Biomedical Science and Engineering, 2010, 3, 167-180 **JBiSE**
doi:10.4236/jbise.2010.32022 Published Online February 2010 (http://www.SciRP.org/journal/jbise/).

Design and development of a new dedicated RF sensor for the MRI of rat brain

Aktham Asfour

Joseph Fourier University of Grenoble, Grenoble, France.
Email: Aktham.Asfour@ujf-grenoble.fr

Received 14 October 2009; revised 13 November 2009; accepted 16 November 2009.

ABSTRACT

The design and development of a new dual-frequency RF probe-head are presented. This probe was initially dedicated for the MRI of both proton (^{1}H) and hyperpolarized Xenon-129 (HP ^{129}Xe) in the rat brain at 2.35 Tesla. It consists of a double-tuned (100 MHz-27.7 MHz) volume coil, which could be used for both transmitting and receiving, and of a receive-only single-tuned (27.7 MHz) coil. The double-tuned coil consists of two concentric birdcage resonators. The inner one is a low-pass design and it is tuned to 27.7 MHz, while the outer one, tuned to 100 MHz, is high-pass. The receive-only coil is a surface coil which is decoupled from the double-tuned volume coil by an active decoupling circuitry based on the use of PIN diodes. A home-built Transmit/Receive (T/R) driver ensures biasing of the PIN diodes in both volume and surface coils. The original concepts of the design are addressed, and practical details of realization are presented. One of the underlying ideas behind this work is to proceed well beyond the application to the MRI of HP ^{129}Xe. Actually, this design could be easily adapted for a large palette of other MRI applications. Indeed, we tried to make the design versatile, simple and easy to replicate by other research groups, with a low-cost, minimum development time and accepted performances. The prototype was validated at 100 MHz and at 26.4 MHz (sodium-23 resonance frequency at 2.35 T). MRI experiments were performed using phantoms. In vivo ^{1}H images and ^{23}Na spectra of the rat brain are also presented.

Keywords: MRI; RF Coils; Double-Tune; Active Decoupling; Proton; Sodium-23; Hyperpolarized Xenon-129

1. INTRODUCTION

Nuclear Magnetic Resonance (NMR) and Magnetic Resonance Imaging (MRI) are important diagnostic and analytical tools for biomedical studies. During the last two decades, and since the MRI of hyperpolarized xenon-129 (HP ^{129}Xe) was initially demonstrated in 1994 [1] in mouse lungs, the MRI of hyperpolarized gases (^{129}Xe, ^{3}He…) have become widespread for a large palette of applications in biology and medicine. Particularly, the MRI of injected or inhaled HP ^{129}Xe is a promising noninvasive method for the investigation of brain function and clinical use. In fact, several studies carried out in our laboratory and by some research groups in the world, have already demonstrated that the MRI of HP ^{129}Xe may allow quantitative measurement of the cerebral blood flow (CBF) with a high spatial resolution [2,3,4,5]. This physiological parameter, which is defined as the blood supply to the brain in a given time and per mass unit of brain tissue[1], is tightly regulated to meet the brain's metabolic demands. The measurement of changes in both global cerebral blood flow (gCBF)[2] and regional cerebral blood flow (*rCBF*)[3] is of great value for functional brain studies as well as for the diagnosis of a large number of brain diseases (Alzheimer, epilepsy, Parkinson, ischemia…). Nevertheless, for such measurements, especially those of the *rCBF*, to become quantitatively reliable by the MRI of HP ^{129}Xe, one must first overcome several experimental and instrumental challenges.

In addition to the understanding of the behavior of the ^{129}Xe in the brain, which is out of the scope of this paper, many instrumental obstacles have to be actually resolved. For example, the experimental set-up for polarization build-up and storage is relatively complicated and require some know-how. One important aspect in building this polarization set-up has already been addressed in our previous works [6,7]. A second instrumental challenge concerns the development of specific radiofrequency (RF) probes for these experiments. In this paper, we deal with this problem and we present an original and versatile design of a dedicated RF double-tuned volume coil actively-decoupled from a simple-tuned receive-only RF surface coil.

To help the reader in better understanding the general context of our research and the goal of this paper, one may

[1]In healthy brain of adult humans, the CBF is regulated to an average of 50 milliliters of blood per 100 grams of brain tissue per minute.
[2]Value of the CBF measured over all the brain.
[3]Value of the CBF measured within a specific brain region.

need to review or to learn some basic principles of a typical NMR experiment as well as of the NMR of HP ^{129}Xe.

As it is well known, when a sample, consisting of NMR-sensitive nuclei (^{1}H, ^{3}He, ^{129}Xe; ^{23}Na…etc.), is subjected to a uniform static magnetic field B_0, a net macroscopic magnetization M of the sample appears in the direction of B_0. This magnetization is proportional, roughly speaking, to the polarizing field B_0, to the density of the nuclei within the sample and to the characteristic gyro-magnetic ratio γ of the nucleus being studied.

If the sample is subjected now to a short pulse (called excitation pulse) of a second radiofrequency magnetic field B_1, applied at the characteristic Larmor frequency f_0 (about 100 MHz for ^{1}H, 27.7 MHz for ^{129}Xe and 26.4 MHz for ^{23}Na at B_0=2.35 Tesla), the net magnetization, M, may be "tipped" or rotated from its initial direction (or from its equilibrium state) by an angle his angle is called "flip angle". It is proportional to B_1 according to the equation $\alpha = \gamma.\tau.B_1$ where the duration of the RF pulse is. At the end of the excitation pulse, a resonance signal (or the NMR signal) at the same frequency, f_0, is received. This signal, which is proportional to the magnetization M and to γ, is processed to be used for obtaining a "fingerprint" of the environment of the nucleus being studied.

At equilibrium and for a same magnetic field B_0, the NMR signal of a given ^{129}Xe population is about 10000 times lower than the one that could be obtained from the same volume of protons. This is because of the intrinsic lower gyro-magnetic ratio and lower density of the xenon. Consequently, at equilibrium, the in vivo-NMR signal of the injected or inhaled ^{129}Xe is not exploitable. To compensate this limitation, hyperpolarizing techniques have been successfully used to dramatically increase the magnetization of ^{129}Xe before using it for the *in vivo* experiments. In this case, the magnetization and the NMR signal levels are typically enhanced by about five orders of magnitude.

In NMR/MRI experiments, the well-tuned (to the frequency f_0) RF probe has usually a dual role: it ensures the excitation of the sample (*i.e.*, it creates the RF field B_1) and it receives the weak NMR signal from this same sample. Usually, both excitation (transmission) and receiving processes are produced in the same coil. Nevertheless, there are cases where these processes are produced by two or more different coils. Generally, according to considerations related to the spatial homogeneity of the excitation field B_1 and to the receiving sensitivity, RF coils may be categorized, roughly speaking, as either volume coils or surface coils. Volume coils create homogeneous spatial distribution of B_1 and guarantee the possibility to image deep organs. Surface coils allow high sensitivity, and hence high signal-to-noise ratio (SNR), for surface regions (the rat brain could be considered as surface region). These surface coils present however a poor B_1 homogeneity when compared with volume coils. This homogeneity decreases generally when one moves away for the centre of the coil.

Both volume and surface coils could be used for both transmission and receiving. However, when B_1 homogeneity during the transmission period is required, the use of a transmit volume coil is necessary. On the other hand, when this homogeneity is not an issue, a surface coil may be preferred to optimize the SNR of the detected NMR signals. The association of a volume coil, for transmission, decoupled from a surface coil, for receiving, is usually used when both B_1 uniformity and high SNR are required.

For our experiments of measuring the *rCBF* by the NMR of HP ^{129}Xe, a dedicated RF probe has to be built. Actually, the measurement method of the gCBF requires knowledge of the global (over all the rat brain) flip angle [2,3,4,5]. This angle depends, remember, on B_1. The determination of a global flip angle can be easily performed. However, when local or regional cerebral blood flow (*rCBF*) values (within a specific brain region or inside a pixel of the MRI image) have to be measured, the local flip angles (which depend on the local values of B_1) have to be accurately estimated. This estimation is not a trivial task. This is why it's generally assumed that local flip angles are close enough to the global value. Nevertheless, when a surface coil is used for transmission, the estimated global flip angle could be very different from the local values due the inherent non-uniformity of the B_1 field distribution. This may produce inaccurate results in the *rCBF* values. For example, Venkatesh *et al.* have noted a 20% difference between the decay times (parameter directly related to the *rCBF*) obtained with a surface coil and those obtained with a volume coil used for both transmission and receiving [3]. Moreover, since Kilian *et al.* [2] used a surface coil in their human brain measurements, it is possible that their results contain a systematic error due to inaccurate estimation of the local flip angles. The same problem was also encountered in our experiments [5]. In all these experiments, the use of surface coils was initially motivated by the desire to obtain a high SNR in the MRI images.

To overcome this problem, the idea we develop here consists in using a volume coil for transmitting so as the global flip angle will be close enough to the local ones thanks to the high B_1 homogeneity guaranteed by this type of coils. The detection of the NMR signals will then be performed by a surface coil positioned inside the volume coil. In this situation the advantage the inherent high sensitivity associated with the surface coil is retained.

The two coils must be decoupled so as when the first is active, the second must be deactivated. In other words, during transmission, the volume coil is active or "on" while the surface coil is "off". During receiving, the transmit volume coil has to be deactivated and the sur-

Copyright © 2010 SciRes.

face one has to be active. Both transmit and receive coils must be well-tuned to the resonance frequency of ^{129}Xe (27.7 MHz at 2.35 T).

Moreover, for the *rCBF* measurements by MRI, the final "ideal" probe must satisfy more stringent requirements. Actually, in addition to the transmission and receiving at the frequency of ^{129}Xe, one has to be able to perform ^{1}H-MRI experiments (at 100 MHz) without changing the probe and without moving the sample under test (rat in our application). In fact, acquiring ^{1}H images is necessary to localize anatomical structures in the rat brain. These anatomical images are to be superposed to ^{129}Xe images to identify structures where inhaled or injected ^{129}Xe could be localized in the rat brain. On the other hand, the procedure of homogenization of the static magnetic field (shimming), which is essential before every MRI acquisition, must be performed using ^{1}H NMR signals. Actually, since this shimming procedure requires repetitive excitations and detections, it can not be accomplished on the ^{129}Xe signals because the artificial magnetization (non equilibrium state) of the HP ^{129}Xe is not renewable when destroyed by an RF excitation pulse.

In both anatomical image acquisition and shimming procedures, a high SNR of the detected ^{1}H signals is not an issue and a same transmit-receive volume coil tuned to 100 MHz could be adequate. This coil must however be decoupled from both transmit volume and receive-only ^{129}Xe coils.

To summarize: the final "ideal" NMR probe that we developed consists of a transmit volume coil actively decoupled from a receive-only surface coil working at 27.7 MHz, and a transmit/receive volume coil for the ^{1}H MRI at 100 MHz. The decoupling between the ^{1}H coil and the ^{129}Xe coils will be performed geometrically.

This novel configuration, which actually associates three MRI coils in a same probe, is new and has not been published. In fact, due to the variety of size and experimental protocols encountered with small-animal imaging experiments, it is usually advisable and may be necessary to build a probe optimized for each experimental set-up and for each application. However, it is important to notice here that another objective of this work is to proceed well beyond this specific application to the MRI of HP ^{129}Xe. Actually, the current design could be adapted or could inspire other designs for a palette of MRI applications in the rat brain. Generally, for such applications, the "ideal" imaging/spectroscopy coil would be one which provides high sensitivity, high B_1 homogeneity, and operation on two or more frequencies without retuning requirement or cables changes. The problem of sensitivity can be addressed using surface coils [8]. The homogeneity requirements can be met by the use of adequate coil geometry (*i.e.*, birdcage design [9]). The problem of acquiring data from two different nuclei (usually proton and a second nucleus like ^{129}Xe, ^{23}Na sodium, ^{31}P…) requires the use of an efficient double-tuned coil (volume or surface coils) [10,11,12,13,14, 15,16,17]. While these problems have been addressed individually, there have been no published designs that have integrated all these features into one design. The goal of this work is to approach performances as outlined above. Another underlying idea is to make this specific probe easy to replicate, by other research groups with a low-cost, minimum development time and accepted performances. To allow for easy extension of this design to other frequencies (nuclei) and dimensions, we describe in some details the practical aspects of the workbench design as well as the coil characterization and MRI/NMR testing using phantoms. The probe is validated at the ^{1}H frequency and the sodium frequency (26.4 MHz at 2.35 T) since this last is very close to the xenon frequency. In vivo MRI images of the rat brain were obtained at ^{1}H frequency as well as NMR signals at the sodium frequency.

All developed circuits and any other details on developed probe could be obtained by simply writing to authors.

2. MATERIALS AND METHODS

2.1. The Double-Tuned Volume Probe

We built a double-tuned volume probe using the birdcage design [9]. This design ensures inherent high B_1 homogeneity within the coil region. It is therefore well-suited for the MRI of HP ^{129}Xe. The design is shown in its low-pass and high-pass versions in **Figure 1**. It consists of two circular loops, referred to as end-rings, connected by a number of equally spaced straight segments referred to as legs or rungs. Depending on the version, the tuning capacitors are placed in the legs (low-pass) or in the end-rings (high-pass).

A single-tuned birdcage will resonate in several modes. A birdcage with N legs has N/2 resonance modes (assuming N is even) [9,17], with the most useful to MRI being Mode 1 (fundamental mode). In this mode, the currents in the legs follow a cosine distribution as one moves radially around the coil. This sinusoidal distribution of currents is essential to create a very homogenous transverse magnetic field B_1.

For our application, it is necessary to double-tune the birdcage. The sinusoidal optimum current distribution should be maintained at each frequency. Double-tuning a birdcage resonator is not a trivial task and it has been subject of many publications [10,11,12,13,17]. The method to choose depends actually on the desired performances at each frequency. Double-tuned birdcages have been used at relatively low field (≤ 1.5 T). Few designs at higher fields have been proposed. For example, Fitzsimmons *et al*. [10] presented a double-tuned birdcage coil at 2 T. It was dedicated for the MRI of proton (85.5 MHz) and the NMR spectroscopy of phos-

Copyright © 2010 SciRes.

phorus (34.6 MHz) of the rat abdomen. They derived their coil in quadrature operation for both proton and phosphorus channels. The coil was used for both transmission and receiving at each frequency. One of the originalities of the double-tuned birdcage that we propose here is that it has to work at higher field (2.35 T) for the MRI of the rat brain. More important is the fact that, to the knowledge of the author, a double-tuned birdcage associated with an actively decoupled receive-only surface coil has not been published.

The double-tuned birdcage we built consists of two birdcages in a concentric configuration as it is seen in **Figure 2**.

Each resonator consists of eight legs. This number represents a compromise between B_1 homogeneity and complexity of realization. The inner coil, a low-pass birdcage, had a diameter of 9 cm, a length of 13 cm, and was tuned to the xenon frequency. The outer coil, a high-pass design, had a length of 16 cm, a diameter of 10.5 cm, and was tuned to the proton frequency. We verified that no proton resonance modes occur at the xenon frequency. Conversely, no xenon modes occur at the proton frequency. The inner birdcage was rotated within the outer birdcage until minimum coupling occurred. This positioned the legs of the inner coil midway between the legs of the outer one. Also, the outer bird

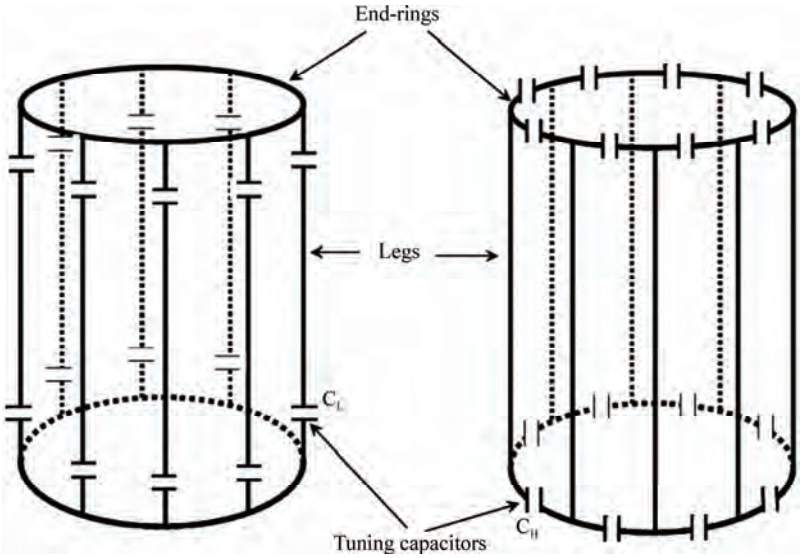

Figure 1. Spatial representation of the low-pass (left) and high-pass (right) birdcage resonators. C_H (high-pass) and C_L (low-pass) are the tuning capacitors.

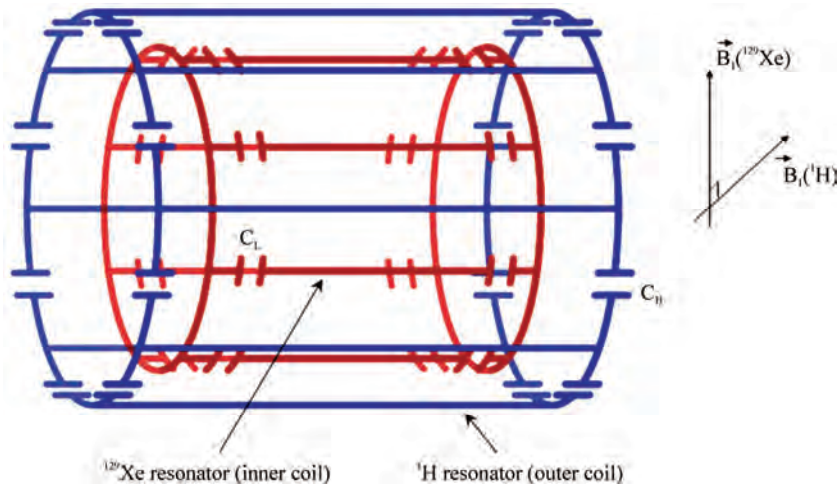

Figure 2. A simplified scheme of the developed imbricate birdcage resonators. The inner coil is low-pass and the outer one is high-pass. In linear polarization operation, the coils should be derived in such a way that their B_1 fields are orthogonal allowing efficient geometric decoupling between the resonators.

Copyright © 2010 SciRes.

cage was made longer than the inner one, minimizing coupling between the pairs of end rings. Realistically, one cannot achieve perfect isolation between the two coils since the legs of the coils are in close proximity. The coupling is only reduced. For our application, since the resonance frequencies of the coils are far away from each others, this geometric decoupling could be accepted. Quantitative measurements of the isolation between the two coils are given in Section 3.

The calculation of the necessary tuning capacitances for both coils was performed using the free Birdcage-Builder software from the Penn State University [18]. The practical used values for these tuning capacitors were close to the calculated ones.

Variables capacitors were used to perform a final fine tuning when the coils are placed inside the magnet and loaded by the sample (**Figure 3**). For the low-pass birdcage, the fine tuning is achieved by adjusting tow diametrically opposed capacitors (C_{LT} in **Figure 3**). This method allows only a limited tuning range. Otherwise, it destroys the original ideal sinusoidal current distribution between the legs [17]. After testing the resonator inside the magnet and with different loads (phantoms, rats), we limited the tunable range of the resonator to sufficient range of about 500 kHz, so as the current deviation from its ideal is less than 10% [17].

For the high-pass resonator, the fine tuning is accomplished by connecting two diametrically opposed points of one end-ring by a tuning variable capacitor C_{HT}. In practice, the connection of these points is made by adding a second circular loop, parallel to the end-ring as shown in **Figure 3**. To preserve the symmetry of the birdcage, the adjustable tuning capacitors C_{HT} was balanced by a fixed capacitor of 8.2 pF connected across the second end ring using a circular loop (not shown in **Figure 3**).

Both coils were derived in linear polarization operation in such a way that theirs B_1 fields are orthogonal as it was shown on **Figure 2**. We used balanced capacitive coupling to match their impedances to the real value of 50 at the working frequency [17]. The coupling scheme of the low-pass resonator is shown together with the active decoupling circuitry in **Figure 4**. In this scheme, the capacitive coupling, accomplished through the capacitors C_T and C_{M1}, C_{M2} and C_{M3}, is preceded by a balun (balanced-unbalanced). This balun is required for the probe circuit, not only due to the necessity of equilibrating the probe coil and consequently minimizing dielectric coil losses in the sample, but also for blocking unwanted common mode currents. The balun we built is widely used in radio technologies [17,19]. It consists of a simple "trap" circuit where the loop formed by the coaxial cable is tuned by a capacitor, C_B, to form a high impedance circuit at the xenon frequency.

The capacitive coupling scheme for the low-pass birdcage is straightforward to be generalized to proton resonator. It will not be given here, but the interesting reader may simply write to the author for more details.

As it was outlined in a previous paragraph, the transmit-only birdcage coil for ^{129}Xe (inner coil) must be decoupled from the receive-only surface coil (described in the next section). During transmission, this is mandatory since a coupling between the coils would result in deleterious consequences for the homogeneity of the B_1 field and in a possible destruction of the receive coil. During receiving, part of the electromagnetic energy received by the receive coil will be dissipated in the transmit volume

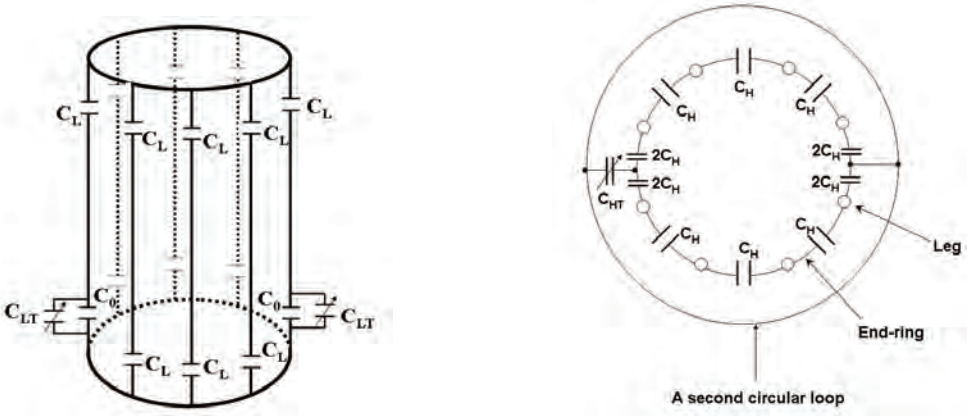

Low-pass resonator High-pass resonator

Figure 3. The fine tuning of the resonators. Low-pass resonator: C_L=340 pF (220 pF+120 pF chip capacitors from American Technical Ceramics Corp. ATC), C_{LT}=1.5-55 pF (adjustable capacitor NMAT55HVE from Voltronics). High-pass resonator (only one end-ring is shown): C_H=40 pF (18 pF+12 pF chip capacitors from ATC Corp.), C_{HT}=1-15 pF (adjustable capacitor NMAT15HVE from Voltronics). To preserve the symmetry of the high-pass birdcage, a tuning capacitor (which balances C_{HT}) should be connected across the second end-ring (not shown in the figure). We used a fixed chip capacitor of 8.2 pF to balance C_{HT}.

Copyright © 2010 SciRes.

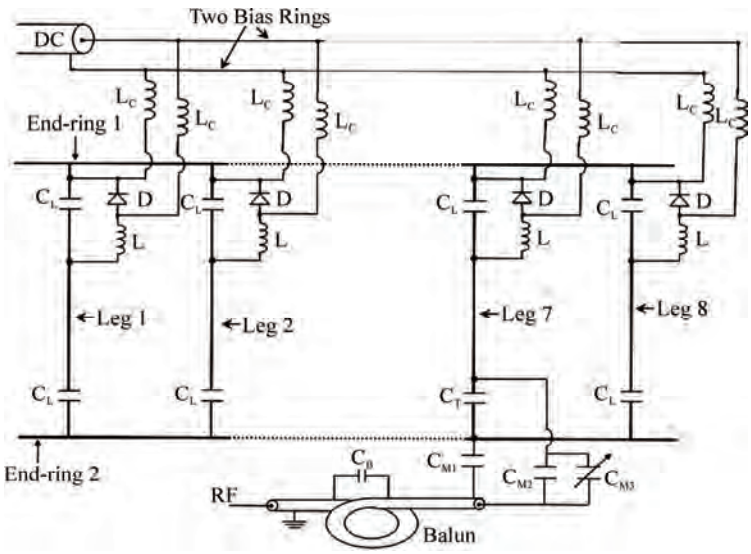

Figure 4. The ^{129}Xe birdcage electrical circuit associated with the active decoupling circuitry. C_L (220+120 pF from ATC Corp.) are tuning capacitors, L_C (8 µH+ 4x1 µH from CoilCraft) are the RF choke inductors, L (90 nH) are parallel inductors (from CoilCraft) and D are PIN diodes (UM4006 from Microsemi Corp). Matching is achieved by the use of balanced capacitive coupling through ATC chip capacitors: C_T=220 pF, C_{M1}=120 pF, C_{M2}=53 pF (10 pF+10pF+33pF). For fine matching, C_{M3} is a variable capacitor with capacitance between 1.5 pF and 55 pF (NMAT55HVE from Voltronics). Notice that $C_T + C_{M2} + C_{M3} \approx C_L$, which is with good agreement with balanced capacitive coupling condition [17]. The adjustable 1.5 pF-55 pF tuning capacitors C_{LT} for fine tuning are not shown (see **Figure 3**). The tuning capacitor C_B for the balun C_B=180 pF+120 pF.

coil resulting in SNR and sensitivity losses. Therefore, the interaction of the volume resonator and the receive coil must be cancelled out.

Decoupling can be achieved in principle geometrically (as in the case of the two concentric birdcages). However, when the coils are tuned to the same frequency, it is difficult in practice to perfectly decouple them by simply adjusting their mutual orientation. Hence, geometric decoupling should be accompanied or replaced by another effective mean that cancels out or, at least, minimize the induced currents in each coil.

This can actually be done by shifting the resonance frequency of one coil with respect to the other during appropriate periods. This detuning method is well described and used to detune a birdcage coil in [20] for example. In this relatively simple method, usually used in commercial coils, the current in the detuned coil is not cancelled out but only reduced.

In more efficient design, the current in the resonator is cancelled out at the working frequency, improving the isolation to a high level. In such a design, which is based on the "pole insertion" technique, an inductance is connected, using switching diodes, in parallel to one or more (depending on the coil structure and type) tuning capacitors, constituting a parallel resonant circuit (pole insertion). If the pole is well-tuned to the working frequency, the resulting "trap" circuit becomes an efficient blocking RF current device. This method was described for the case of a single-tuned high-pass birdcage [21]. In our prototype, we demonstrate that this method can be generalized to the case of a low-pass birdcage which has not been published.

We realized an active decoupling through the use of high voltage PIN diodes (UM4006, Microsemi Corp) distributed across one set of the legs capacitors. The schematic of the decoupling circuitry is shown in **Figure 4**.

For each leg, two bias rails apply the appropriate DC bias, through the RF choke inductors L_C to the PIN diode which, when it is forward-biased, switches an inductor L in parallel with the tuning capacitor C_L. If the value of the inductor L is correctly chosen ($L.C_L.\omega_0^2 = 1$), the resulting parallel circuit presents a high impedance at the working frequency so as the RF current is cancelled out in each leg and the transmit volume coil is "off" (receiving period). When the diode is reverse-biased, it forms an open circuit and the inductor L is disconnected. In this case, the coil is "on" (transmission period).

The inductors L_C in the direct DC path serve as chokes and ensure "isolation" between the RF part and

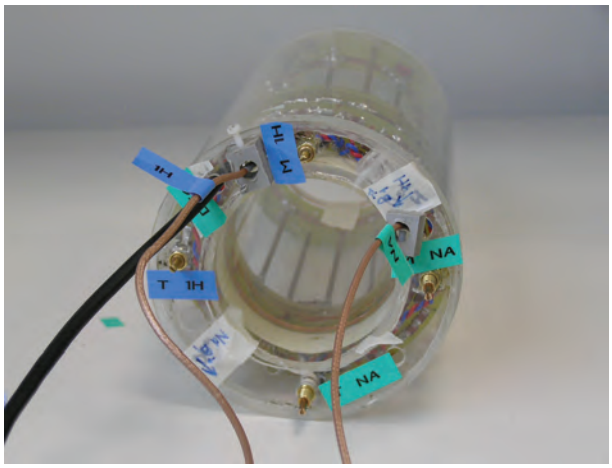

Figure 5. The double-tuned volume coil. We can see (right picture) the four variable tuning and matching capacitors for the two channels.

the DC bias circuit by minimizing RF currents on the DC path.

Figure 5 shows the double-tuned volume coil.

2.2. The Receive-Only Single-Tuned Coil

A surface coil was chosen for the receive-only function. It consists of a single circular loop of 4 cm of diameter (**Figure 6**). The tuning capacitor C_t was distributed into two series capacitors ($2C_t$) positioned in two different physical sites of the loop to reduce the losses associated with the electric field generated by the coil [22,23].

The decoupling of this coil from the transmit volume coil was achieved using the "pole insertion" method as illustrated in **Figure 6**. The PIN diode switches or not in parallel the inductor L_s across one of the distributed tune capacitors ($2C_t$). During the transmission period the coil is "off" (diode is forward-biased), while it is "on" during the receiving period (diode is reverse biased).

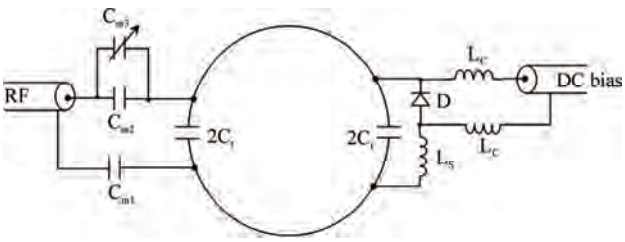

Figure 6. The receive-only coil and its active decoupling circuitry. The fixed tuning is $2C_t$=2x220 pF+2x150 pF+100 pF (chip capacitors from ATC). The adjustable capacitor of 1.5-55 pF (NMAT55HVE from Voltronics) is not shown. The matching capacitors are: C_{m1}=68 pF+10 pF, C_{m2}=56 pF C_{m3}=1.5-55 pF (adjustable capacitors NMAT55HVE from Voltronics). *Ls*=40 nH (3 parallel 120 nH inductor from CoilCraft) is the parallel inductor. D is a PIN diode (UM4006 from Microsemi Corp). *Lc*=8 µH+5x 1 µH are RF choke inductors (from CoilCraft).

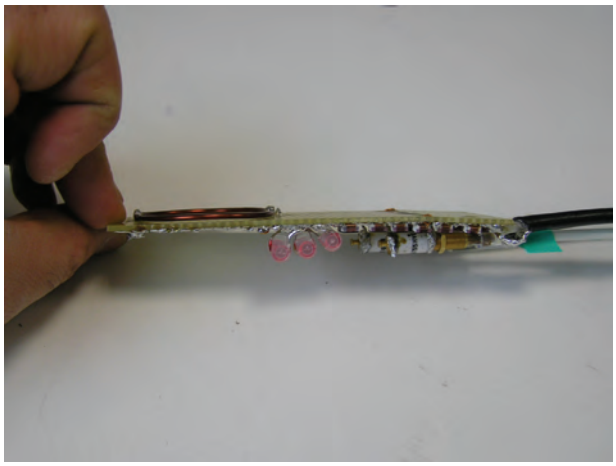

Figure 7. The receive-only surface coil and its circuitry. The loop was fixed on one side of a printed board and all components were soldered on the other side.

Notice finally that the receive-only coil was matched using balanced capacitive coupling (capacitors C_{m1}, C_{m2}, *and* C_{m3} in **Figure 6**). RF choke inductors L_C are used to "separate" the RF circuit from DC bias one. **Figure 7** shows the developed single-tuned receive only coil.

2.3. The T/R Driver

PIN diodes for both transmit and receive-only coils were biased through the use of a home-made T/R driver. This driver provides the gated DC bias necessary for electronically turning coils "on" and "off". We designed the driver with a gated input (a TTL compatible signal supplied by the NMR spectrometer) and two separate TX and RX bias sections. The TX stage applies a –12 Vdc bias (PIN diodes are reverse biased and transmit volume coil is "on") and a 5 Vdc bias (PIN diodes are forward biased and transmit coil is "off"). The RX stage applies –12 Vdc bias (PIN diode opened and receive-only coil is "on") and a 5 Vdc bias (PIN diode closed and the coil is "off"). The driver contains current limitation resistors to limit the maximum output current to 1 A for both TX and RX sections.

The flexibility of the driver allows the possibility to turn "off" and "on" both coils by using a manual switch (without the need to a TTL signal) for fine tuning and matching purposes inside the magnet. Another manual switch allows also the use of volume ^{129}Xe coil for both transmission and receiving. In this situation, the receive-only coil is switched "off" during all the experiment (PIN diode forward biased).The design of the driver was based on the use of bipolar transistors.

3. RESULTS AND DISCUSSIONS

Although this specific probe-head was initially developed for the MRI of HP ^{129}Xe, we performed all the tests

Copyright © 2010 SciRes.

and all the validation experiments at proton and sodium-23 (^{23}Na) frequencies. Actually, it is important to notice that the magnetization of HP ^{129}Xe is artificial and it is therefore not renewable when destroyed by the RF excitation pulses. Clearly, this is not a convenient situation for coil characterization and adjustments. Sodium frequency at 2.35 Tesla (26.4 MHz) is very close to the ^{129}Xe one (27.7 MHz). We could therefore consider that all the tests and measurements conducted at the sodium frequency would be valid at the ^{129}Xe frequency. Validation at the HP ^{129}Xe frequency for in vivo applications will make the subject of a future work.

During all the tests, the receive-only surface coil was placed inside the volume probe in such a way that geometric decoupling between it and the proton volume coil, is always achieved. It is clear here that no geometric decoupling could be realized between the receive-only coil and the sodium volume coil. Only active decoupling between these coils is achieved.

As it was mentioned in a previous section, a single-tuned birdcage will resonate in several modes, with the most useful to MRI being Mode 1. In this mode, a very homogenous transverse magnetic field is created by the sinusoidal distribution of the currents in the legs. It is important for our application to know whether or not this distribution of currents was disturbed by the double-tuned configuration, and consequently to know whether or not the B_1 homogeneity, especially for the ^{23}Na coil, is preserved. Moreover, we are interested in knowing if the receive-only coil would or not disturb the sinusoidal distribution of the currents of the proton coil since only geometric decoupling was realized between these coils. Also, we wanted to know if the only-active decoupling between this receive-only coil and sodium volume coil would be sufficient to preserve the homogeneity of the B_1 without the need of geometric decoupling. All these information could be obtained by measuring the currents in the legs of both birdcages at the proton and sodium frequencies. We measured the currents distribution in each coil by placing a small sense loop adjacent to the legs. The receive-only coil was switched off during all measurements. At the sodium frequency, we measured the currents in the legs of sodium birdcage (inner resonator), as well as the currents induced in the proton legs (outer resonator). Similarly, these currents were measured at the proton frequency. Measurements are shown in **Figure 8**.

At the sodium frequency, the currents in the sodium birdcage (inner coil) follow a cosine distribution as one moves radially around the coil. Small currents are induced in the proton resonator (outer coil). These currents are in phase with and add to the currents in the sodium coil. From this information, one can expect that the transverse magnetic field B_1 created by the sodium coil would still homogenous and would not be disturbed by the proton coil. At the proton frequency, the measurements show strong out of phase currents in the sodium coil. Despite the presence of these currents, the currents in the proton legs still follow the desired sinusoidal distribution as one moves radially around the coil. The coil still creates a homogenous B_1 field. The presence of the out of phase currents in the sodium coil will result, off course, in losses in the efficiency of the proton coil when compared to a single-tuned one.

With the simple measurement method of currents which was based on the use a small sense loop, no changes on currents distribution were observed with or without the presence of the surface coil. One could then argue that the presence of the receive-only coil, in its "off" state, does not disturb the homogeneity maps of B_1 fields of both sodium and proton birdcages.

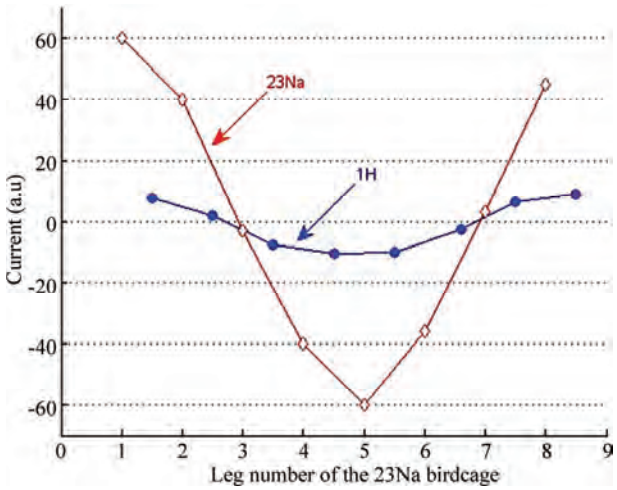

(a) Currents distribution at sodium frequency

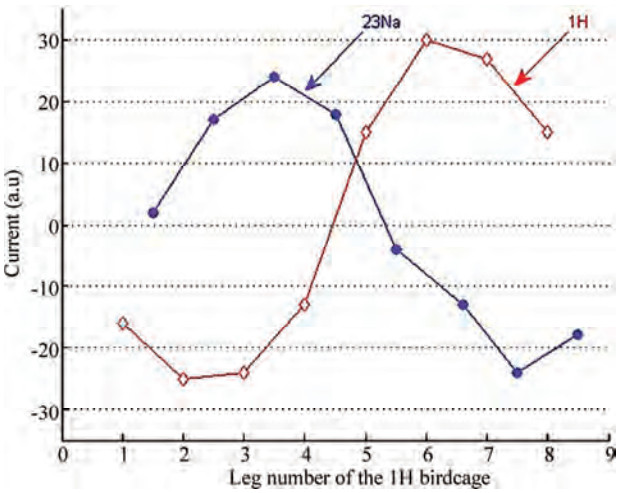

(b) Currents distribution at proton frequency

Figure 8. Currents distribution in the resonators at (a) sodium and (b) proton frequencies.

It's important to evaluate the degree of isolation between the coils. We have conducted isolation measurements between the different coils using a network analyzer. At sodium frequency, the isolation between the proton and the sodium birdcages was greater than 25 dB. At proton frequency, the isolation was lowered to about 16 dB. These measurements are in agreement with current measurements. Actually, at the sodium frequency, very small currents are induced in the proton coil and one can expect good isolation. Conversely, at the proton frequency, where large currents are induced in the sodium coil, the isolation is naturally lowered.

Isolation measurements between the receive-only coil and the two volume coils were also conducted. At the proton frequency, the isolation between the proton birdcage and the surface coil was about 26 dB. This isolation is very good and confirms that the cosine current distribution is not, or little, disturbed by the surface coil. Geometric decoupling between these two coils should sufficient for our application. Isolation between the sodium birdcage and the receive-only coil was also measured, with the only-active decoupling, to be about 31 dB. This excellent isolation between the two coils is essential in maintaining a transmit field homogeneity and in retaining the high sensitivity of the surface coil.

We have realized MRI images using the developed probe. In the first time, images were acquired using phantoms. A variety of phantoms was used to test the developed probe in various conditions and configurations.

The first series of images was realized using the proton birdcage and the sodium birdcage biased as transmit/receive coils. The surface coil was in its "off" state during both transmitting and receiving periods. The phantom (see **Figure 9**) was consisting of three cylindrical tubes with a same height (50 mm). The biggest tube (27 mm of inner diameter) was filled with saline solution (pure water saturated with NaCl). The two small tubes (12.5 mm of inner diameter) were filled with pure water.

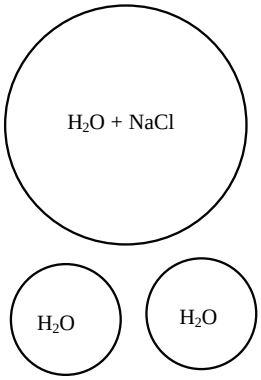

Figure 9. The cross-section (drawn to scale) of the phantom used to validate the double-tune birdcages.

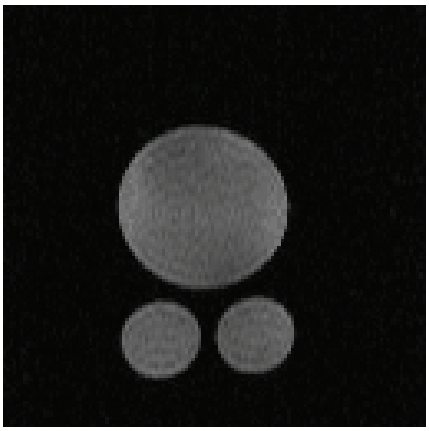

(a)

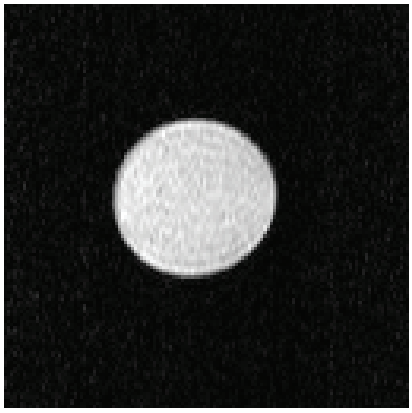

(b)

Figure 10. The cross-sectional (axial) MRI images (displayed to scale) of a phantom acquired at (a) proton frequency (100 MHz) and (b) sodium frequency (26.4 MHz). A spin echo pulse sequence was used to acquire images. FOV (Field of View)=70x70 mm^2, repetition time TR=1000 ms, echo time TE=31 ms, flip angle=90°. Slice thickness for proton images=2 mm. Sodium images were acquired with 2 signal averages and without slice selection.

Figure 10 shows the cross-sectional MRI spin-echo images of the phantom obtained at 100 MHz and 26.4 MHz with a field of view (FOV) of 70x70 mm^2 and an acquisition matrix of 128x64. Before transformation of the acquired data to the image space, zero filling to 128x128 was applied.

In these images, we can see the high homogeneity of the B_1 produced at 26.4 MHz. This confirms the currents measurements addressed above. The sodium birdcage was not disturbed by the proton coil. The homogeneity of the B_1 created at 100 MHz is shown to be also sufficient.

The second series of images was realized with the proton birdcage used for both transmitting and receiving. The sodium birdcage was biased as a transmit-only coil, while the surface sodium coil was biased as a receive-only coil. This is actually the final configuration of use of the developed probe for our application. A three-

Copyright © 2010 SciRes.

compartment cylindrical phantom was used for this experiment (**Figure 11**). It was formed of a small tube (inner diameter=10.5 mm) filled with pure water and placed approximately diagonally inside a larger tube (inner diameter=28 mm) filled with a saline solution. Between the two tubes, we have intentionally conserved an empty space with a variable width as illustrated by **Figure 11**.

Cross-sectional MRI spin-echo images of this three-compartment phantom were acquired at 100 MHz and at 26.4 MHz (see **Figure12**) with a FOV of 50x50 mm^2 and an acquisition matrix of 128x64. Before transformation of the acquired data to the image space, zero filling to 128x128 was applied.

We can recognize on the sodium images the typical sensitivity of a surface coil. This sensitivity decreases when one moves away from the center of the coil. We can, off course, expect a better signal-to-noise ratio with a surface coil when compared with a volume coil. This is actually well-known and no more signal-to-noise ratio characterization is necessary.

The validation of the developed probe was further demonstrated *in vivo* in the rat brain. Firstly, spin-echo images were obtained at the proton frequency. **Figure 13** (respectively **Figure 14**) shows a set of cross-sectional (respectively coronal) images.

Notice that, in the configuration of the developed probe, the filling factor of the outer birdcage (proton coil) is not optimum for the outer coil. Consequently, its SNR performances are relatively reduced when compared with those that could be obtained by a single simple-tuned birdcage. Actually, it is well-known that the SNR is directly proportional to square root of the coil filling factor. This point does not handicap the probe since high SNR performances of the ^1H coil are not an issue in our application. Actually, the ^1H will be only used for acquiring localization (anatomic) images where signal averaging could be applied to enhance the SNR. For shimming purposes, there is no need to have a high SNR.

The developed probe was also tested *in vivo* at the sodium frequency on the same rat. The sodium birdcage was biased as a transmit-only coil, while the sodium surface coil was biased as a receive-only coil. Our goal here is not to have sodium images of the rat brain, but only to demonstrate a basic functioning of the sodium coil *in vivo*. Only sodium NMR signal and spectra in the rat brain were acquired as it is shown in **Figure 15**. We obtained the typical sodium spectra of sodium in the rat brain with a typical peak width of few ppm [24].

In vivo sodium MRI images were difficult to obtain with classical MRI pulse sequences (spin-echo, gradient-echo) except if an incredible number of signal averages (more than 20 hours of acquisition time) is used. Actually, because of the short T2 transverse relaxation time components of sodium in the rat brain (0.7-3 ms or 16-30 ms depending on the value of the magnetic field), the acquisition of sodium images requires the imple-

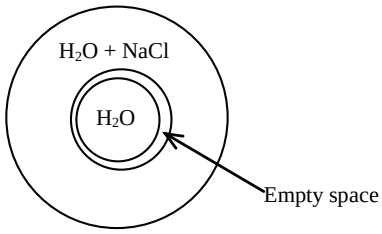

Figure 11. A schematic diagram (drawn to scale) of the cross-section of the three-compartment phantom.

(a) (b)

Figure 12. Cross-sectional (axial) MRI images (displayed to scale) of the three-compartment phantom acquired at (a) proton frequency (100 MHz) and (b) sodium frequency (26.4 MHz). A spin echo pulse sequence was used to acquire images. FOV=50x50 mm^2, flip angle=90°, echo time TE=30 ms, repetition time TR=2000 ms for proton and 300 ms for sodium. Slice thickness for proton images=2 mm. Sodium images were acquired with no slice selection and with no signal averaging.

Copyright © 2010 SciRes.

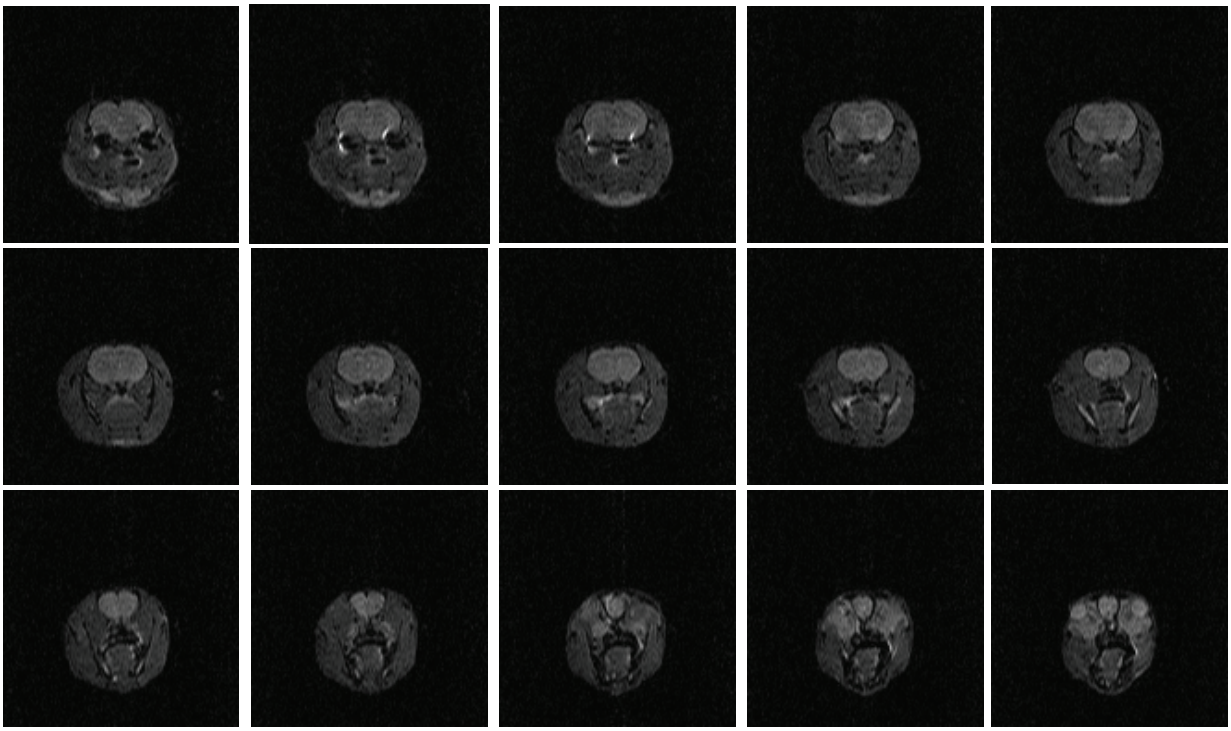

Figure 13. Cross-sectional MRI images of the rat brain acquired at 100 MHz. A spin echo pulse sequence was used to acquire images. FOV (Field of View)=60x60 mm^2, flip angle=90°, echo time TE=30 ms, repetition time TR=4000 ms, slice thickness=1 mm. Acquisition matrix was 128x64. Before transformation of the acquired data to the image space, zero filling to 128x128 was applied.

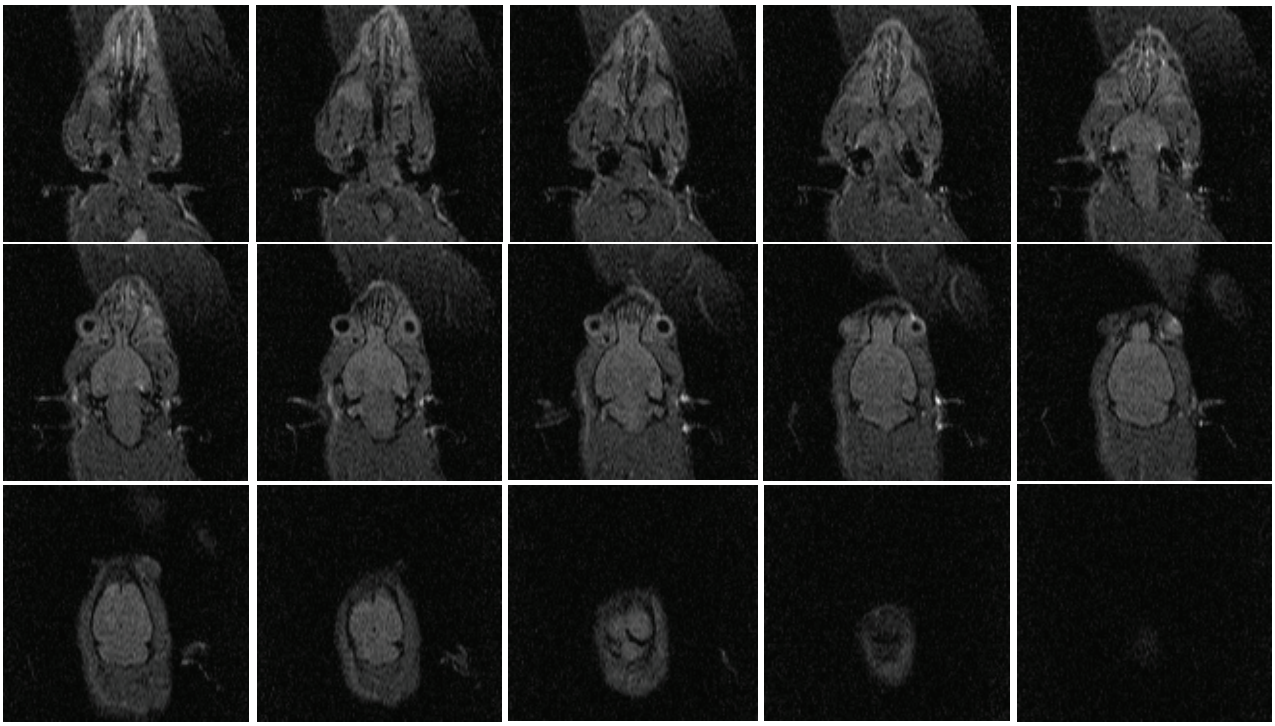

Figure 14. Coronal MRI images of the rat brain acquired at 100 MHz. A spin echo pulse sequence was used to acquire images. FOV (Field of View)=60x60 mm^2, flip angle=90°, echo time TE=17 ms, repetition time TR=4000 ms, slice thickness=1 mm. Acquisition matrix was 128x64. Before transformation of the acquired data to the image space, zero filling to 128x128 was applied.

Copyright © 2010 SciRes.

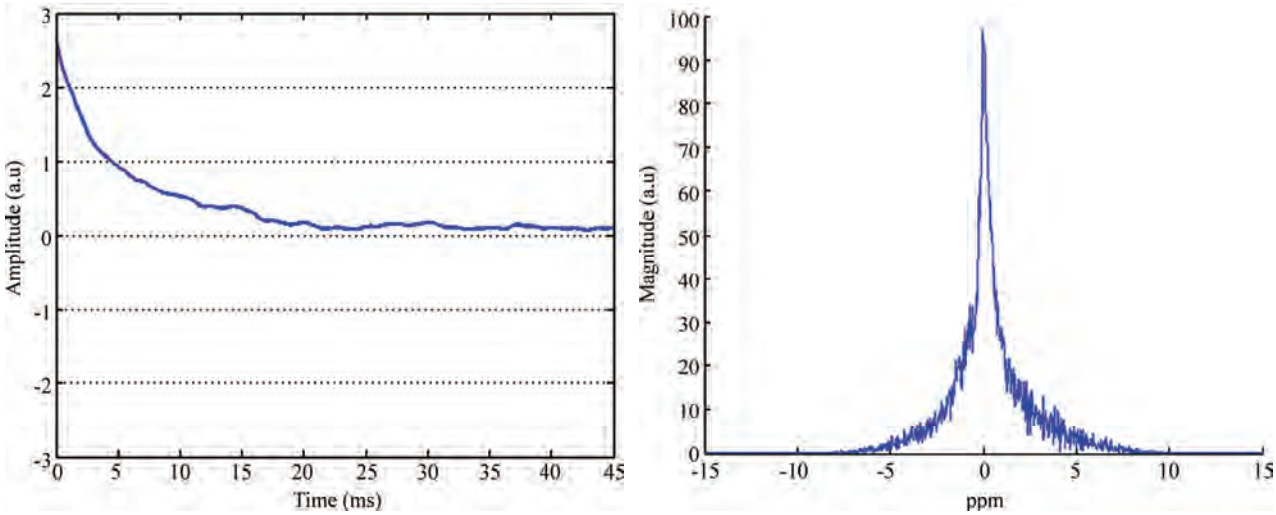

(a) (b)

Figure 15. *In-vivo* sodium (a) NMR signal and (b) its spectrum in the rat brain. A hard non-selective excitation pulse and 512 signal averages were used.

mentation of dedicated three-dimensional (3D) and short echo-time pulse sequences (3D back-projection sequence and 3D GRE for example) [14,25]. The implementation of 3D sequences is out of the scope of our research topics.

Nevertheless, we think that our probe presents no intrinsic limitation for acquiring *in-vivo* sodium images. The only limitation is the available MRI sequence. To demonstrate this without the need to implement new sequences, we tried to acquire sodium image of a phantom containing a sodium concentration as low as those which are generally present in vivo. The sodium transverse relaxation time of the phantom must be longer than its *in-vivo* value to allow the use of a classical spin-echo sequence. So, we used a syringe filled with 20 ml of a physiological serum. The sodium concentration (about 0.1%) in this serum is identical, or at least close, to the *in-vivo* sodium concentrations.

Figure 16 shows transverse, coronal and sagittal images of the phantom at both proton and sodium frequencies. Sodium images were acquired with 64 signal averages.

All these results indicate that the performances of the design presented here are good. We think that these performances would be at least as good as, if not better, at the HP ^{129}Xe frequency. Although, the resonance frequency of sodium and xenon are closed, no significant noise from sodium nuclei will disturb the HP ^{129}Xe signal. Firstly, the excitation plus at 27.7 MHz will not significantly, if never, excite the sodium nuclei. Secondly, the in vivo HP ^{129}Xe signal would be more than nine or ten orders of magnitude greater than an eventual in vivo sodium signal. Moreover, since the quality factor of the receiving coil is relatively high (about 100), its obtained bandwidth is narrow and it will significantly limit the out-of-band noise. In any case, no influence of the sodium nuclei was observed during our HP ^{129}Xe NMR experiment.

We are currently building another prototype that includes shielding of the birdcages to minimize external interferences. Some modifications in the mechanical structure of the probe should be achieved to allow for easy delivering of the hyperpolarized xenon to the rat. The next step of our work is the use of this new probe for *rCBF* in the rat brain. This would be the subject of a future publication. At the same time, a third prototype of the probe is currently being studied for use at a higher magnetic field (4.7 Teslas) for the same application.

Notice finally that the choice of sodium for a first validation of the developed probe is very important, not only because its frequency is close enough to the xenon frequency, but also because of large palette of potential applications of the sodium MRI for both humans and small animals. Actually, MRI is proving to be a very useful tool for sodium quantification in animal models of stroke, ischemia, and cancer in small animals and in humans. For example, ^{23}Na MRI short echo times was used to quantify absolute tissue sodium concentration in patients with brain tumors showing an increase of sodium concentration relative to that in normal brain structures [14,26]. In rabbit models of focal cerebral ischemia, it was shown that there are changes in tissue ^{23}Na signal levels following acute ischemia, which may help to identify necrotic tissue and estimate the duration of the ischemia [27,28]. Recently, the sodium and proton diffusion MRI are shown to be good biomarkers for early therapeutic response in subcutaneous tumors [26]. Recent advances in ultra-high field MRI hardware have

Copyright © 2010 SciRes.

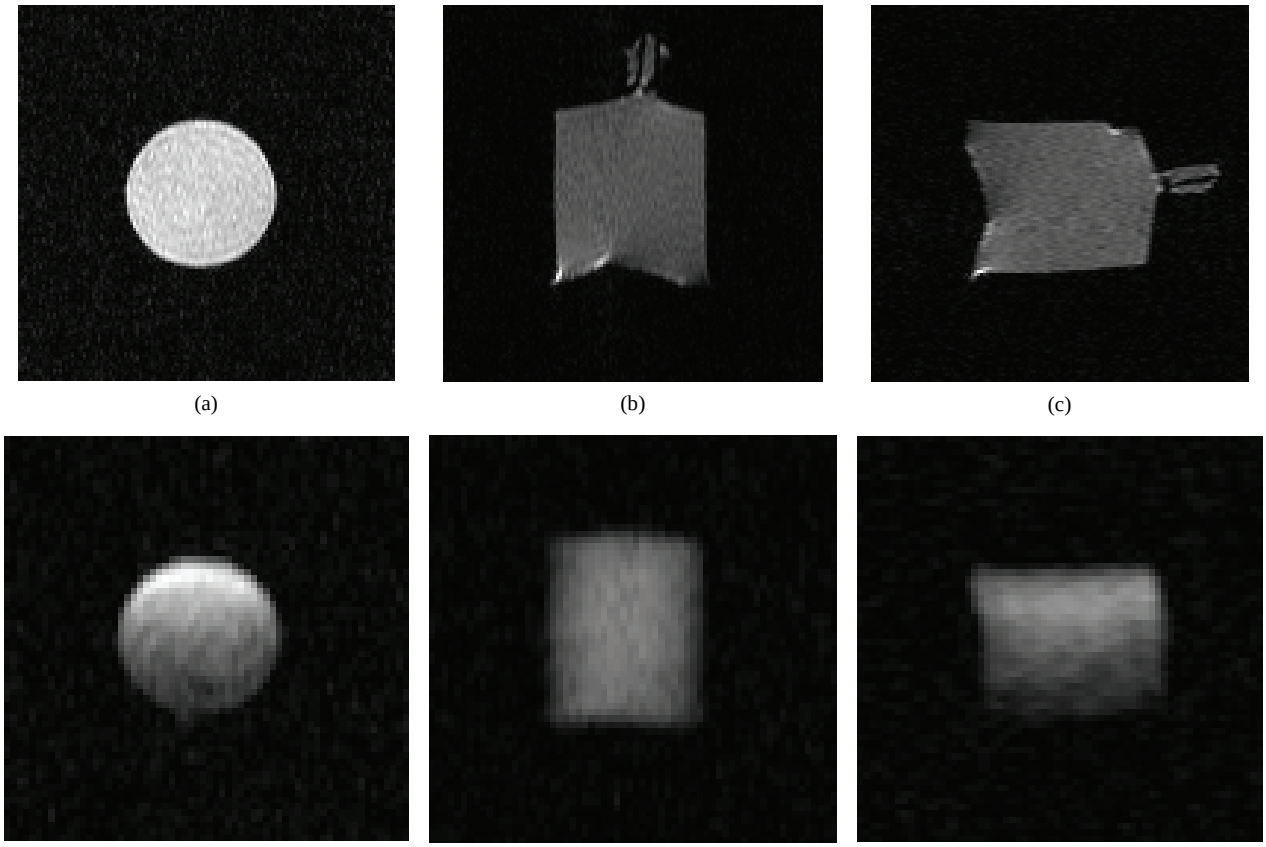

(a) (b) (c)

(d) (e) (f)

Figure 16. Cross-sectional, coronal and sagittal MRI images of the syringe (inner diameter=27 mm) filled with a physiological serum acquired at (a), (b), (c) proton frequency and at (d), (e), (f) sodium frequency. A spin echo pulse sequence was used to acquire images. FOV (Field of View)=70x70 mm^2, flip angle=90°, echo time TE=17 ms, repetition time TR=2000 ms for proton and 500 ms for sodium. Slice thickness for proton images=1 mm. Acquisition matrix was 128x64 for proton and 64x32 for sodium. Before transformation of the acquired data to the image space, zero fillings to 128x128 for proton and to 64x64 for sodium were applied. Sodium images were acquired with 64 signal averages and without slice selection.

allowed the acquisition of ^{23}Na images of the mouse heart [14]. These examples show that in human and animal models, there is a need to obtain interleaved co-registered anatomical (^{1}H) and physiological (^{23}Na) information which may be useful for assessing disease and effective therapeutic intervention. For this purpose, double tuned volume and/or surface coils are required. One of the main advantages of the probe that we presented is the possibility to use it in different configurations according to the application.

Complete schematics of the developed circuits, values and references of all parts, or any other details of design and realization could be obtained by simply writing to the author.

4. CONCLUSIONS

In summary, we have reported the design and testing of a new MRI probe consisting of a double-tuned volume coil actively decoupled from a receive-only coil. This developed probe provides proton and sodium images at 2.35 T. In-vivo and phantom ^{1}H images were acquired with the volume transmit/receive coil. ^{23}Na images of phantoms in both transmit/receive mode and in transmit-only/receive-only mode were acquired. In-vivo NMR signals in the rat brain are also obtained. The results showed acceptable performances of the design. This probe is relatively simple to build and it is low-cost. It should be a suitable tool for the HP ^{129}Xe NMR experiments in the rat brain. In its final version, under construction, it should enhance the quantitative measurements of the *rCBF* and their reliability.

5. ACKNOWLEDGEMENTS

The author wishes to thank Christoph Segebarth, Research Director and Director of the Team 5 of GIN (Grenoble-Institute of Neurosciences) and Jean-Louis Leviel for supporting with enthusiasm the research topic on the HP gases in the laboratory. I thank also Olivier Montigon for his help in the realization of the T/R driver circuitry, Vincent Auboiroux for his participation in the mechanical construction

of the probe. Finally, I am very thankful to Emmanuel Barbier for his support in using his developed MRI sequences and visualization software and for helpful discussions. All these persons are working at the Team 5 of GIN.

REFERENCES

[1] Albert, M.S. *et al.* (1994) Biological magnetic resonance imaging using laser polarized ^{129}Xe. *Nature*, **370,** 199-201.

[2] Kilian, W. *et al.* (2004) Dynamic NMR spectroscopy of hyperpolarized ^{129}Xe in human brain analyzed by an uptake model. *Magnetic Resonance in Medicine (MRM)*, **51,** 843-847.

[3] Venkatesh, A.K. *et al.* (2001) Using dynamic hyperpolarized xenon MR to measure brain perfusion. *Proceeding of the International Society of Magnetic Resonance in Medicine*, **9,** 951.

[4] Swanson, S.D. *et al*. (1997) Brain MRI with laser-polarized ^{129}Xe. *Magnetic Resonance in Medicine (MRM)*, **38,** 695-698.

[5] Duhamel, G. *et al*. (2002) Global and regional cerebral blood flow measurements using NMR of injected hyperpolarized xenon-129. *Acad Radiol*., **9(2),** 498-500.

[6] Asfour, A. *et al*. (2006) Development of a fully digital and low frequency NMR system for polarization measurement of hyperpolarized gases. *Proceedings of the IEEE Instrumentation and Measurement Technology Conference IMTC*, Sorrento, Italy.

[7] Asfour, A. (2008) A new DAQ-based and versatile low-cost NMR spectrometer working at very-low magnetic field (4.5 mT): A palette of potential applications. *Proceedings of the IEEE International Instrumentation and Measurement Technology Conference I^{2}MTC*, Vancouver, Canada.

[8] Ackerman, *et al*. (1980) Mapping of metabolites in whole animals by ^{31}P NMR using surface coils. *Nature*, **283,** 167-170.

[9] Hayes, C.E. *et al.* (1985) An efficient, highly homogenous radiofrequency coil for whole-body NMR imaging at 1.5 T. *Journal of Magnetic Resonance*, **63,** 622-628.

[10] Fitzsimmons, J.R. *et al*. (1993) Double Resonant quadrature birdcage. *Magnetic Resonance in Medicine (MRM)*, **30,** 107-114.

[11] Rath, A.R. (1990) Design and performance of a double-tuned birdcage coil. *Journal of Magnetic Resonance*, **86,** 488-495.

[12] Shen, G.X. *et al*. (1997) Dual-frequency, dual-quadrature, birdcage RF coil design with identical B_1 pattern for sodium and proton imaging of the human brain at 1.5 T. *Magnetic Resonance in Medicine*, **38,** 717-725.

[13] Lanz, T. *et al*. (2001) Double tuned ^{23}Na ^{1}H nuclear magnetic resonance birdcage for application on mice in vivo. *Review of Scientific Instruments*, **72(5),** 2508-2510.

[14] Alecci, M. *et al*. (2006) Practical design of a 4 Tesla double-tuned RF surface coil for interleaved ^{1}H and ^{23}Na MRI of the rat brain. *Journal of Magnetic Resonance*, **181,** 203-211.

[15] Leach, M.O. *et al.* (1986) The design and use of a dual-frequency surface coil providing proton images for improved localization in ^{31}P spectroscopy of small lesions. *Med Phys*, **13,** 510-513.

[16] Volotovskyy, V. *et al.* (2002) Doubly tunable double ring surface coil. *Concepts in Magnetic Resonance*, **B(17B),** 11-16.

[17] Mispelter, J., Lupu, M. and Briguet, A. (2006) *NMR Probeheads for Biophysical and Biomedical Experiments: Theoretical Principles and Practical Guidelines*, Imperial College Press.

[18] Chin, C.L. *et al.* (2002) BirdcageBuilder: Design of specified-geometry birdcage coils with desired current pattern and resonance frequency. *Concepts in Magnetic Resonance*, **15(2),** 156-163.

[19] *The ARRL Handbook for Radio Amateurs*, Published by the American Radio Relay League, 1996.

[20] Streif, J.U.G. *et al*. (2003) A coil combination for magnetic resonance perfusion imaging of mice in vivo at 7 T. *Review of Scientific Instruments*, **74(5),** 2843-2848.

[21] Barberi, E.A. *et al.* (2000) A transmit-only/receive-only (TORO) RF system for high-field MRI/MRS applications. *Magnetic Resonance in Medicine (MRM)*, **43,** 284-289.

[22] Décorps, M. *et al*. (1985) An inductively coupled, series tuned NMR probe. *Journal of Magnetic Resonance*, **65,** 100-109.

[23] Hoult, D.I. and Lauterburg, P.C. (1979) The sensitivity of the zeugmatographic experiment involving human samples. *Journal of Magnetic Resonance*, **34,** 425-433.

[24] Naritomi, H. *et al*. (1987) In vivo measurements of the intra- and extra-cellular $^{+}$Na and water in the brain and muscle by nuclear magnetic resonance spectroscopy with shift reagent. *BIOPHYS Journal, Biophysical Society*, **52,** 611-616.

[25] Schepkin, V.D. *et al*. (2006) Sodium and proton diffusion MRI as biomarkers for early therapeutic response in subcutaneous tumors. *Magnetic Resonance Imaging*, **24,** 273-278.

[26] Ouwerkerk, R. *et al*. (2003) Tissue sodium concentration in human brain tumors as measured with ^{23}Na MR imaging. *Radiology*, **227,** 529-537.

[27] Bartha, R. *et al*. (2004) Sodium T2*-weighted MR imaging of acute focal cerebral ischemia in rabbits. *Magnetic Resonance Imaging*, **22,** 983-991.

[28] Wang, Y. *et al*. (2000) Brain tissue sodium is a ticking clock telling time after arterial occlusion in rat focal cerebral ischemia. *Stroke*, **31,** 1386-1391.

Copyright © 2010 SciRes.

J. Biomedical Science and Engineering, 2010, 3, 181-186 **JBiSE**
doi:10.4236/jbise.2010.32023 Published Online February 2010 (http://www.SciRP.org/journal/jbise/).

Imaging characteristics of metallic interbody spacers: in vitro score evaluation of susceptibility artifacts considering different MRI sequences

T. Ernstberger[1,2], G. Heidrich[3], G. Buchhorn[4]

[1]Clinic for Spinal Surgery, Klinikum Bad Bramstedt, Bad Bramstedt, Germany;
[2]Department of Orthopedic Surgery, University of Goettingen, Goettingen, Germany;
[3]Department of Diagnostic Radiology, University of Goettingen, Goettingen, Germany;
[4]Biomaterials Laboratory/Department of Orthopedic Surgery, University of Goettingenm, Goettingen, Germany.
Email: ernstberger@klinikumbb.de, ternstberger@med.uni-goettingen.de

Received 2 December 2009; revised 10 December 2009; accepted 14 December 2009.

ABSTRACT

Aim: Intervertebral spacers for anterior spine fusion are made of different materials, such as titanium, carbon or cobalt-chrome, which can affect the post-fusion MRI scans. Implant-related susceptibility artifacts can decrease the quality of MRI scans, thwarting proper evaluation. This cadaver study aimed to demonstrate the extent that implant-related MRI artifacting affects the post-fusion evaluation of intervertebral spacers. Methods: In a cadaveric porcine spine, we evaluated the post-implantation MRI scans of 2 metallic intervertebral spacers (TiAL6V4, CoCrMo) that differed in shape, material, surface qualities and implantation technique. A spacer made of human cortical bone was used as a control. The median sagittal MRI slice was divided into 12 regions of interest (ROI). Results: No significant differences were found on 15 different MRI sequences read independently by an interobserver-validated team of specialists (*P*>0.05). Artifact-affected image quality was rated on a score of 0-1-2. A maximum score of 24 points (100%) was possible. Turbo spin echo sequences produced the best scores for all spacers and the control. Only the control achieved a score of 100%. The titanium and cobalt-chrome spacers scored 62.5% and 50%, respectively. Conclusions: Our scoring system allowed us to create an implant-related ranking of MRI scan quality in reference to the control that was independent of artifact dimensions. Even with turbo spin echo sequences, the susceptibility artifacts produced by the metallic spacers showed a high degree of variability. Despite optimum sequencing, implant design and material are relevant factors in MRI artifacting.

Keywords: Intervertebral Spacers; Metallic Implant Materials; MRI; Susceptibility Artifacts

1. INTRODUCTION

In the preoperative diagnostics of spinal diseases, magnetic resonance imaging (MRI) is used as a standard procedure that can visualize disc pathologies and neurological changes of the spinal canal with high precision. When anterior spine fusion proves indicated, implantation of intervertebral spacers often represents the treatment of choice. The selection of implant design, implant material and implantation technique is dictated by the diagnostic findings. Intervertebral spacers made of various materials can be used as stand-alone cages for exclusively anterior fusion or in combination with dorsal instrumentation for dorsoventral fusion.

When postoperative complications arise secondary to vertebra fusion, MRI scans are frequently necessary to evaluate implant position and demonstrate any clinically relevant abnormalities and to direct further surgical decision-making [1]. Depending on the material, however, implant-related susceptibility artifacts can decrease the quality of MRI scans, thereby thwarting proper evaluation. Depending on the problem to be clarified, consideration must be given to whether the MRI sequence selected will ensure the most artifact-free visualization and enable proper evaluation of implant positioning and/or pathological processes like tumorous growth or infection.

Recent studies have shown that artifacting, particularly caused by metallic implants, can also be minimized through modification of routine MRI sequences [2,3,4]. This cadaveric porcine study was conducted to determine the extent to which implant-related MRI artifacting affects the evaluation of intervertebral spacers. A scoring system (0-1-2) was developed to rank the artifacting produced by different intervertebral spacer designs compared with a human cortical bone control. Scans taken with 15 different MRI sequences were read independently by an interobserver-validated team of specialists who ranked image

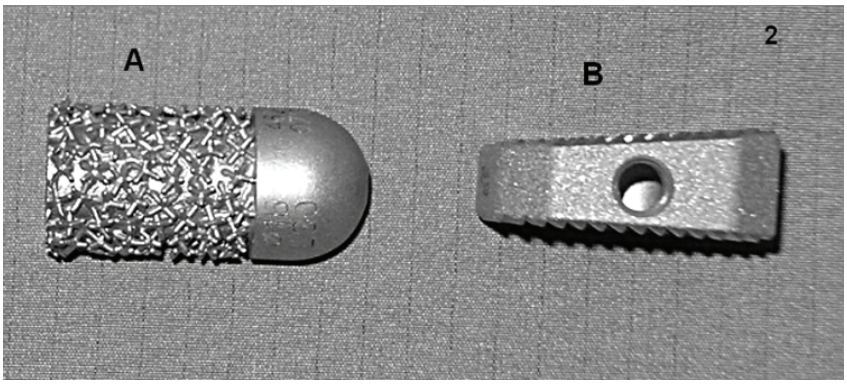

Figure 1. Intervertebrals disc spacers.

Figure 2. Human cortical bone.

quality of the implant, paying special attention to neighboring structures. The scores are presented in tables and possible implant-related factors discussed.

2. MATERIAL AND METHODS

In this study, we performed MRI on 2 implanted metallic intervertebral spacers (TiAl6V4, CoCrMo) (**Figures 1(A)** and **1(B)**) that differed in shape, material, surface qualities and implantation technique. The spinal column of a domestic pig killed for commercial human consumption purchased from a slaughterhouse served as our experimental cadaveric model. The 2 spacers were implanted in the distal third of the thoracic spine and in the entire lumbar spine. Additionally, a piece of human cortical bone was implanted as a control (**Figure 2**).

2.1. Spacers and Control

The Intervertebral Body Spacer (IBS), manufactured by Peter Brehm GmbH, Chirurgie Mechanik, Weisendorf, Germany, is made of a titanium aluminum vanadium alloy. This square implant has an evenly ribbed structure on its upper and lower faces and an edge length of 25x25 mm. The implant used in this study had a maximum height of 10 mm in the anterior segment with a dorsal inclination of 7 degrees.

The cylindrically shaped intervertebral disc dowel (IDD), manufactured by ESKA Implants GmbH & Co., Luebeck, Germany, is made of a cobalt chrome molybdenum alloy and its surface has a three-dimensional tripodal webbed structure. The size of the IDD used in this study measured 35 mm in length and 15 mm in diameter. The German trade name of this implant is Bandscheibendübel™.

2.2. Implantation

Like in the human spine, the size of the vertebrae in the porcine spine increases in the craniocaudal direction, with the lower lumbar vertebrae extending to the maximum dimensions of 25 mm in height, 25 in width and 20 mm in depth. The dimensions of the 3 study spacers and the control were selected to be oversized compared to the intervertebral disc space. The two devices were implanted as stand-alone cages. We refrained from the use of dorsally implanted pedicle screws so as to avoid any potential summation effects on artifact scoring caused by additional materials.

A purely spinal model was chosen instead of a whole pig cadaver, since the size of the clinical field of view routinely focuses on the spine and cuts out any thoracic or abdominal organ structures. During dissection, the paravertebral muscles including the surrounding skin and the psoas muscles of the spine were retained. Special care was taken to ensure that the neurological structures of the spinal canal remained intact.

To determine the distance at which the spacers should be placed and to avoid artifact overlapping of spacers implanted in a single spine, we conducted a preliminary trial that involved embedding the cobalt-chrome IDD–the spacer with the highest magnetization–in a homogenous tissue mass and then performing MR imaging of the tissue-embedded spacer. The measurements showed that a width of 6.5 cm had to be maintained between spacers to avoid the artifact overlapping.

Accordingly, the lumbar and thoracic disc spaces were dissected to achieve a median positioning of the implants. The paravertebral muscles were left intact along with the

Copyright © 2010 SciRes.

skin and psoas muscles. Intervertebral discectomy was performed, and the three spacers and the control were implanted intervertebrally apart at a distance of 6.5 cm. Maximum implantation depth was reached when the implant was aligned with the anterior vertebra face. After implantation was completed, additional tissue mass was padded around the spine to optimize contrast and image quality.

3. MAGNETIC RESONANCE IMAGING

MRI was performed with a 1.5T MRI (Magnetom Symphony, Siemens AG Medical Solutions, Erlangen, Germany). **Table 1** presents the MRI data. The median sagittal MRI slice encompassing all relevant structures, implants and control was evaluated according to an interobserver-validated scoring system.

3.1. Scoring System

A 0-1-2 scoring system was established to rank the MRI scans. An evaluation unit was defined as 2 adjacent vertebrae encompassing the intervertebral disc space. 12 regions of interest (ROI) were demarcated (**Figure 3**). Every ROI could achieve a maximum score of 2 points. A total score of 24 points was equivalent to a score of 100%. Two board-certified specialists (one radiologist (GH) and one spinal surgeon (TE)) experienced in reading spinal MRI evaluated the scans independently of each other. The evaluators scored regions as 0=not distinguishable, 1=partly distinguishable and 2=completely distinguishable. The interobserver validation of the scoring system across all 15 sequences was tested for statistical significance using a *t* test with a significance level of $P>0.05$ (**Table 2**).

4. RESULTS

Table 3 presents the total points scored for each implant in each of the 15 sequences. **Figures 4 I**, **II**, **III** and **IV** depict the artifact range in a selection of 4 MRI sequences.

Table 1. MRI sequence data.

Sequences	FA	TR	TE	ST	BW	FOV	Number of slices	Matrix
T1 FLASH 2D	70	181	4.8	5.5	260	500	19	256 x 256
T1 FLASH 2D FS	70	275	4.76	5.5	260	500	19	256 x 256
T2 MEDIC 2D FS	40	2660	27	3.0	70	500	40	256 x 256
T1 FLASH 3D	60	60	11	3.0	70	500	40	256 x 256
T2 DESS 3D	25	23.68	6.63	1.5	130	500	64	256 x 256
TOF FISP 3D	25	36	4.59	3.0	130	500	32	384 x 384
T2 CISS 3D	70	10.16	5.08	3.0	130	500	64	256 x 256
T1 TSE	150	2260	14	3.0	150	500	40	512 x 512
T1 TSE var	150	600	14	3.0	150	500	40	512 x 512
T1 SE	90	1270	14	3.0	90	500	40	512 x 512
T1 SE var	90	600	14	3.0	90	500	40	512 x 512
T1 SE FS var	90	684	14	3.0	90	500	40	512 x 512
T2 TSE/PD	150	6110	14	3.0	130	500	40	256 x 256
T2 TSE/PD FS	150	6760	14	3.0	130	500	40	256 x 256
STIR	180	10000	38	3.0	130	500	40	256 x 256

Key: FLASH=Fast Low Angle Shot, MEDIC=Multi Echo Data Image Combination, DESS=Dual Echo Steady State, FS=Fat Saturated, FISP=Fast Imaging with Steady Precession, CISS=Constructive Interference in Steady State, SE=Spin Echo, TSE=Turbo Spin Echo, PD=Proton density, STIR=Short Tau Inversion Recovery, TOF=Time of Flight, TR=Time of Repetition, TE=Time of Echo, FA=Flip Angle, ST=Slab Thickness, BW=Band Width, FOV=Field of View, var=varied.

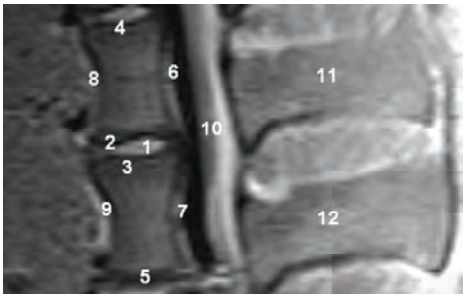

Figure 3. MRI evaluation unit with ROI.

Table 2. Interobserver validation across all 15 sequences.

	Mean score value		Standard deviation		P value
	Spinal surgeon	Radiologist	Spinal surgeon	Radiologist	
IBS	12.87	12.8	±1.25	±1.32	P = 0.58
IDD	8.33	8.33	±3.02	±2.85	P = 1.0
Control	20.13	20.4	±2.67	±2.79	P = 0.1

Copyright © 2010 SciRes.

Table 3. Total scores.

MRI Sequence	IBS		IDD		Control	
	1	**2**	**1**	**2**	**1**	**2**
T1 FLASH 2D **TR:**181 **TE:**4	13	13	9	8	18	18
T1 FLASH 2D FS **TR:**275 **TE:**4	13	13	10	10	19	19
T2 MEDIC 2D FS **TR:**2660 **TE:**27	11	11	4	4	18	18
T1 FLASH 3D FS **TR:**60 **TE:**11	10	10	5	6	15	15
T2 DESS 3D **TR:**23 **TE:**6	13	12	6	6	21	21
T2 CISS 3D **TR:**10 **TE:**5	13	12	7	7	22	23
T1 SE **TR:**1270 **TE:**14	13	14	12	12	22	23
T1 TSE TR:2260 TE:14	***15***	***15***	***12***	***12***	***24***	***24***
T1 TSE TR:600 TE:14	***15***	***15***	***12***	***12***	***24***	***24***
T1 SE **TR:**600 **TE:**14	13	13	12	12	23	23
T1 SE FS **TR:**684 **TE:**14	13	13	8	7	22	23
PD+ T2 TSE **TR:**6110 **TE:**14	13	13	8	8	19	20
PD+ T2 TSE FS **TR:**6760 **TE:**14	13	13	7	7	17	18
STIR **TR:**10000 **TE:**38	13	13	10	10	19	19
TOF FISP 3D **TR:**36 **TE:**4	12	12	3	4	19	18

Key: 1) spinal surgeon; 2) radiologist.

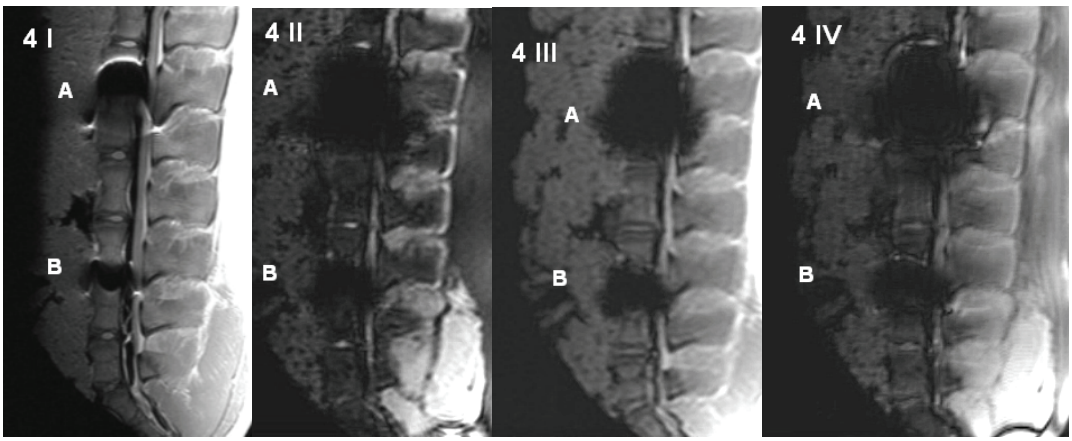

Figure 4. I-IV: Artifact range of the different MRI sequences [I: T1 TSE (TR: 2260, TE: 14); II: T2 DESS 3D (TR: 23, TE: 6); III: T1 FLASH 2D (TR: 181, TE: 4); IV: TOF FISP 3D (TR: 36, TE: 4)].

The results showed that the T1-TSE sequences produced the best imaging scores for all implants. In these sequences, the human cortical bone control achieved the maximum possible score of 100%, i.e. was completely distinguishable (**Figure 5**, **Table 3**). Therefore, we used these two sequences as a basis for following comparison

Copyright © 2010 SciRes.

of the imaging quality of the study implants.

4.1. IBS

In the T1-TSE sequences, the titanium IBS implant achieved an imaging score of 62.5% compared to the control (**Figure 4(IA)**, **Table 3**). The susceptibility artifact border was clearly distinguishable from its surroundings. As a result of artifact extension, the implant-bone contact area was not distinguishable. The image quality was not sufficient to determine exact implant position.

4.2. IDD

In the T1-TSE sequences, the IDD implant achieved an imaging score of 50 % compared to the control (**Figure 4 (IB)**, **Table 3**). As a result of artifacting, the implant-bone contact area was not distinguishable. The distant vertebral end plates were completely distinguishable; the anterior edge of the lower vertebra and the spinous process were partly distinguishable. As with the titanium IBS implant, the image quality was not sufficient to determine exact implant position in relation to the spinal canal.

4.3. Interobserver Validation

The results of the interobserver validation are listed in **Table 3**. There was no statistical significance between the evaluators with respect to t-test correlations ($P>0.05$).

5. DISCUSSIONS

The disadvantages associated with bone grafting alone has led to the development of intervertebral spacers to enhance anterior spinal fusion [5,6,7]. The use of intervertebral spacers of different designs and materials has thus become increasingly widespread in clinical routine because they offering immediate load transmission with direct primary stability. Post-fusion MRI scans are used for further diagnostics to demonstrate any progressive degenerative changes, infections, fractures and/or tumors. However, implant-related susceptibility artifacts can negatively impact the complex post-fusion evaluation of MRI scans. Depending on the spacer material, a local magnetic field gradient of varying susceptibility results in the area between structures. In these border areas, the respective spins gyrate with different frequencies and cause image distortions and susceptibility artifacts [8,9,10].

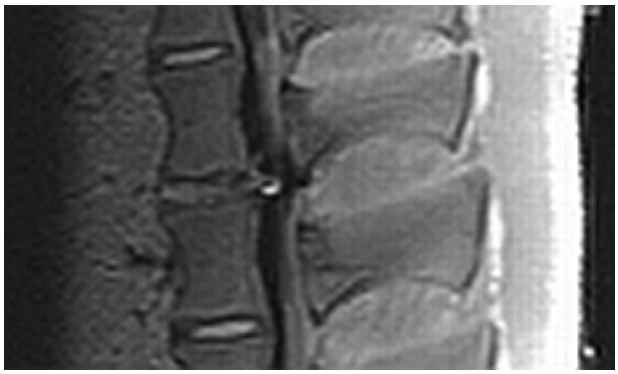

Figure 5. MRI slice human cortical bone (T1 TSE TR:2260 TE:14).

Our image quality scoring system gave special consideration to the following material-related implant characteristics:

1) Distinguishability of implant shape and position;

2) Distinguishability of implant from anatomically neighboring structures;

3) The extent of image distortions and susceptibility artifacts.

Optimum MRI visualization of the different intervertebral spacers depends on the aim of diagnosis. MRI diagnostics are insofar subject to different requirements depending on the various postoperative pathologies in relation to the implant situation. Optimum MRI image distinguishability of the intervertebral spacers and the equivalent control was achieved using T1 TSE sequences. The imaging quality of the human cortical bone used as a control scored 100% according to the study scoring system and was therefore used as a basis to rank the intervertebral spacers examined. The scores were stated as a percentage compared to the control. Our interobserver-validated scoring system allowed us to create a unique implant-related ranking of MRI scan quality in reference to a control that was independent of artifact dimensions.

The MRI imaging behavior of metallic spinal implants is well documented in the literature [9,10,11,12,13,14,15]. However, the aims of the published studies differed in that most focused on determining sequence-related artifact size.

According to our study results the implant position in relation to the spinal canal_was best visualized using T1 TSE sequences. In studies by Rudisch *et al.* [16] and Thomsen *et al.* [17], titanium materials showed a lower artifact range than cobalt chrome**.** Consistent with our results, the best MRI quality was achieved for both metallic spacers with T1 TSE sequences. The other MRI sequences produced no further advantages.

Studies on metallic artifacts in MRI of the anterior spine have been conducted by Vaccaro *et al.* [15] and Wang *et al.* [18]. In one cadaveric study, Vaccaro *et al.* [15] examined the MRI artifact rates of different metal particles introduced in predefined intervertebral drill holes and subsequently embedded in paraffin. Vacarro could not demonstrate any significant artifacts in T1- or T2 SE sequences, probably due to the fact that the particle density was lower than that produced by metal implants commonly used in clinical practice. The metallic artifacts appearing in the gradient echo sequences proved a connection between artifact size and nickel content of the alloys examined. An increasing nickel content reduced susceptibility artifacting.

Copyright © 2010 SciRes.

In another cadaveric artifact study, Wang *et al.* [18] described the MRI behavior of an intervertebral spacer made of titanium. Using T1 SE sequences, the implant-related artifact rate of the titanium spacer was primarily limited to the implant's direct surroundings and anatomic neighboring structures were clearly distinguishability. In our study, when T1 TSE sequences were used to image both metallic spacers, neither implant shape nor implant position could be distinguished with certainty. In a phantom study by Rudisch *et al.* [16], the relevance of metallic artifacts and implant-related characteristics, such as implant material, shape and position, was demonstrated in addition to an impact by the selected MRI sequence. In spite of the use of optimum MRI sequences, variability in the amount of susceptibility artifacts must be accounted for when evaluating MRI scans of metallic spine implants.

6. CONCLUSIONS

The designs and materials of the intervertebral spacers currently used in anterior spine fusion cause susceptibility artifacts that can be rated by validated scoring systems. Of 15 sequences tested, T1 TSE sequences produced the best spacer imaging for both metallic implants tested. An interobserver-validated scoring system proved effective in ranking the relevance of spacer material on MRI imaging quality. Studies are ongoing to further develop MRI scoring systems and establish optimum imaging sequences for post-fusion diagnostics.

REFERENCES

[1] Van Goethem, J.W., Parizel, P.M. and Jinkins, J.R. (2002) Review article: MRI of the postoperative lumbar spine. *Neuroradiology*, **44,** 723-39.

[2] Herold, T., Caro, W.C., Heers, G., Perlick, L., Grifka, J., Feuerbach, S., Nitz, W. and Lenhart, M. (2004) Influence of sequence type on the extent of the susceptibility artifact in MRI: A shoulder specimen study after suture anchor repair. *Rofo*, **176,** 1296-301.

[3] Schenck, J.F. (1996) The role of magnetic susceptibility in magnetic resonance imaging: MRI magnetic compatibility of the first and second kinds. *Med Phys*, **23,** 815-50.

[4] Malik, A.S., Boyko, O., Atkar, N. and Young, W.F. (2001) A comparative study of MR imaging profile of titanium pedicle screws. *Acta Radiol*, **42,** 291-3.

[5] Goulet, J.A., Senunas, L.E., DeSilva, G.L. and Greenfield, M.L. (1997) Autogenous iliac crest bone graft: Complications and functional assessment. *Clin Orthop*, **339,** 76-81.

[6] Summers, B.N. and Eisenstein, S.M. (1989) Donor site pain from the ilium: A complication of lumbar spine fusion. *J Bone Joint Surg Br*, **71,** 677-80.

[7] Brantigan, J.W. and Steffee, A.D. (1993) A carbon fiber implant to aid interbody lumbar fusion: Two-year clinical results in the first 26 patients. *Spine*, **18,** 2106-7.

[8] Fellner, C., Behr, M., Fellner, F., Held, P., Handel, G. and Feuerbach, S. (1997) Artifacts in MR imaging of the temporomandibular joint caused by dental alloys: A phantom model study at T1.5. *Rofo*, **166,** 421-8.

[9] Fritzsche, S., Thull, R. and Haase, A. (1994) Reduction of artifacts in magnetic resonance images by using optimized materials for diagnostic devices and implants. *Biomed Tech (Berl)*, **39,** 42-6.

[10] Henk, C.B., Brodner, W., Grampp, S., Breitenseher, M., Thurnher, M., Mostbeck, G.H. and Imhof, H. (1999) The postoperative spine. *Top Magn Reson Imaging*, **10,** 247-64.

[11] Rupp, R., Ebraheim, N.A., Savolaine, E.R. and Jackson, W.T. (1993) Magnetic resonance imaging evaluation of the spine with metal implants: General safety and superior imaging with titanium. *Spine*, **18,** 379-85.

[12] Ortiz, O., Pait, T.G., McAllister, P. and Sauter, K. (1996) Postoperative magnetic resonance imaging with titanium implants of the thoracic and lumbar spine. *Neurosurgery*, **38,** 741-5.

[13] Petersilge, C.A., Lewin, J.S., Duerk, J.L., Yoo, J.U. and Ghaneyem, A.J. (1996) Optimizing imaging parameters for MR evaluation of the spine with titanium pedicle screws. *AJR Am J Roentenol*, **166,** 1213-8.

[14] Wang, J.C., Sandhu, H.S., Yu, W.D., Minchew, J.T. and Delamarter, R.B. (1997) MR parameters for imaging titanium spinal instrumentation. *J Spinal Disord*, **10,** 27-32.

[15] Vaccaro, A.R., Chesnut, R.M., Scuderi, G., Healy, J.F., Massie, J.B. and Garfin, S.R. (1994) Metallic spinal artifacts in magnetic resonance imaging. *Spine*, **19,** 1237-42.

[16] Rudisch, A., Kremser, C., Peer, S., Kathrein, A., Judmaier, W. and Daniaux, H. (1998) Metallic artifacts in magnetic resonance imaging of patients with spinal fusion: A comparison of implant materials and implant sequences. *Spine*, **23,** 692-9.

[17] Thomsen, M., Schneider, U., Breusch, S.J., Hansmann, J. and Freund, M. (2001) Artifacts and ferromagnetism dependent on different metal alloys in magnetic resonance imaging: An experimental study. *Orthopade*, **30,** 540-4.

[18] Wang, J.C., Yu, W.D., Sandhu, H.S., Tam, V. and Delamarter, R.B. (1998) A comparison of magnetic resonance and computed tomographic image quality after the implantation of tantalum and titanium spinal instrumentation. *Spine*, **23,** 1684-8.

Copyright © 2010 SciRes.

J. Biomedical Science and Engineering, 2010, 3, 187-192 **JBiSE**
doi:10.4236/jbise.2010.32024 Published Online February 2010 (http://www.SciRP.org/journal/jbise/).

Iterative spectral subtraction method for millimeter-wave conducted speech enhancement

Sheng Li[1,2], Jian-Qi Wang[1*], Ming Niu[1], Xi-Jing Jing[1], Tian Liu[1]

[1]Department of Biomedical Engineering, the Fourth Military Medical University, Xi'an, China;
[2]The Key Laboratory of Biomedical Information Engineering of Ministry of Education, and Department of Biomedical Engineering, School of Life Science and Technology, Xi'an Jiaotong University, Xi'an, China.
Email: *sheng@mail.xjtu.edu.cn

Received 4 November 2008; revised 4 December 2009; accepted 7 December 2009.

ABSTRACT

A non-air conducted speech detecting method has been developed in our laboratory by using millimeter wave radar technology. Because of the special attributes of the millimeter wave, this method may considerably extend the capabilities of traditional speech detecting methods. However, radar speech is substantially degraded by additive combined noises that include radar harmonic noise, electrocircuit noise, and ambient noise. This study, therefore, proposed an iterative spectral subtraction method which can be adaptively estimate noise spectrum at every iteration, and reduce the musical noise remained in the previous spectral subtraction process. Results from simulations as well as evaluations confirm that the proposed method satisfactorily reduces whole-frequency and musical noises and produces good speech quality.

Keywords: Millimeter Wave; Speech Detecting; Speech Enhancement

1. INTRODUCTION

The speech, which is produced by speech organ of human beings [1,2], is well known that it can be spread and perception by means of air, and can be detected and recorded by acoustic sensors. However, air is not the only medium which can spread and be used to detect speech. For example, voice content can be transmitted by way of bone vibrations. This vibration, therefore, can be picked up using the bone-conduction sensors at special location [3]. Other medium, such as infrared ray, ultrasound wave, laser light also can be used to detecting the non-air spread speech or noise for some special applications [4].

Li Zong Wen (1996) [4] reported another medium, millimeter wave (MMW) radar, as well as light radar and laser radar, can detect and identify out exactly the existential speech signals in free space from a person speaking through the electromagnetic wave fields by principle and experiment. Since the microwave radar has low range attenuation, and has attribute of noninvasive, safe, fast, portable, low cost fashion [5], it may extend traditional speech detecting method to a large extent, and provide some exciting possibility of wide applications: the speech and acoustic signal directional detection in complex and rumbustious acoustic environment, due to its better sense of direction; the tiny acoustic or vibrant signal detection which cannot be detected by traditional microphone; the microwave radar also can be used in the clinic to assist diagnosis or to measure speech articulator motions [6].

However, there has been little previous research work concentrated on the research of speech which is produced by MMW radar, some studies with respect to the MMW radar speech concentrated on the MMW non acoustic sensors [5,7], in order to measure speech articulator motions, such as vocal tract measurements and glottal excitation [5].

Although MMW radar provides another method to detect speech, the MMW radar speech itself has several serious shortcomings including artificial quality, reduced intelligibility, and poor audibility. This is not only because some harmonic of the EMW and electrocircuit noise are combined in the detected speech due to the different detecting methods from traditional air conduct speech, but also the channel noise, as well as ambient noise combined in the MMW radar speech. These combined noise components are quite larger and more complex than traditional air conduct speech, and are the biggest problem which must be resolved for the application of the MMW radar speech. Therefore, speech enhancement is a challenging topic of MMW radar speech research.

The spectral subtraction method is the most widely used, and has been shown to be an effective approach for noise canceling, in order to improve the intelligibility and quality of digitally compressed speech. Due to the

simplicity of implementation, and low computational load, the spectral subtraction method is the primary choice for real time applications [8]. In general, this method enhanced the speech spectrum by subtracting an average noise spectrum from the noisy speech spectrum, here the noise is assumed to be uncorrelated and additive to the speech signal. The phase of the noisy speech is kept unchanged, since it is assumed that the phase distortion is not perceived by human ear.

However, the serious draw back of this method is that the enhanced speech is accompanied by unpleasant musical noise artifact which is characterized by tones with random frequencies. Although many solutions have been proposed to reduce the musical noise in the subtractive-type algorithms [9,10,11,12,13], results performed with these algorithms show that there is a need for further improvement. Furthermore, in order to prevent destructive subtraction of the speech while removing most of the residual noise, it is necessary to propose a new approach to improve the subtraction procedure.

Therefore, the purpose of this investigation is motivated by the need of improving EMW radar speech, especially in the electronic environments. An iterative spectral subtraction algorithm is proposed to adaptively estimate noise spectrum at every iteration, and reduce the musical noise remained in the previous spectral subtraction process. The results suggest that for the proper iteration number, the proposed iteration number can significantly remove the musical noise, and improve the speech quality.

2. METHODS

2.1. The Description of the System

The schematic diagram of the speech-detection system is shown in **Figure 1**. A phase-licked oscillator generates a very stable MMW at 34 GHz with an output power of 50 mW. The output of the amplifier is fed through a 6 dB directional coupler, a variable attenuator, a circulator, and then to a flat antenna. The 6 dB directional coupler branches out 1/4 of the amplifier output to provide a reference signal for the mixer. The variable attenuator controls the power level of the microwave signal to be radiated by the antenna. The radiated power of the antenna is usually kept at a level of about 10–20 mW. The flat antenna radiates a microwave beam of about 9º beam width aimed at the opposing human subjects standing or sitting directly in front of the antenna. The echo signal is received by the same antenna, which is a 34G Hz MMW signal modulated by the speech which is produced by the larynx of the opposing human subjects. This signal is then mixed with reference signal in a double-balanced mixer. The mixing of the amplified speech signal and a reference signal in the double-balanced mixer produces low-frequency signals and is amplified by a signal processor and then passed through a A/D converter before reaching computer to get further processor. For More details of description of the system, the reader is referred to [14] and [15].

2.2. Iterative Spectral Subtraction Method

The iterative spectral subtraction algorithm is based on the assumption that the additive noise will be stationary and uncorrelated with the clean speech signal. If $y(n)$, the noisy speech, is composed of the clean speech signal $s(n)$ and the uncorrelated additive noise signal $d(n)$, then:

$$y(n) = s(n) + d(n) \tag{1}$$

The power spectrum of the corrupted speech can be approximately estimated as:

$$|Y(\omega)|^2 \approx |S(\omega)|^2 + |D(\omega)|^2 \tag{2}$$

where $|Y(\omega)|^2$, $|S(\omega)|^2$ and $|D(\omega)|^2$ represent the noisy speech short-time spectrum, the clean speech short-time spectrum, and the noise power spectrum estimate, respectively.

Most of the subtractive-type algorithms have different variations allowing for flexibility in the variation of the spectral subtraction. Berouti *et al*. (1979) [16] proposed the generalized spectral subtraction scheme is described as follows:

$$|\hat{S}(\omega)|^\gamma = \begin{cases} |Y(\omega)|^\gamma - \alpha|\hat{D}(\omega)|^\gamma, \text{ if } & \dfrac{|\hat{D}(\omega)|^\gamma}{|Y(\omega)|^\gamma} < \dfrac{1}{\alpha+\beta} \\ \beta|\hat{D}(\omega)|^\gamma, \quad \text{otherwise} & \end{cases} \tag{3}$$

where $\alpha(\alpha > 1)$ is the over-subtraction factor [16], which is a function of the segmental SNR. $\beta(0 \le \beta \le 1)$ is the spectral floor, and γ is the exponent determining the transition sharpness. Here we set $\gamma = 2$ and $\beta =$ 0.002.

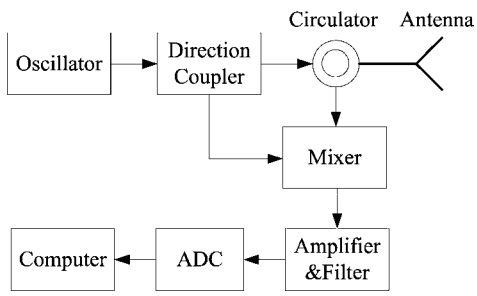

Figure 1. Schematic diagram of the speech-detection system.

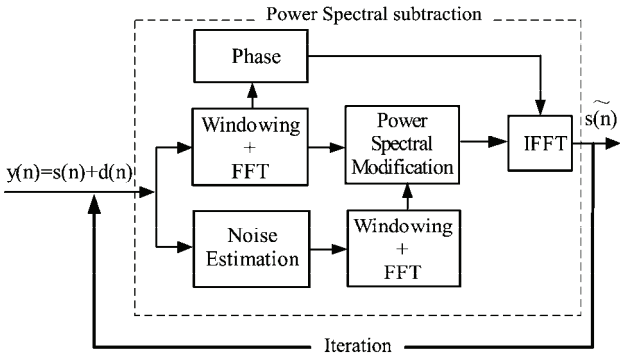

Figure 2. The proposed speech enhancement scheme.

In order to decrease the musical noise, which is produced by the speech enhancement procedure, an iterative spectral subtraction algorithm is proposed in this study. The iterative method is motivated from Wiener filtering which is one of the speech enhancement techniques [17,18]. In this study, the output of the enhanced speech using traditional spectral subtraction method is used as the input signal of the next iteration process.

Figure 2 shows the scheme of the proposed MMW speech enhancement algorithm. It can be seen from the figure that after the first spectral subtraction process, the type of the additive noise is changed to the musical noise. As the output signal is used as the input signal of the next iteration process, the musical noise is reestimated, this new estimated noise, furthermore, is been used to process the next spectral subtraction (that is, subtracted by the new noisy speech), therefore, an enhanced output speech signal can be obtained, and the iteration process goes on. If we regard the process of noise estimate and the spectral subtraction as a filter, then the output signal of the filter is used not only for designing the filter but also as the input signal of the next iteration process. More important, this filter can be refreshed adaptively by reestimate the musical noise so that to improve the speech quality effectively.

2.3. Noise Estimation

The noise in the radar speech, which included of each order of the EMW harmonic, the channel noise, the ambient noise combined in the MMW radar speech, and so on, is highly nonstationary noise, it is imperative to update the estimate of the noise spectrum frequently. This study adopted the minimum-statistics method proposed by Cohen and Berdugo (2002) [19] for noise estimation, since this method is computationally efficient, robust with respect to the input signal-noise ratio (SNR), and have an ability to quick follow the abrupt changes in the noise spectrum. The minimum tracing is based on a recursively smoothed spectrum which is estimated using first-order recursive averaging

$$\left|\hat{D}_{(k,l)}(\omega)\right|^2 = \lambda_D \left|\hat{D}_{(k-1,l)}(\omega)\right|^2 + (1-\lambda_D)\left|\hat{Y}_{(k,l)}(\omega)\right|^2$$
$$0 < \lambda_D < 1, \quad (4)$$

where $\left|\hat{D}_{(k,l)}(\omega)\right|^2$ and $\left|\hat{Y}_{(k,l)}(\omega)\right|^2$ are the kth components of noise spectrum and noisy speech spectrum at the frame l, and λ_D is a smooth parameter. Let $p'(k,l)$ denote the conditional signal presence probability in Cohen and Berdugo (2002) [19], then Eq. (4) implies

$$\left|\hat{D}_{(k,l)}(\omega)\right|^2 = \hat{\lambda}_D(k,l)\left|\hat{D}_{(k-1,l)}(\omega)\right|^2 + (1-\hat{\lambda}_D(k,l))\left|\hat{Y}_{(k,l)}(\omega)\right|^2 \quad (5)$$

where $\hat{\lambda}_D(k,l) \triangleq \lambda_D + (1-\lambda_D)p'(k,l)$ is a time-varying smoothing parameter. Therefore, the noise spectrum can be estimated by averaging past spectral power values. For More details of description of this algorithm, the reader is referred to [19,20].

3. EXPERIMENTS

Ten healthy volunteer speakers, 6 males and 4 females, participated in the radar speech experiment. All the subjects were native speakers of Mandarin Chinese. Their ages varied from 20 to 35, with a mean age of 28.1 (SD =12.05). All the experiments were conducted in accordance with the terms of the Declaration of Helsinki (BMJ 1991; 302, 1194), and appropriate consent forms were signed by the volunteers. Ten sentences of Mandarin Chinese were used as the speech material for acoustic analysis and acceptability evaluation. The lengths of the sentences varied from 6 words (5.6 s) to 30 words (15 s). The sentences were spoken by each participant in a quiet experimental environment. The speakers were instructed to read the speech material at normal loudness and speaking rates.

For the perceptual experiment, eight listeners were selected to evaluate the acceptability of each sentence based on the criteria of mean opinion score (MOS), which is a five-point scale (1, bad; 2, poor; 3, common; 4, good; 5, excellent). All the listeners were native speakers of Mandarin Chinese, had no reported history of hearing problems, and were unfamiliar with MMW radar speech. Their ages varied from 22 to 36, with a mean age of 26.37 (SD = 4.63).

In order to test the effectiveness of the proposed method, two different types of background noise, namely, white Gaussian noise and speech babble noise, were added to the enhanced MMW radar speech; both noises were taken from the Noisex-92 database. These two representative noises have a greater similarity to actual talking conditions than the other noises. Noises with SNRs of 0 dB were added to the original MMW radar speech signal.

Copyright © 2010 SciRes.

4. RESULTS AND DISCUSSIONS

In order to evaluate and compare the performance of the proposed enhancement algorithm, two other algorithms are performed in this study, they are: traditional spectral subtraction method and noise-estimation algorithm [21]. For the purpose of analyzing the time-frequency distribution of the original/enhanced speech, speech spectrograms were provided since they have been identified as a well-suited tool for observing both the residual noise and speech distortion. In addition, results are also measured subjectively by Mean Opinion Score (MOS) in conditions of additive white Gaussian noise as well as Bobble noise (for MOS) for the algorithm evaluation.

Figure 3 shows the spectrograms of the original radar speech (a), the enhanced speech using traditional spectral subtraction algorithm (b), the enhanced speech using noise-estimation algorithm (c), and the proposed iterative spectral subtraction algorithm (d) (the iteration number is set to 5). The speech material is a Chinese sentence "Di si jun yi da xue" (in English, the Fourth Military Medical University).

Because of its different speech detecting theory and working conditions, non-air conducted speech has some special attributes. As stated earlier, the most important is that combined noises are introduced into the original MMW radar speech. These noises can be clearly seen in **Figure 3(a)**, especially in the speech-pause region. It can also be seen from the figure that the combined noise is mainly concentrated in the low-frequency components, roughly below 3 KHz. **Figure 3(b,c)** shows that the spectral subtraction algorithm and the noise estimate algorithm are effective in reducing the combined radar noises. However, there are still too much remnant noise in the enhanced speech, especially in the frequency section in which the noise are concentrated, suggesting that the noise reduction are not satisfactory. **Figure 3(d)** shows that the proposed algorithm not only greatly reduces the low-frequency noise, in which the combined radar noise is concentrated, but it also completely eliminates the high-frequency noise. It can be seen from the figure that in the speech-pause regions the residual noise

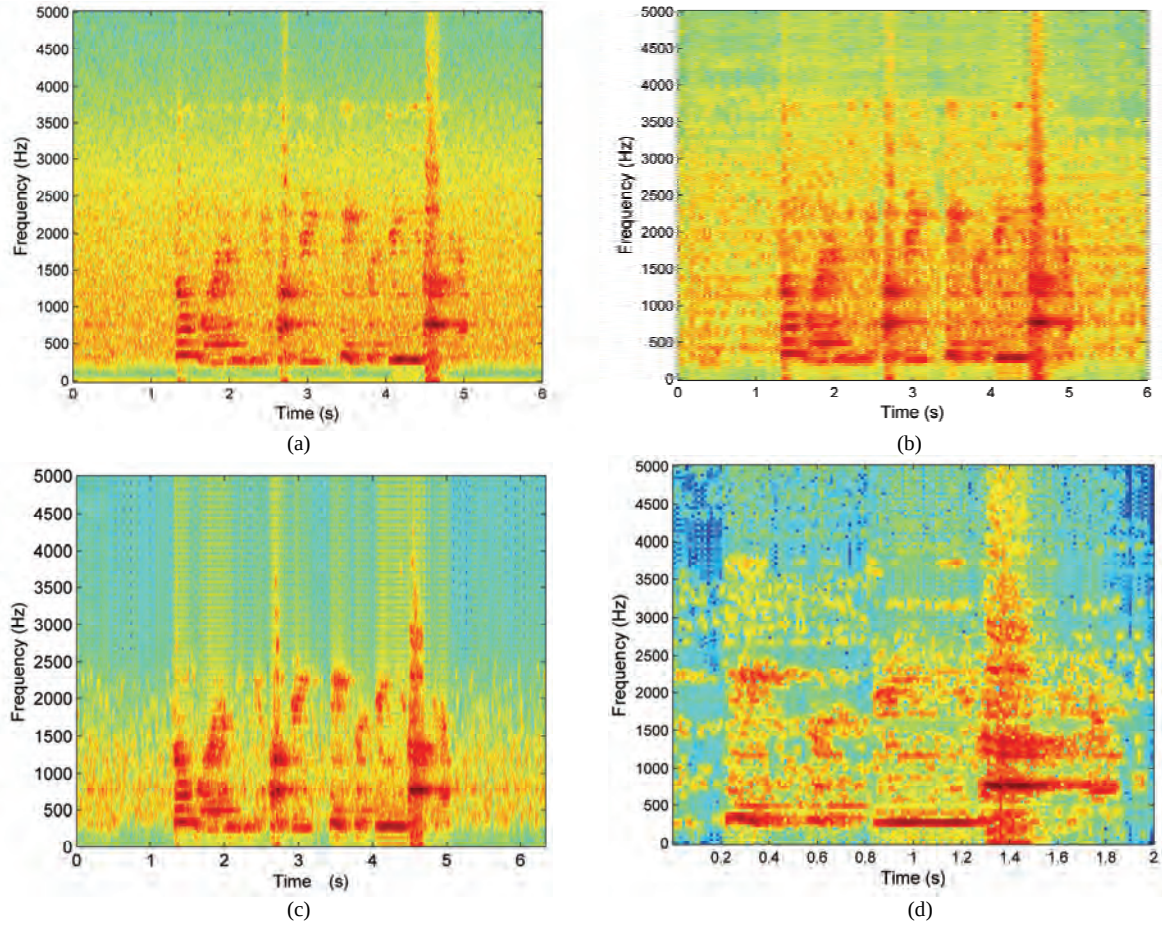

Figure 3. The Spectrogram of the sentence "Di Si Jun Yi Da Xue". (a) The original spectrogram of the millimeter wave conducted speech. (b) Enhanced radar speech obtained by the traditional spectral subtraction method. (c) Enhanced radar speech obtained by the noise estimated algorithm. (d) Enhanced radar speech obtained by the proposed algorithm.

Copyright © 2010 SciRes.

is almost eliminated. Moreover, it is clear that the residual noise is greatly reduced and has lost its structure. These results suggest that the proposed algorithm achieves a better reduction of the whole-frequency noise than traditional spectral subtraction methods.

The perceptual score of the noisy speech and the en hanced noisy speech are shown in **Figure 4**. Mean Opinion Scores (MOS) were used for 100 sentences produced by ten volunteer speakers. The noisy speech in the cases of the additive white and babble noises had SNR inputs of 0 dB. It can be seen from the figure that the original noisy speech has "bad" perceptual effects, but the score of the enhanced speech obtained by using the proposed algorithm is much better. Comparing the two noises, it can be seen from the figure that the MOS for white noise is a little higher than for babble noise. This suggests that the proposed algorithm is more "sensitive" to white noise, however, the difference is small.

The iteration times is another important factor which has effects on the performance of speech enhancement. In order to explore the relationship between the performance of speech enhancement and the iteration times, the variation of the mean segmental SNR of the radar speech with iteration times are shown in **Figure 5**. It can be seen from **Figure 5** that the SNR increased as the iteration number increased, which suggest the larger iteration number will corresponding to the better speech enhancement performance and the less musical noise. However, both performed waveform and the corresponding spectrogram suggest that the larger iteration number would eliminate part of the normal speech component to some extent while it works overmuch effectively on reducing the musical noise, therefore, the proposed iteration number for the radar speech is 3 to 5.

As a single channel subtractive-type speech enhancement method, the algorithm proposed in this paper can be applied for the enhancement of non-air conducted speech using available electronics. For example, a millimeter wave conducted speech enhancing system, into

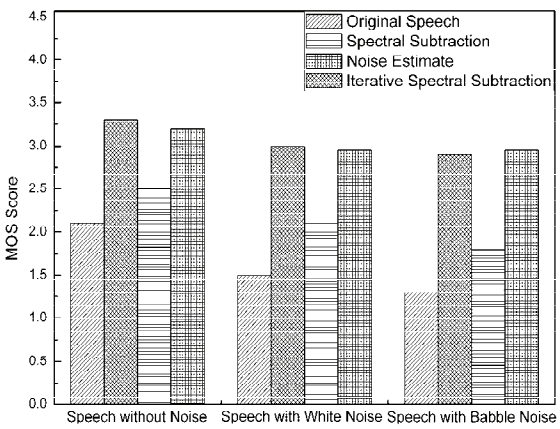

Figure 4. Perceptual results of the noisy and enhanced noisy speech based on the MOS criteria.

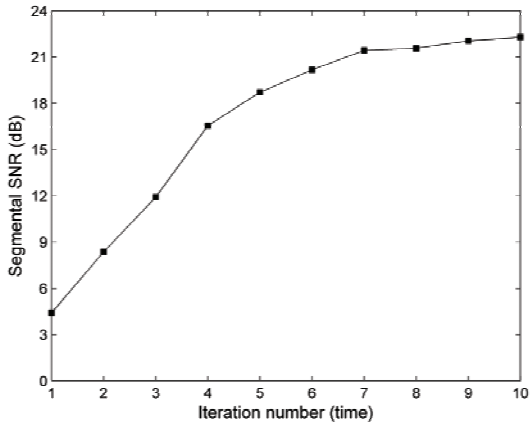

Figure 5. Variations of mean segmental SNR of the MMW radar speech with iteration times.

which this algorithm is embedded, can be developed. With the help of digital signal processing (DSP) technology, the speech enhancement function can be realized with a microprocessor and implanted into a radar-telephone, radar-microphone, or other electronic equipment. Different enhancement algorithms, suitable for different noise conditions, can be selected by a switch. With the development of efficient enhancement methods, the quality of non-air conducted speech will be vastly improved and will provide better perception.

5. CONCLUSIONS

As a non-air conducted speech, MMW radar speech may have greater advantage and wider applications than air conduct speech. However, the complex noises added in the radar speech decreased the speech quality to a large extent. Therefore, an improved spectral subtraction method, iterative spectral subtraction algorithm are used in this study in order to decrease the complex noise and the musical noise. The results from both simulation and evaluation suggest that for the proper iteration number, this method achieves a better reduction of the whole-frequency noise, the musical noise, and yields good speech quality.

6. ACKNOWLEDGEMENTS

This work was supported by the National Natural Science Foundation of China (NSFC, No. 60571046), and the National postdoctoral Science Foundation of China (No. 20070411131). We also want to thank the participants from the E.N.T. Department, the Xi Jing Hospital, the Fourth Military Medical University, for helping with data acquisition and analysis.

REFERENCES

[1] Li, S., Scherer, R.C., Wan, M., Wang, S. and Wu, H. (2006) The effect of glottal angle on intraglottal pressure. *Journal of the Acoustical Society of America*, **119(1)**, 539–548.

[2] Li, S., Scherer, R.C., Wan, M., Wang, S. and Wu, H. (2006) Numerical study of the effects of inferior and su-

perior vocal fold surface angles on vocal fold pressure distributions. *Journal of the Acoustical Society of America*, **119(5)**, 3003–3010.

[3] Yanagisawa, T. and Furihata, K. (1975) Pickup of speech signal utilization of vibration transducer under high ambient noise. *J. Acoust. Soc. Jpn*, **31(3)**, 213–220.

[4] Li, Z.-W., (1996) Millimeter wave radar for detecting the speech signal applications. *International journal of Infrared and Millimeter Waves*, **17(12)**, 2175–2183.

[5] Holzrichter, J.F., Burnett, G.C. and Ng, L.C. (1998) Speech articulator measurements using low power EM-wave sensors. *J. Acoust. Soc. Am*, **103(1)**, 622–625.

[6] Hu, R. and Raj, B. (2005) "A robust voice activity detector using an acoustic Doppler radar," in *IEEE Workshop on Automatic Speech Recognition and Understanding*, 319–324.

[7] Quatieri, T.F., Brady, K., Messing, D. and Campbell, J.P., (2006) Exploiting nonacoustic sensors for speech encoding. *IEEE Transactions on Audio, Speech and Language Processing*, **14(2)**, 533–544.

[8] Boll, S.F. (1979) Suppression of acoustic noise in speech using spectral subtraction, *IEEE Transactions on Acoustics, Speech and Signal Processing*, **27**, 113–120.

[9] Lockwood, P. and Boudy, J. (1992) Experiments with a nonlinear spectral subtractor (NSS), hidden Markov models and projection, for robust recognition in cars. *Speech Commun*, **11**, 215–228.

[10] Hansen, J.H.L., (1994) Morphological constrained feature enhancement with adaptive cepstral compensation (MCE-ACC) for speech recognition in noise and Lombard effect. *IEEE Trans. Speech Audio Process*, **2**, 598–614.

[11] Liu, H., Zhao, Q., Wan, M. and Wang, S. (2006) Application of spectral subtraction method on enhancement of electrolarynx speech. *J. Acoust. Soc. Am*, **120(1)**, 398–406.

[12] Kamath, S. and Loizou, P. (2002) A multi-band spectral subtraction method for enhancing speech corrupted by colored noise. *IEEE International Conference on Acoustics, Speech, and Signal Processing*, **4**, 4160–4164.

[13] Udrea, R.M., Ciochina, S. and Vizireanu, D.N. (2005) Multi-band bark scale spectral over-subtraction for colored noise reduction. *International Symposium on Signals, Circuits and Systems*, **1**, 311–314.

[14] Wang, J.Q., Zheng, C.X., Jin, X.J. and Lu, G..H, (2004) Study on a non-contact life parameter detection system using millimeter wave. *Space Medicine & Medical Engineering*, **17(3)**, 157–161.

[15] Wang, J., Zheng, C., Lu, G.. and Jing, X. (2007) A new method for identifying the life parameters via radar. *EURASIP Journal on Advances in Signal Processing*, **2007(1)**, 8–16.

[16] Berouti, M., Schwartz, R. and Makhoul, J. (1979) Enhancement of speech corrupted by acoustic noise, Proc. *IEEE Int. Conf. Acoust., Speech, Signal Process*, 208–211.

[17] Lim, J.S. and Oppenheim, A.V. (1978) All-Pole Modeling of Degraded Speech. *IEEE Trans. Acoust. Speech, Signal Processing*, ASSP, **26**, 197–210.

[18] Ogata, S. and Shimamura, T. (2001) Reinforced spectral subtraction method to enhance speech signal, Electrical and Electronic Technology. *TENCON. Proceedings of IEEE Region 10 International Conference*, **1**, 242–245.

[19] Cohen, I. and Berdugo, B. (2002) Noise estimation by minima controlled recursive averaging for robust speech enhancement. *IEEE SIGNAL PROCESSING LETTERS*, **9(1)**, 12–15.

[20] Cohen, I. and Berdugo, B. (2001) Speech enhancement for non-stationarynoise environments. *Signal Processing*, **81**, 2403–2418.

[21] Rangachari, S. and Loizou, P. C. (2006) A noise-estimation algorithm for highly non-stationary environments. *Speech Communication*, **48**, 220–231.

Copyright © 2010 SciRes.

J. Biomedical Science and Engineering, 2010, 3, 193-199 **JBiSE**
doi:10.4236/jbise.2010.32025 Published Online February 2010 (http://www.SciRP.org/journal/jbise/).

Classification of non stationary signals using multiscale decomposition

Marwa Chendeb[1,2], Mohamad Khalil[2*], David Hewson[1], Jacques Duchêne[1]

[1]ICD, FRE CNRS 2848, University of Technology of Troyes, Troyes, France;
[2]LaSTRe Laboratory, Engineering Section 1, Lebanese University, Tripoli, Lebanon.
Email: *mkhalil@ieee.org

Received 15 July 2008; revised 5 December 2009; accepted 11 December 2009.

ABSTRACT

The aim of this article is to develop an automatic algorithm for the classification of non stationary signals. The application context is to classify uterine electromyogram (EMG) events to prevent the onset of preterm birth. The idea is to discriminate between the events by allocating them to the physiological classes: contractions, foetus motions, Alvarez or Long Duration Low Frequency waves. Our method is based on the Wavelet Packet (WP) decomposition and the choice of a best basis for classification purpose. Before classification, there is a need to detect events in the recorded signals. The discrimination criterion is based on the calculation of the ratio between intra-class variance and total variance (sum of the intra-class and inter-class variances), calculated directly from the coefficients of the selected WP. We evaluated the performance of the algorithm on real signals by using the classification methods Neural Networks (NN) and Support Vector Machines (SVM). Subband energies of the best selected WP are used as effective features. The determined best basis is applicable to a wide range of uterine EMG signals from large range of patients. In most cases, more than 85% of events are well classified whatever the term of gestation.

Keywords: Uterine EMG; Preterm Birth; Wavelet Packet; Best Basis; Event Classification

1. INTRODUCTION

The automatic classification of non stationary signals is an important studied problem especially as the nonstationarity precludes classification in the time or frequency domain [1]. The aim of this paper is to use the nonparametric representation wavelet packet transform (WPT) which is suitable for nonstationary signals and choose among the wavelet packets (WPs) the best basis for classification. The application context is the classification of uterine electromyographic (EMG) events used for the prevention of preterm birth. The progress of labour can be assessed non-invasively using EMG signals from the uterus (the driving force for contractility) recorded from the abdominal surface [2,3].

Preterm labour and resultant preterm birth are the most important problems in perinatology [2,4,5]. Knowledge of labor commencement, as well as the possible prediction of its starting time, would be of great interest in terms of limiting unnecessary stays in hospitals and adapting treatment to the actual state of the pregnancy. The principal events extracted from the relevant activities of uterine EMG are the contractions (CT). Other events can be of value for pre-term birth diagnosis: Alvarez (Alv) waves, foetus motions (MAF) and long-duration low-frequency (LDBF) waves [2] (**Figure 1**). Several works have been carried out on mammals, with electrodes placed on the uterine surface [2,5]. They demonstrated a modification in electrical activity during both preterm and term labor. In [6] the uterine EMG signals are classified using artificial neural networks method to distinguish the normal term labour from abnormal preterm labour signals. [7] applied the wavelet transform on the uterine signals recorded using abdominal surface electrodes. In literature, the best basis algorithm is used to find the best-adapted WP for a lot of goals such the detection [8,9], denoising [10], feature extraction and classification [11,12], etc. Saito and Coifman introduced the Local Discriminant Bases (LDB) to search a best basis for classification [12]. Wavelet packet analysis is used to extract the features of the sample DNA sequences in [13]. An index of discrimination based on Kullback-Leibler distance is proposed as a way to select most discriminant wavelet packets for texture classification in an image [14].

In this work, classification of uterine EMG events by allocating them to the physiological classes: CT, MAF, Alv, or LDBF waves.is based on their energy distribution throughout the wavelet packet transform (WPT) which is used because it is characterized by the frequency

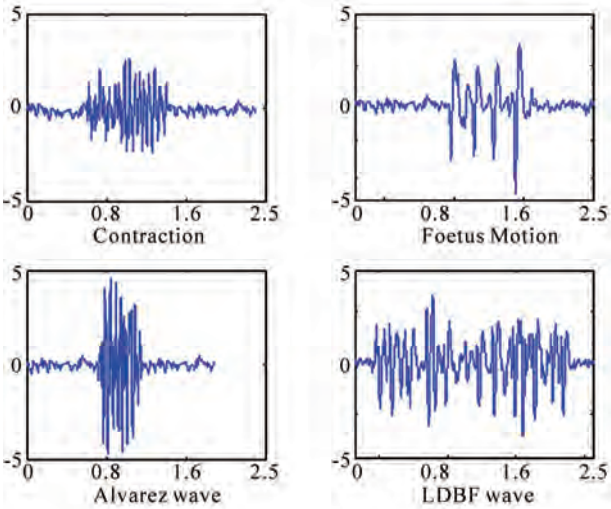

Figure 1. Samples of various events appearing in the uterine EMG recordings. X axis: minutes; Y axis: Amplitude scale in arbitrary units.

content of the packets [2,3]. Only a few WP of the redundant tree is relevant for classification purpose to define the features of events. The idea behind WP selection (best basis for classification) is to define an index for discrimination purpose. The ratio (for each WP) between intra-class and total variances (intra-class and inter-class variances), calculated directly from the wavelet packet coefficients (WPC) is the proposed discrimination criterion. An additional characteristic, the duration of the events, is also taken into consideration, as previous studies have shown its importance in terms of discrimination [3].

This paper is organized as follows. In Section 2, the signal composition and the used data are presented. In Section 3, WP decomposition is briefly described. The detection step is mentioned in Section 4. The index discrimination, the best basis for classification and the classification methods are displayed in Section 5. The performance of the method using real datasets is shown in Section 6. Discussion and conclusion are in Sections 7 and 8 respectively .

2. SIGNAL DESCRIPTION

2.1. Signal Composition

Uterine EMG signals are the electromyographic (EMG) activity of the uterus during labor recorded using abdominal electrodes placed across the maternal abdomen. Recordings were carried out in Amiens hospital setting under the supervision of the research group of Pr. Catherine Marque at the University of Technology of Compiègne, France [2,10]. They can be described by a random process that is composed of the EMG signal, the superimposed events and the noise due to the environment, especially electrode and instrumentation noise. When the uterus contracts, an electrical activity is generated and the contractions can characterize the uterus states. The superimposed signals correspond to short potentials or artifacts which appear randomly throughout the signal, such as foetus motions, Alvarez waves and other superimposed events [2,3,15]. Alvarez waves appear during the first 30 weeks of the human pregnancy. Other waves have been recently discovered, such as LDBF waves, whose impact on obstetrical diagnosis has not yet been clearly identified. The evoked events present different time and frequency features deduced from spectral analyses. At mi term, the frequency of contractions is less than 0.2 Hz and at late term, it is greater than 0.5 Hz. Alvarez frequency band is 0.2 Hz to 1 Hz. MAF frequency is less than 0.5 Hz and LDBF waves have a very low frequency [2]. The contractions and the Alvarez events have the same frequency contents but the length of a contraction is greater than that of an Alvarez wave. The same interpretation can be used for the LDBF events and the foetus motion related events (very short) (**Figure 1**). The normalized amplitude is used throughout the paper.

Classical signal pre-processing includes the necessary step of signal to noise ratio (SNR) improvement. The denoising techniques based on the wavelet packet transform are widely used [8,16]. In the present work, the selection of a specific WP subset (best basis) automatically improves the SNR by keeping only the WPs containing the useful uterine information.

2.2. Data Description

The group named (CLASS) was defined in order to test classification efficiency. It contains 100 real events of each class (CT, Alv, MAF, LDBF, and noise) identified by an expert. Half of them are belonging to the training set (train_CLASS), the others are belonging to the test set (test_CLASS).

The acquired initial real uterine EMG signals were amplified and filtered between 0.2 and 6 Hz to eliminate the continuous component and the artefacts due to powerline interference. The sampling frequency was set to Fe=16 Hz.

3. WAVELET PACKET TRANSFORM

WPT is an extension of Discrete Wavelet Transform (DWT) and can be obtained by a generalization of the fast pyramidal algorithm [17]. It enables non-stationary signals with different frequency features to be distinguished. Each detail and approximation coefficient's vectors are filtered and down-sampled using *lo*(*n*) and *hi*(*n*), the two impulse responses of low-pass and high-pass analyzing filters. Each node is associated with a subspace $\Omega_{j,n}$ generated by an orthonormal basis $\{\psi_{j,n}\}_{n\in Z}$, with j being interpreted as a scale parameter,

and *n* as a sequence parameter. The wavelet packet coefficients (WPC) at each node *(j,n)* are computed as [17]:

$$\left(C_{j,n}(k)\right) = \left\langle f(t), \psi_{j,n}(t - 2^j k)\right\rangle \quad (1)$$

where f(t) is the initial signal and k is the time-localization index. In the following, each WP is characterized by the sequential index v obtained by according sequential numbers to the WP (see **Figure 2**). In fact, WPC carry the same information as the reconstructed signals. As WPT is a linear transformation, WPC exhibit the same statistical properties as the initial signal [8]. Consequently, WPC of the real noise follow the normal distribution [15].

4. DETECTION

To detect events, several methods can be used. In our last work [15] an algorithm of best basis for detection is proposed. It is based on the Kullback Leibler distance as a criterion to select the best WPs which show clearly the events. After choosing the best basis, the detection algorithm DCS (Dynamic Cumulative Sum) is applied on every selected wavelet packet coefficients. After the delay correction and the change time fusion [15], the uterine events of the real signals are obtained.

5. CLASSIFICATION

After change detection, the problem consists in identifying the detected events by allocating them to physiological classes: contractions, foetus motions, Alvarez waves, LDBF waves, or noise. In this section, the classification criterion is described. The approach of best basis is proposed for the classification task. The principal features for the classification methods are the variances of the selected packets. The duration of events was introduced as an additional feature to improve the correct classification rate (CCR).

5.1. Classification Criterion

An important criterion to discriminate between classes is to minimise the intra class variance and to maximise inter-class variance. In [18] an index which maximises the Euclidian distance between the classes was used. The most discriminant coefficients of all packets were selected as a criterion for classification [19]. In our work, the ratio between intra-class variance and total variance (sum of inter-class and intra-class variances) calculated for each WP seems to be an efficient index for discrimination. As the uterine EMG events are characterised by their frequency content, the variances of selected WPs produce useful information to identify events.

For the level of decomposition J, the number N of packets is:

$$N = 2^{J+1} - 1 \quad (2)$$

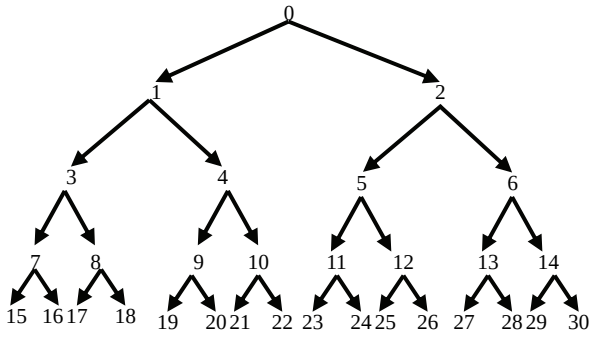

Figure 2. Wavelet packet decomposition tree.

Suppose that the ith class is composed of mi elements, so the gravity center of this class is:

$$\hat{g}_i^v = \frac{1}{m_i}\sum_{q=1}^{n_i} x_{iq}^v \quad (3)$$

where x_{iq}^v is the qth element of class i (i = 1.5) and WP number v.

The gravity center global of WP v is:

$$\hat{g}^v = \frac{1}{m}\sum_{q=1}^{M} m_q \hat{g}_q^v \quad (4)$$

where M is the number of classes (in our case M =5) and m is the total number of samples.

The intra-class variance $\hat{\Sigma}_w^v$ of a WP number v is defined as:

$$\hat{\Sigma}_w^v = \frac{1}{m}\sum_{i=1}^{M}\sum_{q=1}^{m_i}\left(x_{iq}^v - \hat{g}_i^v\right)^2 \quad (5)$$

where $\hat{g}_i^v$ is the center of gravity of the packet *v* and class *i*, mi the number of elements of class *i*, *M* the total number of classes and x_{iq}^v is the qth element of the packet v and class *i*.

The inter-class variance $\hat{\Sigma}_B^v$ of WP v is written as:

$$\hat{\Sigma}_B^v = \frac{1}{m}\sum_{i=1}^{M} m_i\left(\hat{g}_i^v - \hat{g}^v\right)^2 \quad (6)$$

where g^v is the centre of gravity for all classes.

The total variance $\hat{\Sigma}$ is equal to the sum of the inter-class and intra-class variances [20]:

$$\hat{\Sigma}^v = \hat{\Sigma}_w^v + \hat{\Sigma}_B^v \quad (7)$$

For each packet *v*, define the discrimination criterion as follows:

$$R^v = \frac{\hat{\Sigma}_w^v}{\hat{\Sigma}^v} \quad (8)$$

Copyright © 2010 SciRes.

5.2. Best Basis Selection for Classification

The goal of this part is to retain only the wavelet packets that are able to discriminate between events in a specific class of signals (uterine EMG in our application). If the distances between classes are important and each class is strongly concentrated, the ratio R^v of packet v is small. In this case, the classes are well separated and the packet is one of the best WPs for classififcation.

The values of criterion R^v are calculated for all WP and sorted in ascending order. There is a clear gap between the values of R^v corresponding to the packets that are relevant for classification and the others (**Figure 3**), a threshold can be indicated. As the tree is highly redundant, there is a need for further step to reduce the number of selected packets based on the frequency contents of events. In our case, the packets which contain the bandwidths of the events are retained as best basis for classification. The variances of the retained WPs (best basis) are used as features for the classification methods.

5.3. Classification Methods

Classification has been achieved using the two methods: neural networks (NN) [21] and Support Vector Machines (SVM) [22,23].

5.3.1. Neural Networks

The Multi Layer Perceptron (MLP) is widely used to solve classification problems using supervised training for instance, the feed forward technique, which is used to minimize error. A multilayer perceptron is a feedforward artificial neural network model that maps sets of input data onto a set of appropriate output [24].

Such a network is based on the calculation of the output (direct calculation, weights are fixed) and adjustment of the weight by minimizing an error function. The process continues until the outputs of the network

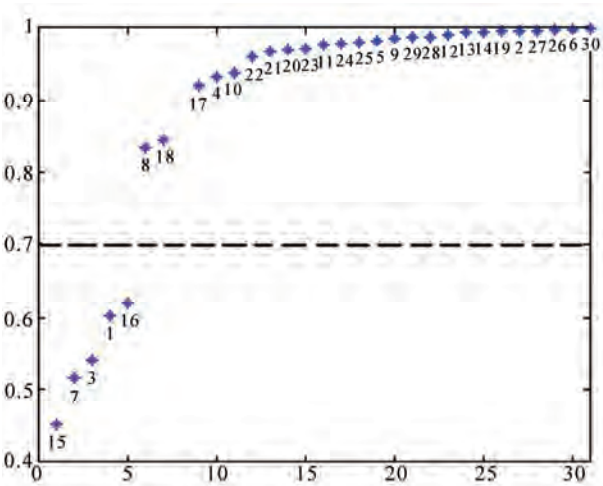

Figure 3. R^v values of each WP plotted in ascending order. X axis: arbitrary units. Y axis: R^v values.

be come close to those desired. The network is defined by the transfer function of the neuron, the number of layers and the number of neurons in each layer. The number of inputs is equal to the dimension of the input vectors (in this case the variances of the selected packets). The number of outputs depends on the number of classes. Various transfer functions (sigmoid, hyperbolic tangent, linear, etc) can be used as neural activation functions [24].

5.3.2. Support Vector Machines

The SVM method is a new discriminator based on the construction of an optimal hyperplane, which is constructed in such a way that it maximizes the minimal distance between itself and the learning set.

Support vector machine is a learning technique which is well-founded in modern statistical learning theory [22]. It uses the training data to create the optimal separating hyperplane between two classes. The optimal hyperplane maximizes the margin of the closest data points. In this way the SVM minimizes the misclassification probability of new cases. The optimal separating hyperplane is computed as a decision surface of the form:

$$g(\mathrm{y}) = \mathrm{sgn}\left(\sum_{i=1}^{l_s} d_i \alpha_i K(\mathrm{y}_i, \mathrm{y}) + b\right) \tag{9}$$

where x_i are support vectors which are determined from the training data, $K(\mathrm{y}_i, \mathrm{y})$ is the inner product kernel which must satisfy Mercer's theorem [22], and is used to map the data from its original dimension to higher dimension so that the data is linearly separable in the mapped dimension, l_s is the number of support vectors, d_i is the class indicator $\left(d_i \in \{-1,+1\}\right)$ of x_i, and b is bias. The coefficients α_i are calculated by solving the quadratic programming problem:

$$\text{Maximize} \quad \sum_{i=1}^{l} \alpha_i - \frac{1}{2}\sum_{i,j=1}^{l} d_i d_j \alpha_i \alpha_j K\left(y_i, y_j\right) \tag{10}$$

$$\text{Subject to} \quad \sum_{i=1}^{l} \alpha_i d_i = 0, \qquad 0 \le \alpha_i \le C \qquad for \quad i = 1,\ldots,l$$

where C is a user specified positive regularization parameter used to control he amount of allowed overlap between classes. Given the expression of g(y), the decision is based on the sign of g(y). In this work a radial basis function (RBF) is chosen as inner product kernel, which is defined as:

$$K(u,v) = \exp\left(-\frac{\|u-v\|^2}{2\sigma^2}\right) \tag{11}$$

where $\sigma \succ 0$ is a user specified constant which defines the kernel width. In RBF kernel support vector machine, number and value properties of support vectors deter-

Copyright © 2010 SciRes.

mine the number of kernels and their centers [8]. Using RBF as an inner product kernel provides classification of a non-linear set of data, which means perfect discrimination of the prostate texture features.

To discriminate between the various uterine events, the SVM multiclass method [23] was used. It is based on building a model SVM for each group of events, enabling discrimination in comparison to the other groups.

6. RESULTS ON CLASSIFICATION

As the main discriminant feature of the events contained in uterine EMG recordings is the frequency content, the decomposition was performed up to level 4. The used wavelet is symlet 5 [15]. For this, every event was decomposed onto 30 WP (**Figure 2**). This choice is justified by the fact that the level 4 is the limit where WP still contain relevant information related to all the uterine events. For example, the WPs 15 and 16 correspond to the frequency bands which belong MAF and LDBF waves.

In detection case, the decomposition level is limited to 3 because the goal was to choose the best packets for detection whatever the events [15]. To decide which packets were able to classify the events, the values Rv of the discrimination criterion were computed on each packet using equation 8 (there are 30 packets). The events of train_CLASS were used (see Subsection 2.2). **Figure 3** shows the criterion values in ascending order. The selection of the discriminant WP was made by applying a threshold and selecting those WP which have the smallest criterion values.

By examining **Figure 3** there is a clear threshold for Rv. In first step, the packets 1, 3, 7, 15 and 16 were selected. These packets correspond to the bandwidths [0, 4], [0, 2], [0, 1], [0, 0.05] and [0.05, 1] Hz, respectively. The second step consists in eliminating the redundant packets by keeping only the packets which correspond to the frequency contents of events. As the contractions and Alvarez waves have a frequency band less than 1 Hz, MAF frequency is less than 0.5 Hz and LDBF waves have a very low frequency (see Subsection 2.1), only the packets 7, 15 and 16 are retained as best basis for classification.

In order to demonstrate that Rv is a good criterion to discriminate between uterine classes, the validation step is carried out. The classification methods MLP and SVM were applied on the test_CLASS to evaluate the Correct Classification Rate (CCR).

In the current application, a two layer feed forward network is created. The first layer has five tansig $\left(f(n)=\frac{2}{1+e^{-2n}}-1\right)$ neurons, the second layer has ten purelin ($f(n) = n$) neurons.

For the SVM method, the CCR were calculated for some kernels (linear, polynomial, sigmoid and Gaussian Radial Basis Function (GRBF)) [22]. The kernel GRBF gave the best CCR, it is defined as follows [22]:

$$K(u,v)=\exp\left(-\frac{\|u-v\|^2}{2\sigma^2}\right) \tag{12}$$

To provide the reader with the performance improvement of the best basis with respect to the DWT, we also present the CCR produced by using the packets 2, 4, 8 and 16 corresponding to the DWT. The variances of packets 2, 4, 8 and 16 were used as features for the classification methods. The best basis method was evaluated by comparing the results with those obtained using the DWT. Results are summarized in **Tables 1,2**, showing the performance of the use of the variances of the selected WP as features for the classification methods. **Table 1** shows the CCR of MLP classifier for the best basis selection and DWT. The CCR were calculated for large values of the regularization parameter C and σ for the SVM method [22,23] (C = [0.0001, 0.001, 0.01, 0.1, 1, 10, 100, 1000, 10000, Infinity] and σ = [0.1, 0.2, 0.4, 0.6, 1, 5, 10]). C controls the tradeoff between the complexity of the machine and the number of non- separable points. C and σ are chosen for each class in such a way that the best correct classification rates are obtained. The optimal values of C and σ are presented in **Table 2** for the best basis selection and DWT.

Event duration is used as an additional feature to improve the correct classification rate. The correct classification and false alarm rates are presented in **Table 3** after including the event durations in the case of best basis. The results are well improved specifically for Alvarez and MAF waves.

7. DISCUSSION

This paper developed a best basis selected from the set of WP tree for classification. The uterine EMG events are characterized by their frequency content justify the use of WPT. WP tree reduction is generally guided by a certain criterion (depending on the WPT objectives) based on the knowledge of a data (often statistical) model or the availability of training data. The mother wavelet choice in the current work was based on the minimum delay induced by applying detection algorithms directly on the wavelet packet coefficients. The choice was made using all available EMG events, leading to the selection of the Symlet 5 wavelet [15]. This choice is probably due to the symmetrical shape of the associated filters. It is better to study the influence of

Table 1. Correct classification rates in the cases of best basis (WP: 7, 15 and 16) and DWT (WP: 2, 4, 8 and 16) for MLP method.

SVM	CT	ALV	MAF	LDBF	Noise
best basis	0.80	0.80	0.86	0.88	0.94
DWT	0.52	0.62	0.62	0.66	0.94

Copyright © 2010 SciRes.

Table 2. Correct classification rates in the cases of best basis (WP: 7, 15 and 16) and DWT (WP: 2, 4, 8 and 16) for SVM method.

SVM	CT	ALV	MAF	LDBF	Noise
best basis	0.82 σ =5, C=Inf	0.64 σ =10, C=Inf	0.8 σ =5, C=Inf	0.88 σ =1, C=Inf	0.82 σ =5, C=100
DWT	0.54 σ =1, C=10	0.50 σ =0.2, C=Inf	0.60 σ =0.2, C=Inf	0.50 σ =0.4, C=10000	0.90 σ =0.6, C=1000

Table 3. Correct classification probabilities (a) and false alarm rates (b) for the two methods after including event duration (best basis case).

Method	CT		ALV		MAF		LDBF		Noise	
	(a)	(b)	(a)	(b)	(a)	(b)	(a)	(b)	(a)	(b)
MLP	0.86	0.04	0.96	0.11	0.98	0	1.00	0.12	0.86	0.04
SVM	0.88	0.04	0.86	0.12	0.96	0	0.98	0.03	0.90	0.18
	σ =5, C=Inf		σ =5, C=1		σ =5, C=1		σ =10, C=1		σ =0.6, C=1	

other wavelets to choose the best wavelet for classification.

The best basis was searched for classification. Four levels were needed as they corresponded to the relevant bandwidths for event discrimination such as foetus motions and LDBF waves.

The ratio between intra-class and inter-class variances appeared as a good discrimination criterion for the choice of the best basis for the classification of uterine EMG events. The best basis for classification was selected by choosing all packets that scored a ratio lower than a defined threshold as explained in Section 4. A second step based on the frequency contents of events is introduced to eliminate the redundant packets. In order to ensure the performance of the selection of best basis, we asked an expert in uterine EMG events to indicate, from an arbitrary data set, which WP could discriminate between the uterine events at best. She selected the same WP obtained by our algorithm.

This result illustrates the coincidence between the automatic unsupervised learning and direct supervised selection. Two classification methods (Neural Networks (MLP) and Support Vector Machines) were applied on validation and test data. The main issues related to the use of MLP were the choice of the activation functions of the hidden and output layers and the definition of the number of hidden neurons. Results were satisfactory with or without the use of the event duration as a complementary feature.

For SVM method, the parameter (C and σ) values that produced the best CCR were selected. These values were different according to whether the duration of the events was used or not. The CCR were greatly improved by the introduction of the event duration, whatever the classification method.

8. CONCLUSIONS

The method proposed for event classification in uterine recordings based on a WPT, and best basis selection in order to reduce the WP tree produced very satisfactory results. The ratio between intra-class and total variance was found to be a good criterion well adapted for the choice of the best discriminant packets. Two proposed classifiers (Neural Networks and SVM) for the identification of the detected events by allocating them to physiological classes (CT, MAF, Alv or LDBF waves) were used. On average more than 85% of the events were correctly classified, regardless of the pregnancy term. The training data permits to choose the best basis relevant to the uterine EMG events but the algorithm can be used for other similar situations. As perspectives the study must continue in order to show the performance of the algorithm when applying it to other non stationary data.

Uterine electrical activity is increasingly used as a relevant index for the characterization of the uterine contraction within the scope of pregnancy and parturition monitoring. A further step would be the production of a sufficiently large database to improve the current knowledge on the actual recording contents and their correlation to a diagnosis of possible premature birth.

REFERENCES

[1] Gretton, A. et al. (2001) Nonstationary signal classification using support vector machines. *11th IEEE Workshop on Statistical Signal Processing Proceedings*, pp. 305–308.

[2] Devedeux, D., Marque, C., Mansour, S., Germain, G., Duchene, J. (1993) Uterine electromyography: a critical review. *Amer. J. Obstet. Gynecol*. **169(6)**, 1636–1653.

[3] Khalil, M., Duchene, J. (2000) Uterine EMG analysis: a dynamic approach for change detection and classification. *IEEE Trans. Biomed. Eng*, **47(6)**, 748–756.

[4] Garfield, R.E., Saade, G., Buhimschi, C., Buhimschi, I. et al. (1998) Control and assessment of the uterus and cervix during pregnancy and labour. *European Society of*

Human and Embryology, **4(5)**, 673–695.

[5] Doret, M., Bukowski, R., Longo, M., Maul, H., Maner, W.L., Garfield, R.E. and Saade, G.R. (2005) Uterine electromyography characteristics for early diagnosis of mifepristone-induced preterm labor. *Obstetrics and Gynecology*, **15(4)**, 822–830.

[6] Lu, N., Wang, J., McDermott, I., Thornton, S. et al. (2009) Uterine electromyography signal feature extraction and classification. *International Journal of Modelling, Identification and Control*, **6(2)**, 136–146.

[7] Eswaran, H., Wilson, J.D., Murphy, P., Preissl, H., Lowery C.L. (2002) *The Journal of Maternal-Fetal & Neonatal Medicine*, **11(3)**, 158–166.

[8] Ravier, P. and Amblard, P.O. (2001) Wavelet packets and de- noising based on higher-order-statistics for transient detection. *Signal Processing*, **81(9)**, 1909–1926.

[9] Hitti, E. and Lucas, M.F. (1998) Wavelet-packet basis selection for abrupt changes detection in multicomponent signals. *Proc. EUSIPCO*, Island of Rhodes, Greece, 1841–1844.

[10] Leman, H. and Marque, C. (2000) Rejection of the maternal electrocardiogram in the electrohysterogram signal, *IEEE Trans Biomed Eng*. **47(8)**, 1010–1017.

[11] Yang, B., Yan, G., Yan, R., Wu, T. (2007) Adaptive subject-based feature extraction in brain–computer interfaces using wavelet packet best basis decomposition. *Medical Engineering & Physics*, **29(1)**, 48–53.

[12] Saito, N. and Coifman, R.R. (1994) Local discriminant bases. A. F. Laine and M. A. Unser Editors, *Wavelet Applications in Signal and Image Processing {II}, Proc. SPIE 2303*, 2–14.

[13] Zhao, J., Yang, X.W., Li, J.P. and Tang, Y.Y. (2001) DNA sequences classification based on wavelet packet analysis from "wavelet analysis and its applications book". *Springer Berlin / Heidelberg editor*.

[14] Rajpoot, N.M. (2002) Texture classification using discriminant wavelet packet subbands. *45th Midwest Symposium on Circuits and Systems*, **3**, 300–303.

[15] Chendeb, M., Khalil, M. and Duchêne J. (2006) Methodology of wavelet packet selection for event detection. *Signal Processing*, **86**, 3826–3841.

[16] Nadernejad, E. (2008) μPET data de-noising using wavelet packets. *Contemporary Engineering Sciences*, **1(2)**, 91–104.

[17] Mallat, S. (1999) a wavelet tour of signal processing, *Academic Press, San Diego, CA*.

[18] Sheng, S., Yanda, L. (1997) "Best Bases for Classification". *Technical Report of pattern Recognition and Signal Processing Lab, department of Automation, Tsinghua University*.

[19] Fukunaga, K. (1990) "Introduction to statistical pattern recognition". *Academic Press, Inc*.

[20] Dubuisson, B. (1990) "Diagnostic et reconnaissance des formes". *Editions Hermes*.

[21] Turkoglu, I., Arslan, A. and Ilkay, E. (2003) An intelligent system for diagnosis of the heart valve diseases with wavelet packet neural networks. *Computers in Biology and Medicine*, **33(4)**, 319–331.

[22] Gunn, S.R. (1998) Support vector machines for classification and regression. *Technical Report, School of Electronics and Computer Science, University of Southampton*.

[23] Mayoraz, E. and Alpaydin, E. (1998) Support vector machines for multi-class classification. T*echnical Report IDIAP*.

[24] Haykin, S.S., Gwynn, R. (2008) Neural networks and learning machines. *Prentice Hall, 3rd edition*.

Copyright © 2010 SciRes.

J. Biomedical Science and Engineering, 2010, 3, 200-205 **JBiSE**
doi:10.4236/jbise. 2010.32026 Published Online February 2010 (http://www.SciRP.org/journal/jbise/).

Performance comparison of three artificial neural network methods for classification of electroencephalograph signals of five mental tasks

Vijay Khare[1], Jayashree Santhosh[2], Sneh Anand[3], Manvir Bhatia[4]

[1]Department of Electronics and Communication Engineering, Jaypee Institute of Information Technology, Noida, India;
[2]Computer Services Centre, Indian Institute of Technology, Delhi, India;
[3]Centre for Biomedical Engineering, Indian Institutes of Technology, Delhi, India;
[4]Department of Sleep Medicine, Sir Ganga Ram Hospital,New Delhi, India.
Email: vijay.khare@jiit.ac.in; jayashree@cc.iitd.ac.in; sneh@iitd.ernet.in; manvirbhatia1@yahoo.com

Received 4 November 2008; revised 4 December 2009; accepted 7 December 2009.

ABSTRACT

In this paper, performance of three classifiers for classification of five mental tasks were investigated. Wavelet Packet Transform (WPT) was used for feature extraction of the relevant frequency bands from raw Electroencephalograph (EEG) signal. The three classifiers namely used were Multilayer Back propagation Neural Network, Support Vector Machine and Radial Basis Function Neural Network. In MLP-BP NN five training methods used were a) Gradient Descent Back Propagation b) Levenberg-Marquardt c) Resilient Back Propagation d) Conjugate Learning Gradient Back Propagation and e) Gradient Descent Back Propagation with movementum.

Keywords: Electroencephalogram (EEG); Wavelet Packet Transform (WPT); Support Vector Machine (SVM); Radial Basis Function Neural Network (RBFNN); Multilayer Back Propagation Neural Network (MLP-BPNN); Brain Computer Interface (BCI)

1. INTRODUCTION

Brain Computer Interface (BCI) system have the potential to offer a new nonmuscular communication channel, which enable severely handicapped persons to communicate with their external surroundings using the brain's electrical activity measured as electroencephalogram (EEG) [1,2,3,4,5]. There are various types of EEG based BCIs. Evoked potentials (EPs) based BCI depend on the brain's response to external events. Two types of evoked potentials have been widely explored in the field of BCI, namely P300 and Steady State Visual Evoked Potential (SSVEP). P300 is a electrical potential that appear 300 ms after task-related stimuli at Centro-Parietal location. The amplitude of the P300 depends on the frequency of stimuli occurrence like less frequent stimuli produce larger response (vice versa). P300 has been used to develop virtual keyboards and control of a wheelchair. Visual evoked potential (VEP) reflect electrophysiological mechanisms underlying the processing of visual information in the brain and change in response to visual stimuli. Flicker stimuli of variable frequency (2–90 Hz) elicit a Steady State Visual Evoked Potential (SSVEP) in the EEG which is characterized by an oscillation at the same frequency as the stimulus. Thus SSVEP can be detected by examining the spectral content of the signals recorded in the visual region, namely the occipital region. SSVEP were used to control flight simulator and functional Electrical stimulator (FES). Spontaneous BCIs are based on the analysis of the EEG phenomenon associated with various aspect of the brain function related to mental tasks carried out by the subject at his /her own will. EEG based of this kind BCI can use slow potential shifts and variation of rhythmic activity control. Slow cortical potentials (SCPs) are shifts in the depolarization level of upper cortical dendrites and reflect very low frequency, slow change in potential shifts, often developing over 0.5–10 seconds. A thought translation device was designed for cursor movement using SCP. Surface electrical potentials reflect electrical activity of large synchronous groups of neuron in the brain. This is recorded by electrodes placed in standard positions on the scalp and has amplitude between 2–100 microvolt with a frequency spectrum ranging from 0.1 to 100 Hz. The frequency bands of delta (0.5–4.0 Hz), theta (4.0–8.0 Hz), alpha (8.0–13.0 Hz), beta (13.0–22.0 Hz), gamma (30.0–40.0 Hz) and μ- rhythms (8.0-13.0 Hz) are examples of rhythmic activity. Most BCIs make use of spontaneous electroencephalogram (EEG) to distinguish between mental states. The past two decades have witnessed the importance of innovative BCI with voice,

vision and a combination of these, as a communication platform [6,7,8,9]. Effective attempts have been made to achieve successful BCI systems based on bioelectric signals. They were mainly to help patients with various neuromuscular disorders by providing them a way of communication to the world, through extracting information about their intensions. So far the accuracy of the classification has been one of the main pitfalls of the existing BCI systems, since it directly affects the decision made as the BCI output. The speed &accuracy could be improved by implementing better methods for feature extraction and classification [10].

In this study, wavelet packet transform method was used to capture the information of mental tasks from eight channel EEG signals of nine subjects. The coefficients of wavelet packet transform were used as the best fitting input vector for classifiers. The three classifiers (MLP-BP NN , SVM and RBFNN) were used to compare the performance in discrimination of five mental tasks.

2. METHODOLOGY

2.1. Subjects

Nine right-handed healthy male subjects of age (mean 23yr) having no sign of any motor- neuron diseases were selected for the study. A pro-forma was filled in with detail of their age & education level as shown in **Table 1** The participants were student volunteers for their availability and interest in the study. EEG data was collected after taking written consent for participation. Full explanation of the experiment was provided to each of the participants.

2.2. EEG Data Acquisition

EEG Data used in this study was recorded on a Grass Telefactor EEG Twin3 Machine available at Deptt. of Neurology, Sir Ganga Ram Hospital, New Delhi. EEG recording was done for five mental tasks for five days, from ten selected subjects. Data was recorded for 10 sec during each task and each task was repeated five times per session per day. Bipolar and Referential EEG was recorded using eight standard positions C3, C4, P3, P4,

Table 1. clinical characteristics of subjects.

Subject No.	Subject Name	Age	Educational Status
1	Subject 1	22	BE
2	Subject 2	21	BE
3	Subject 3	23	BE
4	Subject 4	27	M.TECH
5	Subject 5	23	BE
6	Subject 6	22	BE
7	Subject 7	27	M.TECH
8	Subject 8	22	BE
9	Subject 9	22	BE

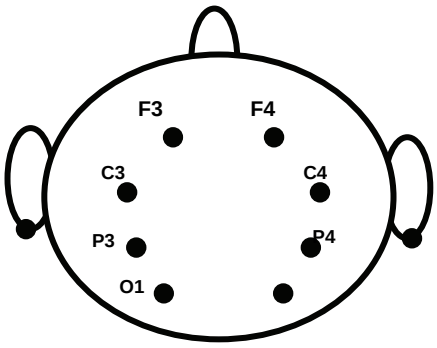

Figure 1. Montage for present study.

O1 O2, and F3, F4 by placing gold electrodes on scalp, as per the international 10–20 standard system of electrode placement as shown in **Figure 1** The settings used for data collection were: low pass filter1 Hz, high pass filter 35 Hz, sensitivity 150 micro volts/mm and sampling frequency fixed at 400 Hz. The reference electrodes were placed on ear lobes and ground electrode on the forehead. EOG (Electooculargram) being a noise artifact, was derived from two electrodes placed on outer canthus of left and right eye in order to detect and eliminate eye movement artifacts.

2.3. Experiment Paradigm

An experiment paradigm was designed for the study and the protocol was explained to each participant before the experiment. In this, the subject was asked to comfortably lie down in a relaxed position with eyes closed. After assuring the normal relaxed state by checking the status of alpha waves, the EEG was recorded for 50 sec, collecting five session of 10sec epoch for the relaxed state. This was used as the baseline reference for further analysis of mental task. The subject was asked to perform a mental task on presentation of an audio cue. Five session of 10sec epoch for each mental task were recorded (as shown in **Figure 2**). The whole experimental lasted for about one hour including electrodes placement.

Data collected from nine subjects performing five mental tasks were analyzed. The following mental tasks were used.

Relaxed:The subject was asked to relax with their eyes closed. No mental or physical task to be performed at this stage.

Arithmetic Task:The subject was asked to perform arithmetic simple (trivial multiplication) and arithmetics

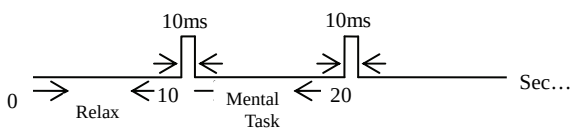

Figure 2. Timing of the protocol.

Copyright © 2010 SciRes.

complex (nontrivial multiplication).An example of a trivial calculation is to multiply 2 by 3 and nontrivial task is to multiply 49 by 78. The subject was instructed not to vocalize or make movements while solving the problem. EEG signal were recorded corresponding.

Geometric figure Rotation:The subject was given 30 seconds to see complex three dimensional objects, after which the object was removed. The subject was instructed to visualize the object being rotated about an axis.The EEG signals were recorded during this period.

Movement Imagination: The subject was asked to plan movement of the right hand and corresponding EEG signals were recorded during this period.

2.4. Feature Extraction

The frequency spectrum of the signal was first analyzed through Fast Fourier Transform (FFT) method. The FFT plot of signals from the all electrode pairs were observed and maximum average change in EEG amplitude was noted as shown in **Figure 3.**

For relaxed, the peaks of power spectrum almost coincide for central area in the alpha frequency range (8–13 Hz) [11,12]. EEG recorded with relaxed state is considered to be the base line for the subsequent analysis. Mu rhythms are generated over sensorimotor cortex during planning a movement. For movement imagery of right hand, maximum upto 50% band power attenuation was observed in contralateral (C3 w.r.t C4) hemisphere in the alpha frequency range (8–13 Hz) [13]. For geometrical figure rotation, the peak of the power spectrum was increased (upto 100%) in right hemisphere rather than left in the occipital area for the alpha frequency range (8–13 Hz) [22]. For trivial multiplication, the peak of the power spectrum was increased (75%) in left hemisphere rather than right hemisphere in the frontal area for the alpha frequency range (8–13 Hz) [23]. For non trivial multiplication, the peak of the power spectrum was increased (120%) in left hemisphere rather than right hemisphere in the parietal area for the alpha frequency range (8–13 Hz).

The data was preprocessed using Wavelet packet transform to extract the most relevant information from the EEG signal [14]. By applying Wavelet packet trans

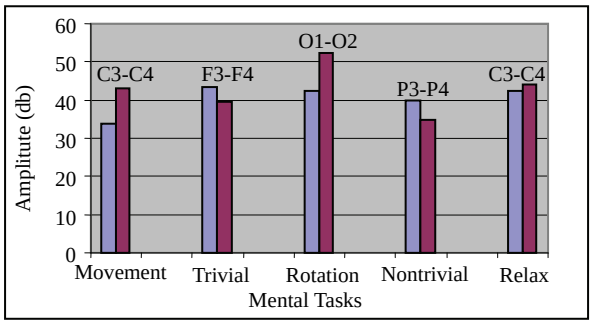

Figure 3. Maximum average change in amplitude of PSD.

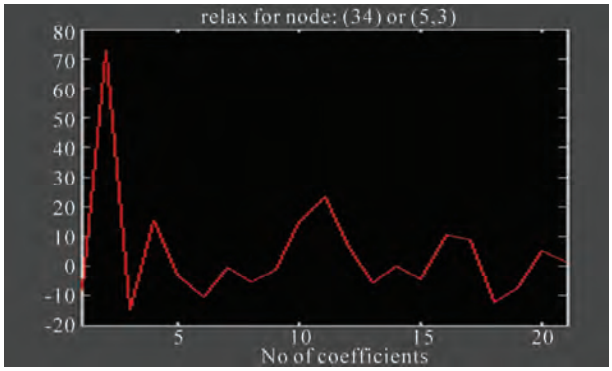

Figure 4. Wavelet coefficient for relax task.

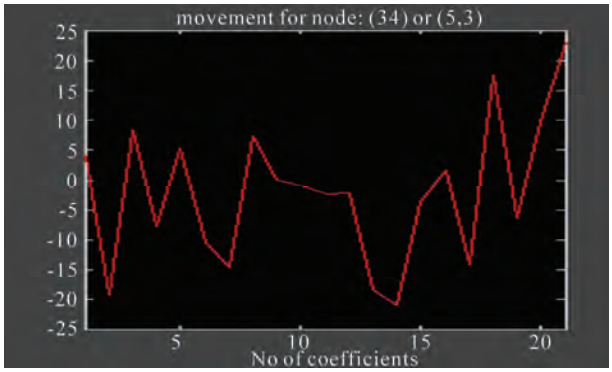

Figure 5. Wavelets coefficient for right hand movement task.

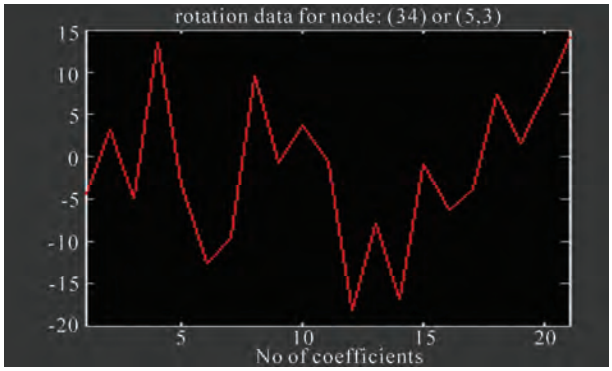

Figure 6. Wavelets coefficient for geometrical figure rotation task.

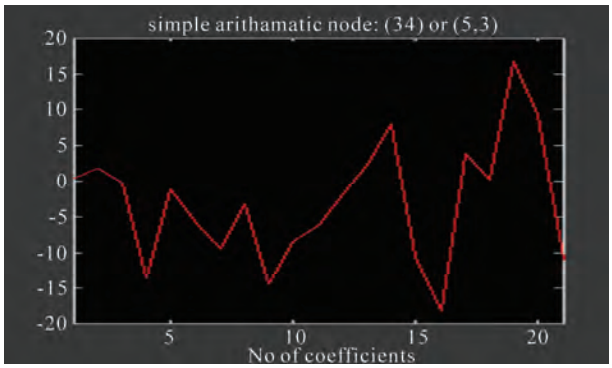

Figure 7. Wavelets coefficient for simple arithmetic task.

Copyright © 2010 SciRes.

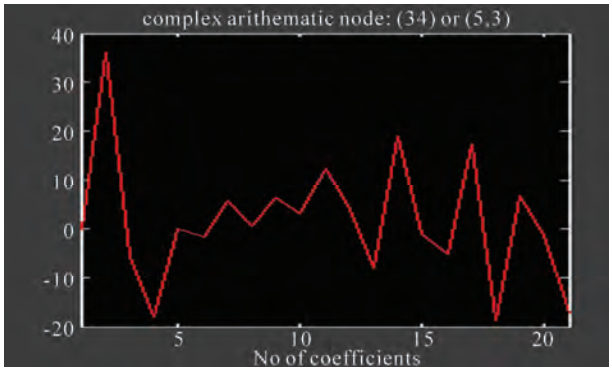

Figure 8. Wavelets coefficient for complex arithmetic task.

form on the original signal wavelet coefficients in the (8–13 Hz) frequency band at the 5th level node (5, 3) were obtained as shown in **Figures 4-8** We were able to reduce 1 second of EEG data to 21 coefficients. The signal was reconstructed at node (5, 3). These coefficients are scaled and used as the best fitting input vector for classifiers.

2.5. Classifiers

We have compared three classifiers: Multilayer Back propagation Neural Network (MLP-BPNN), Support Vector Machine and Radial Basis Function Neural Network to discriminate various mental activities. All three classifier were fed with the same dimensional feature data under identical conditions.

1) Multilayer Back propagation Neural Network

For this classifier, a two layer feed forward neural network was used with topology of {10, 1} 10 neurons in hidden layer and 1 neuron in output layer. The neural network was designed to accept a 21 element input vector and give a single output. The output neuron was designed to give 0 for baseline (relax task) and 1 for mental task. The five different training methods used for this classifier were Gradient Descent, Levenberg-Marquardt, Resilient Back propagation, Conjugate Gradient Descent and Gradient Descent back propagation with movementum [15,16,17]. Parameter used for five training methods of neural network for classification of five mental tasks as shown in the **Table 2.**

2) Support Vector Machine

Input data as two sets of vectors in an n-dimensional space, an SVM will construct a separating hyperplane in that space, one which maximizes the margin between the two data sets.The solution of the SVM is based only on those data points that are at the margin and called support vectors [18].

A kernel is utilized to map the input data to a higher dimensional feature space so that the problem becomes linearly separable. The kernel plays a very important role in the performance of the SVM applications. In the present study linear and polynomial kernel functions have

Table 2. Parameter used for different algorithms with to pology {10, 1}.

Gradient descent method	
Topology {10,1}	A=.01
MSE=1exp-(5)	
Epoch=5000	
Levenberg-Marquardt	
Topology {10,1}	Mu=.01
MSE=1exp-(5)	
Epoch=5000	Mu_dec=0.1and Mu_inc =10
Resilient Back propagation	
Topology {10,1}	A=.01
MSE=1exp-(5)	
Epoch=5000	B=0.75 and β_1=1.05
Conjugate gradient descent	
Topology {10,1}	A=.01
MSE=1exp-(5)	
Epoch=5000	
Gradient descent with momentum	
Topology {10,1}	A=.01. Mu = 0.01
MSE= 1e-5	
Epoch=5000	

work (RBFNN) classifier was used. A two layer network was implemented with 21 input vectors, a hidden layer with Gaussian activation function consisting as many as hidden neurons as input vectors and one neuron in the output layer [19].The output layer has 1 neurons and neuron gives output as 1 for a particular task. In case of relax task, this value is 0.

2.6. Performance

The study evaluated the performance of three classifiers for classification of five mental tasks. 60% of entire EEG data (five sessions, five mental tasks with nine subjects) was taken as training data. Remaining 40% of EEG data was taken as test data and the performances were recorded. The entire analysis of the recorded data was carried out using Matlab® 7.0 from Mathworks Inc., USA.

Performance (RC) is calculated in percentage (%) as ratio between correctly classified patterns in the test set to the total number of patterns in the test set [20].

$$Rc = \frac{\text{Number of correctly classified test patterns}}{\text{Total number of patterns in the test set}}$$

3. RESULTS & DISCUSSION

Nine right-handed male subjects participated in the experiments. The subjects were asked to perform five mental tasks namely relaxed, movement imagery, geometrical figure rotation and arithmetic task (trivial and non trivial multiplication). Out of 50 sec data recorded data the most relevant one second epoch of signal were used for classification of each mental task. WPT is an

Copyright © 2010 SciRes.

excellent signal analysis tool, especially for non stationary signals. Hence in the present study, WPT was used for feature extraction [21].

As per literature [11,12,13,22,23] most prominent area of brain for domain of information during five mental tasks was shown in **Table 3** For relaxed, the peaks of power spectrum almost coincide in central area at a particular base frequency .For arithmetic simple (trivialmultiplication), it was observed that the amplitude of the power spectrum for alpha frequency range (8–13 Hz) increased left hemisphere rather than right hemisphere in frontal region.

For arithmetic complex (non trivialmultiplication), it was observed that the amplitude of the power spectrum for alpha frequency range (8–13 Hz) increased left hemisphere rather than right hemisphere in parietal region. For geometrical figure rotation, the peak of the power spectrum in the alpha frequency range (7–13 Hz) increased right occipital area. For movement imagery, the peak of the power spectrum in the alpha frequency range (7–13 Hz) had an attenuation central area.

The present study was a comparison of three classifiers to discriminate five mental tasks effectively. **Tables 4-6** shows the performance of neural network with resilient back propagation training method, support vector machine and radial bases function Neural Network for classifying of mental tasks w.r.t baseline as shown in **Figure 9**.

From **Tables 4-6** we can say that RBF neural network method has best performance among all the classifiers for classification of mental tasks w.r.t baseline. By using RBF Neural Network 100% accuracy was obtained. While classification ,Resilient back propagation training method showed better performance than other (Gradient Descent method Levenberg-Marquardt, Conjugate Gradient Descent and Gradient Descent back propagation with movementum) back propagation training methods.

Table 3. Domain of information.

Tasks	Domain of information	(Contralateral/ Ipsilateral)	Type of change in amplitude of alpha rhythm(8-13
Movement Imagination	Central	Contralateral	Decreased
Arithmetic Simple	Frontal,	Ipsilateral	Increased
Geometrical figure rotational	Occipital	Ipsilateral	Increased
Arithmetic complex	parietal	Ipsilateral	Increased
Base line	Occipital, Central	Contralateral	Coincide

Table 4. Comparisons of different NN training methods.

Tasks / Method	Baseline and Arithmetic simple	Baseline and Arithmetic complex	Baseline and Rotation	Baseline and movement
Gradient Descent Back Propagation	95%	95%	87.5%	90%
Leveberg-Marquardt	95%	90%	90%	92.5%
Resilient Back Propagation	97.5%	95%	95%	95%
Conjugated Gradient BP	97.5%	92.5%	92.5%	92.5%
GD BP with Momentum	95%	95%	90%	90%

Table 5. Comparisons of different kernel function.

Tasks / Method	Baseline and Arithmetic simple	Baseline and Arithmetic complex	Baseline and Rotation	Baseline and movement
Linear Function	57.5%	55%	57.5%	57.5%
Polynomial Function	55%	57.5%	62.5%	62.5%

Table 6. Performance using radial basis function.

Tasks / Method	Baseline and Arithmetic simple	Baseline and Arithmetic complex	Baseline and Rotation	Baseline and movement
Radial bass Function network	100%	100%	100%	100%

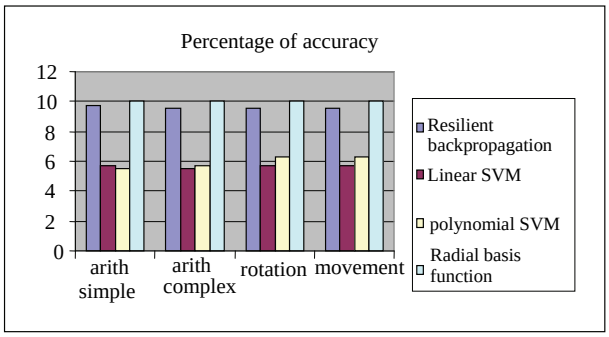

Figure 9. Performance of comparision using three classifiers.

4. CONCLUSIONS

This for various applications of BCI systems, it is necessary that EEG feature related to the human intentions were to be uniquely identified as accurate as possible. In this study, nine healthy male subjects were selected to investigate three classifiers of discriminating five mental

Copyright © 2010 SciRes.

tasks (relaxed state, movement imagery of right hand, geometrical figure rotation, arithmetic simple task, arithmetic complex task) effectively.

The result showed the performance of neural network with resilient back propagation training method, support vector machine and radial bases function Neural Network for classifying of mental tasks w.r.t baseline. RBF (Radial Basis Function) neural network method has best performance among all the classifiers for classification of mental tasks w.r.t baseline. By using RBF Neural Network 100% accuracy was obtained. While classification, Resilient Back Propagation training method showed better performance than other (Gradient Descent method, Levenberg-Marquardt, Conjugate Gradient Descent and Gradient Descent Back Propagation with movementum) back propagation training methods. The main conclusion is that the Radial baisis function network was found to be most suitable in various applications of BCI systems.

5. ACKNOWLEDGEMENTS

The authors would like to acknowledge their gratitude to the staff of EEG Laboratory at Sir Ganga Ram hospital, New Delhi for the help in carrying out the experiment.

REFERENCES

[1] Lotte, F., Congedo, M., Lecuyer, A., Lamarche, F., Arnaldi, B. (2007) A review of classification algorithms for EEG bases brain computer interface. *Journal of Neural Engineering*, **4**, 1-13.

[2] Wolpaw, J.R., Birbaumer, N., Farland, D.J., McPlurtscheller, G., Vaughan, T.M. (2002) Brain computer interfaces for communication and control. *Clinical Neurophys*, 767-791.

[3] Pfurtschelle, G., Flotzinger, D. and Kalcher, J. (1993) Brain computer interface a new communication device for han- dicapped people. *J Microcomput. Applicate*, **16**, 293-299.

[4] Wolpaw, J.R., Vaughan, T.M. and Donchin, E. (1996) EEG based communication prospects and problems. *IEEE Transactions on Rehab. Engineering*, **4,** 425-430.

[5] Keirn, Z.A. and Aunon, J.I. (1990) A new mode of communication between man and his Surroundings. *IEEE Transactions on Biomed. Eng*, **37**, 1209-1214.

[6] Wolpaw, J.R., Leob, G.E., Allison, B.Z. Donchin, E. Turner, J.N. (2006) BCI meeting 2005-wokshop on signals and rerecording methods. *IEEE Transactions on Neural Systems and Rehabilitation Engineering*, **14**, 138-141.

[7] Muller, G.R., Scherer, R., Braunesis, C., Pflurtscheller, G. (2005) Steady state visual evoke potential based communication impact of harmonic frequency components. *Journal of Neural Engineering*, **2**, 123-130.

[8] Elean, A., Curran and Jamaica Strokes (2003) Learning to control brain activity: a review of the production and control of EEG components for driving bain compute interface systems. *Journal of Brain and Cognition*, **51**, 326-336.

[9] Wolpaw, J.R., Farland, D.J., McVaughan, T.M. (2003) The wads worth centre brain computer interface research and development program. *IEEE Transactions on Neural System and Rehabilitation Engineering*, **11**, 204-207.

[10] Boostani, R., Graimann, B., Moradi, M.H, Plurfscheller, G. (2007) Comparison approach toward finding the best feature and classifier in cue BCI. *Journal of Medical and Biological Engineering and Computing*, **45**, 403-413.

[11] Pfurtscheller, G., Neuper, C., Schlogl, A. and Lugger, K. (1998) Separability of EEG signals recorded during right and left motor imagery using adaptive auto regressive parameters. *IEEE Transactions on Rehabilitation Engineering*, **6**, 316-325.

[12] Palaniappan, R. (2006) Utilizing gamma band to improve mental task based brain-computer interface design. *IEEE Transactions on Neural Systems and Rehabilitation Engineering*, **14**, 299-303.

[13] Santhosh, J., Bhatia, M., Sahu, S., Anand, S. (2004) Quantitative EEG analysis for assessment to plan a task in ALS patients, a study of executive function (planning) in ALS. *Journal of Cognitive Brain Research*, **22**, 59-66.

[14] Akay, M. (1995) Wavelet in biomedical engineering. *Journal of Annals of Biomedical Engineering*, **23**, 529-530.

[15] Ravi, K.V.R. and Palaniappan, R. (2006) Neural network classification of late gamma band electroencephalogram features, Journal of Soft Computing A Fusion of Foundations. *Methodologies and Applications*, **10**, 163-169.

[16] Haykin, S. (2000) Neural Network a comprehensive foundation. 2nd edition, *Prentice Hall*.

[17] Hagen, M., Demuth, H. and Beale, M. (1996) Neural Network design. *Boston MA, PWS Publishing*.

[18] Zhou, S.M., Gan, J.Q., Sepulveda, F. (2008) Classifying mental tasks based on features of higher-order statistics from EEG signals in brain-computer interface. *Information Sciences: an International Journal*, **178**, 1629-1640.

[19] Chen, S., Cowan, C.F.N. and Grant, P.M (1991). Orthogonal least squares learning algorithm for radial basis function networks. *IEEE Transactions on Neural Networks*, **2**, 302-309.

[20] Cheng, M., Gao, X., Gao, S., Xu, D. (2002) Design and implementation of a brain computer interface with high transfer rates. *IEEE Transactions on Biomedical Engineering*, **49**, 1181-6.

[21] Ting, W., Zhenga, Y.G, Bang-huaa, Y., Hong, S. (2008) EEG feature extraction based on wavelet packet decomposition for brain computer interface. *Measurement, Elsevier Journal*, **41**, 618-625.

[22] Nikolaev, A.R. and Anokhin, A.P. (1998) EEG frequency ranges during reception and mental rotation of two and three dimensional objects. *Neuroscience and Bheaviour Physiology*, **29**, 203-223.

[23] Osaka, M. (1984) Peak alpha frequency of EEG during a mental task: task difficulty and hemisphere difference. *Journal of Psychophysiology*, **21**, 101-105.

Copyright © 2010 SciRes.

J. Biomedical Science and Engineering, 2010, 3, 206-212 **JBiSE**
doi:10.4236/jbise.2010.32027 Published Online February 2010 (http://www.SciRP.org/journal/jbise/).

Pressure shift mediated anoikis of endothelial cells in the flow field in vitro

Jia Hu[1], Er-Yong Zhang[1], Jiang Wu[2], Wei-Lin Xu[3], Huai-Qinq Chen[2], Ying-Kang Shi[1], Ying-Qiang Guo[1,3*]

[1]Dept. Thoracic & Cardiovascular surgery, West China Hospital of Sichuan University, Chengdu, China;
[2]Institute of Biomedical Engineering, West China Medical Center, Sichuan University, Chengdu, China;
[3]The State Key Lab of Hydraulics on High Speed Flow, Sichuan University, Chengdu, China.
Email: *drguoyq@hotmail.com

Received 16 November 2008; revised 10 December 2009; accepted 13 December 2009.

ABSTRACT

Dramatic changes of pressure in the local circulation flow field would lead to alterations in biorheological characteristics of Endothelial cells(ECs), and futher resulted in the apoptosis induced by loss of anchorage, a form of cell death known as anoikis. In this study, we set levels of pressure(negative and positive pressure) loaded ECs groups and non-activated cultured ECs ,single shear stress loaded ECs as control group to demonstrate the effects of pressure shift on cell morphogenesis and adhesion. Furthermore, we investigate the effects of pressure shift on ECs proliferation and apoptosis to elucidate the influences of pressure shift on vitality of ECs. We present these data here to suggest that the negative pressure might be another important factor beyond velocity and shear stress in biomechanical impairment on ECs, then to trigger the apoptosis with the extracellular matrix (ECM) detachment (anoikis). As the negative pressure is thought to play a role in the anoikis process, these results have implications for both the path- ogenesis and therapeutics investigations of stenostic vessel diseases and the future vascular tissue engineering.

Keywords: Endothelial Cells; Anoikis Cell Adhesion; Pressure; Flow Field

1. INTRODUCTION

The role of the Extracellular matrix (ECM) goes beyond providing the physical scaffold on which the Endothelial cells (ECs) adhere, it also provides ECs with information for proliferation, migration, differentiation and survival through the structural and functional links. Loss of these links with ECM could induce apoptosis which has been termed as anoikis, a Greek ancient word meaning "homelessness". Previous Hydrodynamics investigations on the mechanisms of the cardiovascular wall damage, in vitro assays and in vivo models, focused on the relationship between the velocity, shear stress and the ECs, while investigations on the pressure shift (especially the negative pressure) mediated anchorage-related apoptosis (anoikis) of ECs in vitro were rarely described. Based on the engineering hydrodynamics advance, the dilated downstream of the stenosis could lead to a decrease of wall pressure and an increase of pressure pulsation, further resulted in a low pressure environment to generate the cavitation phenomenon which would damage the wall structure severely [1,2]. We therefore suggest that the distribution and variations of pressure located downstream of the stenostic vessel may be another factor for biomechanical impairment on ECs, then may contribute to the pathogenesis of cardiovascular stenostic diseases.

In the present study, we developed an efficient assay for the effects of pressure shift on the expression of cytoskeleton(F-actin), Vascular adhesion molecule (VCAM) and one of the important transmembrane heterodimeric receptors(IntegrinαVβ3). Combined with our analysis of Ecs proliferation, apoptosis and the expression of apoptosis-associated protein (Caspase-3, P53, Bcl-2 and Fas), we also presented correlative evidence that the negative pressure played a certain role in the genesis and progress of anoikis in the flow field in vitro.

2. MATERIALS AND METHODS

2.1. Cell Cultures and Maintenance

Human umbilical vein ECs EA.Hy926 obtained from Jiangsu Institute of Hematology were cultured in a 5% CO_2 atmosphere at 37³C, in RPMI medium (Gibco BRL, USA) supplemented with 10% fetal bovine serum(FBS). Cells were detached by D-Hank's solution with 0.25% trypsin 1ml and then repelleted to suspend in the RPMI medium. The supernatants were collected and centrifuged at 1000rpm for 5min in a MIKRO12–24 centri-

*The study supported by NSF of China (Grant NO. 30700149, 30670515 and Youth Scientific Fund of Sichuan University (Grant NO.06062).

fuge at 4℃. The purified cells were collected, tested as previously described [3,4] and viability was determined by trypan blue exclusion. After been attached to the fibronectin plates (plastic plates coated for 30min at 37℃ in CO_2 incubator with 50ug/ml of fibronectin, washed twice with D-Hanks solution before use), the cells were grown at 37℃ in 5% CO_2 incubator (Heraeus, Germany) with RPMI medium to confluence.

2.2. Levels of Pressure Loading in the Flow Experiment

The flow system was remanufactured from the system which was previously described by H.Q. Chen [5] (**Figure 1**). The plastic slides containing the endothelial monolayer were inserted into the parallel-plate flow chamber that was installed between the upper and lower reservoir connected by tubing. Continuous flow in this system was maintained by circulating cell culture medium (as arrow shown in **Figure 1**) by a peristaltic pump installed between the upper and lower reservoir, while altitude difference provided constant flow through the chamber to expose the bottom of the inserts to laminar flow at a consistent levels of pressure. As the periodical fluctuation of the pressure that caused by the peristaltic pump and fluid flow could interfere the experiment results, we set two reservoirs as a feedback regulator to maintain consistent and steady pressure. The numerical analysis of the chamber flow performed by Fluent 6.0 indicated the flow in chamber was 1) laminar flow; 2) two-dimensional flow; 3) sufficient developed steady flow; 4) the pressure distributed in chamber averagely; 5) maintained steady flow in negative pressure environment. We set nonactivated cultured ECs(Con), single shear stress (1.85 dyn/cm^2) loaded ECs (S-con)as control groups and levels of pressure loaded groups in the context of low shear stress (1.85dyn/cm^2): –10cmH_2O(N_{10}), –20cmH_2O(N_{20}), –40cmH_2O(N_{40}), +20cmH_2O(P_{20}) and +40cmH_2O(P_{40}).

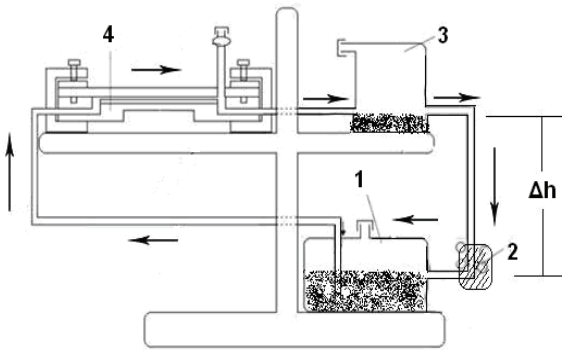

Figure 1. The schematic diagram of the improved paral alized by using BODIPY FL phalloidin (Molecularlel plate flow chamber: 1) upper reservoir; 2) peristaltic pump; 3) lower reservoir and; 4) flow chamber.

2.3. F-actin and Adhesion Molecule Analysis

Loaded by levels of pressure for 2h and fixed by 4% paraformaldehyde at 4℃ for 15min, ECs were permeabilized in 1% Triton X-100 and then F-actin was visu Probes, USA). The cell membranes were imaged at an excitation of 505nm and emission of 512nm by the laser confocal scanning microscope (Bio-Rad Mre-1024ES) and fluorescence density value analysis of F-actin were tested by IMAGEPRO plus 5.0(Media Cybernetics Inc.). The collected cells were incubated with specific monoclonal antibody (PE-VCAM monoclonal antibody in 1:40 dilution, FITC-IntegrinαVβ3 monoclonal antibody LM609 in 1:100 dilution) respectively for 20 minutes. Cells were then resuspended in PBS to a density of 2～3×10^{5}cells/ml. The levels of cell surface fluorescently labeled protein were quantified by immunofluorescent flow cytometry (ELITE ESP, Coulter, USA): we set the fluorescent density value of non-activated cultured ECs(Con) as 100% and the fluorescent density value of other groups as Related fluorescent density value (RF%).

2.4. Proliferation and Apoptosis Assay

To label chromosomal DNA with propidium iodide (PI), the pressure loaded cells were washed twice with PBS, 0.25% trypsin and the resulting cell pellet was resuspended at 1×10^5 cells/ml in PBS containing 100ug/ml of PI and 500mg/ml RNase (Sigma; St. Louis, MO) for a 30min incubation at 4℃. The stained cells were then analyzed by flow cytometry and quantification was performed by using Cell Quest (Becton－Dickinson, Mountain View, CA). We use PI [Proliferation Index, PI=(S + G_2M) / ($G_{0/1}$+ S + G_2M) × 100%] and AI (Apoptosis Index, AI=number of cells displaying red fluorescence lower than the G0-G1 diploid peak / total number of cells × 100%) to assay ECs proliferation and apoptosis changes in cell cycle. RT-PCR technology as previously described [6,7,8] and Western blot analysis were applied to caspase–3, p53, Bcl–2 and Fas protein expression assay.

2.5. Statistics

All experiments were repeated three times. Statistic information was analyzed by one sample T-test with SPSS11.5 and differences at $P<0.05$ were considered statistically significant.

3. RESULTS

3.1. The Effects of Pressure Shift on Cells Morphological Changes

Stained green-fluorescence, the F-actin filament of non-activated cultured ECs(Con) showed no oriented

Copyright © 2010 SciRes.

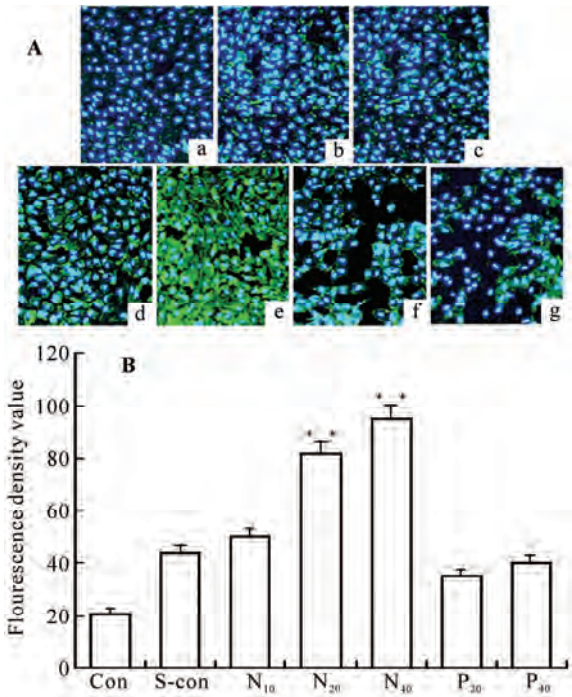

Figure 2. The effects of pressure shift (loaded for 2h) on F-actin A. The variations of the distribution and organization of F-actin (A: con; B: S-con; C: N_{10}; D: N_{20}; E: N_{40}; F: P_{20}; G: P_{40}) B. The quantitative analysis of the effects of pressure shift on F-actin expression (n=6, **compared with S-Con group p<0.01).

shear stress for 2h (S-con), the F-actin filament showed a tendency to orient parallel to the long axis of the cells (**Figure 2 B**). As the negative pressure increasing, the redistribution and organization of F-actin were more obviously oriented parallel to the long axis of the cells and flow vector (**Figure 2 c, d, e**). However, the F-actin filament presented no orientation propensity to the positive pressure changes (**Figure 2 f, g**). As the fluorescence value density of BODIPY FL phalloidin was consistent with the F-actin content, we analyzed the expression of F-actin by testing the green-fluorescence value density with Image Pro Plus 5.0. The expression of F-actin was generally enhanced by the increasing negative pressure (n=6, compared with S-con p<0.01), while no significant change of F-actin expression was observed in the positive pressure loaded group.

3.2. The Effects of Pressure Shift on Cell Adhesion Molecules

When exposed to levels of pressure and loaded for 2h, the expression of VCAM and IntegrinαVβ3 demonstrated significant changes with different tendency:

1) VCAM expression up-regulated with increasing positive pressure and down-regulated with gradually increasing negative pressure;

Table 1. The effects of pressure shift (loaded for 2h) on the expression of VCAM and IntegrinαVβ3 (n=6,**compared with S-Con group p<0.01).

Groups	Assay Items (relative fluorenscence values)	
	VCAM	Integrin αVβ3
con	100±0	100±0
S-con	110.7±31.2	151.5±16.9
N10	113.8±11.3	152.5±29.7
N20	108.7±11.8	217.4±50.2**
N40	78.3±4.9**	328.7±14.5**
P20	144.7±22.6**	233.2±31.7**
P40	155.8±24.5**	270.3±23.5**

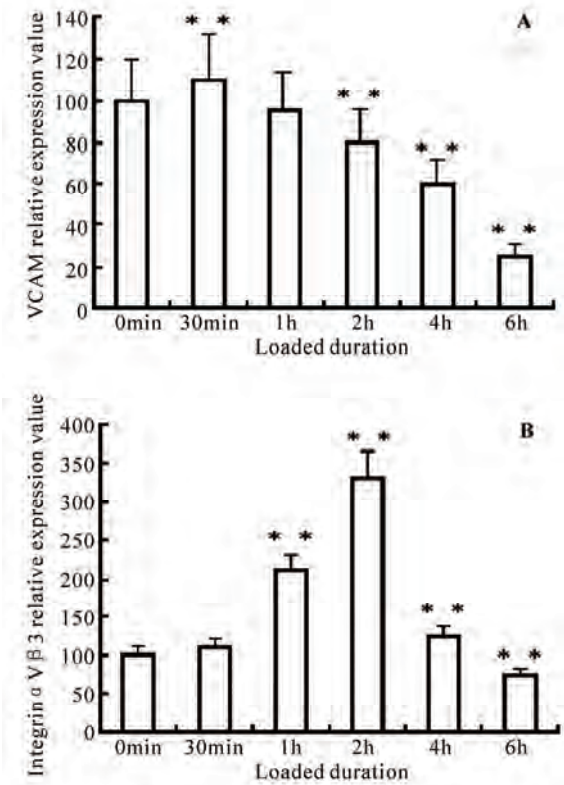

Figure 3. The duration-dependent effects of –40cmH_2O pressure on the expression of VCAM and IntegrinαVβ3 A. The variations of VCAM expression B. The variations of IntegrinαVβ3 expression (n=6**compared with S-Con group p<0.01).

2) The increasing negative and positive pressure both resulted in the intensified expression of the IntegrinαVβ3 (**Table 1**).

As –40cmH_2O pressure caused a significant changes in the expression of VCAM and IntegrinαVβ3, we further studied the duration-dependent effects of the –40cm H_2O pressure on the expression of VCAM and Integri-

Copyright © 2010 SciRes.

nαVβ3: VCAM expression down-regulated with the pressure loaded duration while the expression of IntegrinαVβ3 up-regulated initially and started to decrease gradually after pressure loaded for 2h (Electronic supplementary Material).

3.3. The Effects of Pressure Shift on ECs Proliferation and Apoptosis

As Loaded by levels of pressure for 2h, groups of ECs show different viability changes: 1) certain proliferative activity could be observed in the low negative pressure loaded groups (N_{10}, N_{20}) and significant apoptosis only occurred in the –40cm H_2O pressure loaded group (N_{40}); 2) significant changes of proliferation and apoptosis were not observed in the positive pressure loaded groups(P_{20}, P_{40}). We therefore analyzed the time course of the –40cmH_2O pressure-induced proliferation and apoptosis changes in ECs (**Table 2**).

As the RT-PCR results showed, the expression of caspase-3 was only significantly up-regulated in N_{40} group. We therefore investigated the duration dependent effects of –40cmH_2O pressure on caspase-3 and apoptosis associated protein: P53、Bcl-2 and Fas by Western blotting analysis (**Figure 4**): the expression of Caspase-3, Bcl-2 and Fas protein up-regulated with duration-dependence in –40cmH_2O pressure loading, while P53 protein showed a fluctuated increasing expression during the first 4h negative pressure (–40cmH_2O) loading and sharply decreased back to the baseline in the next 2h.

Table 2. The duration-dependent effects of －40cmH2O on the cell cycle, proliferation and apoptosis index ($\bar{x} \pm s$, n=6).

Group	Cell cycle distribution (%)			PI (%)	AI (%)
	G0/G1	S	G2/ M		
0 min	59.1±4.9	19.8±5.8	22.7±1.5	41.4±7.9	0.1±0.1
15 min	57.8±2.5	22.9±7.8	22.2±5.6	44.8±7.5	0.4±0.0
30 min	67.2±4.4	22.5±1.2	10.9±4.1	33.2±6.6	6.5±0.6
1 h	82.6±3.6	7.6±0.5	11.9±4.6	18.4±5.1	10.2±0.3
2 h	81.6±7.5	6.8±0.4	11.2±6.7	17.4±2.0	18.4±0.6
4 h	83.6±11.2	7.0±0.2	9.1±0.5	15.2±7.3	19.4±024
6 h	90.6±13.3	5.3±0.3	5.2±1.6	10.1±5.9	27.6±1.1

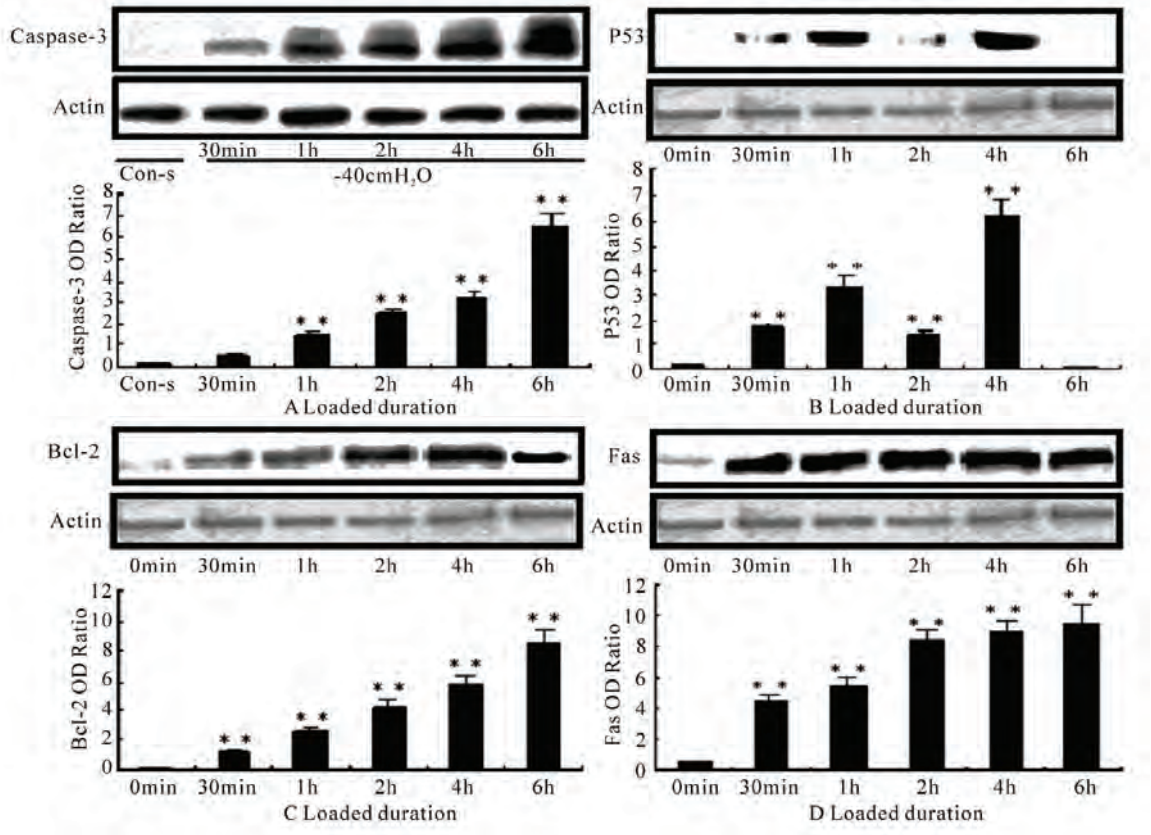

Figure 4. Western blotting results of anoikis-associated proteins A Caspase-3; B P53; C Bcl-2; D Fas protein.

Copyright © 2010 SciRes.

4. DISCUSSION

Anchorage-related apoptosis appeared in ECs which were experimentally detached from their extracellular matrix had suggested the role of ECM as a suppressor of apoptosis induced by biomechanical forces [9]. Since the discovery of adhesion-activated tyrosine kinase pp125 FAK [10,11], a web of signaling networks spread out and revealed the multiple pathways that could regulate the adhesion-related apoptosis(anoikis). Through these pathways, variety of biomechanical factors in flow field was capable of triggering the anoikis process. Many studies demonstrated [12,13] that observable changes in cytoskeleton and viability of ECs only occurred under the condition of loaded shear stress>8 dyn/cm2 and duration>24h. To differ the focus from previous reports in the literature, we therefore adopted extremely low shear stress(1.85dyn/cm2) and short pressure loading duration (≤6h) to evaluate the pressure shift effects specifically.

The cytoskeleton, particularly the content and distribution of F-actin, is a strong determinant in the mechanical properties of ECs, such as cell shape, stiffness and cytoplasm viscosity. We had identified that the significant changes in F-actin expression and cell shape were only observed after certain negative pressure exposure for 2h(N_{20} and N_{40} group). Interestingly, up-regulated expression of F-actin and streamlined cell shape resulted in down-regulated expression of VCAM、up-regulated expression of apoptosis-associated protein(especially Fas protein) and increased Apoptosis Index(AI%). However, these findings were different from previous studies that streched cells were found to be susceptible to rescuing from anoikis [14,15]. As our previous data demonstrated [5], when exposed to high shear stress, the adhesion ability of cells enhanced with the concentrated distribution of F-actin from the cortex to the perinuclear area of cells. We therefore considered that the increasing negative pressure may disassembly the F-actin filaments to monomers but inhibited its reorganizaton in the perinuclear area of cells, further resulted in the increased amount of F-actin presenting only in the cortex but sharply decreased the adhesion ability. Some evidence demonstrated that the cytoskeletal disruption regulated the FasL expression and were associated with anoikis [16], which was coincident with our findings in the consistent up-regulation of F-actin and Fas expression with negative pressure(–40cmH_2O) loaded for 2h. However, the detailed mechanism of this process remains to be determined by further investigations. In the experiment, we demonstrated the readily apparent differences between F-actin and ECs viability of negative versus positive pressure loaded ECs, which implied that the negative pressure could regulate both signaling molecules and apoptosis-related protein that were associated with the cytoskeleton, and as such may together regulate anoikis by serving as sensors of cytoskeletal integrity.

Sufficient and appropriate adhesion to the ECM, represented by the VCAM, is critical for proper ECs function and signaling. With the organization of the cytoskeleton and transduction of biochemical signals, the external (ECM) to internal (ECs) signaling transduction are mediated by the integrins [17]. As the member of the integrin family, IntegrinαVβ3 is capable of recognizing and bind many ECM proteins and induce intracellular biochemical responses to regulate anoikis process[18]. Therefore as a signaling transductant, the expression of IntegrinαVβ3 were observed significantly up-regulated in both positive and negative pressure groups with enough loaded duration and intensity (**Table 1**). Furthermore, we demonstrated the up-regulated expression of VCAM with low AI% in positive pressure loaded groups(P_{20}, P_{40}) and significant down-regulated expression of VCAM accompanied by high AI% in N40 group with duration-dependence, which implied that the negative pressure (–40cmH_2O) induced apoptosis could be adhesion-dependant. However, in our time course experiment on IntegrinαVβ3 and apoptosis-associated proteins (**Figure 4**), the up-regulated expression of IntegrinαVβ3 in ECs were consistent with the intensified expression of Caspase-3、Bcl-2 and Fas protein when exposed to –40cmH_2O pressure loaded for 2h, during which the expression of VCAM showed insignificantly changing. The findings give evidence of the IntegrinαVβ3 mediating some proapoptotic responses that could contribute to the integrated mechanism of negative pressure induced anoikis process with adhesion-independence. In support of our findings, previous studies [19] suggest the apoptotic effects observed with IntegrinαVβ3 antagonist (echistatin) in ECs were not due to detachment but rather due to activation of intracellular signals.

Multiple pathways could initiate the caspase activation to induce anoikis process converging at the level of effector caspases-3 [20]. As two main pathways in which caspases cascade are initially activated, the death receptor pathway and mitochondrial pathway are regulated by a host of key effector proteins, such as P53、Bcl-2 and Fas proteins which have been previously confirmed as important regulators in different pathways [21,22]. As we noted, the expression of P53 showed a fluctuated increasing within 4h negative pressure (–40cmH_2O) loading (**Figure 4**), which might imply the multiple functions of P53 protein in regulating the early stage of anoikis process. During the first 2h, P53 expression up-regulated initially and then down-regulated with the up-regulation of Bcl-2 expression. Meanwhile, the decreasing PI% that still exceeded the gradually increasing AI% (**Table 2**). Published studies [23] demonstrated that P53 could encode a transcription factor to activate genes

Copyright © 2010 SciRes.

involved in growth arrest (p21, GADD45) and also could control the anti-apoptotic protein Bcl-2 in mitochondrial pathway. Therefore, we considered the main function of P53 protein during the first 2h was inducing the growth arrest to reduce the sensitivity of ECs to apoptosis. While the slight down-regulated P53 expression on the 2h checkpoint could be explained by some evidence that P53 and Bcl-2 may combined as p53-Bcl2 complexes in contributing to the direct mitochondrial p53 pathway of apoptosis [24]. Although much of p53-mediated apoptosis signals were through mitochondrial pathways, p53 inducible genes could alter the localization of death receptors normally found in the cytoplasm to the cell surface to enhance the sensitivity to death receptor-mediated apoptosis (Fas) [25]. Therefore, at the end of the first 2h, the homeostasis in the proliferation and apoptosis of ECs broke down (AI% started to exceed PI %) with the significantly up-regulated Fas expression and P53 expression. Meanwhile, the expression of VCAM showed a significant down-regulation, which further supported the notion that the negative pressure induced apoptosis could be adhesion-dependent (anoikis). As we noted, the P53 expression surprisingly decreased back to the baseline with up-regulated Bcl-2 expression after being loaded by negative pressure ($-40cmH_2O$) for 4h. During the same period, consistent with the up-regulated Fas expression, the expression of Caspase-3 still up-regulated with increasing AI%, which indicated the predominating function of Fas protein in the latter stage(after 4h) of negative pressure induced anoikis process.

We have confirmed a certain role of negative pressure, particularly $-40cmH_2O$ pressure, in biomechanical impairment on ECs with adhesion-dependence. While our preliminary investigations on the mechanism of negative pressure induced anoikis demonstrated that P53 acts dual function in regulating the early stage of anoikis process and Fas protein (death receptor pathway) predominated the end stage of the negative pressure induced anoikis process. These data give us insights into integrated investigations on mechanisms of downstream vascular impairment in stenostic vessel diseases (eg. atherosclerosis, post-stenostic aneurysm formation) and Integrin$\alpha V\beta 3$, P53, Fas represent attractive targets for protective therapeutics aiming at downstream vessels for a better long-term results in the patients with stenostic vessel dieases. However, the key to anoikis regulation depends on the sum of intrinsic and extrinsic input, It will be of interest for us to sort out the precise manner by which the architectural state of the cytoskeleton, integrin signal transduction events and posttranslational apoptotic factors are interrelated.

REFERENCES

[1] Xu, W.L., Liao, H.S., Yang, Y.Q. *et al*. (2002) Turbulent flow and energy dissipation in plunge pool of high arch dam. *J Hydraulic Research*, **40**, 471–476.

[2] Xu, W.L., Wang, W., Yang, Y.Q. *et al*. (1999) Numerical modeling of the water-air two-phase jet into a plunge pool. *J Hydrodynamics*, **11**, 1–5.

[3] Heurkens, A.H., Gorter, A., Vreede, T.M. *et al*. (1991) Methods for the detection of anti-endothelial antibodies by enzyme-linked immunosorbent assay. *J Immunol Methods*, **141**, 33–39.

[4] Edgell, C.J., McDonald, C.C. and Graham, J.B. (1983) Permanent cell line expressing human factor VIII related antigen established by hybridization. *Proc Natl Acad Sci*., **80**, 37342–37371.

[5] Chen, H.Q., Wei, T., Chen, Y.S. *et al*. (2004) Effect of steady and oscillatory shear stress on F-actin content and distribution in neutrophils. *Biorheology*, **41**, 655–664.

[6] Klein, D. (2002) Quantification using real-time PCR technology: Applications and limitations. *Trends Mol Med*, **8,** 257–260.

[7] Cosa, G., Focsaneanu, K.S., McLean, J.R.N. *et al*. (2001) Photophysical properties of fluorescent DNA-dyes bound to single- and double-stranded DNA in aqueous buffered solution. *Photochem Photobiol*, **73**, 585–599.

[8] Ginzinger, D.G. (2002) Gene quantification using real-time quantitative PCR: an emerging technology hits the main stream. *Exp Hematol*, **30**, 503–511.

[9] Meredith, J.E., Fazeli, B. and Schwartz, M.A. (1993) The extracellular matrix as a cell survival factor. *Mol Biol Cell*, **4**, 953–961.

[10] Schaller, M.D., Borgman, C.A., Cobb, B.S. *et al*. (1992) pp125 FAK, a structurally distinctive proteintyrosine kinase associated with focal adhesions. *Proc. Natl. Acad. Sci*., USA, **89**, 5192–5196.

[11] Schaller, M.D. and Parson, J.T. (1993) Focal adhesion kinase: an integrin-linked protein tyrosine kinase. *Trends Cell Biol*., **3**, 258–262.

[12] Dewey, C.F., Bussolari, S.R., Gimbrone, M.A. *et al*. (1981) The dynamic response of vascular endothelial cells to fluid shear stress. *J. Biomech Engineering*, **103**, 177–188.

[13] Davies, P.F. (1995) Flow-mediated endothelial mechanotransduction, *Physiol Rev*., **75**, 519–560.

[14] Chen, C.S., Mrkisch, M., Huang, S. *et al*. (1997) Geometric control of cell life and death. *Science*, **276**, 1425–1428.

[15] Flusberg, D.A., Numaguchi, Y. and Ingber, D.E. (2001) Cooperative control of Akt phosphorylation, bcl-2 expression, and apoptosis by cytoskeletal microfilaments and microtubules in capillary endothelial cells. *Mol. Biol. Cell*, **12**, 3087–3094.

[16] Ishida, K., Nagahara, H. and Kogiso, T. (2003) Cell adhesion aside from integrin system can abrogate anoikis in rat liver cells by down-regulation of FasL expression, not by activation of PI-3K/Akt and ERK signaling pathway. Biochem. Biophys. *Res. Commun*, **300**, 201–208.

[17] Frisch, S.M., Screaton, R.A. (2001) Anoikis mechanisms. *Curr Opin Cell Biol*., **13**, 555–562.

[18] Stupack, D.G. and Cheresh, D.A. (2002) Get a ligand, get a life: integrins, signalling and cell survival. *J. Cell Sci*., **115**, 3729–3738.

[19] Brassard, D.L., Maxwell, E., Malkowski, M. *et al*. (1999) Integrin$\alpha V\beta 3$-Mediated Activation of Apoptosis. *Exp*

Cell Res., **251**, 33–45.

[20] Simpson, C.D. *et al*. (2008) Anoikis resistance and tumor metastasis. *Cancer Lett.*, doi:10.1016/j.canlet.2008.05.029.

[21] Kitsis, R.N. and Mann, D.L. (2005) Apoptosis and the heart: a decade of progress. *J. Mol Cell Cardiol*, **38**, 1–2.

[22] Stoneman, V.E.A., Bennett, M.R. (2004) Role of apoptosis in atherosclerosis and its therapeutic implications. *Clin Sci*., **107**, 343–354.

[23] Mercer, J., Mahmoudi, M. and Bennett, M. (2007) DNA damage, p53, apoptosis and vascular disease. *Mutat Res.*, **621**, 75–86.

[24] Tomita, Y., Marchenko, N., Erster, *et al*. (2006) WT p53, but not tumor-derived mutants, bind to Bcl-2 via the DNA binding domain and induce mitochondrial permeabilization. *J. Biol Chem.*, **281**, 8600.

[25] Fais, S., Milito, A.D. and Lozupone, F. (2005) The role of FAS to ezrin association in FAS-mediated apoptosis. *Apoptosis*, **10**, 941–947.

Copyright © 2010 SciRes.

J. Biomedical Science and Engineering, 2010, 3, 213-216 **JBiSE**
doi:10.4236/jbise.2010.32028 Published Online February 2010 (http://www.SciRP.org/journal/jbise/).

Mg/Al complex oxides-A new type of solid basic catalyst for epoxidation

Heng Miao[1], Shi-Chao Xu[2*], Hai-Nan Wang[1], Wen-Xia Qin[1], Lin Lin Zhang[1], Ji-Mei Zhang[1], Juan Yang[1], Zhao Dai[1], Guo Zheng[1], En-Qi Tang[1]

[1]School of Environmental and Chemical Engineering, Key Laboratory of Hollow Fiber Membrane Materials and Membrane Processes (Ministry of Education), Tianjin Polytechnic University, Tianjin, China;
[2]Key Laboratory of Hollow Fiber Membrane Materials and Membrane Processes (Ministry of Education), and Research Institute Biologic and Spinning Materials, Tianjin Polytechnic University, Tianjin, China.
Email: *Justinxu777@gmail.com

Received 30 November 2008; revised 21 December 2009; accepted 22 December 2009.

ABSTRACT

Hydrotalcites known as anionic clays are found in nature. Hydrotalcites, hydrotalcite-like compounds, and calcined hydrotalcites (as mixed or complex oxides) as highly active, selective catalysts play an important role in many base/catalyzed reactions. Mg/Al hydrotalcite (MAH) as precursor was used to prepare Mg/Al metal complex oxides (MAO), used as epoxidation catalysts in the current research. In this paper, some primary physical and catalytic properties of MAH and MAO were investigated. The results indicated that the qualified MAH (Mg/Al mol ratio of 3) can be achieved when the suspension was crystallized under 80°C for 16h, and after being filtered, dried at 100 °C for 5h in a oven. MAO was prepared by calcining MAH for 4h in a muffle furnace, and calcination temperature was determined to be 500 °C by a differential scanning calorimeter (DSC). Crystal structure and parameters of MAH and MAO were characterized by X/ray diffraction (XRD), good crystal structure was observed and typical peaks of MAH were detected when 2θ was at 11.5 (003), 23.0 (006), 35.0 (009), and 61.0 (110), respectively. The morphology of calcined precursor, i.e. MAO, was investigated with scanning electron microscopy (SEM); the finer lamellar structure and smaller average size of 3μm was observed. Molding research was performed and confirmed by SEM, the results indicated that the surface bulge and cavity with size of several micrometers were increased, which simultaneously suggested the increasing of specific surface area. The catalytic activity of molding MAO was finally examined by using octanol as starting reagent and ethylene oxide as reactant, and narrower molecular distribution was observed comparing with the traditional catalyst-KOH.

Keywords: Mg/Al Hydrotalcites; Mg/Al Metal Complex Oxides; Molding, Epoxidation

1. INTRODUCTION

Recently Widely used in the varies fields, narrow distribution polyether shows advantages [1,2,3] consisting of low pour point, less pollution, and good compatibility. It has a relatively deep theoretical research and catalytic properties study at the laboratory stage at home and abroad in recent years. Currently, the study on hydrotalcites, as a kind of catalyst for synthesizing narrow distribution polyether, mainly deals with two aspects: one is the pure theoretical study, such as the characterization of hydrotalcites and surface property, etc; the other is water gas shift, nitrobenzene reduction, methane oxidation, and so on. However there is less report about the catalytic activity for ring-opening ethylene oxide [4,5] forming polyether. Although I. Hama [6,7,8] has made an initial attempt in this aspect, the effect of narrow distribution was not ideal and it had a certain distance applied in industrialization.

With its fast reaction rate and narrow molecular weight distribution, Mg/Al metal complex oxides (MAO), as one kind of narrow distribution catalyst, obtained extremely potential development. Based on the previous research, the preparation conditions of MAO which showed greater maneuverability and repeatability, is further improved in this paper. The precursor of Mg/Al hydrotalcites (MAH) was synthesized by the precipitation method, and the MAO power was formed after HT being calcined at high temperature, showing high catalytic activity and selectivity. Furthermore, drawing lessons from the technology [9] of preparing the porous ceramic materials, the molding MAO presenting great activity and selectivity was obtained through studying the molding and granulating of HT. The catalyst separated easily from the product can be used repeatedly, so

it can reduce production cost and improves the production of polyether quality.

2. EXPERIMENTAL

The precursor [10] hydrotalcite (HT) was synthesized by co-deposition method described as follows.

A homogeneous solution was formed after mixing the solution of magnesium and aluminium nitrates (solution A) (keeping the Mg:Al molar ratio to a value of 3:1, note: According to similar procedures reported previously, this proportion can get a better ethoxylation performance of the MAO catalyst [6]). The second solution (solution B) was obtained by adding sodium carbonate to sodium hydroxide. Then under intensely stirring, solution A and B was dipped into distilled water in parallel flow way and pH was adjusted to 9.0, controlling the drip speed at a certain amount. A precipitate was formed, and the suspension was crystallized at 80ºC, filtered and dried at 100ºC for 5h. Finally the resulting paste was transferred into a 30 ml crucible which was introduced into a muffle furnace and was calcined for 4h at 500 ºC.

The calcination temperature of Mg-Al hydrotalcite was determined by differential scanning calorimeter (DSC-7, American PE company) at the heating rate of 20 ℃/min under nitrogen protection. The structure of MAH and MAO were studied by the D/max-IIA powder X/ray diffractometer (RIGAKU, JAPAN), with mono-chromatized Cu K radiation (= 0.154 nm) at 40Kv and 100mA. The spectra were collected on an angle 2θ domain ranging from 4 to 65º with a step of 0.06 and an acquisition time of 2 s on each step. Scanning electron micrographs (SEM) were obtained over on the FEI Q200 SEM under the 20KV. Thin layer chromatography (TLC) was used to analyze the qualitative and quantitative of MAO. Camag III TLC scanner was selected with the steam as the coloration and the detective wavelength at 430nm, baked 5min at 110℃.

3. RESULTS AND DISCUSSION

The endothermic and exothermic process of MAH which determines the calcination temperature of MAH was studied by DSC shown in **Figure 1** There was an endothermic peak between 200~270℃, indicating that it lost the water within the structure of MAH which was the first stage weightlessness. The other peak which was the second stage weightlessness was between 370~470℃ and the structure of MAH was destroyed at this stage, CO32-at layer space and OH- on the layer were resolved CO2 and H2O. To get the stable structure of catalyst and better alkalescence catalyst effect, 500℃ was selected as calcination temperature.

XRD patterns of the MAH and MAO samples were shown in **Figure 2** It revealed that there were four diffraction maximums at 2θ=11.5°, 23.0°, 35.0°, 61.0° in **Figure 2(A)**, indicating that crystalline structure of MAH is regular. The pattern of MAO prepared by calcining MAH at 500℃ was recorded in **Figure 2(B)**, showing that the four diffraction maximums were weaken or disappeared obviously with the calcination temperature

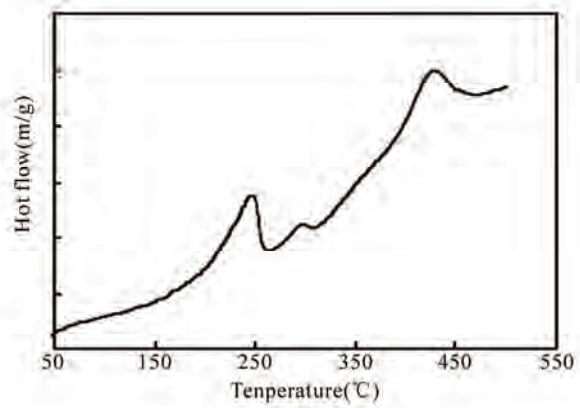

Figure 1. DSC analysis of MAH.

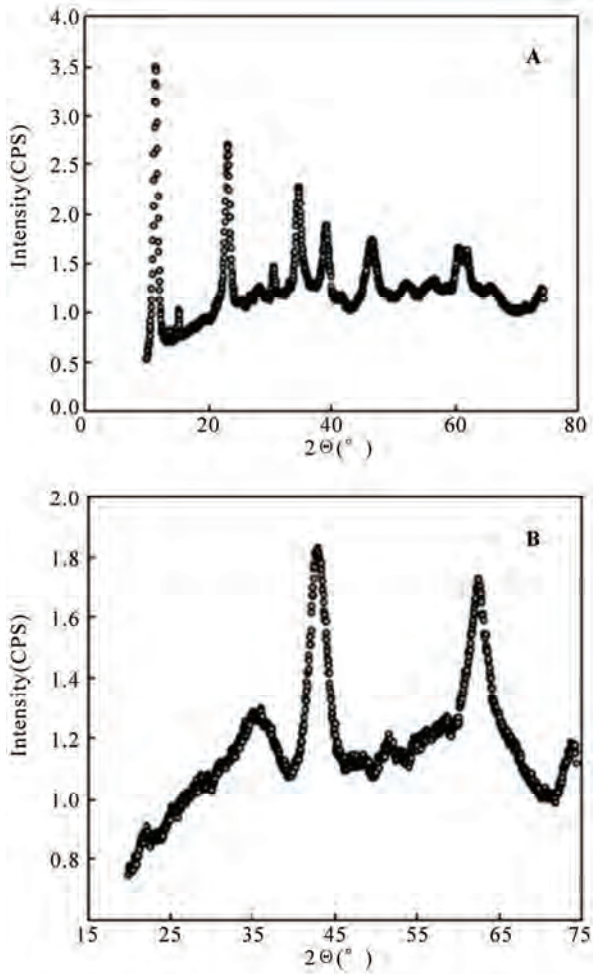

Figure 2. XRD patterns of MAH (A) and MAO (B). (Room temperature, 40kv, copper target, 10°/min).

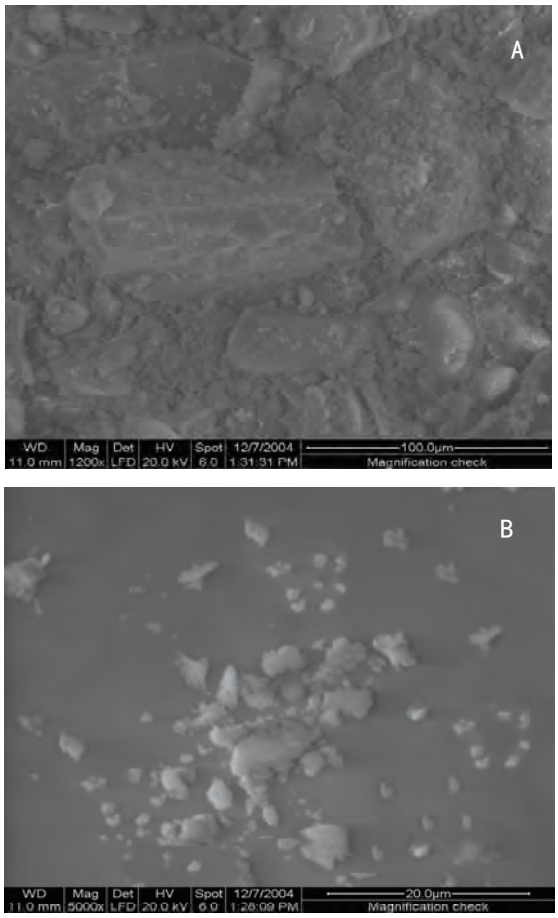

Figure 3. SEM image of MAH (A) and MAO (B).

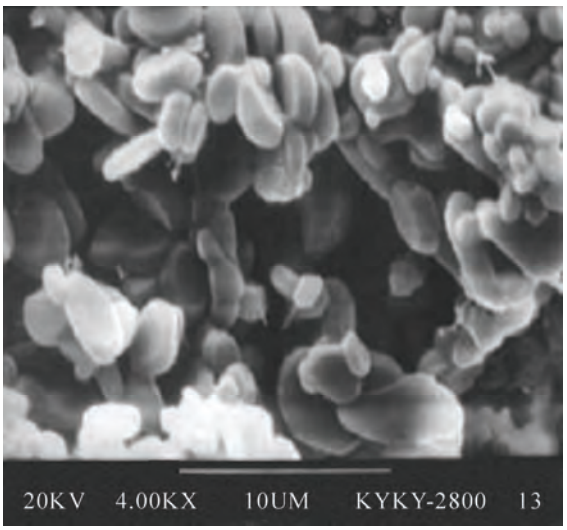

Figure 4. SEM image of molding MAO.

increasing. It indicated that the characteristic structure of HT was destroyed.

The structure of MAH and MAO were characterized [11,12] by SEM, as shown in **Figure 3.** It presented that the form of MAH (**Figure 3(A)**) about 30μm in diameter was not regular. From **Figure 3(B)**, it can be clearly observed that the shape of MAO which was about 3μm in diameter, smaller than the MAH was oval. From the result of SEM images, it can be confirmed that the particle size was decreased significantly after calcination.

The structure of molding MAO was also detected by SEM which was shown in **Figure 4.** There were higher pore-forming rate of molding MAO whose internal arrangement was regular.

The qualitative and quantitative of MAO was analyzed by thin layer chromatography. The orbit of molding MAO catalyzed products (d) had a series of peaks compared with other three orbits, shown in **Figure 5.** It presented that molding MAO had PEG, standard samples but did not have octanol, indicating that MAH had reacted completely, and the products didn't contain the unreacted raw material. It showed that the molding MAO possessed the better catalysis selectivity compared with MAO.

4. CONCLUSION

We systematically investigated the optimum synthesis conditions of MAH and MAO, and the results of SEM and TLC confirm the formation of molding MAO. Conclusions were shown as follows:

MAH can be successfully synthesized by the codeposition method when the mole ratio of the raw materials was Mg/Al=3, NaOH/(Mg+Al)=2.5, NaOH/Na2CO3=4. The crystallizing time was 20h and the titration speed was less than 20ml/l. The process showed good stability and reproducibility. MAO was obtained after calcining MAH which presented best ethoxylation catalytic activity and selectivity.

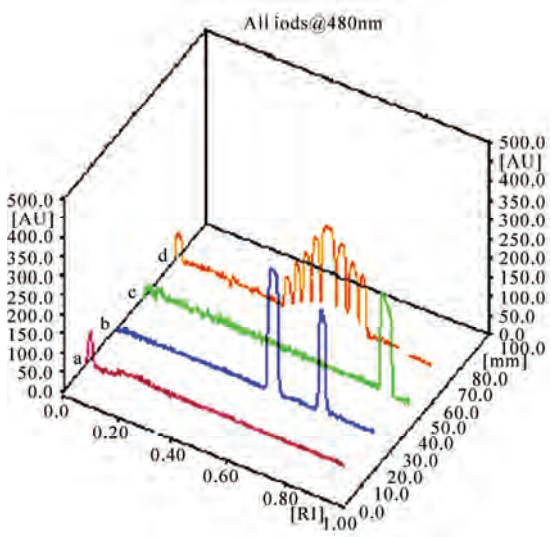

Figure 5. Thin layer scanning of molding MAO catalyzed product (a, PEG; b, control; c, octanol; d, molding MAO catalyzed product).

Copyright © 2010 SciRes.

The size of MAH and MAO calculated from SEM data was about 30 and 3μm respectively, indicating that the particle size was decreased significantly after calcining. The structure of molding MAO was also confirmed by the results of SEM and TLC. There were higher pore-forming rate of molding MAO whose internal arrangement was regular.

REFERENCES

[1] Jana, S.K., Kubota, Y., and Tatsumi, T., Catal, J. (2008) **255**, 40-47.

[2] Wang, H., Chen, J., Cai, Y., Jia, J., Liua, L., and Tengb, H.H. (2007) Applied clay science, **35**, pp. 59-66.

[3] Liu, Y., Lotero, E., Goodwin, Jr.J.G., and Mo, X. (2007) Applied catalysis A. **331**, 138-148.

[4] Lenard, M., Storaro, L., Frattinic, R., Casagrande, M., Marchiori, M., Capannelli, G., Uliana, C., Ferrarib, F. and Ganzerl, R. (2007) Catalysis communications, **8**, 467- 470.

[5] Maggi, R., Malmassari, C., Oro, C., Pela, R., Sartori, G., and Soldi, L. (2008) Synthesis, 53-56.

[6] Huang, J.W. (2002) Study on synthesis of fatty alcohol polyether with narrow range distribution rroperties and application after its phosphate esterification [D]. *Tianjin Polytechnic University*.

[7] Jia, L.W. (2003) The study of ethoxylation catalyzed by Mg-Al complex mental oxides and enzymes [D]. *Tianjin Polytechnic University*.

[8] He, H.M., Sun, T., Jiang, D.P. *etc*. (1994) Study on preparation and characterization of hydrotalcites pillared with tri-atomic heteropoly anions of P-W system [J]. *Chinese J Inorg Chem.*, **10(3)**, 272-277.

[9] Huang, Z.T., Zeng, Z.H., Zhong, B.K. *etc*. (1999) The technique and application of inorganic membrane [M]. *China Petrochemical Press*, 16-150, 151-158.

[10] Natta, G. (1954) Rend. Ist. Lombardo. Sci. letter [M]. **78 (1)**, 3071, 336.

[11] Zhou, G.D., Guo, K.X. (1999) The diffraction of crystal and quasicrystal [M]. *Perking University Press*.

[12] Liang, D.C. (1990) X-ray crystallographic basis [M].

Copyright © 2010 SciRes.

J. Biomedical Science and Engineering, 2010, 3, 217-220 **JBiSE**
doi:10.4236/jbise.2010.32029 Published Online February 2010 (http://www.SciRP.org/journal/jbise/).

Biclustering of time-lagged gene expression data using real number

Feng Liu, Lingbing Wang

International School of Software, Wuhan University, China.
Email: wolflf@126.com

Received 28 September 2008; revised 30 November 2009; accepted 30 December 2009.

ABSTRACT

Analysis of gene expression data can help to find the time-lagged co-regulation of gene cluster. However, existing method just solve the problem under the condition when the data is discrete number. In this paper, we propose efficient algorithm to indentify time-lagged co-regulated gene cluster based on real number.

Keywords: Microarray; Gene Expression; Bicluster; Mean Squared Reside

1. INTRODUCTION

With the development of technology, some computational methods are widely used in the field of analyzing gene expression data. Among them, the clustering and biclustering techniques can detect the similar genes and similar samples from the microarray based on the fact that the similar genes have the similar expression levels under the similar condition, which means that the samples should be gotten under the similar conditions such as the sampling spot, sampling time and the sampling temperatures. However, the samples are always gotten at different period of time because the expression data are always measured from different laboratory and different purpose [1,2,3]. That is to say, the expression data re not simultaneously co-expressing but time-lagged expressing. As a result, the genes expression products may affect other genes' expression during the biology process. Such effect can be divided into two phenomenons: activation and inhibition. Under the activation process, one gene expression can activate another gene expression. On the contrary, a part of gene can inhibit the other gene expression under the inhibition process. To be concluded, some genes can activate or inhibit the other genes with time lagged. That is defined as the time-lagged gene expression. In this paper, we present an efficient method to bicluster of the time-lagged gene expression data. In the Section 2, we describe the related work. The method is presented in Section 3. The experiment result is given in Section 4 and the conclusion is given in Section 5.

2. RELATED WORKS

However, all the methods discussed above usually analyze two genes at the same time which have the drawbacks as following: firstly, the approaches are clearly computationally inefficient in practice. When given n genes, $n(n\text{-}1)$ times comparison cannot be avoided. Secondly, relationship between the genes is unclosed enough using the methods. At the end, the methods merely reflect the relationship between two genes rather than various relationships among genes.

To solve the problems, Ji L. *et al* [3] presented an algorithm to identify time-lagged gene clusters using gene expression data. However, they just dealt with the discrete data rather than the real data. In this paper, we propose an algorithm to identify the localized time-lagged gene clusters from real data.

3. DEFINATIONS AND CONCEPTS

Definition 1. (Time-lagged Continuous Column Linear Bicluster): Let G be the set of genes and T the set of conditions (time spots). Let $X(G,T)$ be the DNA expressional matrix using real numbers. Let $B(I, S, q)$ be the subset of the expression data which denotes the ith gene's q continuous expression data from the time S_i, where I is the subset of G, S is a set of the ith gene's expression time, and q is the expression length. Then, $B(I, S, q)$ is defined as Time-lagged Continuous Column Linear Bicluster only if each element is identical in difference vectors between rows (or columns) in the matrix $B(I, S, q)$.

According to the definition mentioned above, there is linear relationship between difference vectors in Time-lagged Continuous Column Linear Bicluster B(I,S,q), which are defined as the bicluster's eigenvector.

Definition 2. (The Largest Time-lagged Continuous Column Linear Bicluster): Let $X(G,T)$ be the expression matrix and $B(I, S, q)$ the time-lagged continuous column linear bicluster. If there isn't any time-lagged continuous column linear bicluster $B'(I', S', q)$ which satisfies $I \subseteq I'$

and $q' \geq q$, $B(I, S, q)$ is defined as the largest time-lagged continuous column linear bicluster.

To detect the relationship between genes, those biclusters will be scored by *Mean Squared Reside* as reference [9] mentioned. According to reference [9], a bicluster will be regard as perfect when $MSR(I,J)=0$. Due to the noise, as *Cheng & Church* [9] did, we propose Time-lagged Continuous Column δ-bicluster as follows:

Definition 3. (Time-lagged Continuous Column δ-bicluster): Given a threshold $\delta(\delta>0)$,the bicluster $B(I, S, q)$ is defined as the time-lagged Continuous Column δ-bicluster if $MSR(I,J) \leq \delta$ where $MSR(I,J)$ is the mean squared reside of $B(I, S, q)$.

Definition 4. (The Largest Time-lagged Continuous Column δ-bicluster): Given a threshold $\delta(\delta>0)$ and δ-bicluster $B(I, S, q)$, $B(I, S, q)$ is the Largest Time-lagged Continuous Column δ-bicluster if there does not exist any time-lagged continuous column linear bicluster $B'(I', S', q)$ which makes $MSR'(I,J) \leq \delta$, $I \subseteq I'$ and $q' \geq q$, then bicluster $B(I, S, q)$ is defined a largest bicluster.

4. ALGORITHMS

4.1. Enumeration-Fast Graded Greedy Algorithm

As all the definitions shown above, a bicluster is a perfect cluster when $MSR(I,J)=0$. However, the number q is always unknown, so the largest bicluster can not be easily found as reference [9] does. In this paper, we propose a method to enumerate q and then analysis the matrix as follows.

4.1.1. Step 1: Matrix Transformation

To simplify the problem, a new matrix is generated from the original one at different time spots for a given q. For example, given the genes expression matrix $X(G,T)$ with n genes and m conditions as **Table 1**, and a new matrix $M(R,C)$ of $n \times m$ rows and q columns is generated from the original matrix $X(G,T)$ with n rows and m columns as **Table 2** shows.

After the transformation, the question can be transferred to find the δ-cluster with largest row subset I which make the $MSR(I,J) \leq \delta$.

4.1.2. Step2: Generation of δ-cluster

To find the *δ-cluster*, a greedy algorithm is designed by deleting one or some rows in order to cut down $MSR(I,J)$. However, research shows that the algorithm can't be applied directly into the matrix $M(R, C)$. As an alternative method, the *δ-cluster* can be agglomerated from the primary clusters $M(R, C)$ as the following steps.

4.1.2.1. Finding the Primary Clusters

As other agglomerated clustering methods, each row can be regarded as a cluster and then clusters with the shortest distance can be combined together. Given the matrix

Table 1. Original matrix $X(G,T)$.

Gene/Time	T1	T2	T3	T4	T5
G2163	-0.44	-0.44	0.08	0.35	0.26
G1223	-1.51	-1.57	-1.35	0.04	1.3

Table 2. Transformed matrix $M(R,C)$.

-0.44	-0.44	0.08	0.35
-0.44	0.08	0.35	0.26
0.08	0.35	0.26	-0.44
0.35	0.26	-0.44	-0.44
0.26	-0.44	-0.44	0.08
-1.51	-1.57	-1.35	0.04
-1.57	-1.35	0.04	1.3
-1.35	0.04	1.3	-1.51
0.04	1.3	-1.51	-1.57
1.3	-1.51	-1.57	-1.35

$X(G,T)$ with n rows and m columns and denoted the transformed matrix $M(R, C)$ with $n*m$ rows and q columns, thus the computing complexity is $O((nm)^2)$ to enumerate all of the primary clusters. In general, the magnitude of n is 10^4~10^5, and m is 10^1~10^2 the same as q, which shows the difficulty of computing. To solve this problem, we may try to find sub-clusters of the largest bicluster as primary clusters.

Firstly, each row should be regarded as a bicluster's eigenvector. So bicluster A and bicluster B can be regarded as coessential clusters if there exists the linear relationship between *A's* eigenvector a and *B's* eigenvector b. According to the definition of bicluster, a larger bicluster can be formed by combining A and B, and the eigenvector of new bicluster should be $(a + b)/2$. Thus, the largest biclusters can be found by the combination of all the coessential clusters by the steps. Through this method, the perfect linear clusters can be found.

However, the noise signal can't be avoided in real number. So, in this paper, *Mean Squared Reside* is introduced to measure the quality of bicluster as follows:

Algorithm 1: Finding certain primary clusters

Input: $M(R,C)$, a transformed genes expression matrix of size $s \times q$.
Output: k primary clusters
Iteration:
Step1：Initialize each row as a primary cluster and regard it as an eigenvector.
Step2：Compare the eigenvector of each cluster and combine the biclusters with equivalent eigenvector.
Step3：Return k primary clusters.

4.1.2.2. Greedy Expanding

In this phase, we calculate the largest biclusters whose $MSR(I,J) \leq \delta$. A bicluster $B(I,J)$ is the largest continuous column bicluster only if there is not any other continu-

ous column bicluster $B'(I',J')$, which allows $I \subseteq I'$ and $J \subset J'$, or $I \subset I'$ and $J \subseteq J'$. According to Cheng &Church's greedy algorithm [9], for any given bicluster $B(I,J)$, the *MSR* of new bicluster $B'(I \cup R,J)$ will not expand, where R stands for a row set as follows:

$$R = \{i \notin I; \frac{1}{|J|}\sum_{j \in J}(a_{ij} - a_{iJ} - a_{Ij} + a_{IJ})^2 \le MSR(I,J)\}$$

So this greedy method can be adopted in adding some rows into the bicluster as Algorithm 2 shows:

Algorithm 2: Greedy Expanding

Input: $M(R,C)$, a transformed genes expression matrix of size $s \times q$, and there are k primary clusters
Output: k primary clusters
Iteration:
Step1: Initialize each cluster C_i ($1 \leqslant i \leqslant k$)
Step2: Compute the set of columns $Q=\{q_1,q_2,\ldots,q_m\}$ which not belongs to any of the primary cluster.
Step2.1: Compute the MSR score if row j ($j \in Q$) is added to cluster C_i.
Step 2.2: Add the row with the least MSR into cluster C_i, and delete it from set Q
Step 2.3: Compute the MSR of C_i and go to step 2 if it is less than δ.
Step 3: Go to Step1 to calculate the next cluster until all the primary clusters are calculated.
Step7: output the k primary clusters

4.1.2.3. Rapid Expansion of Classification

However, the algorithm above repeats Step2~Step5 too frequently. Thus, we improve the algorithm based on the Greedy Principle.

Firstly, scoring the primary cluster $B(I,J)$ with α, and the largest cluster $B'(I',J')$ with δ. If the count of the steps is no more than k, the increment of each step will be $(\delta-\alpha)/k$. Thus, the increment to the cluster of adding each row should be no more than $(\delta-\alpha)/k$. And then, an improved algorithm will be introduced:

Algorithm 3: Rapid expansion of classification

Input: $M(R,C)$, a transformed genes expression matrix of size $s \times q$, and there are k primary clusters
Output: k clusters
Iteration:
Step1: Initialize each cluster C_i ($1 \leqslant i \leqslant k$)
Step2: Compute the set of columns $Q=\{q_1, q_2,\ldots,q_m\}$ which not belongs to any of the primary cluster.
Step3: For each row j in Q and each cluster C_i.
Step 3.1 Calculate MSR score if row j is added to cluster C_i.
Step 3.2: Add the rows into each cluster C_i if their MSR score is less than $(\delta - \alpha)/r$.
Step 3.3 Delete the rows from set Q
Step 3.4: Recompute the MSR of C_i, and go to Step 3 if their score is less than δ and Q is not null.
Step 4: Delete several rows to make each bicluster's score less than δ by the algorithm proposed by Cheng & Church.
Step5: Print out the k clusters

4.1.3. Phase 3: Generation of the Sequential δ-cluster

In this phase, the time-lagged bicluster the is extracted from δ-clusters.

Firstly, assuming $I=\{r_1,r_2,\ldots,r_p\}$ as a set of the rows of δ-cluster $B(I,J)$. There r_i represents the *ith* row in $M(R,C)$. Secondly, assume that $G=\{g_1,g_2,\ldots,g_n\}$ is the gene set of original expression matrix $X(G,T)$. Set $T=\{c_{t1},c_{t2},\ldots,c_{tm}\}$, and q is the number of sequential points of $M(R,C)$. There $\lfloor r_i / m \rfloor$ represents the gene at row i of δ-cluster, and $\lfloor r_i \bmod m \rfloor$ is the start time. Then the target bicluster $B(I', S, q)$ will be got.

4.1.4. The Overall Algorithm:

Generally, q is a positive integer within 100, and we enumerate all possible q. The overall algorithm is:

Algorithm 4: the overall algorithm

Input: Gene expression matrix $X(G,C)$ with m rows and n columns, threshold α、δ and q.
Output: the best time-lagged bicluster.
Iteration:
Step1: For each different q
Step1.1: Transform the matrix to M(R,C)
Step1.2: Find the k-best primary cluster using Algorithm 1.
Step1.3: Expand the clusters using Algorithm 3.
Step1.4: Print out the k best clusters and transform them into sequential δ-clusters
Step1.5: Go to step 1 until all the q is considered.

5. EXPERIMENTS AND RESULTS

Firstly, we randomly generate a 200×20 matrix $X(G,T)$ of positive continuous within 100. Secondly, randomly generate a $k*s$ bicluster $B(I,J)$. At last, replace several rows in $X(G,T)$ by lines of $B(I,J)$ at random points.

If set α=0.2、δ=1、k=4、$4 \le q \le 20$, and the size of $B(I,J)$ is between 5×5～200×20. The algorithm can efficiently find the implanted bicluster.

Additionally, we also add some noise into the matrix. Selecting $\varepsilon|I||J|$ data from $B(I,J)$ and adding a value between $-a$ to a to this matrix. Let k be the quantity of the output of bicluster and each of them is denoted by $B_k(I_k',J_k')$. Accuracy r can be calculated as the overlapped part of $B_i(I_i',J_i')$ and $B(I,J)$ as follows:

$$r = \sqrt{\frac{|I \cap I_i'| * |J \cap J_i'|}{|I \cup I_i'| * |J \cup J_i'|}}$$

If set α=2、δ=20, the ratio r with different a, ε is following:

Figure 1 has shown that the more noise, the worse the result will be. And the stronger noise, the worse the result will be. Under the condition with a few noises, the result is acceptable.

Figure 2 The parameter δ should be increased to improve the algorithm if the noise signal is too strong.

Copyright © 2010 SciRes.

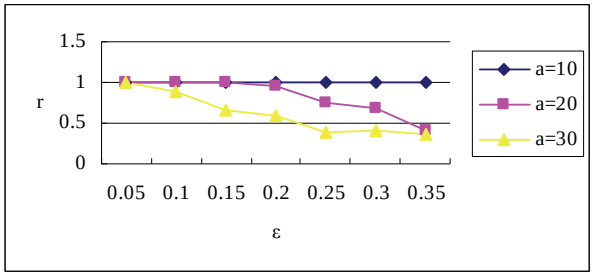

Figure 1. the ratio *r* for different *a*.

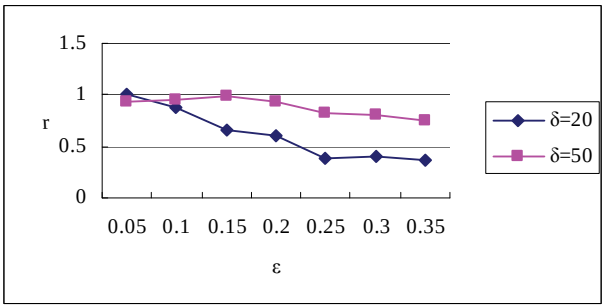

Figure 2. the ratio *r* for different *ε*.

Table 3. Consequences of the biclusters of G-O.

GO ID	Selected gene	All of the gene	*p*-Value
5830	89	151	3.1944E-24
44445	90	172	1.32E-19
3740	99	205	3.024E-18
5842	51	78	4.6627E-17
5840	112	257	2.594E-16
43037	125	310	6.432E-15
15934	62	119	9.927E-14
5829	119	312	3.04E-12
16283	36	58	2.03E-11
5843	36	58	2.03E-11
6416	158	468	7.033E-11
9059	171	531	7.558E-10
5198	116	325	7.7626E-10
16282	37	68	2.138E-9
30529	141	423	2.356E-8

Additionally, we filter those data which own the characteristic of Gaussian Distribution under different conditions. In order to choose a suitable δ, we randomly generate 200 model matrixes of the same size with processed genes expression matrix. The elements of the matrixes are continuously selected from 0 to 500. There the average *MSR* is 18569.8. At the first time when α was combined, it is 1% of *MSR*, but δ, which got from Algorithm 4, is 5% of *MSR*. We test *q* from 8 to 20 and return 10 largest biclusters of each different *q*. Gene Ontology also has been used to evaluate the biclusters and calculate different *p-Value*. There is the output in **Table 3**.

6. CONCLUSIONS

To a continuous matrix, we use the Enumeration-Fast Graded Greedy Algorithm to generate biclusters. Firstly, we transform the gene expression matrix, analysis the matrix by Cheng &Church's Greedy Algorithm, and then generate the time-lagged δ-cluster. This method includes three steps: matrix transformation, generation of δ-cluster and generation of the sequential δ-cluster. And then, both actual data and analogy data has been used to test this algorithm. The conclusion is: when the data is lack of noise signal, the result will be totally correct; when the noise signals added into the matrix, there will be little influence to the result; when testing the actual data, we can generate the bicluster which meet the requirement. All these data can show the reliability of this method.

REFERENCES

[1] Somogyi, R., Sniegoski, C.A. (1996) Modeling the complexity of genetic networks: Understanding muitigenic and pleiotropic regulation. *Complexity*, **1**, 45-63.

[2] Ji, L., Tan, K.-L. (2005) Identifying time-lagged gene clusters using gene expression data. *Bioinformatics*, **21(4)**, 509-516.

[3] kato, M., Tsunoda, T., Takagi, T. (2001) Lag analysis of genetic networks in the cell cycle of budding yeast. *Genome informatics*, **12**, 266-267.

[4] Chen, T., Filkov, V., Skiena, S. (2001) Identifying gene regulatory networks from experimental data. In Proceeding of Third Annual International Conference on Research Computational Molecular Biology (Recomb'99). *ACM press*, **2001**, 94-103.

[5] Barash, Y., Friedman, N. (2002) Context-specific bayesian clustering for gene expression data. *Journal of Computational Biology*, **9**, 169-191.

[6] Kwon, A.T., Hoosand, H.H. (2003) Inference of transcriptional regulation relationships from gene expression data. *Bioinformatics*, **19**, 905-912.

[7] Yeung, L.K., Szeto, L.K., Liew, A.W., Yan, H. (2004) Dominant spectral component analysis for transcriptional regulations using microarray time-series data. *Bioinformatics*, **20(5)**, 742-749.

[8] Cheng, Y., Church, G.M. (2000) Biclustering of gene expression data. *Proceeding of Intelligent System for Molecule Biology (ISMB)*, 93-103.

Copyright © 2010 SciRes.

J. Biomedical Science and Engineering, 2010, 3, 221-225 **JBiSE**
doi:10.4236/jbise.2010.32030 Published Online February 2010 (http://www.SciRP.org/journal/jbise/).

Restriction fragment length polymorphism in the exon 2 of the BoLA-DRB3 gene in Chinese Holstein of the south China

Xiu-Xiang Wu, Zhang-Ping Yang*, Xiao-Long Wang, Yong-Jiang Mao, Shu-Chun Li, Xue-Kui Shi, Ying Chen

Key Lab of Animal Genetics, Breeding & Molecular Design, College of Animal Science and Technology Yang Zhou University, Yang Zhou, Jangsu, China.
Email: *zhangpy65@vip.sohu.com

Received 30 September 2008; revised 28 November 2009; accepted 30 December 2009.

ABSTRACT

The genetic diversity of the exon2 of BoLA-DRB3 (BoLA-DRB3.2) in Chinese Holstein cattle of the south China was investigated by hemi-nested polymerase chain reaction-restriction fragment length polymorphism (PCR-RFLP) technique. Six, four and eleven RFLP patterns were found after digestion with the restriction enzymes Hae III, Bst YI and Rsa I, respectively. The DNA sequence showed and twenty-five DRB3.2 alleles. GLM model analysis indicated that lactation and calving season have positive correlation with SCC (Somatic Cell Count) (p<0.01), BoLA-DRB3.2*3, *8, *18 and *26 were associated with lower SCC (p<0.01). The present findings concluded that mastitis is a severe hinder of milk production and technology. Therefore, future re-searches should focus on associations of mastitis with BoLA haplotypes rather than single BoLA genes

Keywords: PCR-RFLP; BoLA-DRB3.2; Chinese Holstein; Genetic Polymorphism; SCC

1. INTRODUCTION

Major Histocompatibility Complex (MHC), also called Bovine Lymphocyte Antigen (BoLA) has received wide attention because of their association with host immunity. The BoLA gene is located on the short arm of bovine chromosome 23 (BTA23) and consists of three class, I, II and III [1].The class II gene are distributed in two regions, II a and II b, with an approximate recombination frequency of 17% [2]. The DRA, DRB, DQA, and DQB genes are located in the II a region, while the DOB, DYA, DYB and DIB genes in the IIb region. There are at least three DRB-like genes (DRB1, DRB2 and DBR3) in the BoLA region, among which only the DRB3 gene is expressed considerably and is highly polymorphic [1].

A polymerase chain reaction-restriction fragment length polymorphism (PCR-RFLP) technique developed by Van Eijk *et al*. [3] determined alleles in the second exon of BoLA-DRB3 gene (BoL-DRB3.2). This method has advantage of using small amounts of genomic DNA and being adaptable to crude DNA preparations. This advantage will be magnified in case where the studied population is relatively large and the process of extracting DNA with conventional phenol-chloroform methods becomes tedious and labor-intensive. Therefore, PCR-RFLP is a rapid and useful method for DRB3.2 typing in cattle families. But for the outbreed populations sequencing and hybridization techniques are required.

Recently, many researches on BoLA-DRB3 have been reported [4,5,6,7].This study describes genetic variability in the BoLA-DRB3 and its relationship with SCC and production performance in Chinese Holstein cow. This is the first study of the DNA polymorphism of the BoLA-DRB3 gene in Chinese Holstein cows of the south China.

2. MATERIALS AND METHODS

2.1. Animals and DNA Extraction

Chinese Holstein (n=629) from Shanghai Brightlight Dairy Company were used in the current study. Approximately 5mL of blood was collected from each animal via the caudal rein. The blood was anticoagulated with anticoagulant citrate dextrose (ACD) and stored at -20C.Genomic DNA was extracted from whole blood by the phenol-chloroform extraction method described by Sambrook with some modifications. The quality of the genomic DNA was checked by submarine Agarose gel electrophoresis, purity and concentration were check by spectrophotometer DNA samples with good quality, and purity and concentration were used for further analysis.

2.2. PCR Amplification of BoLA-DRB3.2

Exon 2 of BoLA-DRB3 gene (284bp) was amplified by semi-nest PCR, described by Miretti *et al*. [9], to im-

prove the specificity of the PCR product. Primers HL-030 (5'-ATCCTCTCTCTGCAGCACATTTCC-3'), HL-031 (5'-TTTAAATTCGCGCTCACCTCGCCGCT-3') and HL-032 (5'-TCGCCGCTGCACAGTGAAACTCTC -3'), described by Van Eijk [3], were used in the PCR reaction. Briefly, the first stage PCR was performed in a final volume of 20μL containing 50ng of template DNA, 0.5 pm of primer HL-030 and HL-031, 2μL PCR buffer, 1.75mM MgCl2 , 0.25 mM dNTPs, 1.5U Taq DNA Polymerase (Shanghai Sangon). This reaction system was predenatured at 94C for 4min followed by 12 cycles of denaturizing (94C for 1min), annealing (60C for 1min) and elongation (72C for 1min) and a final extension at 72C for5 min. 2μL of the first stage PCR product was used as template DNA.

For the second stage PCR in a final volume of 40μL containing 0.5pM of primer HL-030 and HL-032, 4μL PCR buffer 1.75mM MgCl2, 0.25mM dNTPs, and 2U Taq DNA polymerase. The solution was predenatured at 94C for 4 min followed by 30 cycles of denaturizing (94C for 60s), annealing (63C for 45s), and elongation (72C for 45s) and a final extension (72C for 5min).5μL of the second stage PCR product was electrophoresed on 1.2% agarose gels to check the quality and specificity of DNA fragment amplification.

2.3. RFLP

To examine the nucleotide sequence variability at the BoLA-DRB3.2 locus, three end nucleotide restriction enzymes (Hae III, Bst YI and Rsa I) were chosen based on their cut site and ability to cut DNA in this exon. The second stage PCR products were digested with the restriction enzymes according to the manufacture's instructions. A 15μL of the second stage PCR product containing 8μL, 0.5U of restriction enzymes, and 6.8μL of 1×Buffer were digested at 37C for 12h followed by inacting at 80C (Hae III and Bst YI) or 65C (RsaI) for 20min. The resulting DNA fragment were separated on 14% PAGE gels with 1×TBE buffer (0.9M Tris-Base, 0.09M Boric Acid, 2.5mM EDTA) at 150V for 5h, using Msp I digested pBR322/MspI as a molecular marker. After ethidium bromide (EB) staining, the gels were photographed under UV light and the relative migrations of the DNA bonds were estimated. The restriction patterns obtained were compared with previously described restriction maps [10].

2.4. DNA Sequencing

BoLA-DRB3.2 DNA sequence was performed base on the restriction enzyme sites. The sequence was compared with the gene Bank sequences.
http://www.projects.roslin.ac.uk/bola/bolanom.html

2.5. SCC Analysis

SCC is leukocytes that inter the milk from the alveoli and they are considered an important indicator of mastitis infection. The SCC of the experimental cows was detected every month. In order to express the effect of calving season on SCC, the data are divided into four parts according to calving season.

2.6. Statistic Analyses

GLM (General Linear Model) of SCC and production performance was performed by SAS6.12 (SAS Institute, 1996), the models are as follows:

$$Yijkm = \mu + Li + Sj + \sum blBoLAijkl + eijkm$$

Yijkm: SCC, Milk Yield, Fat Percent Protein percent μ: the average value, Li: lactation number, i=1～4, Sj: calv-ing season=1～4, bl: regression coefficient of allele to SCC, l= 1～22, BoLAijkl: the copy number of BoLA al-lele l in individual ijk, the value is 0, 1 and 2, eijkm: random error.

3. RESULTS

3.1. DRB 3.2 Amplification

DNA bands of the expected size containing 267 bp of exon 2, 3 bp of the 3' intron and 14bp of the 5'intron, were received by semi-nested PCR amplification (**Figure 1**). The specificity of the PCR product was very high, but some nonspecific bands were observed. Although these bands could not be eliminated by modifying PCR conditions, this did not affect the resolution of restriction patterns.

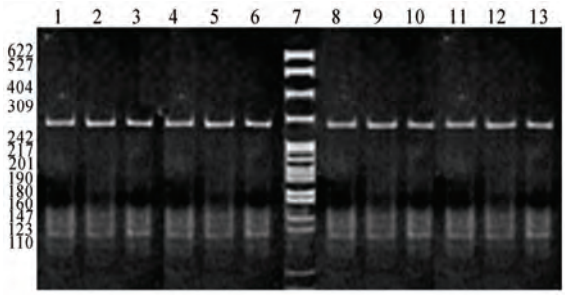

Figure 1. Patterns of the semi-nested PCR.

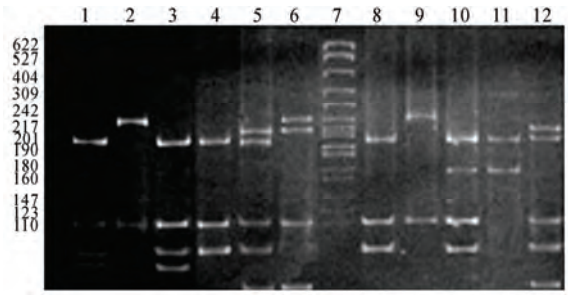

Figure 2. Genotypes of BoLA-DRB3.2 locus digested with Hae III.

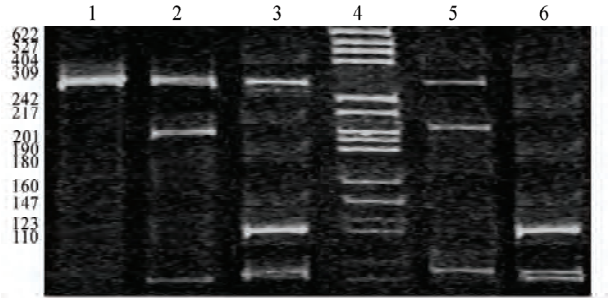

Figure 3. Genotypes of BoLA-DRB3.2 locus digested with Bst YI.

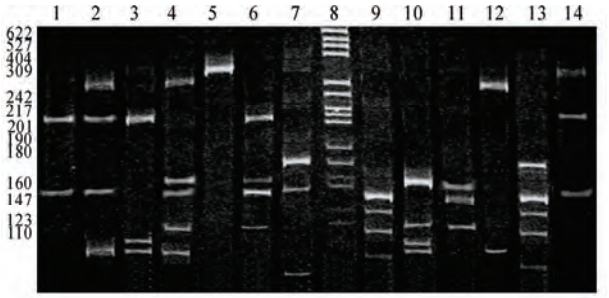

Figure 4. Genotypes of BoLA-DRB3.2 locus digested with Rsa I.

The DNA sequence was 284 bp, containing 267 bp of exon 2, 3 bp of the 3' intron and 14bp of the 5'intron.

3.2. Identification of Restriction Patterns

The 284 bp fragment of the BoLA-DRB3.2 gene in this study were digested with Rsa I, Hae III and Bst YI respectively. Six restriction patterns were identified with Hae III (See **Table 1** and **Figure 2**). Bst YI resulted in four RFLP patterns a,b,d and e (See **Table 1** and **Figure 3**). RsaI restriction patterns were so complex that eleven patterns were revealed in this study (See **Table 2** and **Figure 2**).

3.3. DNA Sequencing and Standard Naming

Combining restriction patterns with Rsa I, Bst YI and Hae III in the whole sample, 22 DRB3.2 alleles found in the study were sequenced (See **Table 2** and **Table 3**). Many mutants were indicated in the cut sites of restriction enzymes by DNA sequencing. The frequency of BoLA-DRB3.2 ranged from 0.003 (2*34) to 0.220 (2*22).

Table 1. Fragment Size and Frequencies of Restriction Patterns Digested with Enzymes.

Enzyme	Restriction Patterns	Fragment Size(bp)	Frequency	Enzyme	Restriction Patterns	Fragment Size(bp)	Frequency
Hae III	a	167/65/52	0.598	Rsa I	b	111/54/50/39/30	0.061
	b	219/65	0.238		d	143/111/30	0.024
	d	190/65/29	0.049		f	141/54/50/39	0.085
	e	167/117	0.037		g	141/104/39	0.082
	f	167/65/48/4	0.061		h	111/69/54/50	0.082
	h	167/65/46/6	0.017		i	180/54/50	0.006
Bst YI	a	199/85	0.095		j	93/78/63/50	0.052
	b	284	0.823		l	234/50	0.113
	d	197/87	0.012		m	111/104/69	0.241
	e	112/87/85	0.070		n	180/104	0.195
					o	284	0.058

Table 2. Allele Frequencies of BoLA-DRB3.2 identified by PCR-RFLP analysis.

DRB3.2	Patterns			Alleles Num	Frequency	DRB3.2	Patterns			Alleles Num	Frequency
Allelle	Rsa I	Bst YI	Hae III			Allelle	Rsa I	Bst YI	Hae III		
*3	b	b	b	41	0.0652	*18	l	b	f	26	0.0413
*6	d	a	a	17	0.0270	*21	l	b	e	23	0.0366
*8	f	a	a	5	0.0079	*22	m	b	a	148	0.2353
*9	f	d	a	8	0.0127	*23	n	b	a	64	0.1017
*10	f	b	a	35	0.0556	*24	n	b	b	58	0.0922
*11	g	e	a	55	0.0874	*26	o	a	b	5	0.0079
*12	h	a	a	13	0.0207	*28	o	b	b	29	0.0461
*13	h	b	a	28	0.0445	*32	m	a	a	13	0.0207
*14	h	b	b	14	0.0223	*33	n	b	f	19	0.0302
*15	i	b	a	5	0.0079	*36	l	b	a	9	0.0143
*16	j	b	d	3	0.0048	*42	f	a	h	11	0.0175

Copyright © 2010 SciRes.

Table 3. The sequences of BoLA-DRB3.2 alleles indicated in the paper.

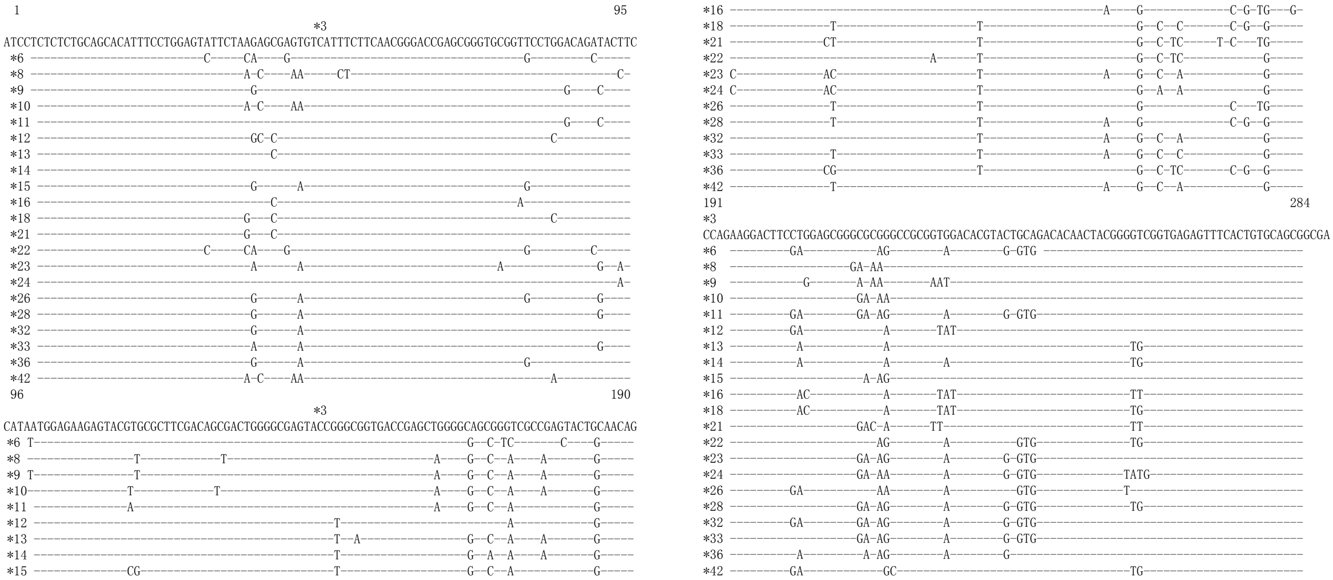

Table 4. The correlation between BoLA-DRB3.2 alleles, lactation, seasons of calving and SCC and performance traits in Chinese Holstein.

Factor	SCC	Factor	SCC
μ	+580.61	μ	+580.61
BoLA-DRB3.2*3	-336.95**	BoLA-DRB3.2*21	-503.95*
BoLA-DRB3.2*6	NS	BoLA-DRB3.2*22	-413.38*
BoLA-DRB3.2*8	-623.01**	BoLA-DRB3.2*23	-345.89
BoLA-DRB3.2*9	NS	BoLA-DRB3.2*24	NS
BoLA-DRB3.2*10	NS	BoLA-DRB3.2*26	-878.14**
BoLA-DRB3.2*11	-341.62	BoLA-DRB3.2*28	-386.66
BoLA-DRB3.2*12	NS	BoLA-DRB3.2*32	NS
BoLA-DRB3.2*13	NS	BoLA-DRB3.2*33	NS
BoLA-DRB3.2*14	NS	BoLA-DRB3.2*36	-395.54
BoLA-DRB3.2*15	NS	BoLA-DRB3.2*42	NS
BoLA-DRB3.2*16	-353.07	Lactation	+195.19**
BoLA-DRB3.2*18	-511.33**	Calving Season	+49.91**

Note:*means significant difference, P<0.05; **means significant difference, P<0.01; NS means no significant difference. The values means regression coefficient, +means positive correlation, -means negative correlation.

3.4. Effect of BoLA-DRB3.2, Lactation and Caving Season on SCC

The effect of BoLA-DRB3.2, lactation and caving season on SCC and production performance are displayed in **Table 4** Lactation and calving season have positive correlation with SCC (p<0.01), most alleles of BoLA-DRB3.2 have negative correlation with SCC, among them, BoLA-DRB3.2*3, *8, *18 and *26 are the most associated with SCC (p<0.01).

4. DISCUSSION

Taking an important role in the immune system of animals and having a close relationship with resistance to diseases, MHC has become a candidate gene and a hot point of recent researches. It is widely said that the high polymorphism of MHC-DRB3 genes was decided by its important function made by class II antigen of MHC in the immune system. In order to adapt to various geographic and climatic conditions, the immune system is highly polymorphic. So the polymorphism of BoLA-DRB3 gene, encoding the main functional area of MHC antigen, is very high.

Miretti *et al*. [9] identified the polymorphism of BoLA-DRB3 gene in Argentinean Holstain using PCR-RFLP. Four patterns a, b, d and e were found with Hae III, three (a, b and d) and eleven patterns (b, c, d, f, g, h, I, j, l, m, n and o) were found with Bst YI and RsaI, respectively. In this research, Hae III f, h and BstYI d were detected.

The most frequent (frequency＞0.05) BoLA-DRB3.2 alleles of 835 Holstein dairy cattle re-ported by Sharif *et al*. [11] were BoLA-DRB3.2*3(0.0652), *8(0.0079), *11(0.0874), *16(0.0048), *22(0.2353), *23(0.1017), *24(0.0922). In the present study, the most frequent alleles were BoLA-DRB3.2*3(0.0652), **11(0.0874), *16(0.0048), *22(0.2353), *23(0.1017), *24(0.0922). Sharif *et al* reported that BoLA-DRB3.2 *8 was the most common allele type in Holstein, However, in this study, the BoLA-DRB3.2 *16 was at low frequency (0.0048), while the BoLA-DRB3 *22 was the most common allele (0.2353). Therefore, BoLA polymorphism information from the research herd seemed representative of the regional Holstein population. These differences may be largely due to the long-term adaptation to different geographical and climatic conditions. Therefore, BoLA polymorphism information from the research herd seemed representative of the regional Holstein population. These differences may be largely due to the long-term conditions.

Many mutants, changing the restriction site and the restriction maps, were identified in the cut sites by DNA sequencing. RFLP, as a method to identify the polymorphism of BoLA-DRB3, can only define the position of mutants. Other methods must be used to find the detail mutants. Result of our study demonstrated that the BoLA-DRB3.2 locus is highly polymorphic in Chinese Holstein. PCR-RFLP may therefore be a rapid and useful method for DRB3 typing and studying the evolutionary changes in dairy cattle.

Sharif reported calving season had no significant effect on SCC, but this research indicated that calving season significantly affect SCC; there was a trend that cows calving in spring and summer have high SCC. Related to BoLA-DRB3.2 and SCC, the result in this research is different from Sharif *et al.* [11], among the most frequently detected alleles, BoLA-DRB3.2*3 has significant correlation to low SCC, BoLA-DRB3.2*8, 18 and 26 maybe have same function, but their frequencies are very low.

Contradictory results from different studies invest-tigating associations between BoLA-DRB3.2 alleles and mastitis indicate that future studies should focus on associations of mastitis with BoLA heliotypes rather than with single BoLA genes.

5. ACKNOWLEDGEMENTS

This The authors appreciate the assistance of the Shanghai Brightlight Dairy Company. This work was supported by 863 high-tech projects "The Breeding technology of Multi-locus Combination of Chinese Holstein" (2008AA10Z144), Natural Science Foundation of Jiangsu Province, College of major projects (09KJA230002), land 863 Na tional key project (2008AA101010).

REFERENCES

[1] Andersson, L. and Davies, C.J. (1994) The major histocompatibility complex. *Cell-Mediated Immunity in Ruminants*, *CRC*, 37-57.

[2] Davies, C.J., Joosten, I., Andersson, L., Arriens, M.A., Bernoco, D., Bissumbhar, B., Byrns, G., van Eijk, M.J., Kristensen, B. and Lewin, H.A. (1994) Polymorphism of Bovine MHC Class II genes. Joint Report of the Fifth International Bovine Lymphocyte Antigen (BoLA) Workshop. *European Journal of Immunogenetics*, **21(4)**, 259-289.

[3] Van Eijk, M.J., Stewart-Haynes, J.A. and Lewin, H.A. (1992) Extensive polymorphism of the BoLA-DRB3 gene distinguished by PCR-RFLP. *Animal Genetics*, **23**, 483-496.

[4] Do Nascimento, C.S., Machado, M.A., Martinez, M.L., da Silva, M.G.B., Martins Guimares, M.F., Campos, A.L., Sousa Azevedo, A.L., Teodoro, R.L., Silva erneque, R. and Facioni Guimare, S.E. (2006) Association of the Bovine major histocompatibility complex (BoLA) BoLA-DRB3 gene with fat and protein production and somatic cell score in Brazilian gyr dairy cattle (Bos indicus). *Genetics & Molecular Biology*, **29(4)**, 641-647.

[5] Nassiry, M.R., Shahroodi, F.E., Mosafer, J.A., Mohammadi, A., Manshad, E., Ghazanfari, S., Mohammad Abadi, M.R. and Sulimova, G.E. (2005) Analysis and frequency of Bovine lymphocyte antigen (BoLA-DRB3) alleles in Iranian Holstein cattle. *Russian Journal of Genetics*, **41(6)**, 664-668.

[6] Rupp, R., Hernandez, A., Mallard, B.A. (2007) Association of Bovine leukocyte antigen (BoLA) DRB3.2 with immune response, mastitis, and production and type traitsin Canadian Holsteins. *Journal of Dairy Science*, **90**, 1029-1038.

[7] Duangjinda, M., Buayai, D., Pattarajinda, V., Phasuk, Y., Katawatin, S., Vongpralub T. and Chaiyotvittayakul, A. (2009) Detection of Bovine leukocyte antigen DRB3 alleles as Candidate markers for clinical mastitis resistance in Holstein x zebu. *Journal of Animal Science*, **87**, 469-476.

[8] Jeseph, S. and Rusell, D.W. (2001) Molecular cloning: A laboratory manual. *Cold Spring Habor Laboratory Press*.

[9] Miretti, M.M., Ferro, J.A., Lara, M.A. and Conte, E.P.B. (2001) Restriction fragment length polymorphism (RFLP) in Exon 2 of the BoLA-DRB3 gene in South American cattle. *Bio Gene*, **39(9-10)**, 311-324.

[10] Maillard, J., Renard, C., Chardon, P., Chantal, I. and Bensaid, A. (1999) Characterization of 18 new BoLA-DRB3 alleles. *Animal Genetics*, **30**, 200-203.

[11] Sharif, S., Mallard, B.A., Wilkie, B.N., Sargeant, J.M., Scott, H.M., Dekkers, J.C.M. and Leslie, K.E. (1998) Association of the Bovine major histocompatibility complex DRB3 (BoLA-DRB3) alleles with occurrence of disease and milk somatic cell score in Canadian dairy cattle. *Animal Genetics*, **29**, 185-193.

Copyright © 2010 SciRes.

Call for Papers

Journal of Biomedical Science and Engineering (JBiSE)

www.scirp.org/journal/jbise

JBiSE, an international journal, publishes research and review articles in all important aspects of biology, medicine, engineering, and their intersection. Both experimental and theoretical papers are acceptable provided they report important findings, novel insights, or useful techniques in these areas. All manuscripts must be prepared in English, and are subject to a rigorous and fair peer-review process. Accepted papers will immediately appear online followed by printed in hard copy.

Subject Coverage

- Bioelectrical and neural engineering
- Bioinformatics and Computational Biology
- Biomedical modeling
- Biomedical imaging, image processing and visualization
- Clinical engineering, wearable and real-time health monitoring systems
- Biomechanics and biotransport
- Software, tools and application in medical engineering
- Biomaterials
- Physiological signal processing
- Biomedical devices, sensors, artificial organs and nano technologies
- NMR/CT/ECG technologies and electromagnetic field simulation
- Structure-based drug design

Editor–in–Chief

Kuo-Chen Chou
Gordon Life Science Institute, San Diego,California, USA

Editorial Board

Prof. Christopher J. Branford-White	London Metropolitan University, UK
Prof. Thomas Casavant	University of Iowa, USA
Dr. Arezou Ghahghaei	University of Sistan ad Baluchistan, Iran
Prof. Reba Goodman	Columbia University, USA
Prof. Fu-Chu He	Chinese Academy of Science, China
Prof. Robert L. Heinrikson	Proteos, Inc., USA
Prof. Zeng-Jian Hu	Howard University, USA
Prof. Sami Khuri	San Jose State University, USA
Prof. Takeshi Kikuchi	Ritsumeikan University, Japan
Prof. Rob Krams	Imperial College, UK
Prof. Lukasz Kurgan	University of Alberta, Canada
Dr. Girdhar K. Pandey	University of Delhi South Campus, India
Prof. Zhi-Pei Liang	University of Illinois, USA
Prof. Juan Liu	Wuhan University, China
Dr. Patrick Ma	The Hong Kong Polytechnic University, Hong Kong (China)
Dr. Bouzid Menaa	Nanotechnology Senior Advisor (SA), Fluorotronics, Inc. (San Diego, CA, USA), USA
Prof. Eddie Ng	Technological University, Singapore
Prof. Harold A. Scheraga	Cornell University, USA
Prof. Hong-Bin Shen	Shanghai Jiaotong University, China
Prof. Mingui Sun	University of Pittsburgh, USA
Prof. Yanmei Tie	Harvard Medical School, USA
Dr. Elif Derya Ubeyli	TOBB University of Economics and Technology, Turkey
Prof. Ching-Sung Wang	Oriental Institute Technology, Taiwan (China)
Prof. Dong-Qing Wei	Shanghai Jiaotong University, China
Prof. Zhizhou Zhang	Harbin Institute of Technology, China
Prof. Jun Zhang	University of Kentucky, USA

Notes for Intending Authors

Submitted papers should not have been previously published nor be currently under consideration for publication elsewhere. Paper submission will be handled electronically through the website. All papers are refereed through a peer review process. For more details about the submissions, please access the website.

Website and E-Mail

www. scirp. org/journal/jbise
Email: jbise@scirp.org

ISSN 1937-6871 (Print), 1937-688X (Online)

Journal of Biomedical Science and Engineering, 2010, 3.
Published Online February 2010 in SciRes (http://www.scirp.org/journal/jbise).

TABLE OF CONTENTS

Volume 3, Number 2, February 2010

Novel method for discerning the action of selection during evolution
M. Yang, A. Solidar, G. J. Wyckoff..... 109

Identification of highly conserved domains in hemagglutinin associated with the receptor binding specificity of influenza viruses: 2009 H1N1, avian H5N1, and swine H1N2
W. Hu..... 114

Effect of deformation rate on the mechanical properties of arterie
J. O. V. Delgadillo, S. Delorme, V. Mora, R. DiRaddo, S. G. Hatzikiriakos..... 124

A method to fabricate small features on scaffolds for tissue engineering via selective laser sintering
S. Lohfeld, M. A. Tyndyk, S. Cahill, N. Flaherty, V. Barron, P. E. McHugh..... 138

Senescence of human vocal fold fibroblasts in primary culture
G. M. Adams, C. C. Xu, R. W. Chan..... 148

Study on synchrony of two uncoupled neurons under the neuron's membrane potential stimulation
Y. P. Peng, J. Wang, Q. X. Miao, H. Y. Lu..... 160

Design and development of a new dedicated RF sensor for the MRI of rat brain
A. Asfour..... 167

Imaging characteristics of metallic interbody spacers: in vitro score evaluation of susceptibility artifacts considering different MRI sequences
T. Ernstberger, G. Heidrich, G. Buchhorn..... 181

Iterative spectral subtraction method for millimeter-wave conducted speech enhancement
S. Li, J. Q. Wang, M. Niu, X. J. Jing, T. Liu..... 187

Classification of non stationary signals using multiscale decomposition
M. Chendeb, M. Khalil, D. Hewson, J. Duchêne..... 193

Performance comparison of three artificial neural network methods for classification of electroencephalograph signals of five mental tasks
V. Khare, J. Santhosh, S. Anand, M. Bhatia..... 200

Pressure shift mediated anoikis of endothelial cells in the flow field in vitro
J. Hu, E. Y. Zhang, J. Wu, W. L. Xu, H. Q. Chen, Y. K. Shi, Y. Q. Guo..... 206

Mg/Al complex oxides-A new type of solid basic catalyst for epoxidation
H. Miao, S. C. Xu, H. N. Wang, W. X. Qin, L. L. Zhang, J. M. Zhang, J. Yang, Z. Dai, G. Zheng, E. Q. Tang..... 213

Biclustering of time-lagged gene expression data using real number
F. Liu, L. B. Wang..... 217

Restriction fragment length polymorphism in the exon 2 of the BoLA-DRB3 gene in Chinese Holstein of the south China
X. X. Wu, Z. P. Yang, X. L. Wang, Y. J. Mao, S. C. Li, X. K. Shi, Y. Chen..... 221

Copyright©2010 SciRes

9771937687001013